UNIVERSITY OF SOUTHAMPTON

FACULTY OF PHYSICAL SCIENCES AND ENGINEERING

Electronics and Computer Science

The Characterization and Enhancement of Light Scattering for Thin Solar Cells

by

David N. R. Payne

Thesis for the degree of Doctor of Philosophy

June 2014

UNIVERSITY OF SOUTHAMPTON

ABSTRACT

FACULTY OF PHYSICAL SCIENCES AND ENGINEERING
Electronics and Computer Science

Doctor of Philosophy

THE CHARACTERIZATION AND ENHANCEMENT OF LIGHT SCATTERING FOR THIN SOLAR CELLS

by David N. R. Payne

Photovoltaic (PV) power is one of the most promising technologies for worldwide clean and sustainable energy production and as the technology begins to enter the mainstream the requirement for efficient use of materials becomes increasingly important. However, reducing material thickness typically lowers optical absorption, leading to lower cell efficiency. One proven method for enhancing absorption in a thin device is by texturing interfaces, typically achieved in the top transparent conducting oxide (TCO) of a thin-film design. This works by scattering transmitted light and therefore increasing its effective optical path length within the absorber layer. However, introducing rough surfaces to a PV device can lead to fabrication issues and also increases surface recombination which is detrimental to the electrical characteristics of the end device. In recent years, possible alternatives to reliance on random texturing have been found through the use of optimized diffraction gratings and the plasmonic effects of metal nanoparticles. In this work, comprehensive optical characterization has been carried out on a range of samples using traditional and novel techniques. In particular, a custom built wavelength and angle resolved scattering (WARS) measurement system has been developed and used to determine key characteristics that would remain undetected by conventional measurements. The investigation of several commercial and experimental TCO films has been carried out and clear links between topography and optical characteristics have been determined. These textured surfaces have also been modelled using finite difference time domain (FDTD) simulations which have shown good agreement with measurement results. This has allowed for further investigation of the effects of TCO topography through simulation which has revealed that scattering is best enhanced by increasing the aspect ratio of the texture rather than the overall scale. Periodic arrays of silver nanoparticles incorporated into a thin-film solar cell back-reflector design have also been extensively characterized and modelled and shown to provide scattering through both diffraction and plasmonic mechanisms, leading to an increase in useful absorption by up to 140% in comparison to a planar device.

Contents

Declaration of Authorship

I, David N. R. Payne , declare that the thesis entitled *The Characterization and Enhancement of Light Scattering for Thin Solar Cells* and the work presented in the thesis are both my own, and have been generated by me as the result of my own original research. I confirm that:

- this work was done wholly or mainly while in candidature for a research degree at this University;
- where any part of this thesis has previously been submitted for a degree or any other qualification at this University or any other institution, this has been clearly stated;
- where I have consulted the published work of others, this is always clearly attributed;
- where I have quoted from the work of others, the source is always given. With the exception of such quotations, this thesis is entirely my own work;
- I have acknowledged all main sources of help;
- where the thesis is based on work done by myself jointly with others, I have made clear exactly what was done by others and what I have contributed myself;
- parts of this work have been published as:

    1. D. Payne, D. Bagnall, 'Measurement and Simulation of the Scattering from Textured TCOs for Light Trapping in Thin Film Photovoltaics', Solar 2014 Conference, May 2014.
    2. D. Payne, D. Bagnall, 'Optimisation of Thin Film Silicon Solar Cell Back Reflectors for Light Trapping Using Periodic Arrays of Silver Nanoparticles', 10th Photovoltaic Science Application and Technology Conference, 2014.
    3. A. Asadollahbaik, S. A. Boden, M. D. B. Charlton, D. Payne, S. Cox, and D. Bagnall, 'Reflectance Properties of Silicon Moth-eyes in Response to Variations in Angle of Incidence, Polarisation and Azimuth Orientation', Optics Express Vol. 22, Iss. S2, 2014.

4. L. Crudgington, A. Rind, D. Payne, D. Bagnall, 'The Effects of Varied Deposition Conditions, including the use of Argon, on Thin-Film Silicon Solar Cells prepared using PECVD', Journal of Molecular Crystals and Liquid Crystals, 2014.
5. R. Sesuraj, D. Payne, T. Temple, D. Bagnall, 'Tuneable Low-loss Plasmonic Mirror for Diffuse Optical Scattering', 9th Photovoltaic Science Application and Technology Conference, 2013.
6. A, Rind, M. Banakar, D. Payne, R. Sesuraj, D. Bagnall, 'Light-trapping for thin film amorphous silicon solar cells', 8th Photovoltaic Science Application and Technology Conference, 2012.
7. D. Payne, T. Temple, D. Bagnall, 'Tuning Light Scattering by Periodic Metal Nanoparticle Arrays for Solar Cell Applications', Materials Research Society: Fall Meeting, 2011.
8. N. McSporran, D. Payne, D. Bagnall, et al., 'Control of TCO Properties to Maximise the Efficiency of Thin Film Silicon Modules', 25th European Photovoltaic Solar Energy Conference, 2011.
9. D. Payne, D. Bagnall, 'Characterisation of the Optical Properties of Periodic Metal Nanoparticle Arrays for Light-Trapping', 7th Photovoltaic Science Application and Technology Conference, 2011.
10. D. Payne, S. Boden, E. Delahoy, D. Bagnall, 'Characterization of Experimental Textured ZnO:Al Films for Thin Film Solar Cell Applications and Comparison With Commercial and Plasmonic Alternatives', 35th IEEE Photovoltaic Specialist Conference, 2010.
11. D. Payne, S. Boden, T. Temple, A. Delahoy, D. Bagnall, 'Characterisation and Enhancement of Light Scattering Through TCOs for Thin Film Silicon Solar Cell Applications', 6th Photovoltaic Science Application and Technology Conference, 2010. (Best Paper award).

Signed:.....

Date:.....

Acknowledgements

I would first like to thank my supervisor, Prof. Darren Bagnall, for offering me the opportunity to undertake a PhD at the University of Southampton and for his continued guidance and support throughout what has been a challenging and rewarding journey. Despite his many other responsibilities, he has always managed to find the time to provide assistance when necessary and to ensure that adequate resources were always available to allow my research to progress. I also offer my sincere appreciation to my respected colleagues Dr. Stuart Boden, Dr. Tristan Temple and Dr. Owain Clark for giving up much of their time to help me by offering their expertise and vast amounts of useful advice. Thanks also to Dr. Martin Charlton for his assistance with several optical experiments and for allowing me substantial use of the motorized goniometer equipment which is in high demand, and to Dr. Harold Chong who not only provides a wealth of knowledge but also manages to perpetually maintain a positive attitude which helps make the Nano Research Group an enjoyable workplace. I would also like to acknowledge the EPSRC for providing the financial support for my work along with Dr. Heather Yates and Dr. Alan Delahoy for providing several of the samples studied within this investigation.

Furthermore, I offer my sincere thanks and appreciation to the many other colleagues and friends at Southampton University who have helped me throughout my research, both academically and personally. In particular, Mehdi, Akhtar, Asa, Lee, Steffi, Rob, Matt and Mike, I have thoroughly enjoyed working with each of you. A special thanks must also go to my good friend and co-worker Katrina Morgan, who has not only regularly assisted me with cleanroom based work but has also been an endless source of entertainment and enthusiasm, able to brighten up even the most demoralizing of days. Outside of work, thanks to my good friends, Andrew, Lee, Tristan, Peter and Matthew with whom I have shared countless good times throughout both my postgraduate and undergraduate studies, often providing stress relief when it has been most needed. I also thank Abigail, Kerry, Lucy, Jae, Bridie, James, Sharon, Jeanne and Amber for their continuing friendship and their support along the way. Finally, I thank my family, all of which have always been encouraging and supportive of my studies, despite my often heavy workload leading to infrequent and short-lived visits home. Without them I would certainly not be where I am today.

Chapter 1

Introduction

1.1 Solar Power and Light-Trapping

As a worldwide community we constantly consume a huge amount of electricity, with global consumption in 2013 estimated to be around 160 PWh [1]. The majority of this energy is produced using fossil fuels, specifically, data from 2012 showed that oil accounted for 33.1%, coal for 29.9% and natural gas for 23.9% [2]. However, the by-products from these methods of electricity generation can have a severely detrimental impact on both the local and global environment. Of particular concern is the worldwide issue of climate change caused by CO_2 emissions from the burning of fossil fuels. Fossil fuel based energy production also faces the serious issue of diminishing resources. The exact extent of the Earth's remaining fuel resources is difficult to determine, but some studies estimate that oil and gas resources will peak in less than 30 years [3]. One solution to reduce CO_2 emissions from energy production is to increase the use of Nuclear power. However, although nuclear power generation is a well established and proven technology, it also presents many risks due to the handling of nuclear waste and the possibility of radiation leaks from damaged power plants. These risks were gravely highlighted by the catastrophic failure at Japan's Fukushima nuclear power plant in 2011. The result of which has severely lowered confidence in nuclear power and has led Japan to reduce it's nuclear power output by 89% in 2012 alone [2]. Although many of these issues surrounding fossil fuels and nuclear power are the subject of much debate, it cannot be denied that these resources are finite and will become increasingly expensive as reserves approach depletion. Furthermore, limited fossil fuel resources are required for applications outside of grid energy production such as the manufacturing of plastics and fuel for aviation. This further emphasises the need for resource reservation and the absolute necessity for alternative, sustainable energy solutions.

Many possible options exist, including established and well understood technologies such as wind, hydro and solar power as well as unproven technologies such as fusion

generators. New and as yet unproven technologies may have a huge impact on energy production in the future but this is likely to be decades away and more immediate medium term solutions are certainly required. Established renewable technologies are therefore essential for the foreseeable future. Whilst wind power is considered to be quite safe, it is also highly unpredictable and subsequently unreliable and there are strict limitations regarding where generators can be placed as they can interfere with crucial radar systems and the local wildlife. Hydro generation is capable of producing huge amounts of electricity and is more predictable than wind power but can only be implemented in very particular geographical locations, limiting the potential for increasing production. Hydro-electricity also requires substantial upfront investment and setup time, and the building of large damns can lead to serious environmental damage [4]. In contrast, solar power can be installed in a variety of environments and is a safe technology. Crucially, the solar power available to us is abundant, virtually limitless in comparison to any other energy source. The sun bathes the earth with a continuous 174 PW of solar energy, 120 PW of which enter the earth's atmosphere and is available to us [5]. The 2013 annual world energy consumption of 160 PWh equates to the amount of energy we receive from the sun in just 80 minutes. However, harnessing enough of this energy to meet the current global demand would require an enormous area of solar cell coverage. For example, if 10% efficient solar cells were used then they would need to cover around 0.16% of the earth's surface to fully satisfy current demand [6]. That equates to roughly 816,000 km^2, which is about the same size as Spain and Italy combined. Naturally, if the efficiency of the devices is improved then less coverage will be required but in any case a very large number of solar modules would need to be manufactured and installed in order for solar to account for a significant portion of energy production. Whilst photovoltaics currently only accounts for a tiny percentage of global power production, the many advantages of solar power have led to the technology leading the growth of renewable electricity generation capacity with market outlooks predicting this growth to continue into the foreseeable future, see Figure 1.1 [7]. Whilst much of this growth is dependant on politics and economics it is also reliant on technological advances leading to higher photovoltaic conversion efficiencies at lower costs.

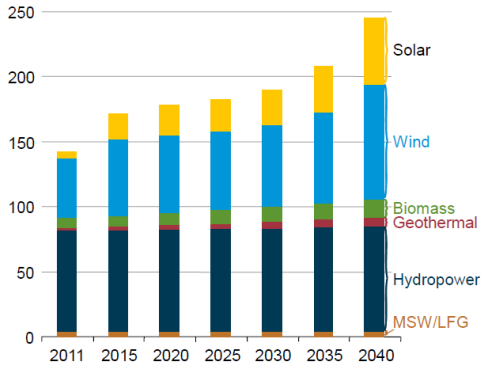

Figure 1.1: Renewable electricity generation capacity by energy source, with predictions up to 2040 [7].

Photovoltaics is traditionally considered to be an expensive method of energy generation but efficiencies are steadily rising whilst fabrication costs gradually decrease leading to better \$/W values. This trend, combined with the increasing cost of energy produced by fossil fuels, means that in some cases grid parity has already been reached, demonstrating that solar power is on the path to becoming a major energy producer. This is backed up by the impressive and steady growth of the photovoltaic (PV) market which has shown a minimum of 35% growth rate for the last ten years [8]. This equates to the overall power produced by PV almost doubling every two years, so whilst solar energy production currently accounts for only a tiny percentage of our overall energy supply, it could become a majority producer in just a few decades. An excellent example of the progress of photovoltaic power generation is the case of Germany in which strong political drives towards renewable energy sources resulted in Germany reaching a 25 GW photovoltaic capacity by the beginning of 2012 [9]. Germany's peak power demand at this point was 80 GW, PV could therefore account for 31% of this. However, it should be noted that one of the few drawbacks of photovoltaic power is intermittency due to the fact that energy is only produced during daylight hours and production can vary significantly. Fortunately, the times that photovoltaic generation is most significant correlate with typical working hours and thus peak electricity demand. This is highlighted in Figure 1.2 which shows electricity production in Germany for the Month of July in 2013, where at some points solar power accounts for around 50% of total production [10].

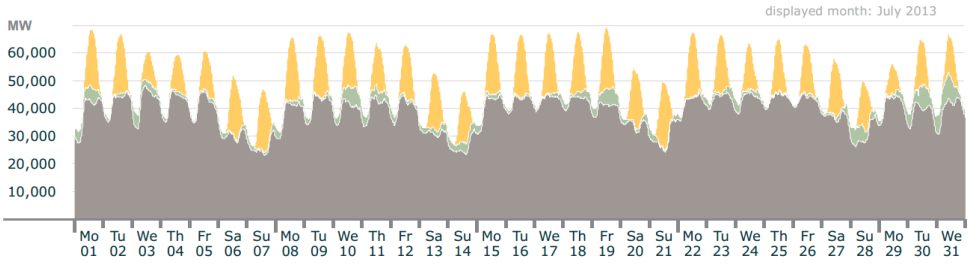

Figure 1.2: Electricity production in Germany for the Month of July in 2013 [10].

The dominant photovoltaic technologies are the 'first generation' devices based on crystalline silicon (c-Si) and multicrystalline silicon (mc-Si) wafers. However, 'second generation' thin-film solar cells should be cheaper to produce. Naturally, thin solar cells use far less materials than conventional bulk cells and are lighter and less wasteful. In some cases it is also possible to fabricate thin cells on flexible substrates, allowing for roll-to-roll production. For a long time amorphous silicon (a-Si) and microcrystalline silicon (μc-Si) based thin-film solar cells were considered a hugely promising technology, largely due to silicon being an abundant, non-toxic and well understood semiconductor material. However, in recent years thin-film silicon research has only produced small, incremental gains in efficiency and growth of the technology has fallen behind c-Si and mc-Si alternatives, as a result of this, most thin-film silicon producers have ceased production in the last two or three years. One of the key drawbacks limiting thin-film

technology is the inherent thinness of the layers that leads to less light absorption than in thicker c-Si and mc-Si devices. This in turn leads to lower short circuit currents and lower overall levels of efficiency and power generation. For thin-film a-Si and μc-Si solar cells, the impact of this issue is traditionally partly alleviated by the use of light-trapping techniques. Although thin-film a-Si and μc-Si based devices are no longer competitive, technological advances are leading to the possibility of thinner c-Si and mc-Si solar cells which could benefit significantly from similar light-trapping approaches.

The most common light-trapping method is to texture the interfaces of the device structure. This causes light to scatter as it enters the device, thus increasing the optical path length of light in the absorber layer and increasing absorption and subsequently current and efficiency. Although much research has been carried out in the area of light-trapping using textured interfaces, there is still some debate regarding the optimal structure for interface texturing and this will vary depending on the exact device structure. This approach is also known to have limitations, the primary one being that whilst increasing the interface roughness will increase light scatter, it also increases surface area which has a detrimental effect on the device. Furthermore, large features can lead to fabrication issues when subsequent layers are deposited. Several alternatives to randomly textured interfaces for light-trapping have therefore been developed, two of the most promising of which are the use diffraction gratings and of the plasmonic properties of metal nanoparticles. These approaches can be applied to photovoltaic devices in a huge variety of novel ways and have the potential to scatter specific wavelengths of light into absorber layers at high angles without causing dramatic increases in surface area or complex device fabrication issues.

This investigation aims to fully explore the light-trapping characteristics of these conventional and novel approaches allowing conclusions to be made regarding the capacity for further improvements to light-trapping and it's role in improving thin photovoltaics. In order to do this a significant amount of work has been focused on the accurate characterization of light scatter and this has led to the development of a custom-built measurement system which is uniquely capable of determining a comprehensive range of optical characteristics beyond that of traditional scattering measurements. This tool, combined with more established measurement techniques has been used to extensively characterize a variety of traditional and novel light-trapping schemes. The measured characteristics have also been used to validate numerical simulations which are then able to be extended to allow for further, more detailed investigation. Throughout this investigation amorphous silicon (a-Si) and microcrystalline silicon (μc-Si) layers have been used as test-bed materials, largely due to the high degree of control offered by their deposition methods. However, the light-trapping mechanisms, design approach, and characterization techniques used here can also be applied to the many alternative materials used for thin photovoltaics.

1.2 Thesis Structure

Chapter 2 of this report begins with the basic background of photovoltaics along with brief details regarding the various core technologies. This is followed by a more in depth explanation of the technology of thin silicon solar cells as this material is used as a test-bed within this investigation. A discussion of the crucial requirement for efficient light-trapping and the underlying physics behind current light-trapping techniques is then detailed along with an overview of the origins and achievements of the various approaches. Optical simulation methods appropriate for the various light-trapping schemes are then discussed with an emphasis on the numerical finite difference time domain (FDTD) technique primarily used within this work. Chapter 3 details the complexities of characterizing the scattering of light and consequential light-trapping. Traditional measurements are reviewed and explained and the novel wavelength and angle resolved scattering measurement technique, developed specifically for this investigation, is described and tested in detail. An investigation into the conventional light-trapping scheme of randomly textured TCOs is given in Chapter 4. This consists of the analysis of several commercial and experimental textured TCOs through surface microscopy and optical characterization. Chapter 5 then extends this work by comparing TCO measurements to numerical simulations in order to first validate the simulation approach and to then extend the simulations to investigate characteristics that cannot be determined experimentally. Chapter 6 is a study of the light-trapping potential of the alternative approach of using periodic metal nanoparticle arrays incorporated into the back-reflector of a thin silicon solar cell device. The influence of array positioning and periodicity are thoroughly examined using experimental measurements and simulations. Overall conclusions and a discussion of potential future work is given in Chapter 7.

Chapter 2

Review of Photovoltaics and Light-Trapping.

In this section a brief overview of photovoltaics technologies is followed by a detailed discussion of thin silicon solar cells. The principles of light-trapping are then discussed with a focus on three main mechanisms for light manipulation; random texturing, diffraction and plasmonics. A brief overview of well established analytical modelling techniques is then followed by detailed information on the numerical technique of finite difference time domain (FDTD) simulations.

2.1 Photovoltaic Technologies

Solar photovoltaic (PV) energy production is based on the photovoltaic effect, this is the process by which electromagnetic radiation (light) is converted into electricity. The effect was first observed in 1839 by French physicist Alexandre-Edmond Becquerel whilst he experimented with electrolytic cells [11]. From then on, various other researchers noted photovoltaic effects in a selection of different materials and in 1883 Charles Fritts developed a 'solar cell' which was fabricated using solid selenium and achieved an efficiency of below 1% [12]. Interest in the field of photovoltaics continued to grow with many notable scientists contributing to research including Nikola Tesla and Albert Einstein [13, 14]. The first published work regarding modern silicon solar cells was carried out by D. Chapin, C. Fuller and G. Pearson at Bell laboratories in 1954 [15]. In this work the authors report on the direct conversion of light to electricity via a p-n junction in silicon (Si) with an efficiency of around 6%. At that time the authors estimated that silicon solar cells could potentially achieve efficiencies of up to 22%. This indicated solar photovoltaic energy as a technology with huge potential as a primary energy source. Research steadily increased from this point onwards and several generations of solar cell devices were developed.

Current photovoltaic technologies can be loosely divided into first, second and third generation (1G, 2G and 3G), see Figure 2.1. 1G devices are traditional crystalline silicon (c-Si) or multicrystalline (mc-Si) solar cells. These were the first type of cells to be made commercially available, and have undergone over 50 years of research and development. They are typically high cost, high efficiency devices with a single p-n junction. The best known design for a 1^{st} generation solar cell is the passivated emitter, rear locally diffused (PERL) cell. This type of cell was optimized in 1999 by Martin Green et al. [16]. At the time of development the cell achieved an efficiency of 24.7% but under the new revision of the solar spectrum standard the calculated efficiency of the cell increased to the significant milestone of 25% [17]. To date, this efficiency for a single junction c-Si solar cell has not been improved upon although theoretically the maximum efficiency that can be achieved within a 1G device is around 30% [18].

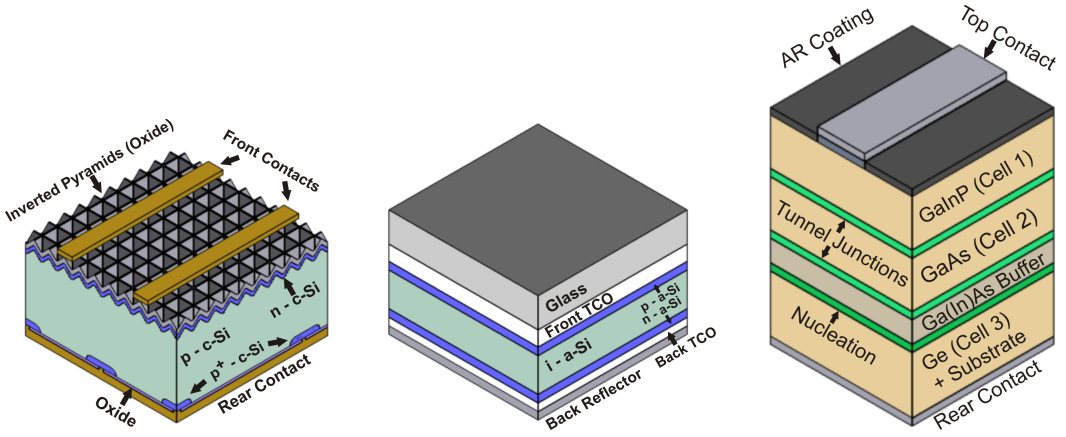

(a) 1G: PERL cell, adapted from [16].

(b) 2G: Thin-film.

(c) 3G: Multi-junction.

Figure 2.1: Example schematics of different generations of solar cells.

2G solar cells expand upon the single junction concept of 1^{st} generation cells but aim to reduce the required device material and processing waste whilst maintaining respectable efficiencies, therefore lowering the \$/W cost. Most 2^{nd} generation solar cells are known as thin-film cells, they typically have thicknesses of the order of single to tens of microns. A variety of materials are used to make thin-film cells, historically the most commonly researched thin-film photovoltaic materials have been various forms of silicon, cadmium telluride (CdTe) and copper indium gallium selenide (CIGS) [19]. However, more recently dye-sensitized solar cells (DSSC) , organic photovoltaics (OPV) and perovskite cells have been the subject of much interest and research. In general, all of these materials absorb the solar spectrum more readily than c-Si, thus very thin absorber layers can be used. Currently, CIGS and CdTe cells have reached higher efficiencies than their thin-film silicon counterparts, however, they also have a number of difficult issues with up-scaling that result in large reductions for module efficiencies [19]. In the case of CIGS there are also concerns regarding limited indium resources. Both DSSC and OPV devices have relatively low efficiencies, and in the case of OPV,

short device lifetimes. Perovskite solar cells have made huge progress in the last 2 years, achieving verified efficiencies of over 14% and must therefore now be considered as one of the most promising thin-film technologies [20, 21]. Thin-film silicon solar cells have shown only incremental progress in recent years, however, a-Si and μc-Si are relatively simple and controllable materials to deposit, they have therefore been used as a test-bed absorber material for this investigation and are discussed in further detail in Section 2.1.1.

3G solar cells aim to provide efficiencies much higher than those achievable by standard single-junction devices. There are several design approaches that can be placed in the category of 3^{rd} generation, the most notable of which are; multi-junction cells, intermediate-band cells, hot carrier cells and spectrum converters [22]. To date the only proven 3G solar cell technology is that of multiple junctions. This technology has been used to create what is currently the highest efficiency solar cell. This cell is based on an InGaP/GaAs/InGaAs structure and has achieved a certified efficiency of 44.4% $\pm$2.6 under concentrated light [23]. The record efficiency for a solar cell under 1 sun illumination stands at 38.8% $\pm$1.9 and was achieved by a five junction GaAs/InP based device [23].

2.1.1 Thin Silicon Solar Cells

The concept of thin solar cells has numerous advantages over bulk alternatives; primarily, less material is required which leads to faster and cheaper fabrication and consequently cheap and lightweight devices. Silicon is an excellent candidate for mainstream solar cell production for several reasons, one of the most significant being the abundance of silicon. Silicon makes up around 27.7% of the Earth's crust, and can therefore easily meet any expected demands. Due to the highly developed microelectronics industry, silicon is also a well understood material with a large range of processing equipment already fully developed.

The absorption characteristics of a semiconductor are dependant on the optical bandgap of the material. The bandgap of c-Si is around 1.1 eV, this means that all wavelengths of light with energy equal to or greater than this bandgap energy may be readily absorbed. Wavelength and energy are related by equation 2.1.

$$E = \frac{hc}{\lambda} \tag{2.1}$$

Where h is Planck's constant ($4.13 \times 10^{-15} eV/s$), c is the speed of light (3×10^8m/s) and λ is the wavelength. For a bandgap of 1.1 eV, wavelengths of around 1100 nm and less can be absorbed. This covers a large part of the solar spectrum, shown in Figure 2.2. However, each absorbed photon only contributes energy equal to that of the bandgap,

excess energy from shorter wavelengths of light will be lost as heat. A bandgap of 1.1 eV is the case for c-Si but silicon can be deposited in a variety of ways leading to different levels of crystallinity such as micro-crystalline and amorphous silicon (μc-Si and a-Si respectively) and this has a strong impact on the bandgap and absorption properties of the material. Whilst μc-Si typically has a similar bandgap to c-Si, a-Si is substantially different and has a bandgap ranging from around 1.7 eV to 1.9 eV [24]. This corresponds to maximum wavelengths of absorption between 620 nm and 730 nm, see Figure 2.2. Thus less of the solar spectrum is absorbed, but each absorbed photon will contribute more energy. The absorption coefficient of a-Si is also much higher than c-Si due to a-Si having a pseudo-direct bandgap.

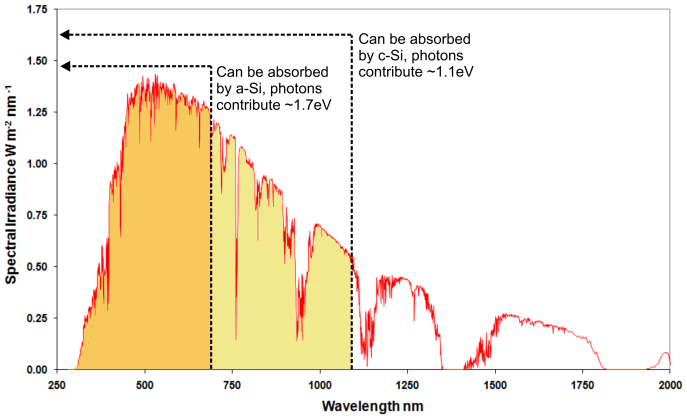

Figure 2.2: AM 1.5 solar spectral irradiance, based on data from ASTMG173-03 std.

It is therefore clear that when designing any single junction device, a compromise must be made regarding the material used and hence the bandgap. It has been calculated that the ideal bandgap for absorbing the most energy from the solar spectrum is around 1.4 eV [25], this shows that neither c-Si or a-Si have the perfect bandgap but they are both reasonably close. This bandgap induced limitation is present in all single junction photovoltaic devices and is known as the Shockley-Queisser limit [18]. For the case of single junction c-Si devices, this limits the maximum theoretical efficiency to around 30%. The most popular method for exceeding this limit within a photovoltaic device is to make a multi-junction cell.

Single Junction Thin Si Solar Cells

The most common type of thin silicon solar cells are based on hydrogenated amorphous silicon (a-Si:H) or hydrogenated micro-crystalline silicon (μc-Si:H). These forms of silicon can be deposited using silane gas and chemical vapour deposition techniques under different conditions. When deposited without the aid of hydrogen, a-Si and μc-Si materials contain large quantities of dangling bonds and these act as recombination centres, dramatically lowering carrier lifetime and also making it impossible to dope

the material and create a p-n junction. Hydrogen is therefore required to passivate a large number of these bonds, enabling doping and increasing carrier lifetime. P-type layers can be fabricated by adding diborane to the gas flow and phosphine can be used to make n-type layers. Doped layers contain several orders of magnitude more defects than undoped layers so a large intrinsic region is required to act as the absorber layer. Traditional bulk semiconductor based solar cells have inter-digitated metal fingers as front contacts, however, for thin-film solar cells the low carrier lifetimes do not allow for spaced out contacts. Therefore a transparent conducting oxide layer covering the entire front surface of the cell is typically used.

Initial research and development showed that thin-film a-Si solar cells could have huge potential, however, enhancements in cell efficiencies have been small and incremental and in recent years the technology has been largely overtaken by alternatives. Whilst a-Si benefits from the advantage of having a high absorption coefficient, it's large bandgap limits the absorption wavelength range and the material suffers from a light induced degradation effect, now known as the Staebler-Wronski effect (SWE) [26]. The result of this phenomena is a significant increase in defects after light soaking which leads to decreased carrier lifetimes. It has been shown that this increase in defect density can be reversed by annealing at temperatures greater than 150° [26], but the device will then degrade again, hence this is not a practical solution for a commercial product. As a results of the SWE, thin-film a-Si:H cells are usually described by their stabilized efficiency which is often around 90% of the initial efficiency [27]. Amorphous silicon thin-film solar cells are typically fabricated using a superstrate configuration with a p-i-n junction. It is preferential that the p-type material is the first part of the junction to be hit by light because holes have a lower mobility than electrons in a-Si:H, as most of the photo-generated carriers are created at the front part of the cell, having the p-layer here means the holes have a shorter distance to travel (from the i layer to the p), so the collection efficiency of holes is increased. A standard a-Si:H thin-film solar cell design with typical layer heights is shown in Figure 2.3. At the time of writing the record efficiency for a stabilized thin-film a-Si:H solar cell was 10.1% ±0.3% [23].

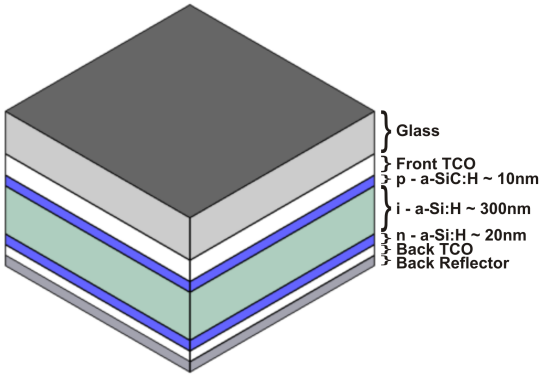

Figure 2.3: Schematic of standard thin-film a-Si solar cell.

Micro-crystalline silicon can be deposited using similar techniques as for a-Si, although deposition parameters require significant alterations and higher temperatures are usually required [28]. Micro-crystalline is a mixed phase state in which the silicon structure essentially consists of small silicon crystals with diameters of a few tens of nanometers embedded in surrounding amorphous material. These crystallites occur in bunches which typically have diameters of around a micron. As the crystallites themselves are within the nanometer range, μc-Si is also sometimes referred to as nano-crystalline silicon (nc-Si). The ratio between a-Si and c-Si can be varied and this has a major effect on the properties of the material. Research has shown that the best μc-Si solar cells require a large proportion of a-Si. One of the most crucial properties that changes with this ratio is the bandgap of the material. As could be expected, micro-crystalline layers with a large percentage of c-Si have a bandgap close to 1.1eV, larger percentages of a-Si lead to a higher bandgap value. The magnitude of the light induced SWE degradation has also been found to be dependent on the ratio of the material structure. A higher percentage of crystallinity leads to a reduced degradation, but even with very few crystallites the degradation is significantly reduced in comparison to pure a-Si:H. Micro-crystalline cells are usually fabricated using a superstrate, p-i-n configuration, similar to a-Si devices. The optimal intrinsic layer thickness in a μc-Si:H cell is between 1μm and 2μm, significantly larger than typical a-Si intrinsic layers. Micro-crystalline cells have shown substantial potential and efficiencies that are in some cases slightly higher than a-Si:H cells. At the time of writing the official record efficiency for a laboratory μc-Si:H solar cell was 10.8% $\pm$0.3% [23]. Whilst a-Si and μc-Si have failed to remain competitive as a commercial technology, the low costs and high level of control available when depositing layers of these materials means that they can still be extremely useful as a test-bed for research and development, particularly for the case of μc-Si which can have similar optical properties to it's crystalline counterpart. This is useful as recent advances in fabrication have led to the possibility of ultra-thin crystalline silicon solar cells achieving respectable efficiencies with a thickness of around 10-20 μm [29]. Ultra-thin c-Si therefore has the potential to reduce material waste for future c-Si solar cell production, but as the thickness of the c-Si layer is reduced, light-trapping techniques will be required in order to maintain high efficiencies. These techniques could be optimized using test μc-Si layers in order to reduce research and development costs.

Multi-junction Thin Silicon Solar Cells

One advancement of thin-film a-Si and μc-Si photovoltaics that should be noted is that of Multi-junction thin silicon solar cells. Multi-junction cells consist of a stack of several p-n junctions, usually two or three. The major advantage of this design is the ability to use different materials for each of the separate junctions. The use of different materials or alloys means that the solar cell structure can have multiple bandgaps. If the top junction (the first part of the junction that light hits) is made from materials with a

large bandgap such as a-Si at 1.7 eV then much of the shorter wavelengths of light will be efficiently absorbed here. Longer wavelength light will simply transmit through the first junction and can then be absorbed in the second junction if a material with a lower bandgap is used (e.g. μc-Si at around 1.1 eV). This means that a large portion of the solar spectrum can be absorbed, similarly to a single junction low bandgap device, but unlike a single junction device, the more energetic shorter wavelengths of light will contribute significantly more energy as they are absorbed by the first, wide bandgap junction. This concept can be expanded to further junctions to allow for even more efficient absorption of the solar spectrum, however, each additional junction adds to the complexity and cost of the cell design and fabrication, so as more junctions are added their associated device efficiency gains will become less worthwhile. Hence the majority of current research is focused on tandem (two junctions) and triple junction architectures. Silicon is a particularly good material for Multi-junction solar cells because as discussed previously, altering deposition parameters allows for different qualities of material and therefore different bandgaps. There are some strict design limitations that apply to all multi-junction cell designs, one of the most significant issues is that with conventional multiple junction cell structure the junctions are effectively joined in series. This means that if one junction provides a low short circuit current (J_{sc}) then this will severely limit the current of the whole cell and consequently lower the overall efficiency. For an optimal device, it is therefore necessary to match the currents generated at each junction.

There are numerous design options for Multi-junction thin-film silicon solar cells, the most established being the micromorph (tandem) cell initially developed in 1996 by researchers at IMT Neuchâtel [30] (seeFigure 2.4).

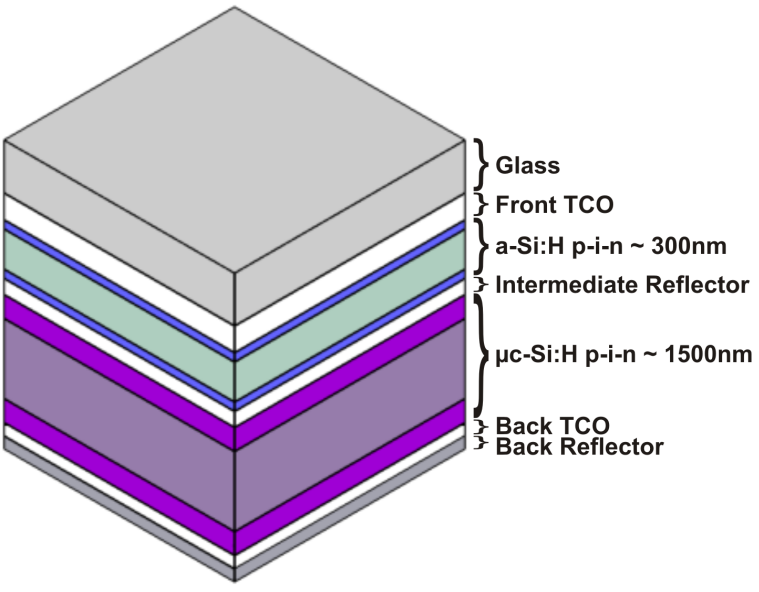

Figure 2.4: Schematic of micromorph solar cell, adapted from [31].

This type of cell design makes excellent utilization of the solar spectrum and has shown superior characteristics in comparison to single junction a-Si:H or μc-Si:H cells. However, current matching is a particular problem for micromorph solar cells because the top a-Si:H layer usually outputs significantly less current than the bottom μc-Si:H layer. Typically the current of the top cell could be enhanced by increasing the thickness of the absorption layer, but in the case of a-Si:H this leads to increases in the light degradation SWE. This means that a compromise must be made between obtaining high, well matched currents and reducing the SWE to allow for a respectable stabilized efficiency. The issue is further exasperated by the fact that the solar spectrum incident on a solar cell will change throughout the course of a day and therefore the current generated by each junction will also change. Various efforts have been made to alleviate this current matching limitation with techniques such as the utilization of intermediate reflectors between the junctions resulting in significant improvements in top cell current [32]. Four terminal devices are another technique for removing the constraint of current matching, this involves using insulating materials to separate the junctions [33]. At the time of writing the highest official efficiency of a micromorph solar cell was 12.3% $\pm$0.3 [23]. Efforts have also been made within the research and development of more ambitious triple junction thin-film silicon solar cells with devices based on an a-Si:H/nc-Si:H/nc-Si:H structure showing stabilized efficiencies of up to 13.4% $\pm$0.4% [23]. In contrast, non-Si based Multi-junction solar cells based on GaAs have achieved the highest verified efficiencies of up to 37.9% under standard test conditions increasing to 44.4% under concentrated light. However, these cells are significantly more complicated and expensive to fabricate.

All of the basic single and Multi-junction cell designs discussed in this section can suffer from a lack of absorption due to thin absorber layers. The respectable efficiencies quoted here have only been achieved with the additional utilization of light-trapping techniques. This topic is the core focus of this report and is discussed in detail in Section 2.2.

2.2 Light-Trapping

Thin photovoltaic devices have many advantages but they also have the significant drawback that thinner layers naturally lead to reduced optical absorption. As light is incident on the surface of a solar cell, some of the light is reflected and some is transmitted into the device. With bulk solar cell devices the majority of light that makes it through the front interface of the cell is absorbed in the relatively thick semiconductor layer. In the case of thin solar cells however, the absorber layers may be so thin that much of the light is transmitted through the semiconductor. The light then hits the back-reflector of the device where it is mostly reflected and therefore given another chance to undergo useful absorption. However, a significant proportion of this reflected light may once again transmit through the active layer and escape from the front surface of the cell. This can lead to significant losses in optical absorption which in turn leads to lower current characteristics and lower overall cell efficiency. The obvious solution to this problem is to increase the thickness of the absorber layer of the solar cell, but doing this can decrease carrier collection and increases the time and costs required to fabricate a device as well as significantly increasing the SWE degradation in the case of a-Si based devices.

Solar cells therefore ideally need to be geometrically thin to enable the extraction of carriers and to reduce costs and waste but optically thick in order to absorb as much light as possible. A popular solution to this problem is to use special techniques to trap light within the cell structure, thus taking advantage of the fact that whilst the vertical thickness of the absorber layer may be very small, it is laterally relatively large. Therefore, if the light is scattered at high angles into the plane of the active layer then the optical path length of the light within the absorber is increased. Furthermore, if the angle of scatter is sufficiently large then the light will experience total internal reflection at the layer interfaces and be effectively trapped within the absorber. Currently the most popular and successful technique for achieving light-trapping is to texture the interfaces within the device structure, a random texture is traditionally used but ordered structures such as diffraction gratings are also known to be effective. Additionally, over the past decade there has been considerable interest and research focused on the possibility of using the plasmonic properties of metal nanoparticles to enhance scattering within a solar cell device. These light-trapping techniques will be discussed in detail in Sections 2.2.1 to 2.2.3.

2.2.1 Random Textured Interfaces

Random textured interfaces are a well established technique traditionally used to achieve light scattering within thin-film a-Si solar cells. The most common method for introducing textured interfaces is to texture the front transparent conducting oxide

(TCO) contact of the device. If the cell is then fabricated in a superstrate configuration then subsequent layers are deposited onto the textured front TCO and the texturing is replicated at other interfaces within the device. Textured interfaces scatter light by introducing angled planes to the incident photons causing light transmitted through the interface to undergo a change in angle due to refraction. The exit angle of the light is dependent on the angle of incidence and the ratio of the refractive index values of the media either side of the interface and can be calculated using Snell's law, shown in Equation 2.2. This effect is illustrated in Figure 2.5.

$$\theta_2 = \sin^{-1}(\frac{n1}{n2}\sin\theta_1) \tag{2.2}$$

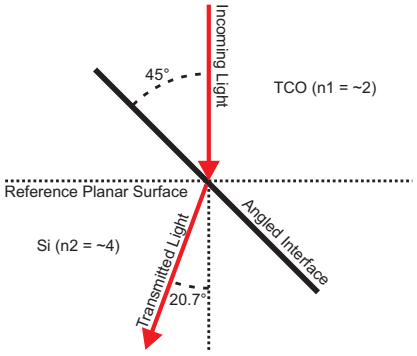

Figure 2.5: Illustration of Snell's Law.

Generally the texturing applied to TCOs is of the nanometer scale with typical features sizes of hundreds of nanometers and RMS roughness ranging from around 20 nm to 200 nm. The relatively large features of the textured interface introduce a broad range of angles to the incident light causing a scattering effect due to Snell's law. The redistributed light will then encounter more textured interfaces which will further enhance scattering, therefore providing a dramatic increase in the optical path length of light within the device as illustrated in Figure 2.6.

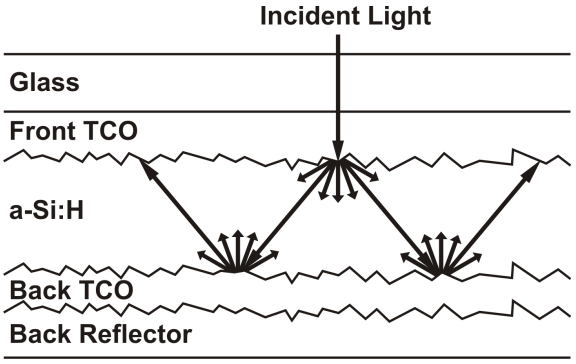

Figure 2.6: Light scattering effect of multiple textured interfaces.

The maximum theoretical enhancement factor achievable using random texturing was determined by Yablonovitch and Cody in 1982 [34] to be $4n^2$, where n is the real part

of the refractive index of the absorbing medium. For c-Si this corresponds to a possible path length enhancement of around 50 times. A greater enhancement may be observed in thin-film a-Si devices due to the higher refractive index of a-Si.

Texturing not only increases the path length of light through scattering but it can also be used to decreased reflectance and therefore increase the overall transmittance of light into a device. In cases where the texturing produces features that are significantly smaller than the wavelength of incoming light, the light cannot resolve the nanoscale features and instead of an abrupt interface encounters an *effective medium* with a graded refractive index as illustrated in Figure 2.7. This effective refractive index gradient has an anti-reflection effect which increases transmittance.

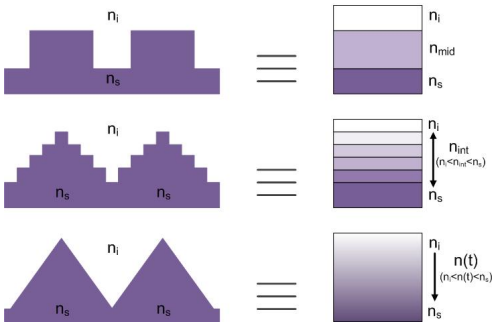

Figure 2.7: Illustration of the graded refractive index effect for sub-wavelength surface features, adapted from [35].

To obtain a good overall improvement from these two effects the surface texturing of the cell has to be carefully optimized so that the feature sizes and shapes interact in a useful way with the relevant wavelengths of light. TCO texturing has been used in numerous solar cell designs and several different TCO materials have been commonly used; the most popular being tin oxide (SnO_2) and zinc oxide (ZnO). The general requirements for a TCO to be used for a solar cell front contact are high transparency in the relevant spectral region, strong scattering of incoming light and physical and chemical properties that are compatible with deposition of subsequent device layers, as well as good electrical properties [36]. SnO_2 and ZnO both satisfy these requirements well. SnO_2 is arguably the most common TCO, typically used for thin-film silicon solar cells. There are several companies such as NSG Pilkington and The Asahi Glass Company that offer commercial SnO_2 layers on glass to be used as solar cell superstrates [37, 38]. The most notable product being Asahi Type-U, a flourine doped tin oxide (FTO) developed in 1992 by the Asahi Glass Company (Figure 2.8). Asahi Type-U consists of feature sizes of the order of 100 nm with angled facets and an overall RMS roughness of around 40 nm [39]. This FTO film was shown to substantially increase device short circuit current (due to light-trapping) with little detrimental effect on open circuit voltage. Asahi Type-U is now considered a well optimized standard for a-Si:H devices and is frequently used for comparison when investigating alternative textured TCOs for a-Si devices [40, 41, 42, 43].

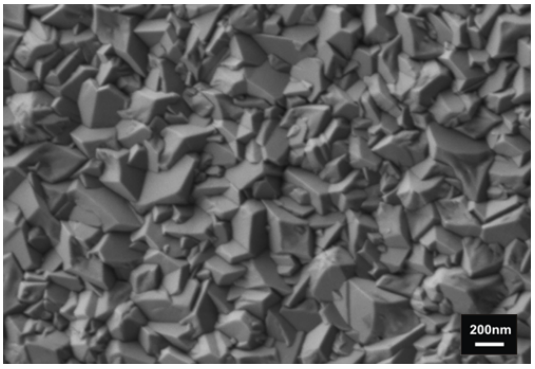

Figure 2.8: SEM image of Asahi Type-U textured FTO.

TCO texturing is an essential technique for light-trapping within thin solar cells, however, the technique does have limitations. One of the major issues with texturing is that nano-textured surfaces with very small features tend to enhance scattering at the shorter wavelengths of light but have very little scattering effect on the longer wavelengths. This is because the longer wavelengths of light cannot resolve the sub-wavelength features of the interface and only experience a graded refractive index. The obvious solution to this is to texture films with larger features, and in general this has been shown to enhance long wavelength scatter. However, increasing the feature size of the TCO leads to a surface with deep valleys and high peaks. Such surfaces can be extremely problematic when depositing the subsequent thin semiconductor layer and can often lead to 'cracks' which are detrimental to the electrical characteristics of the device, thus negating absorption gains from increased scattering (Figure 2.9 [44]). Larger TCO features also increase the surface area of the semiconductor/contact interface and thus lead to higher surface recombination. Hence a compromise must be made between light scattering enhancement and the electrical characteristics of the device.

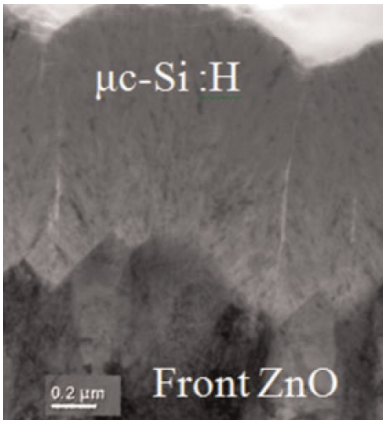

Figure 2.9: TEM image of microcrystalline silicon deposited on a rough ZnO layer, cracks appear as white lines in silicon, reprinted from [44].

The optimal texturing for a specific thin solar cell structure is traditionally determined empirically by fabricating devices on a variety of candidate substrates and measuring the final device characteristics. For a deeper understanding and potentially superior end

results, accurate methods for determining the effects of different surface textures on light transmission are required. This can be achieved through accurate and comprehensive characterization combined with numerical simulation, both of which are key focus points of this work. Further information on textured TCO properties and deposition methods is given in Chapter 4 along with details of the most recent progress in this area.

2.2.2 Diffraction Gratings

The first reported man-made diffraction grating was created by D. Rittenhouse in 1785 [45]. However, diffraction gratings were not used in scientific research until 36 years later in 1821 when J. Fraunhofer used gratings to measure absorption lines of the solar spectrum [46]. Throughout the 19th century diffraction gratings received increasing attention and development and in 1947 Bausch & Lomb began making precision commercial gratings [47].

Diffraction is defined as the classical physics based phenomenon of the apparent bending of light around small objects. When these objects are placed in a periodic manner they are referred to as a diffraction grating. A diffraction grating is a spatial modulation of refractive index, often achieved by regularly spaced voids or alternating materials [47]. White light incident on a diffraction grating is spectrally split into multiple beams which travel in specific directions, the angle of which is dependent on the wavelength of light as depicted in Figure 2.10.

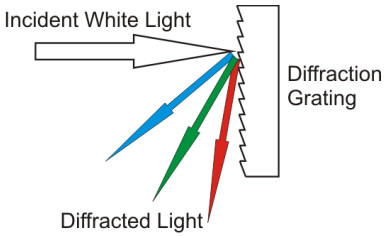

Figure 2.10: Dispersive effect of reflective diffraction grating.

The relationship between the angles of incoming and outgoing beams and the grating period is governed by the grating equation. When a plane wave of light of a particular wavelength (λ) is incident normally to the grating structure, each space in the grating can be considered to be a *point source* propagating in all directions. Light at one particular angle (θ) is the superposition of the components from each slit. In most cases the phases of waves from individual slits will be different and will therefore either partially or entirely cancel each other out. However, in the case where the path difference between neighbouring spaces is equal to an integer multiple of the wavelength of light, the waves will be in phase, leading to constructive interference and hence high intensity light, see Figure 2.11. This matching of path differences and wavelength occurs at a particular angle, θ_m, as described by the grating equation (Equation 2.3) which can be derived geometrically from Figure 2.11 [47].

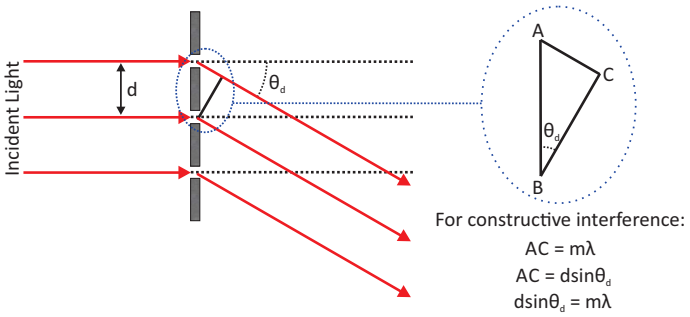

Figure 2.11: Illustration of diffraction geometry for a single order.

$$\theta_d = \sin^{-1}\left(\frac{m\lambda}{d} - \sin\theta_i\right) \tag{2.3}$$

Where d is the grating period, θ_d is the angle of the diffracted beam, λ is the wavelength of light and m is the grating order. For the special case of normal incidence (as depicted in Figure 2.11 the $\sin\theta_i$ term reduces to zero, simplifying the equation.

Diffracted light occurs in multiple orders, the specular reflection or direct transmission is known as the zero order ($m = 0$). Other light intensity maximas occur at different orders, which can be positive or negative. The intensity of diffracted light, also known as the diffraction efficiency, diminishes with increasing diffractive order and will depend on several parameters including the grating material, spacing and groove height [47]. Diffraction gratings can be one, two or even three dimensional and can be fabricated using various techniques and materials depending on the grating requirements.

The ability to split up the wavelengths of broadband light and scatter them to selective angles means that diffraction gratings are a useful tool for light-trapping applications. Diffraction gratings can be used for reflective or transmissive purposes by creating them in reflective or transparent materials respectively. Therefore, for the purposes of light-trapping within solar cells, diffraction gratings could be effectively incorporated anywhere within the device structure. For light-trapping within thin-film solar cells in particular, diffraction gratings have been frequently applied as textured front contacts and as textured back-reflectors. Information regarding recent work utilizing diffraction gratings for photovoltaics is given in Section 6.

2.2.3 Plasmonics

The optical effects of plasmons have been observed under various different circumstances for centuries, although the term 'plasmon' only came about around 60 years ago. In 1955, David Pines described the energy losses of fast electrons travelling though metals, his theory stated that these losses were due to collective oscillations of free electrons within

the metal [48]. He refers to these oscillations as plasmons due to similar earlier work carried out on plasma oscillations in gas discharges [49].

The term plasmon refers to the quantization of plasma oscillations in the same way as a photon is the quantization of an electromagnetic wave. Within a metal nanoparticle plasmons are present in two forms, bulk plasmons and surface plasmons. Bulk plasmons are in the volume of a plasma whereas surface plasmons are only found at the interface of a plasma and dielectric [49]. Surface plasmons are able to couple with incident photons leading to a surface plasmon polariton (SPP) which propagates along the metal surface until absorption or radiation causes it to lose energy. If metal particles are made small enough then the distinction between bulk and surface plasmons disappears as an electromagnetic field is able to penetrate into the volume of the metal and affect free conduction electrons. The field can then shift the conduction electrons relative to the metal ion lattice of the particle, this results in an opposite surface charge on the opposite surface element of the particle which in turn produces a restoring local field within the particle. The combination of shifting electrons and the restoring field lead to oscillator behaviour, see Figure 2.12.

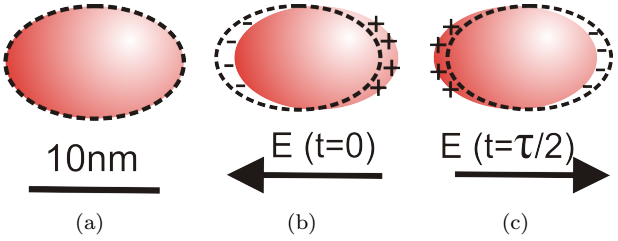

Figure 2.12: When a MNP (a) is exposed to an electric field electrons are shifted relative to the ion lattice (b-c), adapted from [49].

This enables a resonance to occur at a specific frequency, known as the localized surface plasmon resonance (LSPR). Two mechanisms contribute to the majority of the damping of this resonance, they are radiation damping and energetic relaxation. Radiation damping involves the re-radiation of electromagnetic waves and therefore creates a scattering effect which could be utilized for light-trapping purposes. Energetic relaxation leads to energy being dissipated as heat, this has the overall effect of absorption within the MNP and is therefore an undesired effect for photovoltaics [49].

The ratio between scattering and absorption is highly dependent on the particle size: particles which are much smaller than the wavelength of light tend to exhibit higher absorption, larger particles result in greater scattering [50]. Therefore, as with surface texturing, the use of MNPs must be carefully optimized to ensure that the beneficial scattering effects are not negated by the unwanted absorption of the nanoparticles. Interestingly, MNPs typically have an effective optical cross section that is significantly larger than their geometrical cross section [51]. The exact extent of the optical cross section is dependent on nanoparticle properties but can be as large as ten times the

geometrical area. Hence a 10% surface coverage of a solar cell could be sufficient for plasmonic effects to be active across the entire device. It has also been shown that whilst nanoparticles suspended in a homogeneous medium will scatter roughly equally in the forward and backwards directions, particles at or near an interface will preferentially scatter towards the material with the largest permittivity [51].

Arrays of MNPs are highly tunable in that there are several parameters that can be changed which will alter their optical properties. As previously discussed, the intensity of absorption and scattering is heavily dependent on MNP size. The resonance frequency of MNPs is also affected by MNP size as well as shape, particle material and the refractive index of the surrounding medium [52]. MNPs can be distributed randomly or as periodic arrays, creating a diffraction grating (see Section 2.2.2). When fabricated as a diffraction grating the optical properties of the array are highly dependent on the grating period (d), see Figure 2.13(c).

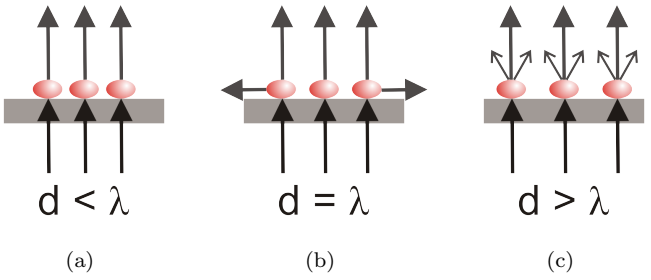

Figure 2.13: Effect of grating period on far field transmission of light, diagram adapted from [49].

If d is less than the wavelength of the incident light then the majority of scattering is prohibited and only occurs in the direction of zero order transmission as depicted in Figure 2.13(a) [49]. In cases where the wavelength of incident light is equal to d, light scattered to the first grating order is transmitted parallel to the grating as shown in Figure 2.13(b). Finally, if d is larger than the wavelength then the light is scattered to specific angles due to interference effects as with a typical diffraction grating (discussed in more detail in Section 2.2.2) [49].

The ability to scatter light of specific wavelengths makes the use of MNPs an attractive concept for light-trapping within solar cells. The magnitude of enhancement due to MNP arrays varies significantly with the type and placement of the array and the type of solar cell investigated. However, when optimized, they have been shown to provide significant improvements over conventional planar solar cells and in some cases results for MNP arrays have even shown improvements comparable to textured devices [53, 54]. Further details regarding the use of plasmonics for thin-film photovoltaics and the latest work in this area are provided in Chapter 6.

2.3 Simulation

There are several possible methods for modelling the optical response of a specific structure or system and each method has distinct advantages and disadvantages. For the case of textured TCOs and nanoparticles, the structures being investigated have characteristic dimensions on a sub-wavelength scale. This means that some of the more common and in many cases simpler optical modelling techniques such as ray tracing can be immediately ruled out as they are only valid for larger geometries. In this section some of the traditional analytical techniques for modelling light-trapping are discussed followed by detailed information on the finite difference time domain (FDTD) numerical modelling technique which is the primary simulation method used in this work.

2.3.1 Analytical Methods

Scalar Scattering Theory

Scalar scattering theory is an approach used to model the scattering from a rough surface. The theory was first developed in 1954 in a paper by Davies which described an approach to obtain the magnitude and shape of scattered electromagnetic waves for a surface with a random roughness of Gaussian distribution [55]. Since then the theory has been developed to give solutions for broader wavelength ranges and different types of surface roughness [56]. More recently this theory has been applied to textured interfaces for photovoltaic applications. The majority of work using analytical approaches such as this aims to quantify the total diffuse light reflected or transmitted from the surface. For the case of textured TCOs used for thin-film solar cells the optical scattering is traditionally quantified using the 'haze' parameter. Haze is the diffuse transmittance or reflectance divided by the total transmittance or reflectance respectively. Hence an interface with a haze value of 1 (or 100%) would scatter all of the incident light.

Scalar scattering theory approaches require a description of the roughness of the investigated surface, for randomly rough surfaces this is not a trivial matter as they cannot be described in a deterministic way and therefore a statistical approach must be taken. This means that any solutions obtained using the analytical scalar scattering approach will inevitably be an approximation. For the typical case in which a random surface has feature heights that can be represented by a Gaussian distribution, the surface can generally be described using the measured route-mean-square (RMS) roughness or in some cases the roughness average (Ra). These parameters can be obtained from measured surface topographic data and are calculated using Equations 2.4 and 2.5.

$$R_a = \frac{1}{n}\sum_{i=1}^{n}|y_i| \tag{2.4}$$

$$R_{rms} = \sqrt{\frac{1}{n}\sum_{i=1}^{n}y_i^2} \tag{2.5}$$

Where n is the number of data points and y_i is the vertical distance of a specific point from the mean line. The measured RMS roughness values can then be combined with the Rayleigh scattering formula leading to Equation 2.6 for the transmittance haze of a textured surface [57].

$$H_T = 1 - exp\left[-\left(2\pi\sigma C\left|n_0 - n_1\right|/\lambda\right)^2\right] \tag{2.6}$$

Where σ equals the RMS surface roughness and C is a fitting parameter. This equation is valid for Gaussian height distributions but more adjustments must be made and solution accuracy is reduced if the roughness has a more complicated distribution. The exponent is sometimes changed from 2 to 3 in order to obtain an improved fit. This solution can provide satisfactory results but the inclusion of the empirical fitting parameter C cannot be theoretically justified.

More recent work has shown significant improvements by using a formula derived using the Fresnel-Kirchoff diffraction formula combined with textured surface information, leading to equations for specular and diffuse reflectance and transmittance [58]. By substituting the Fresnel-Kirchoff based equations into the haze equation and simplifying, an analytical expression for the transmittance or reflectance haze of a textured surface can be determined, shown in Equation 2.7 and 2.8 respectively [58].

$$H_T = \frac{\left(1 - e^{-(2\pi\sigma/\lambda)^2(n-1)^2}\right)\left(1 - e^{-(\pi a\alpha/\lambda)^2}\right)}{1 - e^{-(\pi a\alpha/\lambda)^2}\left(1 - e^{-(2\pi\sigma/\lambda)^2}(n-1)^2\right)} \tag{2.7}$$

$$H_R = \frac{\left(1 - e^{-(4\pi\sigma/\lambda)^2(n-1)^2}\right)\left(1 - e^{-(\pi a\alpha/\lambda)^2}\right)}{1 - e^{-(\pi a\alpha/\lambda)^2}\left(1 - e^{-(4\pi\sigma/\lambda)^2}\right)} \tag{2.8}$$

Where a is the correlation length, determined using surface topographical measurements. This approach has been shown to provide a good match when comparing calculated and measured haze characteristics [58]. However, it has not yet been shown to provide accurate information on the angular distribution of scattered light. In addition, the accuracy of results will diminish as the height distribution of the surface in question strays away from Gaussian. More comprehensive results that are not limited by the

type of surface height distribution can be achieved with numerical simulation methods as detailed in Section 2.3.2.

Mie Theory

Mie theory is the analytical solution of Maxwell's equations for the scattering of light by a homogeneous spherical particle in an infinite medium illuminated by a plane wave. The theory was first developed by the German physicist Gustav Mie in 1908 [59]. The original theory allowed for spheres consisting of absorbing materials (having a complex refractive index) but the surrounding medium was required to have a real refractive index with no imaginary component and therefore could not be absorbing. In the past decade developments have been made to the theory in an attempt to remove this limitation [60].

Mie theory states that the eigenmodes of a spherical particle are either dipolar or multipolar and the strength of their excitation can be determined by the expansion of the incident electromagnetic field into vector spherical harmonic functions. Therefore Mie theory calculations require that the incident plane wave be expressed in spherical coordinates [49]. Input parameters such as the sphere radius and the refractive index of the particle and surrounding medium can then be varied and Mie's equations used to calculate the scattering cross section of a particle as well as the total extinction and total scattering, therefore allowing absorption to be easily calculated.

Within the boundaries of classical physics, Mie theory has no wavelength or particle size limitations. However, refractive index data must be modified when considering very small nanoparticles (<10 nm) due to surface scattering effects [61]. An exception must also be made for particles smaller than a single nanometer as quantum effects render Mie theory invalid. Whilst Mie theory has been instrumental in the understanding of scattering from small particles, it is an analytical approach with severe limitations, a key one being that exact solutions can only be obtained for spheres. Mie theory can be extended for the treatment of non-spheres but accuracy severely diminishes as the shape deviates further from sphericality [62]. For results to be obtained for arbitrary geometries, alternative numerical based methods can be utilized as detailed in Section 2.3.2.

2.3.2 Finite Difference Time Domain

Finite difference time domain (FDTD) is the modelling technique used for the optical simulations in this work. Specifically, the commercial software package *'FDTD Solutions'* by *Lumerical* was used. In this section the key principles of the FDTD method will be outlined along with details regarding how simulations are typically set up and a discussion of the advantages and disadvantages of the technique.

FDTD is a numerical simulation technique based on the modelling of electromagnetic waves in the time domain. A key advantage of working in the time domain is that solutions from a single simulation can be transferred to the frequency domain using Fourier transforms, therefore providing results for a broad range of wavelengths. The FDTD technique involves solving Maxwell's time-dependent curl equations (2.9 and 2.10).

$$\nabla \times \mathbf{E} = -\mu_0 \frac{\partial \mathbf{H}}{\partial t} \tag{2.9}$$

$$\nabla \times \mathbf{H} = \epsilon_0 \epsilon r \frac{\partial \mathbf{E}}{\partial t} \tag{2.10}$$

Where E is the electric field, μ_0 is the permeability of free space, H is the magnetic field, ϵ_0 is the permittivity of free space and ϵr is the complex relative dielectric constant. The method of solving these equations is based on the Yee algorithm, first introduced by Yee in 1966 [63]. It can be seen from Equations 2.9 and 2.10 that the E-field change in time is dependent on the curl of the H field and conversely the H-field change in time is dependent on the curl of the E-field. The Yee algorithm is based on this relationship and uses a leapfrog approach in which the E field for the next time step is calculated using the value of the current E-field and the curl of the H field in space, the H field is then determined in a similar manner. This means that E-field updates are made midway through H-field updates resulting in a central-difference approximation in time which is second-order accurate. This scheme is explicit and therefore does not require simultaneous equations to be solved. To achieve second-order accuracy in space a *Yee lattice* is used. This is a configuration of E and H components in which every E component is surrounded by four H components and every H component is surrounded by four E components as shown in Figure 2.14. This results in central spatial finite difference expressions and therefore central-order approximation and second order accuracy.

The use of Yee cells means that discretization of modelled geometries must be cubic, curved surfaces are therefore typically represented using a staircase approximation. FDTD is a finite difference technique and thus requires a finite simulation region in which electromagnetic fields are to be calculated. The boundaries of this region can be set to act as near perfect absorbers, thus avoiding unwanted reflectance from an artificial

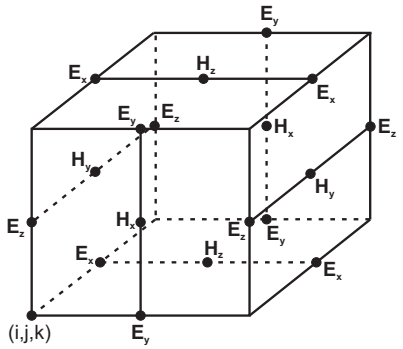

Figure 2.14: Illustration of a standard Cartesian Yee cell [63].

boundary. It is also possible to specify periodic boundaries, in this case the fields on one side of the grid in the direction of the periodic boundary are assumed to be exactly the same as the fields on the opposite side. The use of periodic boundaries allows for the simple and efficient simulation of periodic structures such as diffraction gratings.

Electric and magnetic fields are calculated at all spaces within the simulation region and therefore the material of each cell must be specified. Materials can be specified as arbitrary geometries and are optically defined by their dielectric constants. Dielectric constants are wavelength dependent and the time dependent nature of FDTD means that discrete data for specific wavelength values cannot be used. Dielectric constant data must therefore be fitted to a suitable model [49]. This is a significant drawback to the FDTD method as inaccurate model fits can lead to substantial differences in results. In most cases an acceptable fit tolerance can be easily found. However, for some materials such as metals in particular, the achievable model fit can be far from ideal.

Once a simulation region has been specified, along with the structure and properties of the materials within it, it is then necessary to place a source. The location and direction of which must be defined by the user. Sources are typically plane waves but can also be set to have a Gaussian intensity distribution. Monitors are then placed in a similar way, these record the data for the electromagnetic fields passing through their location. Therefore, placing a source, followed by a slab of material followed by a monitor will result in the monitor recording the transmittance characteristics of the material. If the monitor is placed behind the source then the reflectance characteristics would be recorded. An example diagram of a typical FDTD simulation set-up designed to record the total transmittance and total reflectance of a thin-film on a fused silica substrate is shown in Figure 2.15

The raw FDTD technique is restricted to monitoring near-field data only and therefore extra procedures are required in order to obtain far-field scattering information that can be compared to optical scattering measurements. Whilst the FDTD software used within this work does have specialized monitors that can detect the total scattered field, these monitors in their default state lack the vital angular information needed for

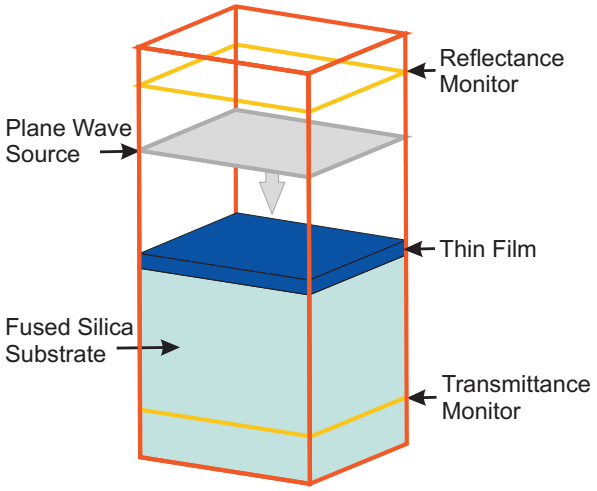

Figure 2.15: Diagram of the FDTD simulation set-up for a thin-film on fused silica.

comparison with detailed scattering measurements. In order to determine this angular information, far-field projections must be implemented. The far-field projection is a Fourier transform based technique in which the 2D near-field monitor data is projected onto a 3D hemisphere and angular scattering information is obtained, see Figure 2.16.

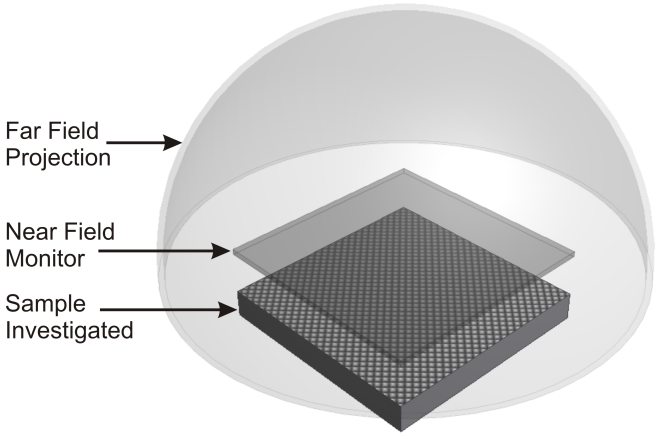

Figure 2.16: Illustration of the far-field projection hemisphere.

The far-field projection routine is a built-in script function of Lumerical's commercial FDTD software and can be carried out in simulation post processing for a single wavelength at a time. In order to obtain all of the relevant results, a custom FDTD script can be created to export the far-field projection data for the full wavelength range of interest. The built-in far-field integration function can also be used to sum up the total light scattered within specific solid angles. The exported data can then be compared to conventional diffuse transmittance/reflectance measurements as well as more detailed wavelength and angle resolved scattering (WARS) measurements.

In summary, FDTD is an extremely powerful modelling technique capable of calculating the broadband optical response of a system consisting of different materials of arbitrary geometries in a single simulation run. The accuracy of results is primarily limited by the model fit to dielectric constant data as well as the cell size used for discretization (limited only by computational power). FDTD simulations are used throughout this work to aid the investigation of a variety of light-trapping techniques. In each case the accuracy of the simulation technique is first gauged by direct comparison with experimental measurements and where possible simulations are then extended to provide unique insights that could not be determined experimentally.

Chapter 3

The Measurement of Optical Scattering

Within the realm of optical measurements the characterization of light scattering is relatively complex and there are many variables that must be clearly defined, such as, the angle at which transmitted or reflected light is considered to be scattered, the normalization procedure for the measurement and the acceptable level of signal to noise ratio. Although clear standards have been published for the measurement to total scattering (ISO 13696 and MF 1048), the more detailed measurement of angle resolved scatter is still left with some ambiguity. Angle resolved scatter can be defined by the bidirectional scattering distribution function (BSDF) of a surface which is a somewhat standardized technique (see ASTM E2387 standard), however, the BSDF describes the intensity of light scattered to all angles, for all angles of incidence. This is extremely difficult and time consuming to measure and for many systems this amount of information is excessive. For example, in the case of solar cells that are mounted on sunlight tracking devices, only the scattering distribution of light entering at normal incidence is of importance, and thus the full measurement of BSDF could be considered an unnecessary and inefficient use of time and resources. Due to the complex nature of scattering measurements and the relative lack of standardization, there are very few commercial systems that offer the accurate and comprehensive measurement of scattered light. Therefore, much of the scattering characterization carried out within this work has been produced using a custom built system. This chapter details both the traditional and the novel techniques used to characterize scattering in this investigation. The challenges encountered are discussed along with the methods used to establish a normalized, reproducible and systematic set of procedures and systems for accurate and effective characterization of optical scattering.

3.1 Conventional Optical Measurements

3.1.1 Reflectance and Transmittance Probes

One of the simplest methods for measuring the optical properties of a material is to use reflectance or transmittance probes. For transmittance measurements this typically involves illuminating one side of the sample, often with light outputted through an optical fibre and then detecting the transmitted light on the other side with another fibre, aligned and connected to a detector such as a spectrometer or power meter. In its simplest form this measurement is carried out at normal incidence and the measured transmittance is normalized with a measurement of the source taken by simply removing the sample from the experiment. This simple experiment can provide an accurate characterization of the direct transmittance through the sample, often referred to as the specular or zero order transmittance. This measurement technique benefits from its simplicity, however, it is limited in that light transmitted through the sample at angles greater than the small solid angle encompassed by the source and detector will not be detected.

A similar measurement can be carried out to determine the specular reflectance of a sample. In this case the sample is illuminated at normal incidence with light outputted via a reflectance probe fibre. This type of probe typically consists of a single fibre bundle at one end which splits to two separate fibres at the other end, one fibre is for the central core to which the detector is connected and the other fibre consists of the surrounding fibres and is connected to a light source in order to illuminate the sample. These measurements are normalized using calibration measurements taken from a sample with well-known optical properties, such as polished silicon. As with the transmittance probe measurement, this technique suffers from the limitation of only detecting reflectance within the solid angle of the probe and detector, essentially the specular reflectance.

These simple probe techniques are useful for quick checks of a sample and basic characterization but they are severely limited as only the specular component of light is measured. For the determination of scattered light more sophisticated measurements are required as detailed in Section 3.1.2 and Section 3.2.

3.1.2 Total Integrated Scattering

Total integrated scatter (TIS), sometimes simply referred to as total scatter (TS) is an efficient measurement technique used to determine the total amount of light scattered by a sample. TIS can be measured using an integrating sphere (IS), this is essentially a spherical cavity with walls coated in a highly reflective diffuser. Typically polytetrafluoroethylene (PTFE) is used for the sphere wall as it is a near Lambertian reflector, meaning that it scatters light almost equally in all directions. Most integrating

spheres have several ports; an input port for incoming light, an exit port for transmitted light, a detector port and in some cases, ports for a second light input and for the exclusion of specular reflectance. The detector port typically houses an optical fibre connector, therefore a fibre can be used to transmit light from within the sphere to a detector such as a spectrometer or power meter. Integrating spheres are extremely versatile and can be experimentally arranged with a huge variety of sources and detectors.

Measurements of total transmittance and total reflectance can be easily carried out using an integrating sphere by either placing the sample at the front or back port of the sphere respectively, see Figure 3.1. For transmittance, the sample is placed at the front port and the back port is covered with a port cap which is ideally made from a material well matched to that of the sphere wall. For transmittance, the measurement can be normalized with a measurement of 100% transmission (empty front port). For reflectance, the sample is placed at the back of the sphere and the normalization is carried out using a measurement of a standard sample with known reflectance.

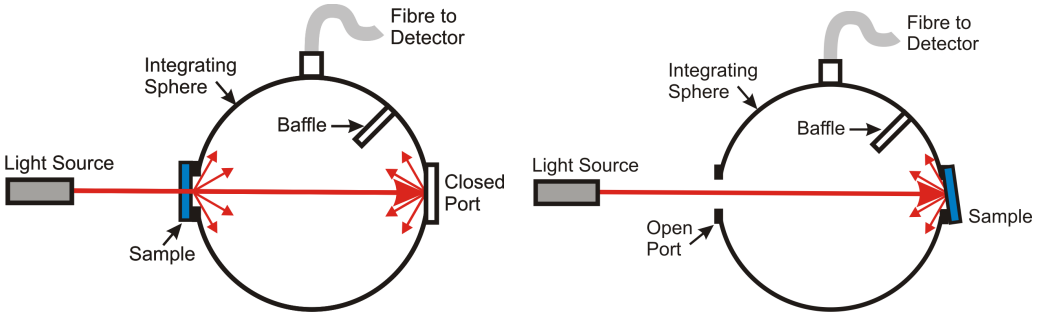

(a) Measurement of total transmittance.

(b) Measurements of total reflectance.

Figure 3.1: Integrating sphere configurations for measurement of total transmittance and reflectance.

TIS is essentially the summation of the total diffuse transmittance and the total diffuse reflectance. Measurement of diffuse transmittance can be carried out by replacing the back port of the sphere with a light trap and therefore removing the specular or zero-order transmission, see Figure 3.2(a). In this arrangement the diffuse transmittance is defined as light transmitted at any angle greater than that between the centre of the input port and the edges of the output port. Most commercial integrating spheres are designed to set this angle to around 5°.

Measurement of diffuse reflectance can be carried out by replacing a separate specular exclusion port cap on the sphere with a light trap. The sphere is constructed in such a way that the back port is at a small angle, typically 8°. The specular exclusion port is positioned on the part of the sphere wall where the specular reflectance of a sample at 8° would fall. Therefore the specular reflectance will be absorbed by the light trap and only the diffuse reflectance will be measured, see Figure 3.2(b).

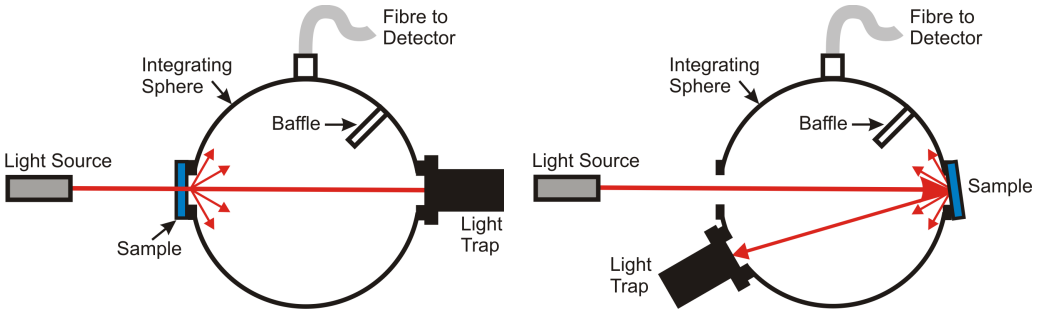

(a) Measurement of diffuse transmittance. (b) Measurements of diffuse reflectance.

Figure 3.2: Integrating sphere configurations for measurement of diffuse transmittance and reflectance.

Integrating sphere measurements are commonly used to characterize TIS and are known to be reasonably accurate and reliable. However, non-uniformities within the sphere and the investigated sample can lead to significant errors. These errors can be minimized by operating the integrating sphere in *double beam* mode. In this mode each measurement is accompanied by another measurement from a source entering through a separate reference port. This source is directed at some part of the inner wall of the sphere, rather than at the sample. Hence changes in this reference beam measurement are only due to alterations within the sphere set-up, such as replacing a port with a light trap. These reference measurements can then be used to further normalize the results leading to increased accuracy and reliability. A comparison of the results for single beam and double beam measurement modes used to investigate polished silicon is shown in Figure 3.3 along with the theoretical expected values.

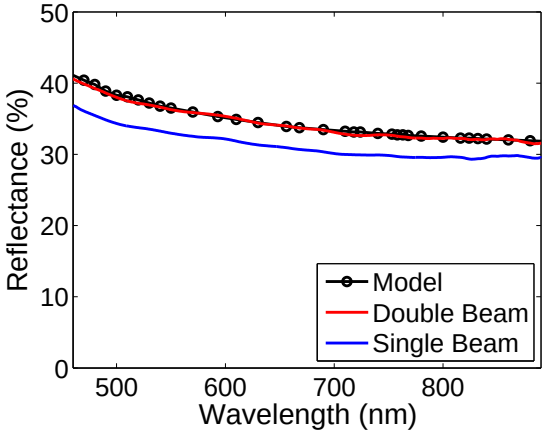

Figure 3.3: Comparison between single beam measurement, double beam measurement and theory.

The results of Figure 3.3 show that the measurement using the double beam method is considerably more accurate than the single beam measurement. These findings are backed up by previous studies found in literature [64]. All IS measurements within this work have therefore been carried out in double beam mode.

Characteristics obtained from integrating sphere measurements can also be used to determine Haze. Haze is the ratio between total and diffuse light and can be determined for both reflectance and transmittance (Equation 3.1).

$$H_T = \frac{Diffuse\ Transmittance}{Total\ Transmittance} \qquad H_R = \frac{Diffuse\ Reflectance}{Total\ Reflectance} \tag{3.1}$$

Therefore a transmittance haze of 1 (or 100%) means that all of the light transmitted by the sample is diffuse. This is a crucial parameter for materials used in photovoltaic devices as it quantifies the amount of scattering provided by the sample and therefore indicates the potential for light-trapping. As an example, the transmittance haze characteristic for the commercial transparent conducting oxide (TCO) Asahi Type-U is shown in Figure 3.4.

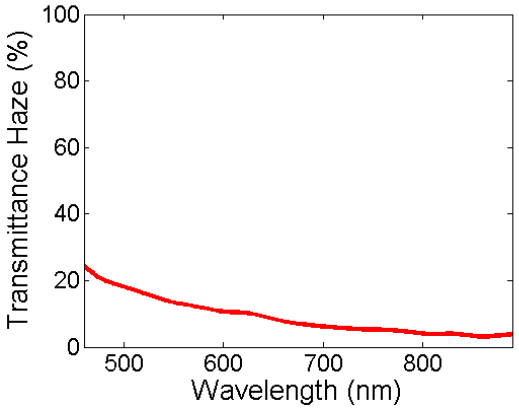

Figure 3.4: Measured haze of Asahi Type-U.

Haze is a quick and useful measurement for obtaining a rough idea of the scattering potential of a sample and is often used as a figure of merit for optical diffusers. However, haze can be misleading as the measurement does not provide any information regarding the angular distribution of scattered light. This means that a surface that scatters 90% of all transmitted light to 10° could have the same haze as a surface that scatters 90% of all transmitted light to 80°, whereas their effectiveness for light-trapping would be significantly different. It is therefore essential to obtain more information about the angular spread of scattered light, this can be achieved using angle resolved scattering (ARS) measurements.

3.1.3 Angle Resolved Scattering

Angle resolved scattering (ARS) measurements can be carried out in transmittance or reflectance. The technique is based on the simple principle of illuminating a sample at normal incidence and sweeping a detector mounted to a rotation arm with the same

centre of rotation as the sample, taking measurements at regular intervals as illustrated for transmittance in Figure 3.5.

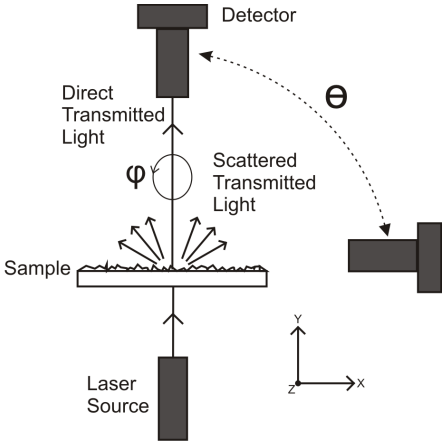

Figure 3.5: Schematic of experimental arrangement for measurement of ARS.

These measurements are typically carried out using a single wavelength laser as a source, often a reasonably high power source is required as the intensity of light scattered to a particular angle is likely to be very low. It is important to note that the measurement only accounts for light scattered in the plane of the detector sweep. Raw measurement results are therefore only representative of scattering into a single two dimensional plane, perpendicular to the sample surface. For the special case of randomly textured surfaces, scattering is roughly isotropic and the two dimensional *in-plane* measurement should give similar results for all azimuth rotations of the sample. However, even for isotropic samples the in-plane measurement of the angular distribution of light is not a true representation of the three dimensional distribution. This is due to the fact that at larger angles of θ, scattered light is distributed over a wider area (see Figure 3.6), hence the measured in-plane value is a smaller percentage of the total light scattered to that angle of θ.

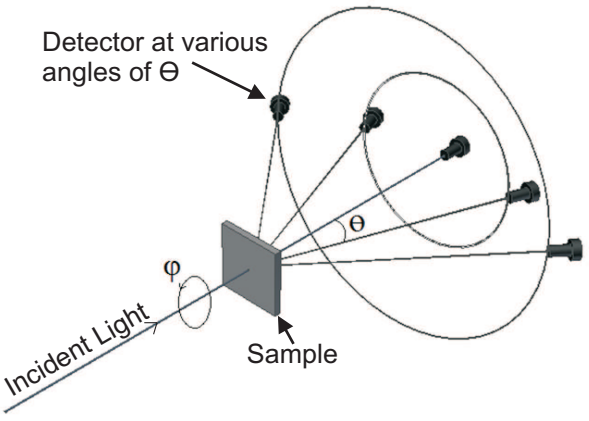

Figure 3.6: Illustration of the 3D distribution of scattered light at various angles of θ.

For the case of isotropic scatterers the measured in-plane scattering can be converted to total scattering mathematically. Specifically, it can be shown that the in-plane scattering can be geometrically converted to total scattering using a $\sin(\theta)$ relationship. In the literature, a $\sin(\theta)$ scale is often used, sometimes combined with a scaling factor (Equation 3.2). However, geometrically the more detailed Equation 3.3 is more accurate and accounts for the linear changes in intensity.

$$Scat_{Total} = Scat_{InPlane} C \sin\theta \tag{3.2}$$

$$Scat_{Total} = \frac{Scat_{InPlane} 4L \sin\theta}{r} \tag{3.3}$$

Where θ is the detector angle, C is a constant scaling factor, L is the length of the detector arm and r is the radius of the detector aperture. It should be noted that for anisotropic scatterers such as diffraction gratings this conversion is not valid and therefore measurements of in-plane scattering must suffice, although taking measurements at different sample azimuth rotations would help to provide a more accurate picture of the total three dimensional scattering.

Systems for measuring angle resolved scattering are typically custom-built for purpose and results are often presented with arbitrary units due to challenges in repeatability and accurate normalization. These systems usually consist of a single wavelength laser, or in some cases, several different single wavelength lasers are used to get ARS results for a discrete range of wavelengths, as is the case for the ALBATROSS measurement system developed at the Fraunhofer institute [65]. However, for the complete picture of scattering from a sample, a more ideal arrangement would be to resolve the scattering over a broad, continuous wavelength range, resulting in wavelength and angle resolved scattering (WARS). The design and development of equipment to enable this WARS measurement is detailed in Section 3.2 and is the core scattering characterization method used within this work.

3.2 WARS System Development

3.2.1 Overview

To fully characterize the optical scattering from a surface it is essential to determine the intensity of transmitted or reflected light at all angles and wavelengths. To obtain this information, wavelength and angle resolved scattering (WARS) measurements can be utilized. This measurement technique is an extension of the ARS measurement technique detailed in Section 3.1.3. Obtaining WARS measurements to a good degree of accuracy is a non-trivial task and presents several challenges. There are therefore few examples of full WARS measurements in scattering studies and although numerous goniometer systems exist for obtaining single wavelength ARS measurements, there are very few commercial products capable of carrying out full WARS characterization and none that are primarily designed and therefore optimized for the purpose. One well established product that can carry out WARS type measurements is the 'Automated Reflectance/Transmittance Analyser' (ARTA) add-on to the PerkinElmer Lambda spectrophotometer [66]. The ARTA is an automated goniometer system in which a sample can be centrally mounted and illuminated at specific angles of incidence and a mini integrating sphere can be positioned at various angles to collect the scattered light, thus allowing ARS measurements to be taken. The use of a tungsten-halogen and deuterium light source along with a photomultiplier R6872 and PbS detector allows for detection over a wavelength range of 175 nm to 3300 nm [67].

Whilst the ARTA is a useful measurement system, is has several limitations that render it unsuitable for the characterization of small (2mm x 2mm) sample areas required for parts of this investigation. In particular the source used cannot be well collimated with a small beam diameter and the angular range of the system is only specified up to 85°. It is also a costly system and there is little documentation showing evidence of good reproducibility of results for light scattered at large angles. As an example, one study carried out by K. Jager at the university of Delft found the system to have varying reproducibility with a typical error of 5-15% [68]. Finally, the system does not provide a simple method for aligning and repositioning samples to a high degree of accuracy which is likely to have a significant effect on measurement reliability. It was therefore decided that a custom built WARS system would be established and used for measurements of wavelength and angle resolved scattering in this work. The starting point for this unique WARS system was a pre-existing custom reflectometer system used solely for measurements of specular reflectance at various angles of incidence.

3.2.2 Hardware

Illumination Source

One of the primary concerns for the characterization of scattered light is the signal to noise ratio, this is crucial as scattered light is typically very low intensity in comparison to its specular counterpart. It is therefore useful to use a powerful illumination source. In order to get results for a broad wavelength range, several different source and detector arrangements could be used. One option is to use a monochromator along with a white light source to sequentially illuminate the sample with different wavelengths which could be detected by a power meter or similar device. Another option is to directly illuminate the sample with a white light source, detecting the scattered light with a broadband spectrometer. Whilst both of these options could work well for a scattering measurement system, the latter option was chosen as it has the potential to provide more rapid and efficient measurements. The ideal source should also be well collimated so as to allow for the accurate detection of scattering at small angles without saturation caused by the divergence of the source itself. Finally, it is useful to have a small, or in the ideal case, adjustable beam diameter. This is to accommodate for different sample sizes and is specifically required for the work carried out in Chapter 6 of this thesis in which small samples created using electron beam lithography are investigated.

With the requirements for high intensity, broadband spectra, good collimation and small spot size established, it was decided that a Fianium super-continuum white light laser would be used as a source. The Fianium SC450-2 has an output power of 2W spread over a broad wavelength range of 450 nm - 2400 nm, the output is a collimated beam with a spot size of around 1.5 mm. One of the drawbacks of a fibre based source such as this is the lack of shorter wavelengths (<450 nm), however, wavelengths shorter than 450 nm are readily absorbed in thin photovoltaic devices and therefore it is the behaviour of longer wavelengths that require detailed investigation and optimization. Another challenge encountered when using a 2W laser source is control of the output power. For scattering measurements it may be necessary to use different power levels for different angles of scatter, and whilst the SC450-2 does have controllable power output, changing the power level using this method also changes the spectrum of the laser which would render results for different power levels less comparable. To solve this problem, two linear polarizers were set-up at the output of the laser. Specifically, two 10 mm Glan-Taylor calcite polarizers mounted on rotation stages were used for this purpose.

With this set-up, the polarization of the light can be controlled using the second polarizer (P2) and the first can be adjusted to any relative angle to the second in order to control the power. When the polarizers are oriented at exactly 90° to each other no light will be transmitted, when they have parallel orientation the maximum amount of light

will transmit. For all angles in-between, the intensity of light will be determined in accordance with Malus' law (Equation 3.4).

$$I = I_0 cos^2 \theta_i \tag{3.4}$$

Where I_0 is the initial intensity and θ_i is the difference in the polarization axis angle of the two polarizers.

As the intensity of light is controlled by a squared cosine function it is extremely sensitive to the angular offset between polarizers. Therefore polarizer P1 is mounted on a motorized stage controlled remotely using a computer. The specific stage used was a PR50-CC which is a DC-motor driven stage with a positional angular resolution of 0.01°. This allows for accurate and reproducible results even when polarizer P1 is altered as long as polarizer P2 remains constant. This power control set-up was thoroughly tested by carrying out measurements of the beam at various polarizer P1 positions and scaling the measurement using Malus' law to determine that the power level change was accurate and that any changes in the spectrum were negligible, a sample of the results are shown in Figure 3.7.

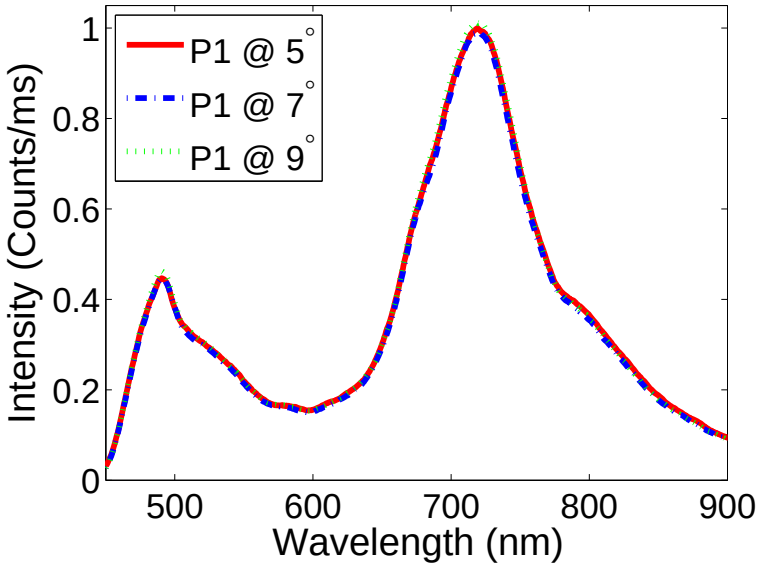

Figure 3.7: Normalized spectrum at different power levels.

The results show that the wavelength spectrum of light experiences negligible changes over the polarization angle range tested and that normalization using Malus' law correctly equalizes the power levels. The difference between data sets has been quantified by calculating the root mean squared error (RMSE). A normalized RMSE of 0.0065 was calculated between 5° and 7°, 0.0065 between 5° and 9° and 0.0066 between 7° and 9°. This shows an average error of around 0.6%. To put this into context, the normalized RMSE between two simultaneous measurements carried out with no changes of the

system and thus demonstrating the typical measurement accuracy is 0.0028, or 0.28%. This demonstrates that the polarization based power control technique is adequately accurate and any changes to the resulting spectrum are negligible and of the same order of magnitude as the overall measurement error.

Detector

The choice of a broadband laser source to be used within this system leads to the requirement for a spectrometer to detect the transmitted or reflected light. In order to achieve a good signal to noise ratio a TE cooled spectrometer optimized for low light conditions was selected. The exact spectrometer model used was a BTC122E by B&WTEK with a 100 μm slit width a wavelength range of 350 nm to 1050 nm and a resolution of <4 nm. The spatial limitations of the WARS system prevent direct mounting of the spectrometer on the detector arm and thus an optical fibre attached to a fibre holder on the detector arm was used to collect light and transmit it to the spectrometer. The first choice for this fibre was a 50 μm core multi-mode fibre patch cable. The use of a small core fibre leads to high angular resolution for scattering measurements and ensures that the fibre is flexible enough to withstand the movement range of the system. However, the small fibre core also significantly increases the alignment sensitivity of the system. Particularly for measurements of the specular beam as the beam's spot size is much larger than the fibre core and therefore the core's position within the beam leads to variations in the overall intensity and spectrum detected. This made accurate normalization of scattering measurements extremely difficult and in turn reduced the reproducibility of results. The alternative solution of simply using a larger fibre in the fibre holder was not possible as the limited bend radius of thicker fibres could lead to breakages when transitioned over the movement range of the detector arm. Therefore a solution was determined in which a mini integrating sphere was mounted on to the arm. The nature of the integrating sphere allows for a top mounted fibre which could be set to experience significantly less stress over the movement range of the stages. A simple proof-of-concept mini integrating sphere prototype was fabricated in order to test this approach. The prototype was designed using Autodesk Inventor software and was constructed from PTFE at the Southampton University ECS workshop. The sphere was designed to have an internal diameter of 1 inch and several inter-changeable apertures of different sizes for the entrance port to allow for a variable compromise between ease of alignment, detected signal intensity and angular resolution. The sphere design and constructed prototype are shown in Figure 3.8.

Several tests were carried out with this mini integrating sphere and it was determined that whilst it did indeed solve the alignment sensitivity issues, therefore providing repeatable results, significant signal power was also lost due to absorption and transmission within the sphere walls and multiple reflections from the interior of the

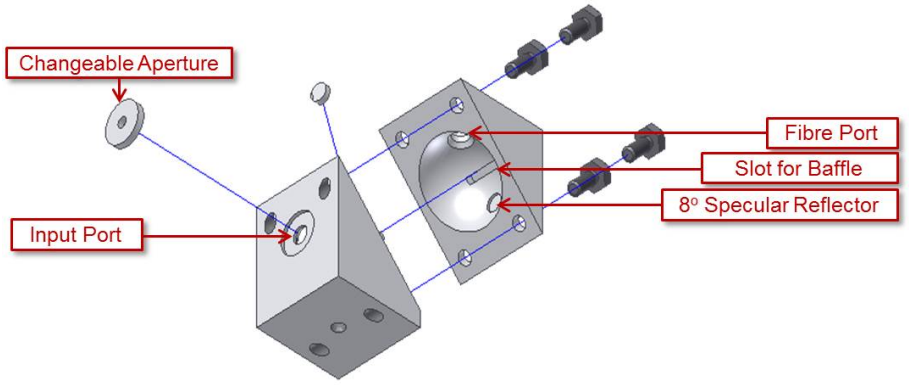

(a) Sphere Design.

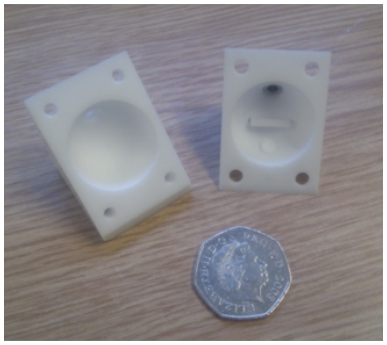

(b) Separate hemispheres.

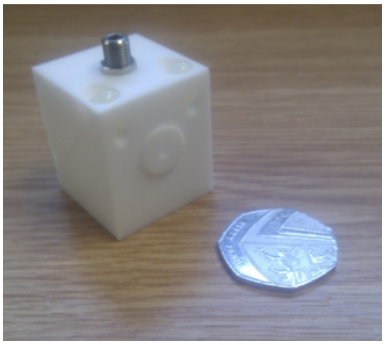

(c) Assembled sphere.

Figure 3.8: CAD design and photographs of fabricated mini PTFE integrating sphere.

sphere causing some light to escape through the entrance port. This led to the undesirable requirement of needing to set a very high laser power during measurements. It is preferable to avoid excessively high input power levels whenever possible due to the possibility of sample damage. To minimize this issue, a new sphere was professionally constructed by Gooch & Housego with an interior coated in Optolon 2^{TM}, this is a barium sulfate based high reflectivity coating used to increase overall reflectivity and scattering, therefore improving the signal to noise ratio.

The simplest way to test that alignment issues within the system had been corrected was to measure the specular reflectance of a known sample at various angles of incidence. This test was carried out on a silicon wafer after full alignment with and without the mini integrating sphere and the resulting comparisons are shown in Figure 3.9. As expected, the results using the integrating sphere showed a far superior match to theory without the need for any calibration. A comparison of theoretical expectations and measurements using the mini integrating sphere detector for the full wavelength range of the WARS system is presented in Section 3.2.5.

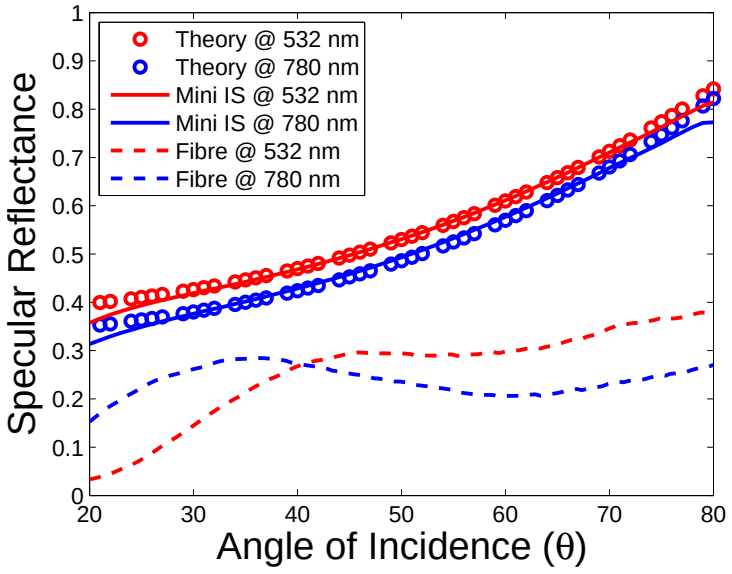

Figure 3.9: Comparison of theoretical expectations and measurements for specular reflectance of silicon Vs. angle of incidence with and without mini IS detector.

Positioning Hardware

The sensitive nature of scattering measurements means that highly accurate sample and detector positioning is required. This is particularly important in order to achieve reproducible results. To this end, the majority of the sample positioning hardware used within the WARS measurement set-up is motorized and controlled via a computer using an XPS universal high-performance motion controller produced by Newport. The base of the set-up consists of two URS100BCC DC motor driven rotation stages which have a 360° continuous motion range and a positional accuracy of 0.023°. A custom built detector holding arm is attached to the lower rotation stage (R1) and the second rotation stage (R2) is mounted on top of the detector arm. The lower stage therefore controls the angle of the detector whilst the upper stage will control the angle of incidence by rotating the sample. The upper stage is also used to counter the bottom stage rotations, therefore allowing the movement of the detector whilst keeping the sample position stationary. The base rotation stages and their positions relative to each-other are illustrated in Figure 3.10.

Two motorized linear translation stages are then mounted onto the top rotation stage (R2) and are positioned at 90° to each-other to allow for X and Y positioning of the sample. The stages used were MFA-CC DC motor driven linear stages, these have a 25 mm travel and a positional resolution of 0.0174 μm. A separate manual translation stage was also placed between the lower rotation stages and the X and Y positioner stages in order to compensate for possible misalignment in the top section of the system. Figure 3.11 shows the default position of these stages.

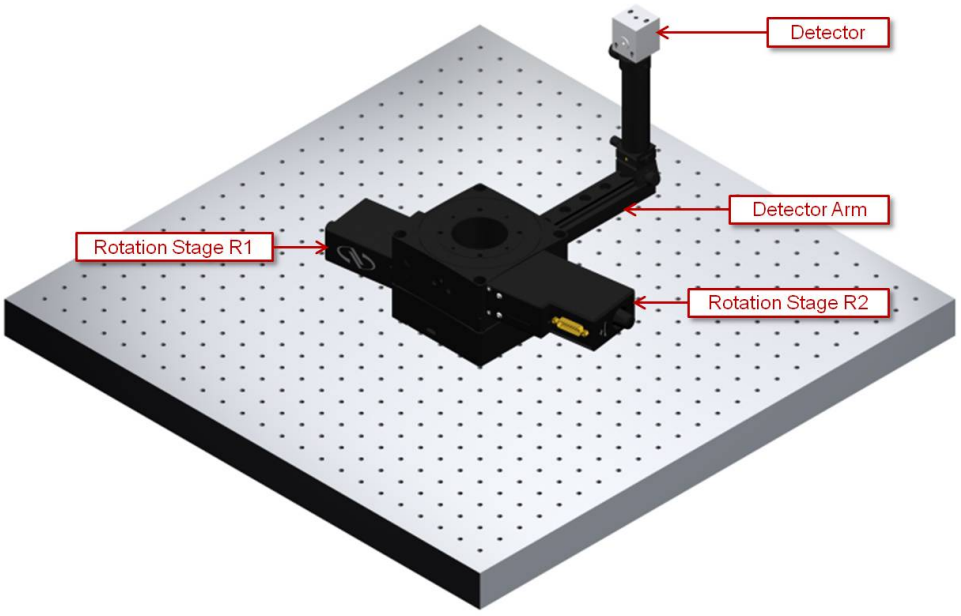

Figure 3.10: Base rotation stages and detector arm.

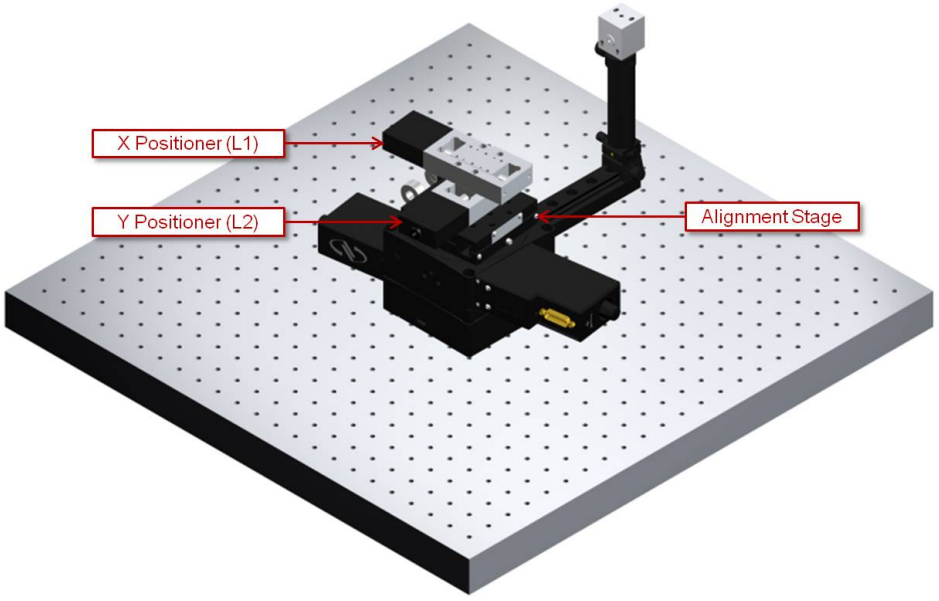

Figure 3.11: X and Y positioner stages.

A further MFA-CC stage was then mounted in an orthogonal position relative to the X and Y positioner stages to allow for movement of the sample in the z direction. Finally a PR50CC rotation stage (R3) was attached to the Z positioner stage and a custom built sample holder was then attached to the rotation stage (R3), see Figure 3.12. This rotation stage controls the tilt of the sample out of the z plane and is used purely for sample alignment.

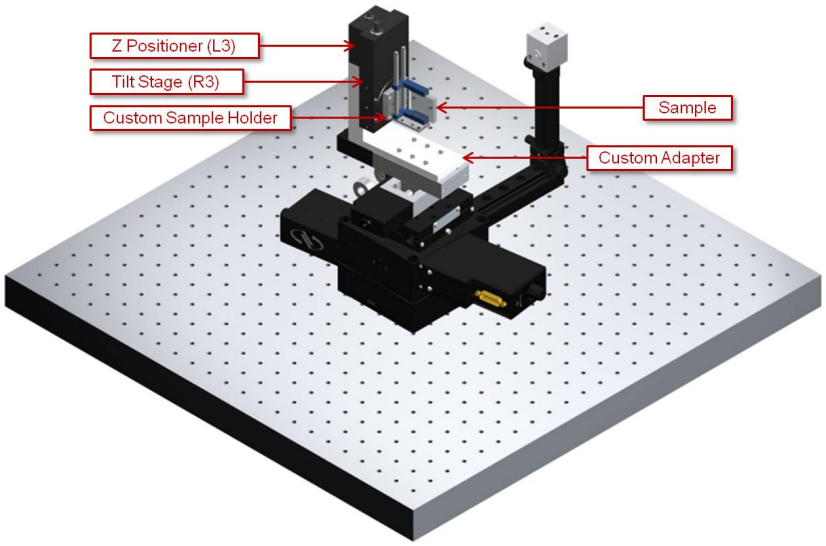

Figure 3.12: Z positioner and tilt stage.

In order to allow for detection of reflected light at small angles and to ensure that the system is kept compact, several mirrors were used to direct the SC450-2 source beam onto the sample, the final mirror is a custom made thin strip of silver coated silicon which is attached to a pillar hanging from an overhead rail. This ensures that the mirror does not physically obstruct the detector or any other moving parts of the system and the thin mirror profile allows for measurements of light reflected at angles as small as 5°. The completed system is illustrated in Figure 3.13. The entire system is built on an anti-vibration optical bench and surrounded by a custom built, light-tight enclosure in order to isolate the system from any external light sources.

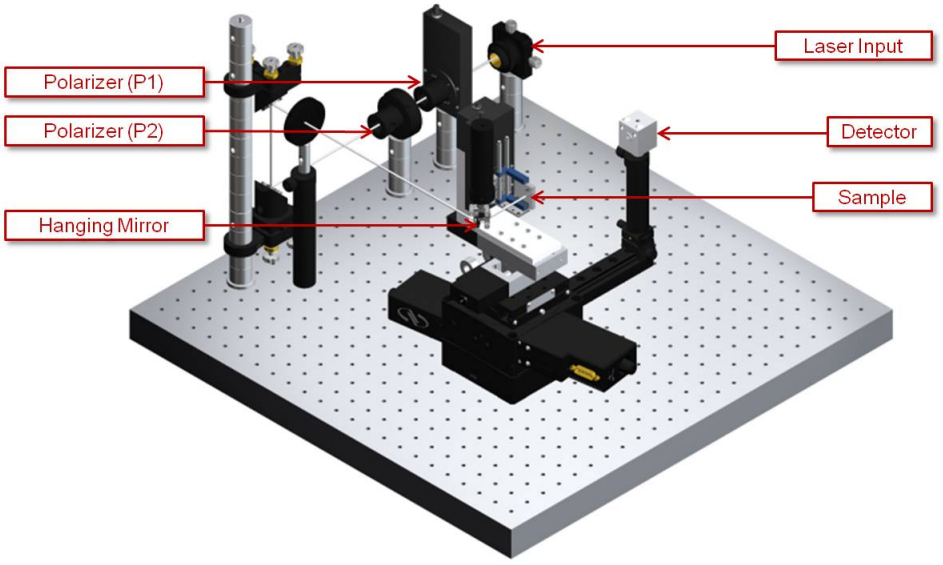

Figure 3.13: 3D drawing of complete WARS setup.

3.2.3 Measurement Process and Control Software

Prior to carrying out the WARS measurement the sample must be mounted and accurately aligned within the system. The laser beam is first aligned using simple double aperture methods to ensure that it is travelling parallel to the plane of the optical table and directly through the centre of the WARS set-up. The sample is then mounted and positioned into the path of the laser. To ensure that the sample is flat the motorized stages are used to adjust the tilt from the z and x planes until the specular reflectance of the sample is passing back through the original path of the laser. Finally, the y position of the sample is aligned by setting the sample to 45 degrees with the detector at 90 degrees. Once in this position, the y position is then adjusted until the specular reflectance from the surface of interest passes through the centre of the detector aperture. The full WARS measurement can then be carried out by directing the source at a chosen area of the sample. The light scattered by the sample is then collected by the mini integrating sphere attached to the rotating detector arm initially positioned at 90° (detecting the largest angle of scatter). Test measurements can be carried out at this angle in order to determine an appropriate polarizer position, and hence input power level, for the scattered light measurements. In most cases a power level corresponding to a minimum signal to noise ratio of 10:1 is selected. The sample and laser are then kept stationary as the detector fibre is rotated around the angle θ in either the clockwise or anticlockwise direction to measure scattering in reflection or transmission respectively. Spectrometer measurements of the light collected by the sphere are taken at regular intervals (typically every 1°) along the sweep of the detector arm. A 3D model of the experiment illustrating the movement range of the detector is shown in Figure 3.14.

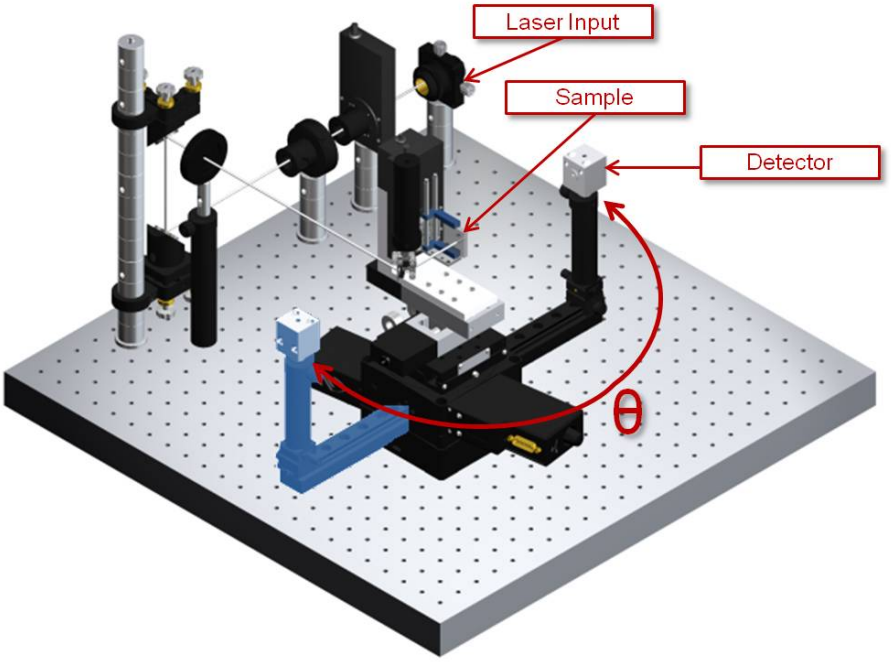

Figure 3.14: 3D model of WARS set-up.

Due to the very low intensity of scattered light, large integration times are required which results in a long measurement time. It is therefore useful to automate the measurement process which also ensures a high degree of measurement repeatability. To achieve this, a graphical user interface was designed in-house using LabVIEW^{TM} development software. The custom built WARS software allows the user to simply and efficiently align the sample and begin the automatic scan. The user defines the start and end position of the detector sweep as well as the step size and starting integration time for the spectrometer (typically 65 seconds). As the detector moves closer to the specular beam, taking regular measurements, the software detects if the spectrometer saturates and automatically lowers the integration time and carries out a repeat measurement when necessary. For the measurement of the directly transmitted (at 0°) or specularly reflected beam the software also alters the power control polarizer rotation to lower the power level of the incident beam. In order to obtain accurate measurements, a 'dark measurement' of the background noise must be taken with the laser source switched off for every integration time used, this process is built-in to the custom software.

There is also built-in functionality for taking area averaged measurements, in this case the user can specify how many areas should be measured and the software will automatically carry out the scan and move to new areas of the sample as appropriate. A screen print of the custom built software's user interface is shown in Figure 3.15.

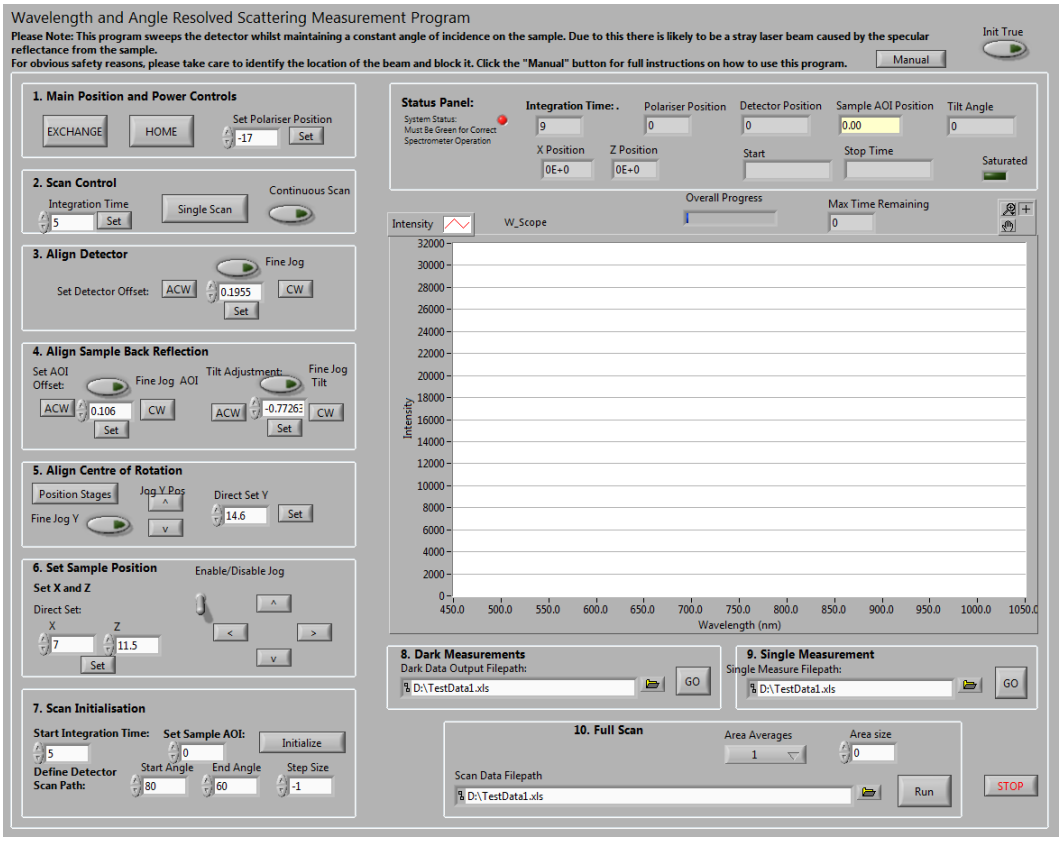

Figure 3.15: Graphical user interface for WARS measurement software.

All raw measurement data is saved into comma separated text files, these files include information on the positions of all stages and the integration time used for each measurement. This data is then used as the input to a custom Matlab script file which processes and plots the data as detailed in Section 3.2.4

3.2.4 Data Processing

The saved measurement data is automatically processed by a custom built Matlab program which normalizes all measurements of scattered light with respect to the source measurement and then outputs various 2D and 3D graphical representations of the results (see Appendix A). The Matlab code assumes a linear relationship between integration time and intensity, and normalizes for integration time accordingly, the accuracy of this linearity assumption is discussed further in Section 3.2.5 . The intensity of the measured specular beam is also modified to compensate for the reduction of input power during the specular measurement process using a scaling factor determined by applying Malus' law as discussed and tested in Section 3.2.2. If required, The Matlab code also converts the measured in-plane data into total scattering data as detailed in Section 3.1.3. Useful data is extracted and displayed by the Matlab script in several different ways, however, the main WARS measurement result is typically presented using a coloured, high resolution contour plot. An example of a typical WARS measurement result for the scattering in transmittance of a textured TCO sample is shown in Figure 3.16.

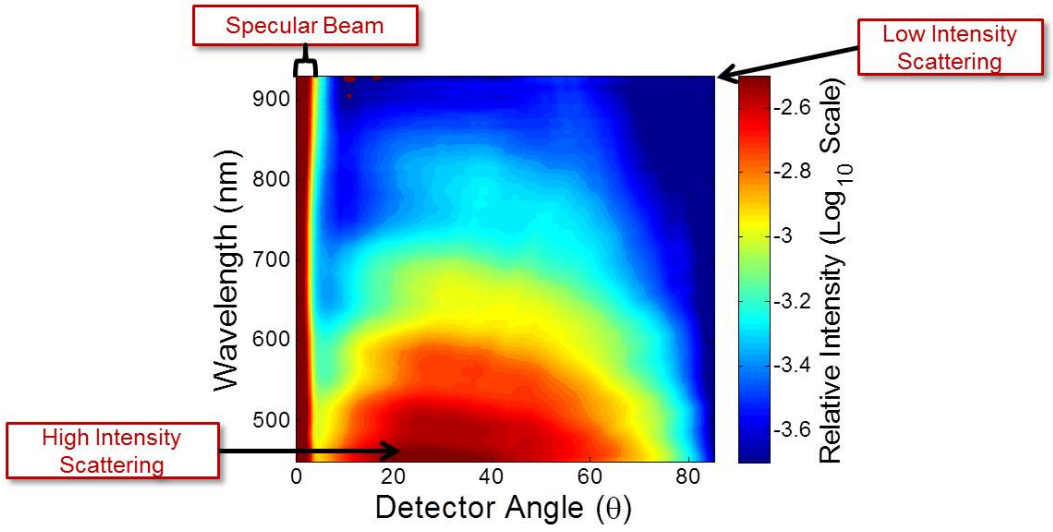

Figure 3.16: Annotated example WARS result for Asahi Type-U TCO.

3.2.5 System Tests and Example Measurements

Several tests were carried out on the WARS system in order to check that results were both meaningful and reproducible. Power control tests were first carried out to ensure that the polarization based control technique worked as expected. The results from this test showed an error of the same order of magnitude as the spectrometer noise, thus indicating that polarization based power changes could be accurately normalized out and any changes to the detected spectrum were negligible, further details and results for this test are shown in Section 3.2.2.

For a typical sample, light intensity scattered to small angles is orders of magnitude higher than the intensity at large angles. Therefore, to ensure an adequate signal to noise ratio is achieved for measurements at every angle, several different spectrometer integration times must be used. The different integration times can be normalized out using the assumption that the relationship between measured intensity and integration time is linear. This assumption was tested by repeating the same measurement over a range of integration times and carrying out the linear normalization. The results are shown in Figure 3.17.

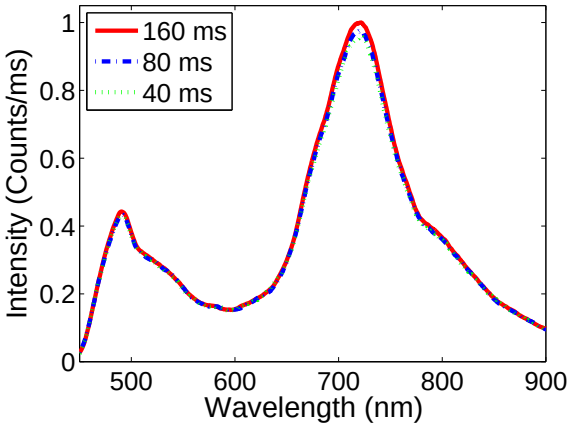

Figure 3.17: Normalized spectrum at different integration times.

The results show that changes in the integration time can be normalized out with only minor alterations to the detected spectrum. The average RMSE between measurements was 0.01, this 1% error is slightly higher than the typical error for the spectrometer, however, this level of error is still acceptable for scattering measurements which will typically be on a logarithmic scale.

To ensure that the system alignment procedure was adequate, specular reflectance versus angle of incidence tests were carried out on polished silicon. An example of these results for specific wavelengths is shown in Figure 3.9 of Section 3.2.2, the full results are shown here in Figure 3.18.

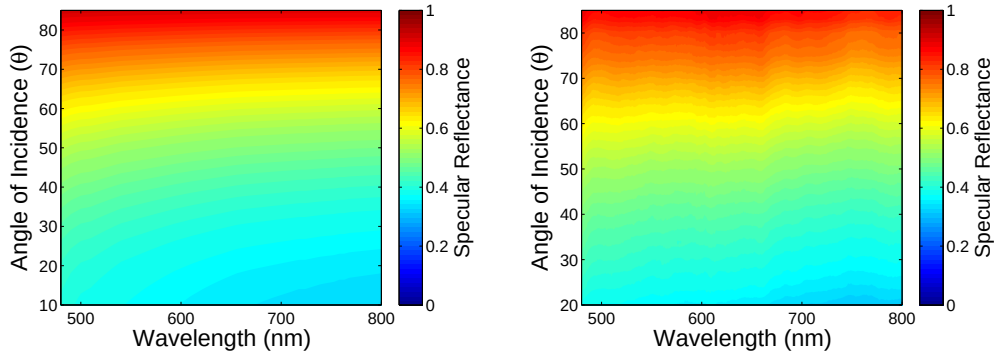

(a) Theoretical expectation.

(b) Experimental measurement.

Figure 3.18: Broadband reflectance Vs. angle of incidence for polished silicon.

A visual comparison of the theoretical and measured results shows that they are in excellent agreement. The level of this agreement was quantified by calculating the RMSE between the calculation and measurement over the wavelength and angle range of interest, omitting the extremes of the ranges. This was calculated using a Matlab script which showed the RMSE to be 0.0865. This is considered a low level of error, particularly for a measurement carried out with no external calibration. The small differences between the measurement and theory could be due to non-ideal alignment of the polarizers, minor sample misalignment or simply small deviations in the optical properties of the silicon compared to the theoretical ideal. This confirms that the system alignment procedure is adequate and that the software and stages work correctly.

To test the accuracy and reliability of full WARS measurements, a method was devised to allow the results of a WARS scan to be compared to measurements of diffuse transmittance or reflectance as measured using the well-established integrating sphere technique detailed in Section 3.1.2. The integrating sphere technique measures the total light scattered at angles between 5° and approximately 90°, theoretically, this should be comparable to the results of a WARS scan if the scattering intensity for all angles between 5° and 90° are summed up. Unlike a standard integrating sphere measurement, the WARS measurement is only in one plane so the results also need to be normalized to account for the out of plane scattering and therefore this comparison method is only valid for isotropic scatterers such as surfaces with random roughness. Finally, a scaling factor will be necessary to account for the detector arm length, aperture size, and losses within the mini integrating sphere collector and fibre of the WARS equipment. This scaling factor should be constant for all samples and, within a reasonable approximation, for all wavelengths. This test was initially carried out on the commercial TCO, Asahi Type-U. The scaling factor was determined as the value which gave the best fit between the integrated WARS results and the known diffuse transmittance of the sample. WARS measurements were then taken for two different TCO samples and the integrated results were modified with the same scaling factor and

compared to the known diffuse transmittance. The WARS system also measures specular transmittance by default, therefore allowing comparisons to be made for specular, diffuse and total transmittance as measured using the two different techniques. Results for the two test TCO samples investigated are shown in Figure 3.19.

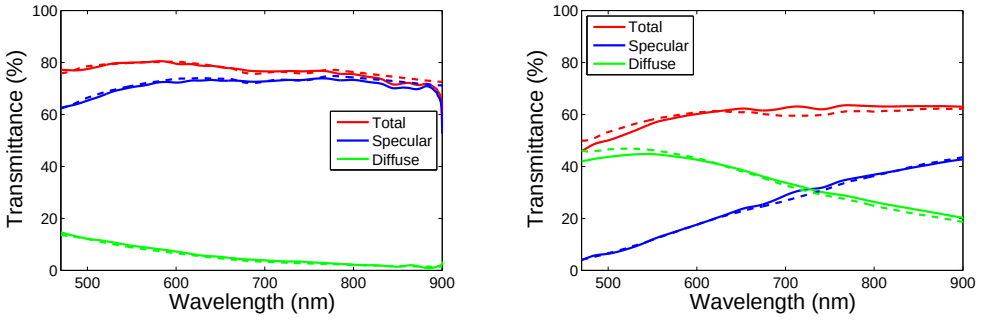

(a) TEC 8 TCO.

(b) ZnO:Al 757.

Figure 3.19: Comparison of total, specular and diffuse transmittance as measured using conventional TIS technique (smooth line) and as calculated by integrating WARS measurement (dashed line).

The results show an excellent agreement for both of the samples. Comparison of the actual data values shows a mean squared error of 0.00267, 0.00554 and 0.0167 for the Asahi Type-U (used to calibrate), TEC 8 and ZnO:Al 757 samples respectively. This is within the margins of error for a typical TIS integrating sphere measurement and therefore demonstrates that the WARS measurements are of similar or higher accuracy.

Finally, to test reproducibility of results, 4 scans were taken of a single sample (Asahi Type-U). The first and second scan were simply repeat measurements, the third scan was a repeat measurement carried out using different power levels and the final scan was a repeat measurement after the sample had been re-mounted and re-aligned within the system. As expected, the change in input power between scan 2 and scan 3 was correctly normalized by the measurement data analysis code and the robust alignment procedure ensured that even after re-mounting and re-alignment, a similar measurement result has been obtained. The RMSE between each of the scans is shown in Table 3.1.

Scans Compared	RMSE
Same Position and Power	0.03
Same Position, Different Input Power Levels	0.053
Re-mounted/Re-aligned	0.064

Table 3.1: RMSE for repeat WARS scans

With the adequacy of the new WARS measurement's reliability and reproducibility confirmed, several unique samples were characterized in order to investigate the potential of this technique as a characterization tool. The sample set consisted of Asahi Type-U TCO (rms roughness 37 nm), a ZnO:Al TCO (rms roughness 118 nm), two different

arrays of randomly arranged metal nanoparticles on glass and two arrays of periodic inverted pyramids etched into silicon with different periodicities. SEM images of the samples and their corresponding WARS results are shown in Figures 3.20 to 3.25.

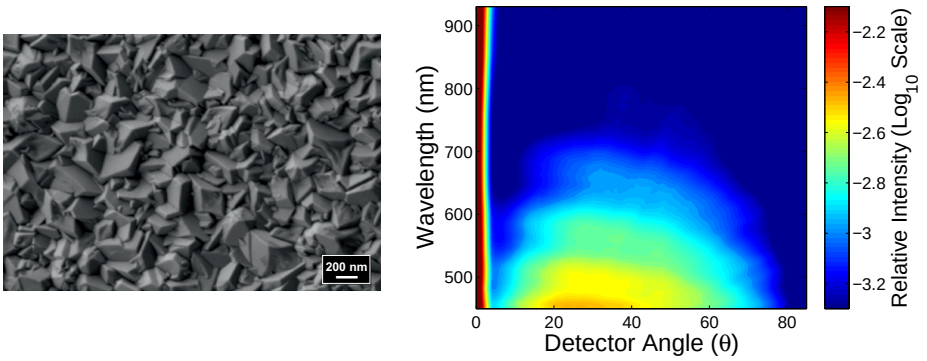

(a) SEM of Surface. (b) Transmittance WARS Measurement.

Figure 3.20: Transparent conducting oxide SnO2:F Asahi Type-U.

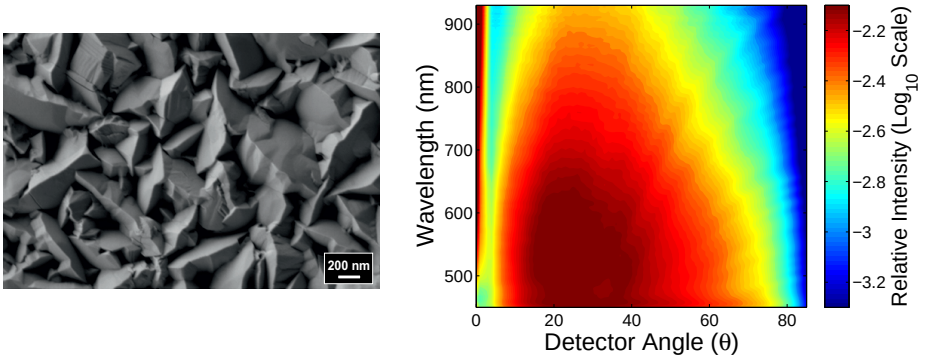

(a) SEM of Surface. (b) Transmittance WARS Measurement.

Figure 3.21: Transparent conducting oxide ZnO:Al 757.

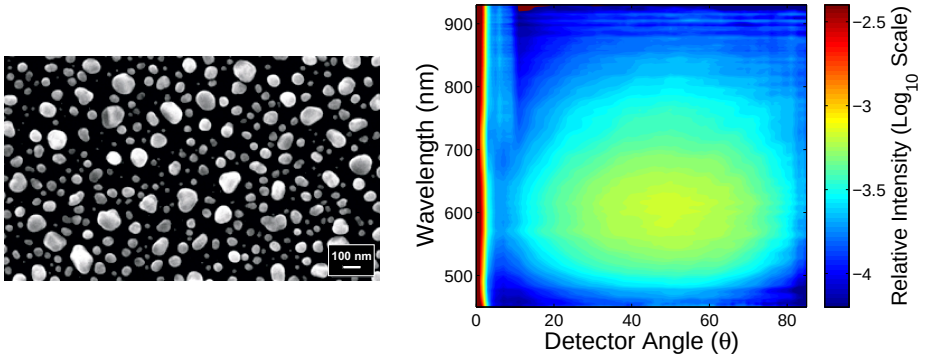

(a) SEM of Surface. (b) Transmittance WARS Measurement.

Figure 3.22: MIF from annealed 7.5nm thick Ag layer.

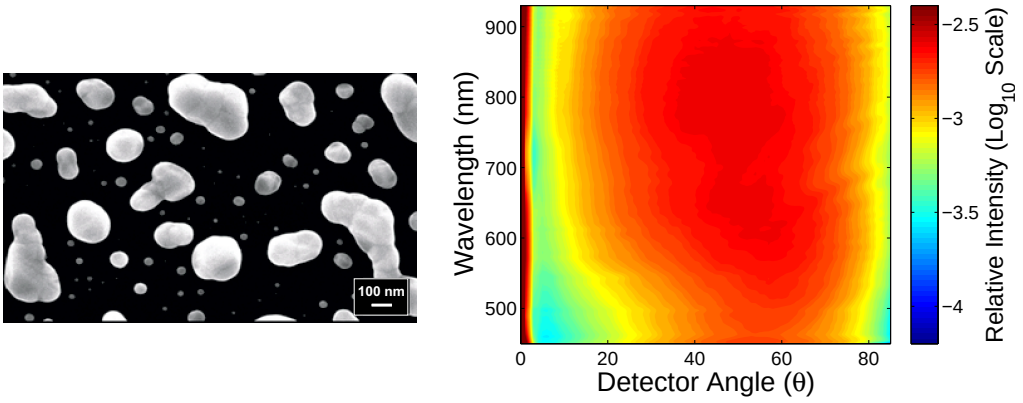

(a) SEM of Surface. (b) Transmittance WARS Measurement.

Figure 3.23: MIF from annealed 20nm thick Ag layer.

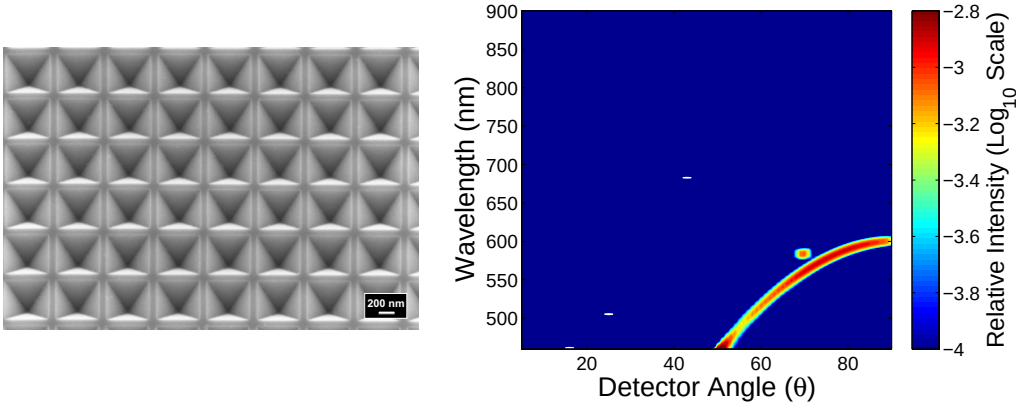

(a) SEM of Surface. (b) Reflectance WARS Measurement.

Figure 3.24: Periodic inverted pyramids in silicon with a 600 nm pitch.

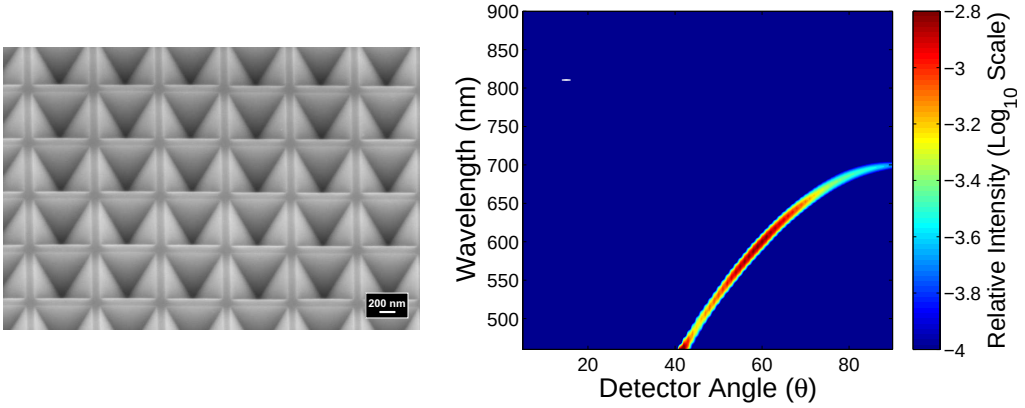

(a) SEM of Surface. (b) Reflectance WARS Measurement.

Figure 3.25: Periodic inverted pyramids in silicon with a 700 nm pitch.

The results of Figures 3.20 to 3.25 showcase the vast variations in scattering profiles that different samples consisting of sub-wavelength features can produce. It is clear that the scattering profile from samples such as these strongly varies for both wavelength and scattering angle and many of these variations would not be detected using simpler TIS or single wavelength ARS measurements. The newly-developed WARS system is therefore uniquely capable of providing the comprehensive determination of scatter from a sample and thus has the potential to reveal features that might normally be overlooked by traditional measurement techniques.

High demand for this versatile system has led to a second version being constructed at the University of Southampton and a third system is now under development at the University of New South Wales, Australia. This latest version of the system will involve several upgrades including automation of the rotation of both polarizers and an extended wavelength detection range up to 1700 nm. More sensitive detectors will also be utilized in order to further reduce measurement noise. The possibility of patenting and commercializing the WARS system is also under discussion as the total cost of around £120,000 is comparable to that of commercial alternatives with the WARS system being uniquely capable of characterizing small area samples and having the potential to provide superior results for a more versatile range of measurements.

Chapter 4

Characterization of Textured Transparent Conducting Oxides

Textured transparent conducting oxides (TCOs) are widely used in thin-film photovoltaics and have proven to be a cheap and efficient technique for increasing device efficiency by increasing absorption of light via scattering. However, their potential is known to be severely limited due to the strong correlation between the size of surface features and the wavelengths of scattered light. To scatter longer wavelengths, larger surface features are required and this increases unwanted surface recombination and can lead to cracks and non-conformal deposition which degrades device characteristics. Optimized textured TCOs must therefore involve a compromise between optical absorption and electrical characteristics. Scattering from textured TCOs is an established field and has undergone significant research, however, the vast majority of this work has relied on simple haze and angle resolved scattering characterization techniques to look at conventional, commercial samples. In this chapter we aim to further investigate the scattering of both commercial and novel, experimental textured TCOs by extensive characterization using the state of the art WARS measurement technique alongside conventional measurements. This allows for a more detailed understanding of the scattering effects of texturing and should help to further optimize light-trapping for thin solar cells, potentially resulting in more efficient devices with little or no change in fabrication costs.

4.1 TCOs for Photovoltaics

The underlying physical principles regarding the use of textured TCOs to enhance light-trapping within thin solar cells are discussed in Section 2. In this section, the deposition methods and typical characteristics of commonly used TCOs will be detailed and recent progress in this area will be reviewed along with a discussion of the challenges and limitations involved with using textured TCOs to achieve light-trapping in photovoltaics.

4.1.1 TCO Materials and Deposition Methods

TCOs deposited on glass are commonly used as superstrates for thin-film solar cells (TFSCs). A superstrate TCO acts as the front electrical contact for the device, therefore the deposited film should have suitable optical and electrical properties for the desired application. For TFSC applications, a low resistivity of around 10^{-4} Ω.cm is generally required along with an average transmittance of at least 85% over the visible/IR wavelength range. The TCO must also be stable at temperatures used in subsequent device fabrication process steps and resistant to the gasses and chemicals used in these processes. Finally the TCO must be relatively cheap and able to be deposited on a large scale. These requirements limit the range of possible TCO materials to just a few commonly used compounds.

One of the most established TCOs used in photovoltaics industry is indium tin oxide (ITO), although fluorine doped tin oxide (FTO) and aluminium doped zinc oxide (AZO) are also frequently used and can provide similar optical and electrical properties [69]. The use of ITO is in general decline largely due to limited indium resources leading to increased costs and unpredictable supply. FTO has therefore become more prevalent as a front contact material in thin-film silicon solar cells and is the TCO used in most commercial Glass/TCO superstrates, such as Asahi Type-U. In recent years, AZO has also received increasing interest in the photovoltaic industry as studies have shown that it can be deposited with an excellent transparency of around 90% and a low resistivity comparable to the best reported for ITO, leading to similar device efficiencies [70]. AZO is also more resistant to hydrogen-rich plasmas which are required for the PECVD deposition of silicon and is therefore particularly promising for use within a-Si and μc-Si based solar cells [69].

TCOs can be deposited using a variety of methods, including chemical vapour deposition (CVD), spray pyrolysis, evaporation and sputtering. Different deposition techniques can result in variations in electrical and optical properties of the TCO as well as changes in the surface roughness of the film. The preferred method depends on the exact TCO type required and the intended purpose. For example, basic tin oxides are often deposited using CVD, in this case surface roughness is a by-product of the TCO deposition itself and can be controlled by deposition parameters. In general, increasing the thickness of a

TCO layer will increase the overall roughness, however, it is difficult to precisely control the shapes of surface features and angles of surface facets as these properties will depend on the crystallographic nature of the TCO and growth nucleation characteristics. For the case of ITO, sputtering or evaporation is typically used, these techniques result in a relatively smooth deposited film. ZnO is often deposited using DC or RF magnetron sputtering but can also be deposited using Metal Organic CVD (MOCVD) or Low Pressure CVD (LPCVD). When smooth films are deposited, etching can be used to create texture. Typically diluted acid or ammonium chloride can be used as an effective etchant [71].

4.1.2 Typical TCO Texture and Optical Characteristics

When a superstrate configuration is used for solar cell device fabrication, the incoming light is first incident on the glass and TCO before entering the absorber layer of the device. This means that texturing the TCO provides an excellent opportunity to scatter incoming light and therefore increase the path length for the first pass. Due to conformal deposition processes, the texture applied to the TCO is typically replicated to some extent at all subsequent interfaces within the device structure, further enhancing the scattering effects.

For textured TCOs used in TFSCs, studies have consistently shown that texturing has the strongest scattering effects on shorter wavelengths of light. Longer wavelengths cannot distinguish the individual interface features and will instead perceive a refractive index gradient, this will not lead to enhanced scattering but can have the benefit of reducing reflectance and therefore increasing overall transmittance at these wavelengths. Increasing the surface roughness has been shown to enhance the haze across all wavelengths, however, this often requires thicker TCO layers, thus increasing parasitic absorption within the TCO. In the case of thin-film a-Si solar cells, increased roughness can also lead to reduced open circuit voltages for the final device, this is attributed to defects in the a-Si caused by the sharp valleys of the textured TCO [72].

For a-Si based solar cell devices, research has shown that a surface roughness of around 40 nm gives a useful level of optical enhancement without having too detrimental an effect on electrical characteristics, therefore providing the most efficient devices. The commercial TCO, Asahi Type-U is a well optimized TCO with an RMS roughness in this range and is frequently used as the standard for comparison when investigating alternative textured TCOs for a-Si devices [40, 41, 42, 43]. However, the high costs of Asahi Type-U are prohibitive for large solar cell module production. Similar, but less expensive TCO on glass superstrates from other companies are also available. Notably, NSG's TEC 8 TCO is an FTO film with a very similar surface structure to Asahi Type-U which exhibits comparable haze and thereby in principle can provide a route to more

cost-effective devices. The surface structure and corresponding haze values measured for these TCOs are shown in Figures 4.1 and 4.2 respectively.

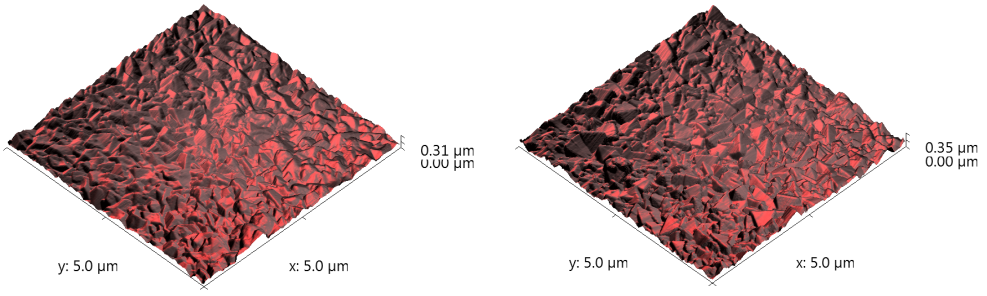

(a) AFM of Asahi Type-U.

(b) AFM of NSG TEC 8.

Figure 4.1: Comparison between surface texture of Asahi Type-U and NSG TEC 8.

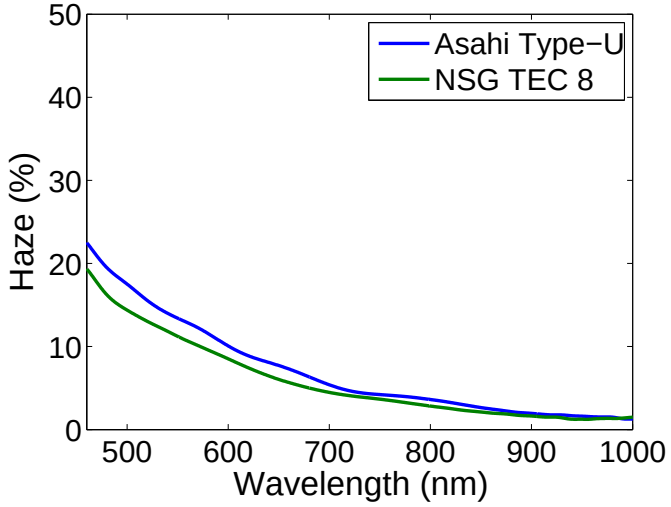

Figure 4.2: Comparison of measured haze values for Asahi Type-U TCO and NSG TEC 8.

The characteristic haze curves shown in Figure 4.2 clearly highlight the strong trend of decreased scatter with increased wavelength. This is a significant issue within TFSC as the longer wavelengths which are close to the band-gap of the absorber material have the lowest absorption coefficient and hence the highest need for light-trapping. Due to the physical mechanisms involved with scattering from textured interfaces, it is unlikely that this trend can be altered without the use of an alternative scattering mechanism. Research should therefore be focused on the analysis and enhancement of the angular distribution of light scattered by TCOs. Increasing the angle of scatter will dramatically increase the path length within a device and could therefore increase absorption, particularly for longer wavelengths of light.

In general, the angular distribution of light scattered by textured TCOs shows the characteristics of an isotropic, near Lambertion scattering profile. However, some

experimental TCOs have shown significant variations on this profile. Examples of published ARS results for two different TCOs are shown in Figure 4.3 [71].

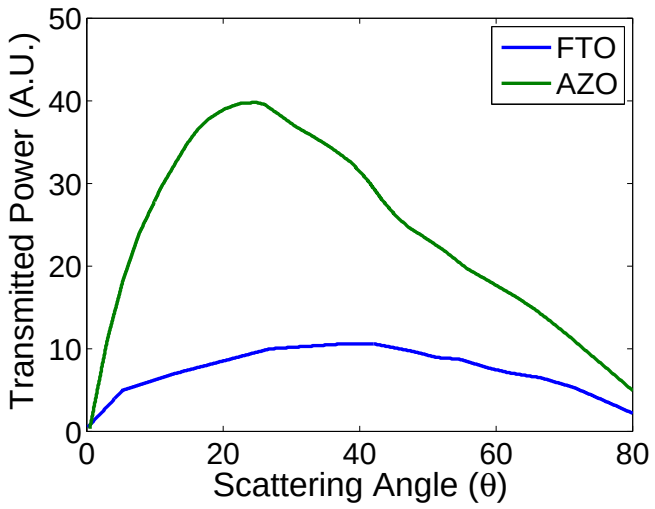

Figure 4.3: Comparison of single wavelength (633nm) ARS measurement of textured FTO (haze 18.3%) and textured AZO (haze 49%). Recreated from [71].

The possibility for variations in the angular distribution of scattering show that there is potential for TCOs to be further optimized. In order to gain a deeper understanding of the angular distribution of scatter for TCOs it is useful to determine the full WARS characteristics. There are very few examples of this kind of comprehensive scattering measurement in the literature, largely due to the complexity and low signal issues involved in the type of measurement required. Zeman et al. have published WARS characteristics (in this case referred to as the 'broad wavelength angle intensity distribution') for several common TCO materials based on measurements carried out using the commercial ARTA measurement device [68] [66]. However, the results from this system showed a significant degree of error, particularly at large scattering angles. In the following sections of this chapter a range of conventional and experimental TCOs will be investigated using a combination of optical characterization techniques. Measurements carried out using the high power WARS system will be used to provide detail of the wavelengths and angles of scattered light. This should lead to a better understanding of the true limits of random texturing and the ability to gauge the potential of adjusting texturing to achieve larger scattering angles.

4.2 Methods

4.2.1 Fabrication

TCO Deposition

Several different sample sets were used for the investigation of light scattering from textured TCOs. These included two commercial FTO based TCOs, three experimental FTO films produced by the University of Salford and three experimental AZO films produced by EPV Solar Inc.

The commercial FTO films investigated were Asahi Type-U [39] and NSG TEC 8 [73]. These TCOs are both known to be well optimized for thin-film a-Si solar cells and are widely used for this purpose. Both commercial TCOs were deposited using atmospheric pressure CVD techniques which naturally create a textured film; the exact parameters of the CVD deposition have not been published. These TCOs are labelled throughout this work with their commercial names; Asahi Type-U and NSG TEC 8.

The experimental FTO films developed by Yates et al. at the University of Salford were also deposited using CVD [74]. The TCOs used in this investigation were deposited at three different temperatures, 580°C, 600°C and 620°C, and are denoted within this work as FTO 580, FTO 600 and FTO 620 accordingly. Altering the temperature affects the growth rate, therefore leading to each sample having a different film thickness and surface roughness characteristics.

Textured AZO films were provided by EPV Solar Inc. on soda-lime glass substrates by reactive hollow cathode sputtering using metallic Zn targets [75]. The deposition pressure was 260 mTorr and the substrate temperature was approximately 230°C. This process results in highly textured surfaces without the need for any post deposition etches. Three films of different thicknesses were prepared in order to vary the average feature size. The samples are labelled as supplied by the company; AZO 758, AZO 459 and AZO 757 in order of thickness.

Amorphous Silicon Deposition

Part of the investigation carried out within this chapter is focused on the optical analysis of thin a-Si layers deposited on selected TCO superstrates. The a-Si layers were all deposited using PECVD, specifically an Oxford Instruments PlasmaLab System 100. This system utilizes an ionized plasma glow discharge to disassociate source gases into their elemental components allowing them to deposit on to the substrate material which is typically heated to a specified temperature. For regular CVD techniques, very high substrate temperatures are required in order to disassociate precursor materials.

However, with PECVD, RF electrodes are used to ionize the atoms of the surrounding gas, forming a plasma in the chamber, thus adding energy to the system whilst maintaining a relatively low substrate temperature. The excitation frequency of this system is 13.56 MHz. Mass-flow controllers (MFCs) are used to supply source gases to the chamber which then combine, providing the atomic species for CVD via a uniform shower-head arrangement. Pressure is regulated within the chamber using a programmable APC valve and a turbo / base pump combination. For the a-Si deposition used within this investigation a substrate temperature of 250°C was used with a chamber pressure of 350 mTorr. An RF Power of 10 W was used and silane (Si_3H_4) and hydrogen (H_2) gasses were introduced to the chamber at a flow rate of 50 sccm. These settings resulted in the deposition of a-Si at a rate of 0.24 nm/sec.

4.2.2 Characterization

Atomic Force Microscopy: Surface Topography

It is essential to obtain accurate information regarding the topography of the TCO surface. For surfaces with features smaller than the wavelength of visible light, such as those used in textured TCOs for photovoltaics, the surface characteristics can not be accurately determined using standard optical microscopes. It is therefore necessary to use more sophisticated techniques such as scanning electron microscopy (SEM) or atomic force microscopy (AFM). For surface roughness characterization, AFM is the preferred technique as it provides specific height information and naturally builds up an accurate 3D image of the surface.

In the AFM technique a probe with a nano-scale tip is mounted on a cantilever which is then scanned across a sample using piezoelectric ceramics for fine x, y and z movement. AFMs can be operated in several modes, the simplest of which is 'contact mode'. In contact mode the probe tip is kept in direct contact with the sample surface. The deflection of the cantilever is measured by directing a laser at the top surface of the cantilever and measuring the position of the reflected beam using a photo-diode array. Feedback is then utilized to move the probe up and down and the cantilever deflection information is processed to obtain accurate height information for the sample. Alternatively, the AFM can be operated in 'tapping mode' in which the cantilever is oscillated close to or at resonance above the sample surface. Changes in the oscillation amplitude, phase and frequency are then recorded and processed to obtain height information for the surface.

There are several feedback parameters that can be adjusted for an AFM scan and these can have a significant effect on the result. It is therefore useful to have some prior knowledge of what the surface should look like before carrying out AFM scans. To this end, several of the investigated TCO samples were first imaged using scanning electron

microscopy. AFM scans were then carried out on each sample in order to get accurate surface roughness information. Figure 4.4 shows a comparison between surface images acquired using SEM and AFM for the Asahi Type-U TCO.

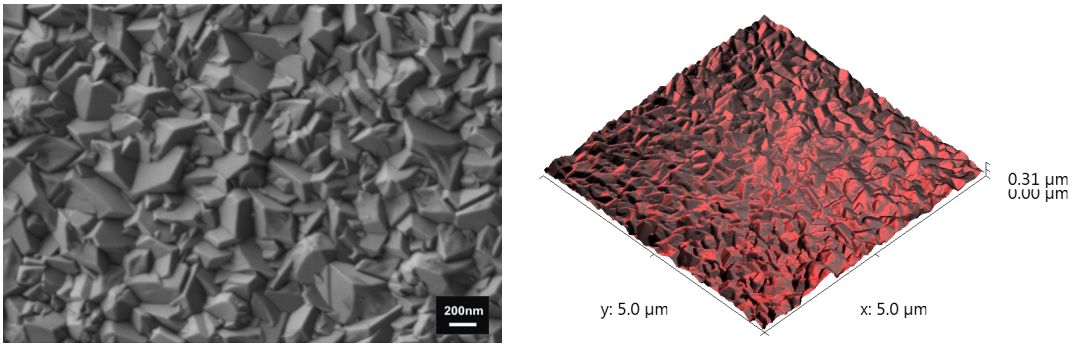

(a) SEM of Asahi Type-U.

(b) AFM of Asahi Type-U.

Figure 4.4: Comparison between SEM and AFM images.

The resolution of AFM is dependent on the exact tool used and the radius of the probe tip. A large variety of AFM probe tips are commercially available with some having particular specifications designed for the measurement of certain surface types. When measuring the topography of textured TCOs with large surface features, it was determined that a high aspect ratio tip should be used as standard tips can introduce an artificial rounding of peaks and valleys. High aspect ratio tips will naturally dull quicker so it is preferable to use them in 'tapping' mode, this mode was used for all AFM scans within this work. For each sample the X and Y scan resolution was set to 512 and several sample areas sizes ranging between 4 x 4 μm and 50 x 50 μm were scanned. The AFM model used was a Veeco Caliber.

Integrating Sphere Optical Measurements

Conventional optical characteristics such as specular and diffuse transmittance and reflectance were determined for each of the investigated samples using integrating sphere based measurements, the general details of which are discussed in Section 3.1.2. The exact arrangement used for this work consisted of an RTC-060-SF sphere used with a Fianium SC450-2 broadband super-continuum laser and a TE cooled B&W Tek spectrometer, allowing accurate measurement of wavelengths between 460 nm and 900 nm to a resolution of around 1 nm. The Fianium laser provides a small spot size of around 1.5 mm diameter with excellent collimation, eliminating the need for lenses within the experiment. The RTC-060-SF integrating sphere is 6 inches in diameter and has a 1 inch specular exclusion port meaning that measurements of diffuse light account for light scattered to angles greater than 5°. The RTC-060-SF sphere can be operated in single or double beam mode as detailed in Section 3.1.2 in which double beam mode was shown to have superior accuracy. This mode has therefore been used for all integrating

sphere measurements. In each case, the TCO coated glass superstrates were orientated so that the light was first incident on the glass and the measurements were carried out in air.

WARS: Optical Scattering

To gain further information on the exact angles and wavelengths of scattered light, WARS measurements were carried out in transmittance for all TCO samples. The general procedure and equipment used for WARS measurements is detailed in Section 3.2. As with the integrating sphere optical measurements, samples were orientated such that light was first incident on the glass substrate. The samples were positioned with the textured TCO/Air interface in the central axis of rotation of the system. Scans were carried out over an angular range of 90 to 0 degrees with a starting integration time of 65 seconds. The input power of the laser was adjusted to ensure that the signal to noise ratio at a scattering angle of 80 degrees was at least 3:1. The mini integrating sphere collector was equipped with a 2 mm aperture and was placed on the rotation arm at a distance of 10 cm from the centre of the sample.

4.3 Results and Discussion

The experimental results for textured TCOs are presented in three sections. The first investigates the commercial standards used for a-Si solar cell production along with experimental FTO films of similar roughness. The second section extends the study by characterizing substantially rougher AZO films to investigate the effects of extreme roughness and variety in the shape of surface features. Finally, the third section examines several different TCOs coated with a 200 nm a-Si layer in order to investigate the actual absorption enhancement caused by different types of texturing.

4.3.1 FTO Samples

To begin the investigation into the light-trapping effects of TCO films, a systematic study of 3 experimental FTO samples of increasing roughness and thickness has been carried out with the results compared to two industry standards; NSG TEC 8 and Asahi Type-U. These industry standard TCOs are typically used for the commercial production of a-Si solar cells and are essential in order to achieve acceptable efficiencies, however, they may not be optimal and the work in this section will investigate the potential of alternative TCOs with similar levels of roughness. The experimental FTO samples were fabricated at the University of Salford by Yates et al., details of the fabrication of these samples and the industry standards are provided in Section 4.2.1. In the following sections, the surface roughness data of each of the investigated TCOs is first obtained using atomic force microscopy (AFM) and then statistically analysed using a variety of methods. The conventional and novel measured optical transmittance characteristics are then presented and analysed in order to determine links between the surface texture and light-trapping ability of the samples.

Surface Topography

To determine the surface topography and roughness parameters of each of the FTO samples, atomic force microscopy has been used, as detailed in Section 4.2.2. The results for the commercial standards and each of the experimental FTO samples are shown as false coloured 3D plots in Figures 4.5 and 4.6 respectively. The plots shown are for a sample area of 4 μm x 4 μm, however, several different sample areas were measured in order to check for consistency in the AFM data and to allow for statistical averaging where appropriate.

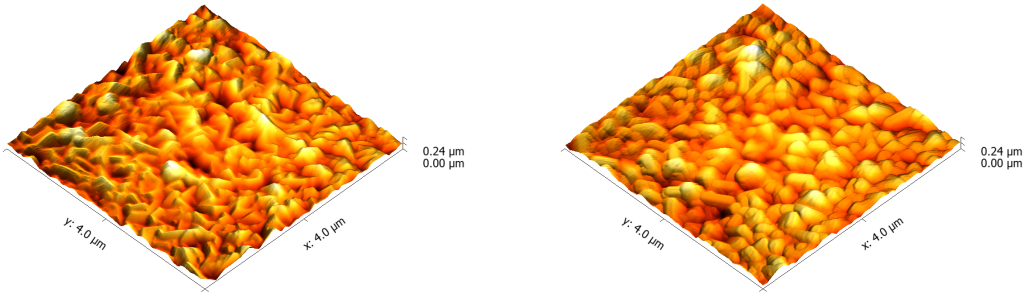

(a) Asahi Type-U. (b) NSG TEC 8.

Figure 4.5: 3D plot of AFM results for commercial FTO samples.

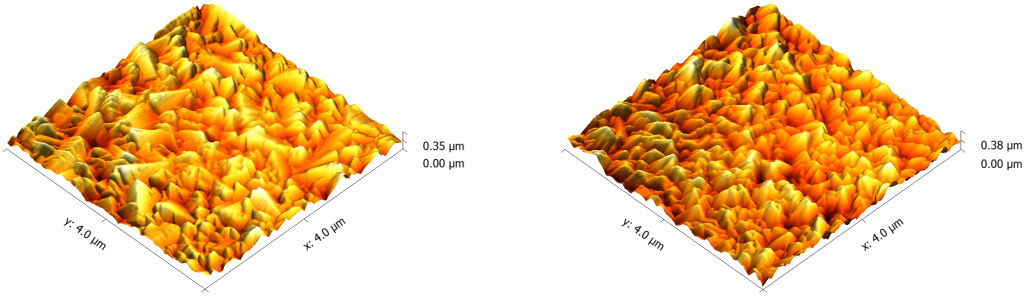

(a) FTO 580. (b) FTO 600.

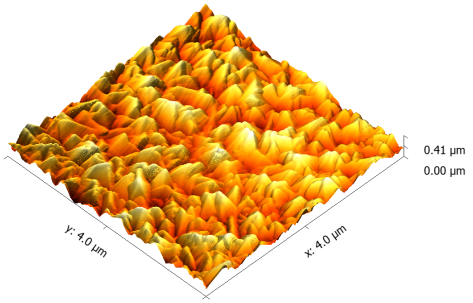

(c) FTO 620.

Figure 4.6: 3D plot of AFM results for experimental FTO samples.

Raw AFM plots are useful for visually comparing surface topography between samples and highlighting differences in feature shapes and sizes. However, in order to determine trends and to quantify surface characteristics, some statistical analysis is necessary. For a randomly rough surface it is useful to determine the height distributions as this gives a convenient overview of the spread of feature sizes. Figure 4.7 shows the height distribution profile for each of the samples.

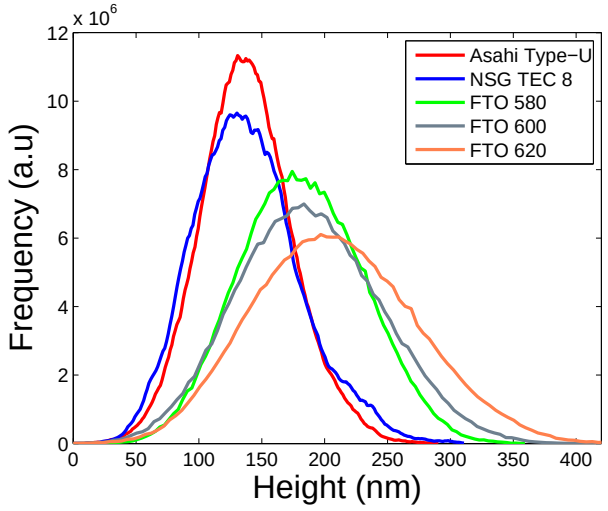

Figure 4.7: Height distribution for experimental and commercial FTO films.

For each of the samples the height distribution appears to be approximately Gaussian, this is typical of surfaces with random roughness and is also an essential assumption for some analytical modelling techniques. As expected, NSG TEC 8 and Asahi Type-U are shown to have similar distributions although NSG TEC 8's is slightly broader. The experimental FTO samples show a clear trend of broadening height distribution with increasing deposition temperature and thus thickness and roughness.

For the investigation of light scattering from rough surfaces it can also be useful to analyse the slope incline distribution of surface facets as previous work carried out at the university of Neuchatel by Domine et al. has shown that this distribution correlates with the angular distribution of scattered light [76]. The incline distribution for each of the samples has therefore been statistically determined and the results are shown in Figure 4.8.

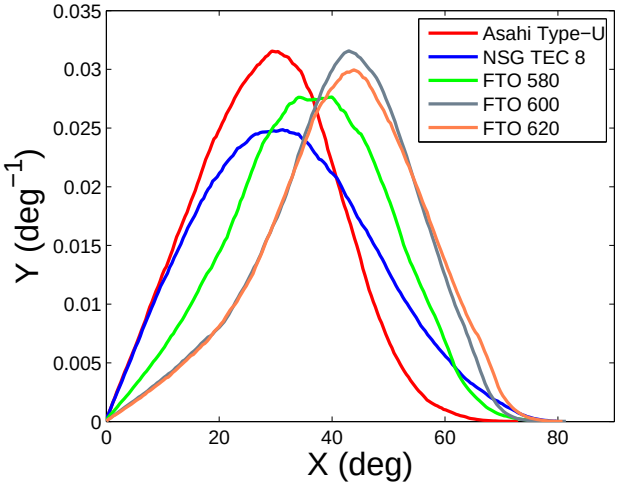

Figure 4.8: Incline distribution for experimental and commercial FTO films.

Once again, the similarities between the two industry standards can be clearly observed, in this case they both show incline distributions centred at around 30 degrees. Interestingly, the experimental FTO films all have slightly narrower distributions centred at larger angles of incline.

Further insight can be gained by quantifying the surface roughness of the samples, this can allow trends and correlations to be highlighted and can also provide input parameters for analytical modelling of the surface. In general, surface roughness is often defined by the roughness average, however, for thin-films the route mean square (RMS) roughness is typically used. These parameters are calculated directly from the AFM data by using Equations 2.4 and 2.5 which are shown in Section 2.3.1. For rough TCOs that are intended to be used as solar cell superstrates, the average inclination angle and surface are ratio (SAR) are also key parameters, where the SAR is the ratio between the actual surface area and that of a flat surface with the same x and y lengths. For each of the investigated samples these parameters have been calculated and are presented in Table 4.1 along with approximate values of film thickness taken from a combination of literature, ellipsometry and SEM cross-sections [77, 78, 74].

Sample Name	R_{RMS} (nm)	R_a (nm)	Thickness (nm)	SAR	Avg Inc. (deg)
Asahi Type-U	28.25	35.7	950	1.21	30.4
NSG TEC 8	33.5	42	600	1.47	30.8
FTO 580	38.6	47.85	1220	1.39	36.8
FTO 600	43.6	54.4	1240	1.52	43.3
FTO 620	50.5	62.6	1280	1.67	43.8

Table 4.1: Statistical quantities of AFM data.

The industry standards are shown to have very similar roughness parameters, with NSG TEC 8 being slightly rougher than Asahi Type-U. The experimental FTO films are rougher in all cases and show a clear trend of increasing roughness with an increase in deposition temperature. The experimental FTOs also have a significantly higher average incline angle which should affect the angular distribution of scattered light. The SAR data shown in the table reveals that increasing roughness average and RMS roughness does not necessarily lead to an increased surface area as the NSG TEC 8 is significantly less rough than FTO 580 yet NSG TEC 8 has a larger SAR.

Optical Results

For each of the three experimental FTO samples and the two industry standards, the total, specular, and diffuse transmittance characteristics were measured using the double beam integrating sphere technique. For a visual comparison of the these optical characteristics the total, specular, diffuse and calculated haze transmittance have been plotted as separate graphs each showing results for all samples in Figure 4.9.

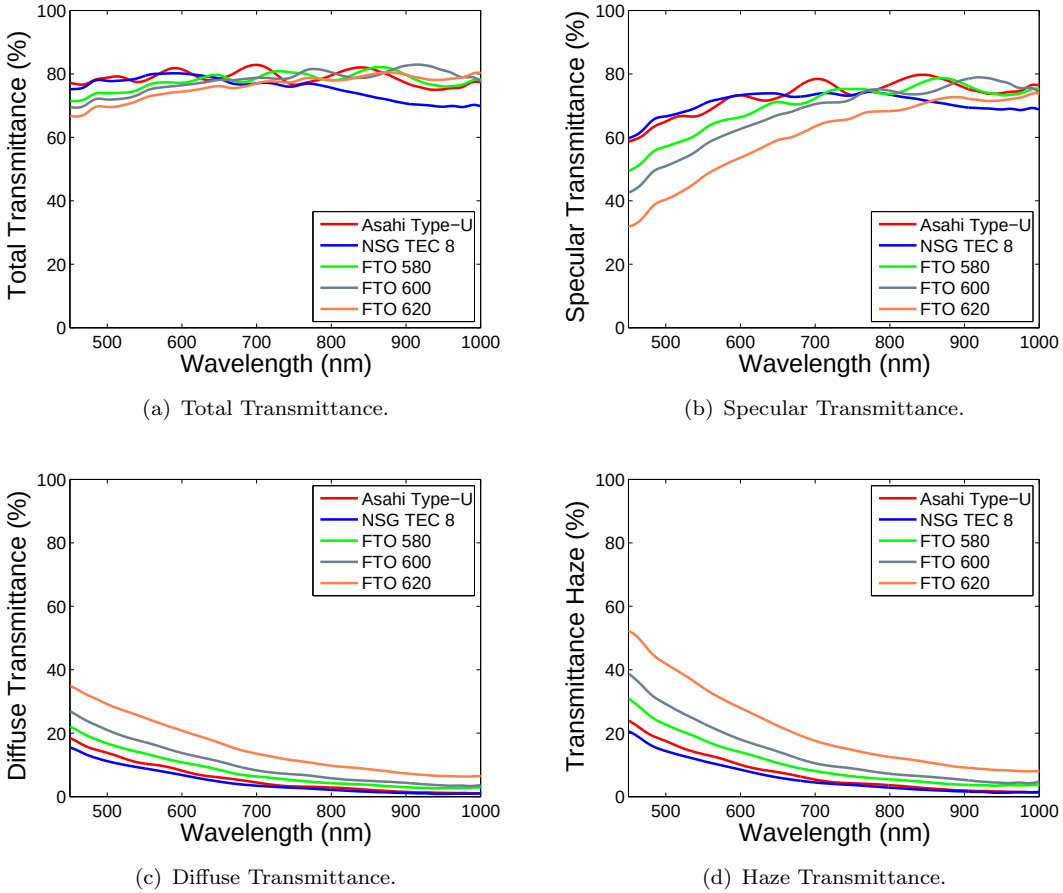

(a) Total Transmittance.

(b) Specular Transmittance.

(c) Diffuse Transmittance.

(d) Haze Transmittance.

Figure 4.9: Comparison of general optical characteristics for FTO samples.

The results show that each of the TCOs exhibit the classic characteristics of high transmittance, with significant diffuse transmittance at wavelengths of around 450 nm, diminishing with increasing wavelength. At short wavelengths the industry standards Asahi Type-U and NSG TEC 8 are shown to have the highest total transmittance which is to be expected as the thickness of these FTO films is less than the experimental samples. The experimental samples show a clear trend of decreased short wavelength transmittance with increasing thickness and roughness, however, at longer wavelengths their transmittance characteristics are nearly equal to each other and the differences between samples are dominated by interference. Asahi Type-U shows similar long wavelength transmittance characteristics but NSG TEC 8's transmittance is significantly reduced at wavelengths of more than 800 nm. The diffuse transmittance and haze measurements both show the same trend of increased intensity with increasing roughness for the experimental FTO samples. However, Asahi Type-U provides a higher diffuse transmittance and haze than NSG TEC 8 despite AFM measurements showing that Asahi Type-U is the smoother of the two TCOs. Asahi therefore appears to scatter more light whilst maintaining a relatively low surface roughness and surface area ratio.

Comprehensive wavelength and angle resolved scattering (WARS) measurements were

carried out in transmittance using the custom built equipment described in Section 3.2 with the measurements parameters as detailed in Section 4.2.2. The conventional optical results and WARS measurements for each sample are shown in Figures 4.10 to 4.14.

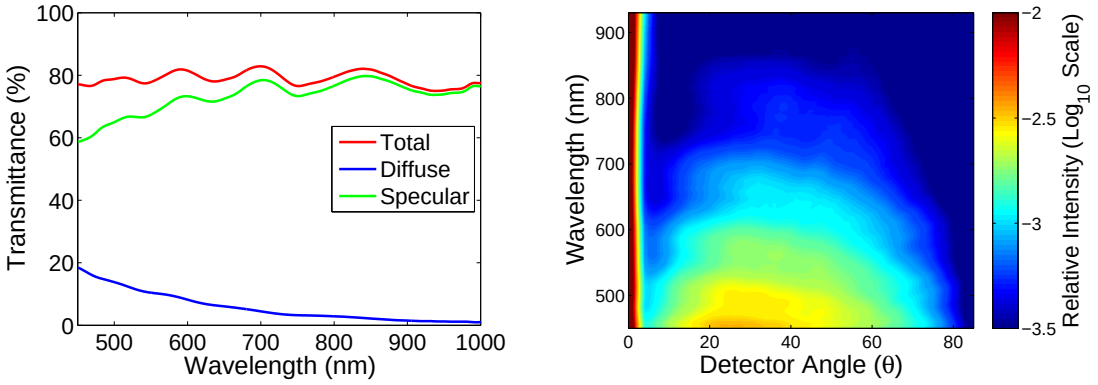

(a) Transmittance measurements. (b) WARS measurements.

Figure 4.10: Optical Characteristics of Asahi Type-U.

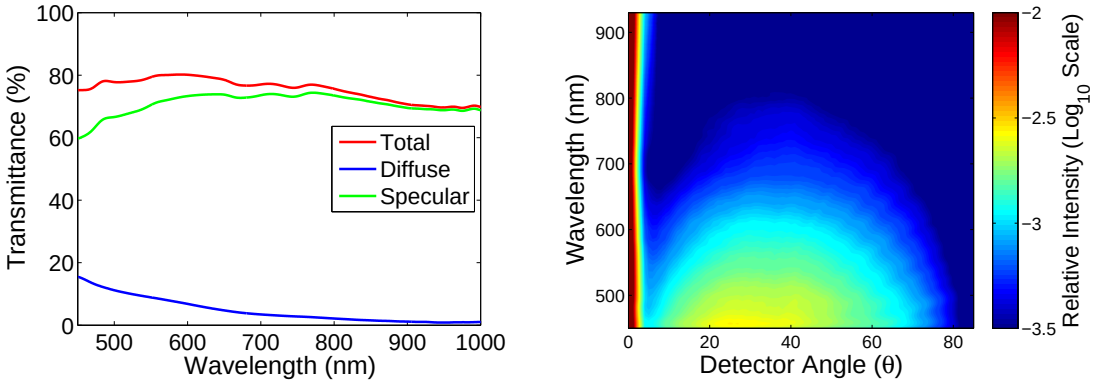

(a) Transmittance measurements. (b) WARS measurements.

Figure 4.11: Optical Characteristics of NSG TEC 8.

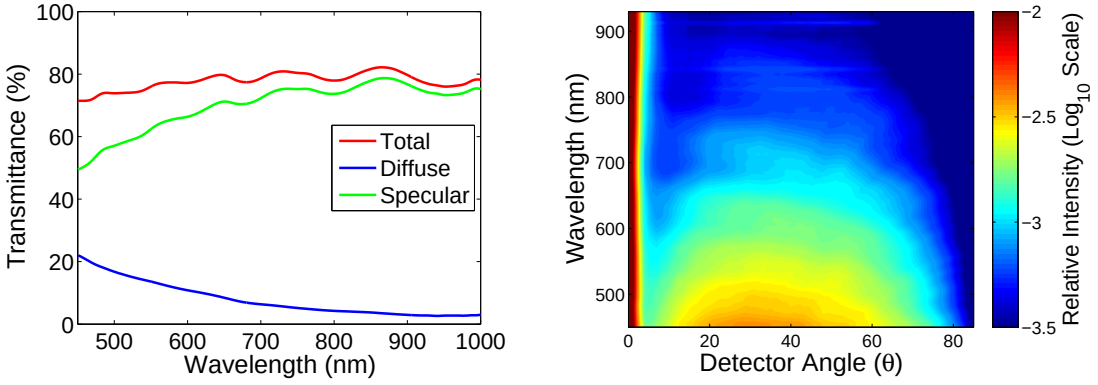

(a) Transmittance measurements. (b) WARS measurements.

Figure 4.12: Optical Characteristics of FTO 580.

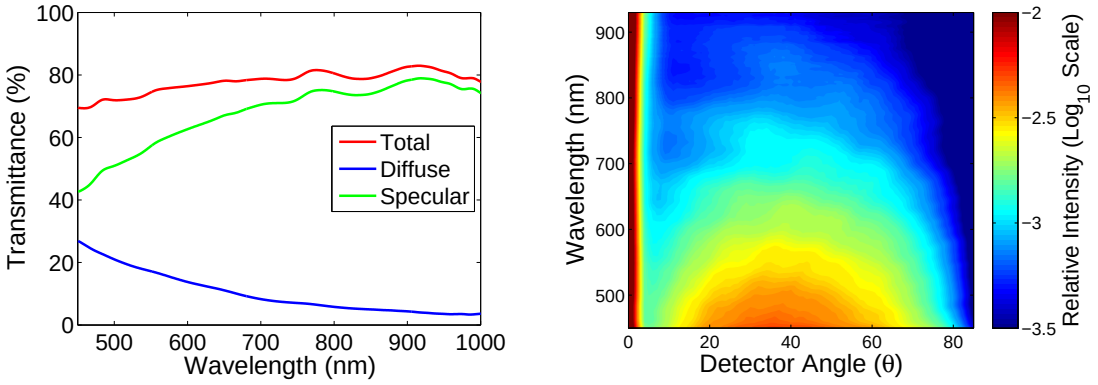

(a) Transmittance measurements. (b) WARS measurements.

Figure 4.13: Optical Characteristics of FTO 600.

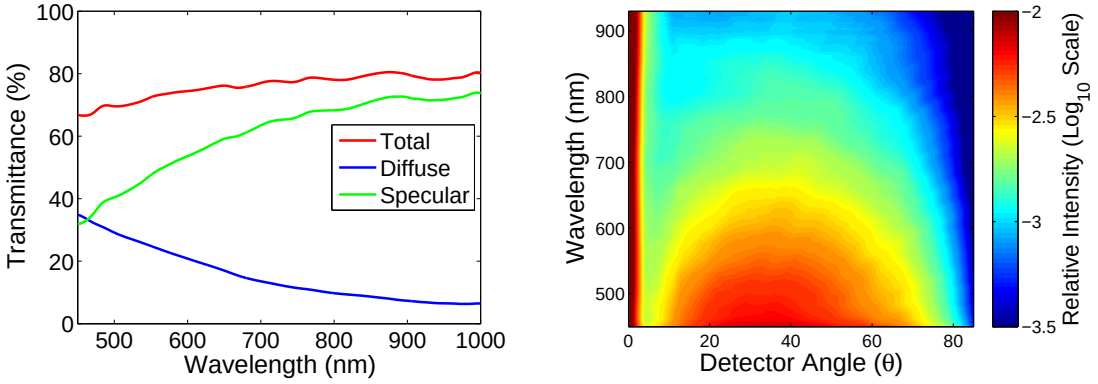

(a) Transmittance measurements. (b) WARS measurements.

Figure 4.14: Optical Characteristics of FTO 620.

The WARS profiles for each of the samples are similar but differences can be observed in the overall intensity of scatter and subtle differences are present in the shape of the angular distribution. For example, the WARS measurement of FTO 580 shows noticeable scattering intensity at wavelengths of 700 - 720 nm at angles of 20 to 40 degrees whereas FTO 600 shows similar levels of scatter to longer wavelengths and slightly larger angles. The WARS plots also reveal that the peak scattering angle can vary with wavelength. For the case of Asahi Type-U the peak scattering angle at 460 nm is around 27 degrees, however, at a wavelength of 650 nm the peak angle is around 40 degrees. In contrast, NSG TEC 8 has a much more Lambertian scattering profile. These subtle differences could not be detected using a TIS measurements or conventional single wavelength ARS. The peak intensity of the WARS profile for Asahi Type-U and NSG TEC 8 is centred at around 30 degrees, whereas for FTO 580 it is centred at 35 degrees and FTOs 600 and 620 are centred at around 38-40 degrees. This correlates well with statistical data for the incline angle distribution presented in Table 4.1, indicating that increased incline angles of facets leads to higher angles of scatter (see Figure 4.15).

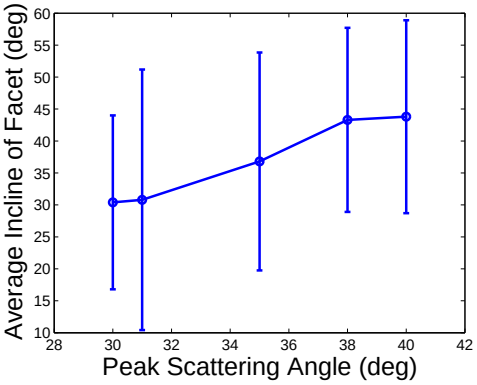

Figure 4.15: Plot of the peak scattering angle for each of the TCOs (averaged over different wavelengths) against the average incline angle of facets, where the vertical bars indicate the spreading of the incline angle distribution (based on FWHM).

The plot in Figure 4.15 is based on the peak angle of scattered light averaged across several wavelengths. In order to directly compare the angular distribution of scattered light, single wavelength ARS data has also been extracted from the WARS measurements of each sample. Example extracted wavelengths of 480 nm and 680 nm are shown for comparison in Figure 4.16.

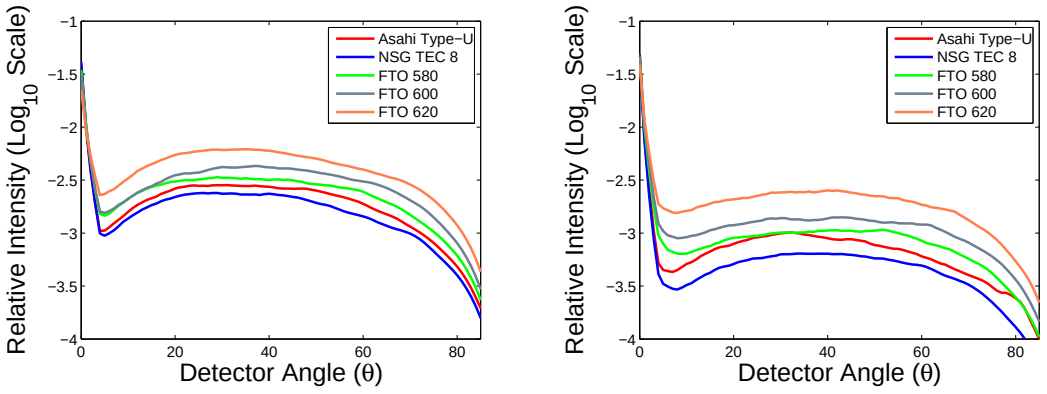

(a) Extracted ARS at 480 nm.

(b) Extracted ARS at 680 nm.

Figure 4.16: Single wavelength ARS data comparison for 480 nm and 680 nm.

The single wavelength ARS data shows remarkable similarities in the angular distribution of scattering for all of the TCO samples. Whilst the intensity of the scattered light changes significantly between samples the shape of the angular distribution of scatter at 480 nm is almost identical. For the wavelength of 680 nm there is more variation in the shape of the scattering profile. In particular, FTO 600 is shown to scatter light very evenly to angles between 20 and 60 degrees. In contrast, Asahi Type-U scatters 680 nm wavelength light predominately to angles of 30 degrees with a noticeable decline in scattering intensity at angles larger than 40 degrees.

Summary

The experimental samples investigated in this section show a systematic increase in surface roughness and thickness with deposition temperature with an rms roughness on a similar scale to the two investigated commercial TCOs; NSG TEC 8 and Asahi Type-U. These commercial TCO films have been optimized for deposition of a-Si solar cells and as such their optical characteristics have shown high overall transmittance with relatively high haze for wavelengths of less than 700 nm. This is suitable for a-Si solar cells as the useful absorption range of a-Si typically diminishes from around 700 nm. Results from the experimental FTOs confirm the theoretical expectation of increased roughness leading to higher levels of diffuse transmittance and the novel WARS characterization technique has been shown to demonstrate subtle differences in the light scatter from samples of relatively similar roughness whilst also highlighting potential links between the incline angle of facets and the angles of scatter for transmitted light.

Whilst this study has been restricted to the surface roughness and optical characteristics of the TCO superstrates in air, full a-Si solar cell devices have been fabricated on a matching set of experimental FTO samples by Yates et al. at the University of Salford [74]. The study showed a clear trend of increasing device external quantum efficiency (EQE) with increasing roughness, with superstrates deposited at 600°C and above showing superior EQE to Asahi Type-U. Short circuit current (Isc) was also shown to increase with roughness due to increased absorption of light. However, open circuit voltage and fill factor were lower for the rougher samples leading to no clear trend in overall cell efficiency with Asahi Type-U shown to be the most efficient. This highlights the need for a carefully chosen compromise between enhanced light-trapping and diminished device electrical characteristics.

4.3.2 High Roughness Experimental AZO Samples

The systematic study detailed in Section 4.3.1 confirms the typical trends expected for the optical properties of textured TCOs with increasing roughness and demonstrates the usefulness of the various characterization techniques used within this work. However, the experimental FTOs studied provided only a small variation in roughness and feature shape in comparison to industry standards. In this section, three aluminium doped zinc oxide (AZO) films with significantly varied surface characteristics will be investigated, with NSG TEC 8 once again used as a standard for comparison. This should help to clarify trends and to determine if the typical Lambertian scattering characteristics can be positively altered by dramatic changes in topography. Whilst large increases in TCO roughness may lead to unsuitable superstrates for a-Si devices, these TCOs could perhaps be used for other absorber materials, such as those with a lower bandgap which require scattering of longer wavelengths. The AZO samples are referred to as AZO 758, AZO 459 and AZO 757 as named by their manufacturer, EPV Solar.

Surface Topography

The AFM technique detailed in section 4.2.2 was used to determine the surface topography of each of the TCOs. The resulting 3D plots are shown in Figure 4.17.

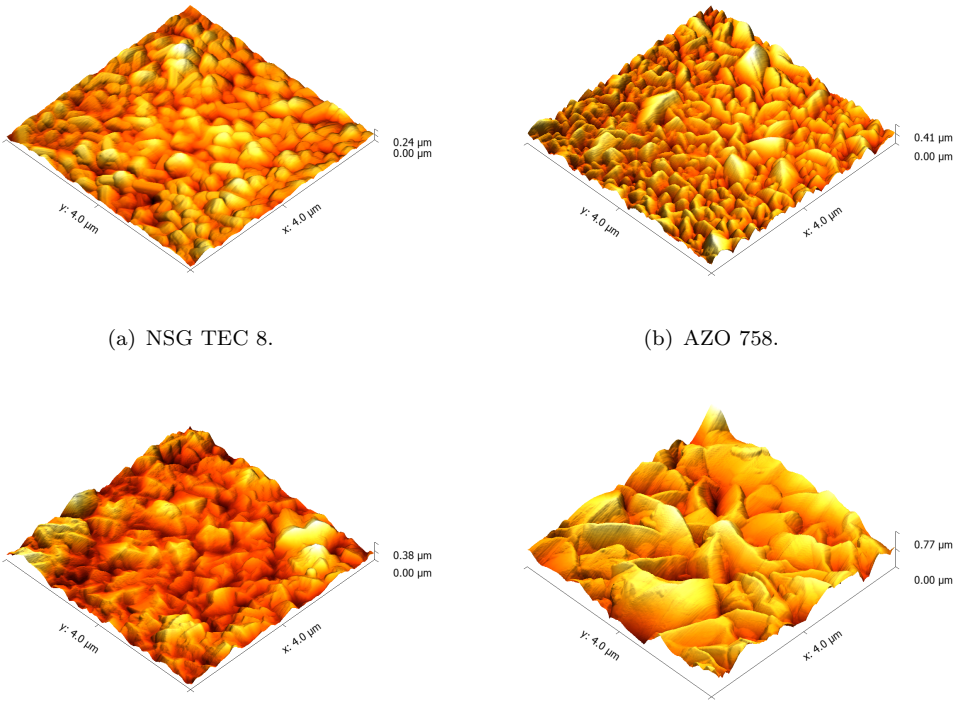

(a) NSG TEC 8.

(b) AZO 758.

(c) AZO 459.

(d) AZO 757.

Figure 4.17: 3D plot of AFM results for NSG TEC 8 and AZO Samples.

The AFM plots show a significant amount of variation between each of the TCO samples. AZO 758 appears to have features of a similar size to NSG TEC 8 but they are sharper and have a higher aspect ratio. In contrast, AZO 459 has low aspect ratio features which are generally much larger in the lateral direction. Finally AZO 757 shows very large, sharp, high aspect ratio features and is a good example of extreme roughness relative to industry standards used for thin-film solar cell superstrates.

The height distribution characteristics determined from analysis of the AFM data for each of the samples is shown in Figure 4.18(a) and the slope incline distribution is shown in Figure 4.18(b).

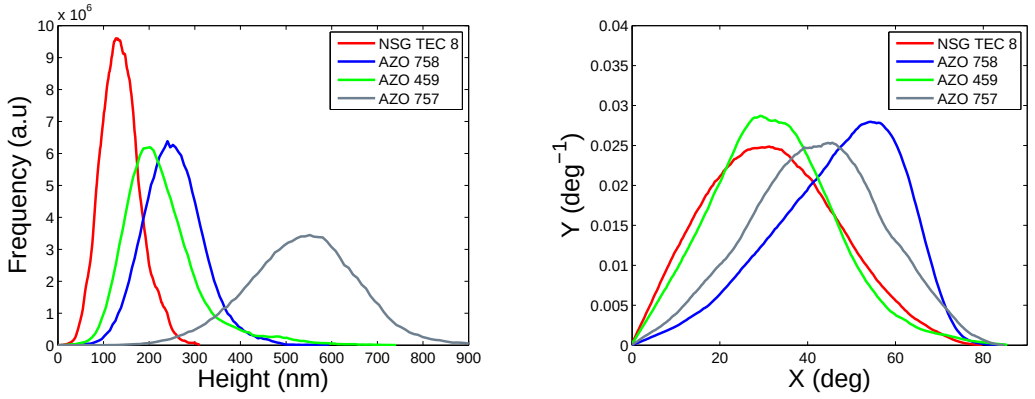

(a) Height distribution.

(b) Incline distribution.

Figure 4.18: Height and incline distribution for experimental AZO samples and industry standard.

The height and incline distributions show that these samples offer substantial variety in terms of roughness. AZO 758 and AZO 459 have similar height distributions with AZO 758 showing slightly higher features on average. The height distributions of AZO 459 and AZO 757 are particularly interesting as they lacks the symmetry shown in most randomly textured surfaces, with the distribution of AZO 459 showing a tail towards larger features and AZO 757 showing a tail towards smaller ones. The incline distributions shows NSG TEC 8 and AZO 459 to have similarly angled facets. AZO 758 is unique in that it has a non-symmetrical incline distribution with a steep average angle of almost 60 degrees. For each of the investigated samples the key roughness parameters have been calculated and are presented in Table 4.2.

Sample Name	R_{RMS} (nm)	R_a (nm)	Thickness (nm)	SAR	Avg Inc. (deg)
NSG TEC 8	33.5	42	600	1.47	30.8
AZO 758	47.8	60	1500	1.66	59
AZO 459	54.3	71.5	1800	1.26	32
AZO 757	92.5	110	3100	1.6	43.4

Table 4.2: Statistical quantities of AFM data.

Optical Results

The overall transmittance properties of each of the samples as measured using the integrating sphere technique described in Section 3.1.2 are shown for comparison in Figure 4.19.

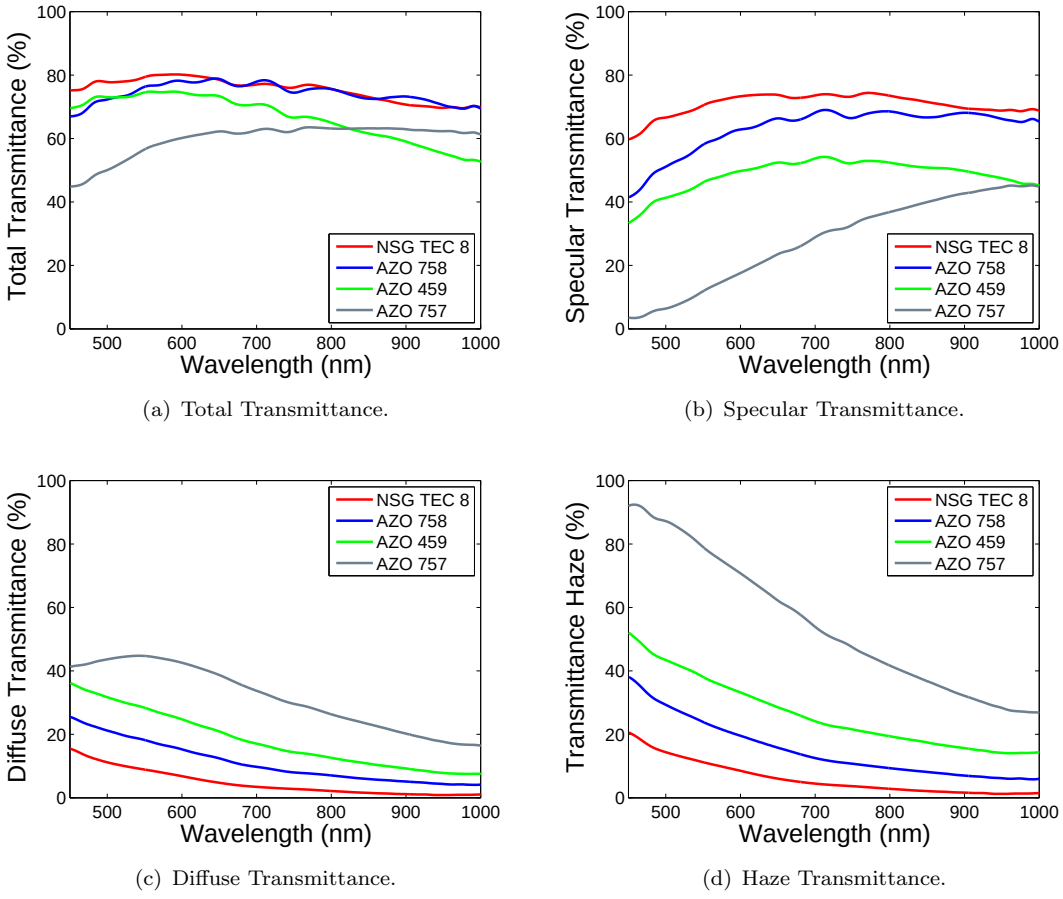

(a) Total Transmittance.

(b) Specular Transmittance.

(c) Diffuse Transmittance.

(d) Haze Transmittance.

Figure 4.19: Comparison of general optical characteristics for AZO samples.

As expected the optical results show the familiar trend of increased diffuse transmittance with increased roughness. The AZO films are shown to have decreased overall transmittance in comparison to NSG TEC 8, this reduced transmittance is partially due to the AZO films being thicker and therefore more absorbing, thus there is a clear trend between total transmittance and film thickness.

For a more detailed optical analysis, the conventional transmittance results and novel WARS results for each of the AZO samples and the commercial FTO are shown in Figures 4.20 to 4.23.

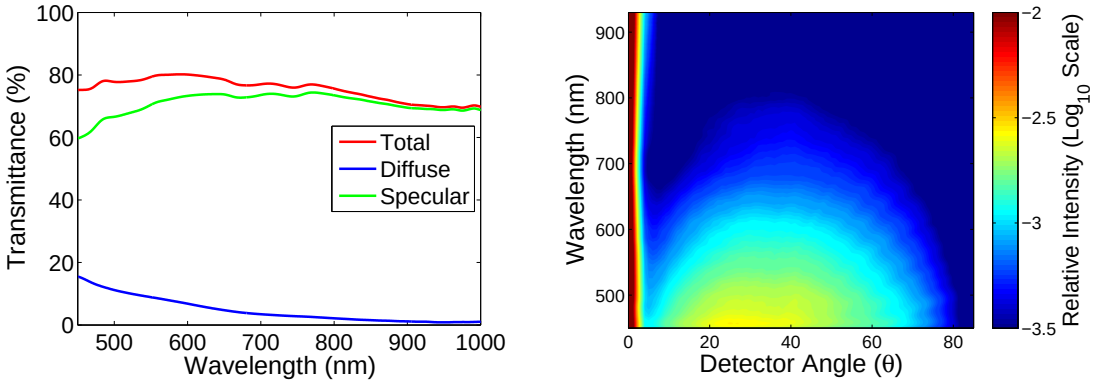

(a) Transmittance measurements. (b) WARS measurements.

Figure 4.20: Optical Characteristics of NSG TEC 8.

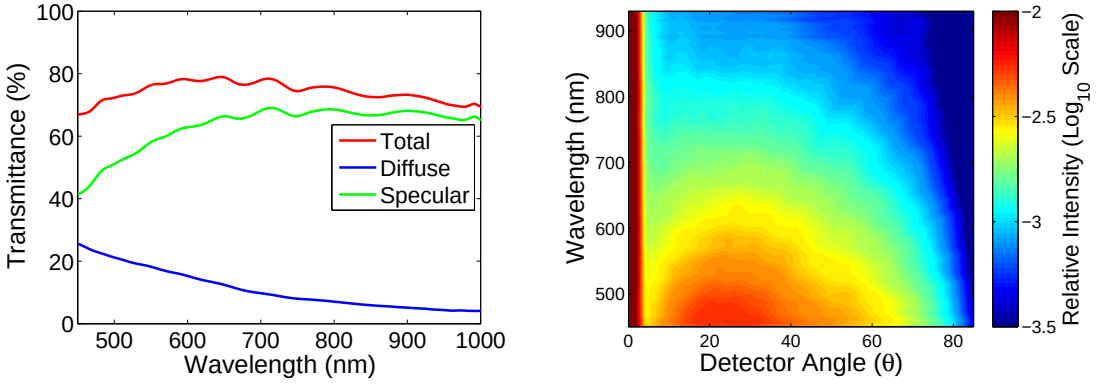

(a) Transmittance measurements. (b) WARS measurements.

Figure 4.21: Optical Characteristics of AZO 758.

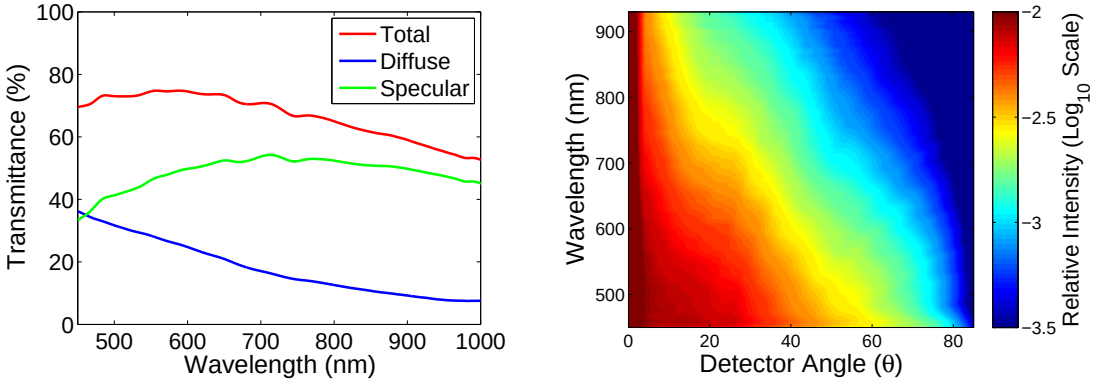

(a) Transmittance measurements. (b) WARS measurements.

Figure 4.22: Optical Characteristics of AZO 459.

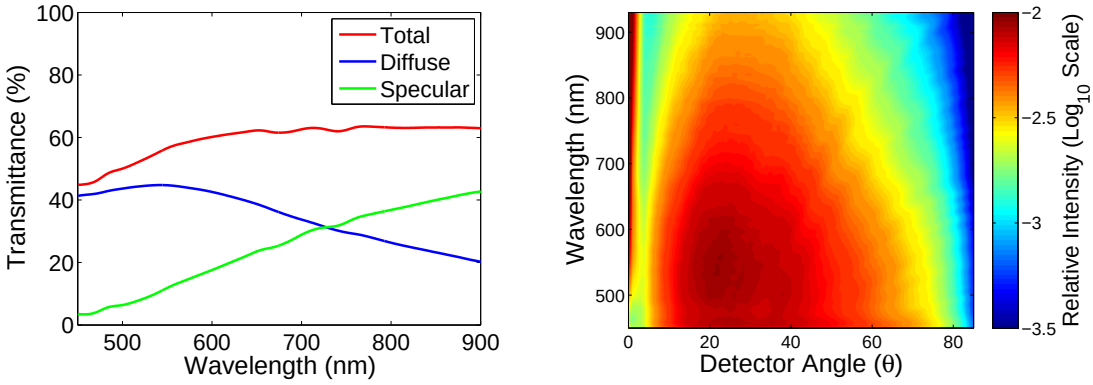

(a) Transmittance measurements.

(b) WARS measurements.

Figure 4.23: Optical Characteristics of AZO 757.

The WARS measurements of the AZO samples are of particular interest as they show characteristics that are not typical for randomly rough surfaces. NSG TEC 8 and AZO 758 both show a conventional, roughly symmetrical scattering profile, however, AZO 459 shows a peculiar non-symmetrical profile where scattering favours smaller angles. AZO 757 also scatters to smaller angles than expected but generally has a more symmetrical profile which is closer in shape to AZO 758 than AZO 459. Unlike the previously studied experimental FTO films, the AZO films do not show a clear correlation between incline distribution and angle of scatter. This could be due to the much higher aspect ratio of features on the AZO causing light scattered from one feature to be incident on a neighbouring feature which in turn would effect the final angle of light as it escapes the TCO layer.

Perhaps the most interesting of the conventional optical results shown in Figure 4.23 is that of AZO 757 which shows almost entirely diffuse transmittance for short wavelengths. It is also the only TCO investigated which has a peak diffuse transmittance that is not at the shortest wavelength measured. This appears to be contrary to theory but further examination of the results reveals that this is due to low total transmittance at shorter wavelengths, causing the diffuse transmittance to be limited. The actual transmittance haze characteristics shown in Figure 4.19(d) take this effect into account and show the typical characteristic of maximum haze at shortest wavelength.

Summary

The results from the AZO samples demonstrate that the typical symmetrical WARS profile for a rough TCO can indeed be altered to less symmetrical shapes. However, for these samples in particular the scattering has only shifted towards smaller angles, although the overall percentage of diffuse scatter is substantially higher than the industry standard. The smaller angles of scatter could be explained by the large angles of the

incline slopes present on these rough, high aspect ratio AZOs. As the measurement is carried out in air, light incident on a TCO/air interface with an angle steeper than 30 degrees will undergo total internal reflection, it could then be reflected back out of the sample, lowering total transmittance, or transmitted after multiple reflections, each of which will affect the final angle of scatter. The limitation of carrying out measurements in air is significant as the scattering into absorbing materials will be dramatically different. However, measurements in air are still useful for determining trends and studying the underlying relationships between texture and scatter. To gain further insight, it is useful to study pseudo-cell structures in which an a-Si layer has been deposited onto the TCO. This allows for investigation of the actual absorption enhancement due to light-trapping.

4.3.3 Textured Oxides with PECVD Deposited Amorphous Silicon

To conclude the experimental investigation into the light-trapping effects of textured TCOs, a 200 nm a-Si layer has been deposited using the PECVD technique detailed in Section 4.2.1 on four different TCO superstrates; NSG TEC 15, NSG TEC 8, Asahi Type-U, and AZO 757. The selected TCOs cover a range of roughness characteristics and it is hoped that optical measurements carried out before and after a-Si deposition will provide insights into the nature and extent of light-trapping caused by these superstrates and help to determine the best topography for maximising useful absorption.

Surface Topography

The surface characteristics of each of the TCOs have been determined using AFM. In this case, AFM measurements have been carried out before and after a-Si deposition in order to observe the conformality of the deposited a-Si and thus how accurately the TCO roughness is replicated. The AFM results are shown in Figures 4.24 to 4.27.

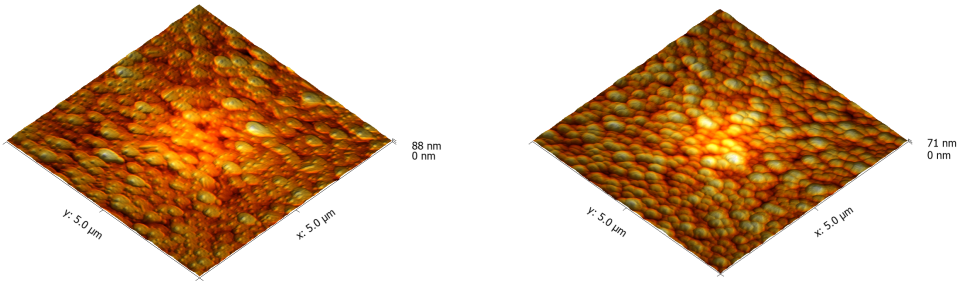

(a) NSG TEC 15. (b) NSG TEC 15 with a-Si.

Figure 4.24: AFM plots of TEC 15 with and without 200 nm a-Si.

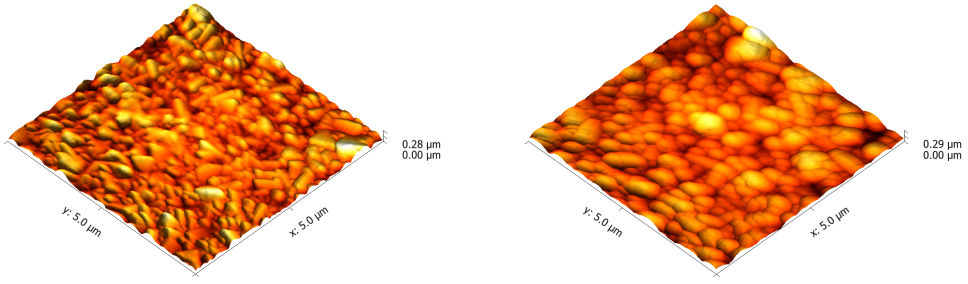

(a) NSG TEC 8. (b) NSG TEC 8 with a-Si.

Figure 4.25: AFM plots of TEC 8 with and without 200 nm a-Si.

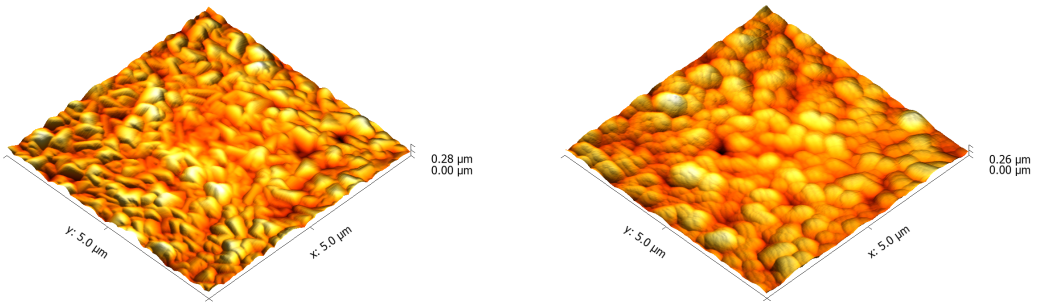

(a) Asahi Type-U. (b) Asahi Type-U with a-Si.

Figure 4.26: AFM plots of Asahi Type-U with and without 200 nm a-Si.

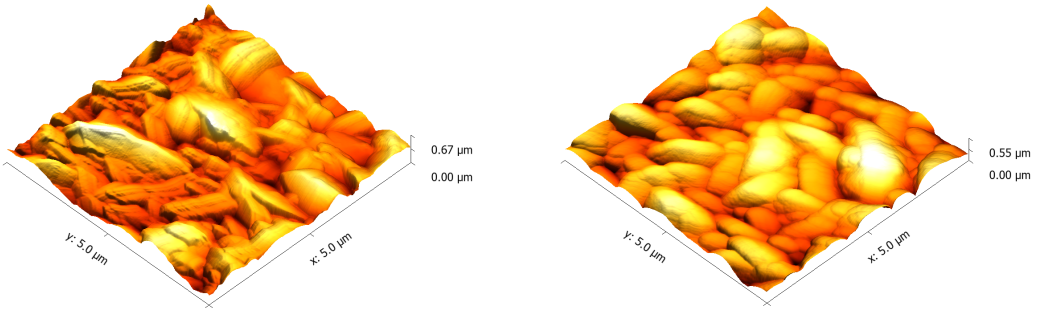

(a) AZO 757 15. (b) AZO 757 with a-Si.

Figure 4.27: AFM plots of AZO 757 with and without 200 nm a-Si.

The AFM plots show a clear smoothing of texture after a-Si deposition, this is to be expected and in general a thicker a-Si layer would result in a smoother final surface. However, the overall height distribution should be similar before and after silicon deposition. This is confirmed by the statistically produced height distributions shown in Figure 4.28. As expected, the height distributions of Asahi Type-U and NSG TEC 8 are very similar whereas the smoother TEC 15 shows a very narrow distribution with a smaller average feature height and AZO 757 shows the opposite, a broad distribution of large features. The addition of a PECVD deposited a-Si layer is likely to have a noticeable effect on the incline distributions of the slopes in TCO surface features as the a-Si rounds of the sharp peaks and valleys present on the bare TCO. The statistically produced incline distribution is shown for both the bare TCO and the 200 nm a-Si coated samples in Figure 4.29. There is some variation between the two graphs but the overall trends in slope distribution between samples remain constant. For the rougher TCOs the slope inclines appear to shift slightly to smaller angles, however, this shift is not apparent for the smoother TEC 15 film.

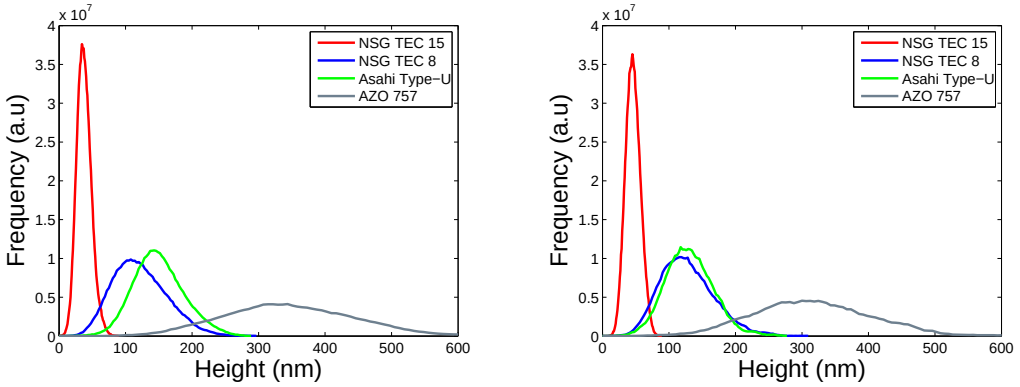

(a) Bare TCO. (b) After a-Si Deposition.

Figure 4.28: Height distribution before and after deposition of 200 nm a-Si.

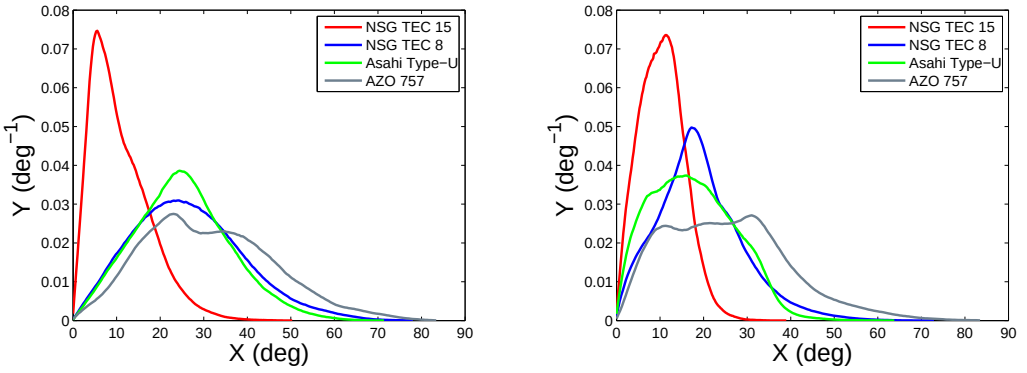

(a) Bare TCO. (b) After a-Si Deposition.

Figure 4.29: Incline distribution before and after deposition of 200 nm a-Si.

The key roughness parameters of each of the TCOs have been quantified before and after a-Si deposition and are presented in Tables 4.3 and 4.4 respectively.

Sample Name	R_{RMS}	R_a	Thickness	Surface Area	SAR	Avg Inc.
NSG TEC 15	8.68	10.94	350	25.8	1.03	5.8
NSG TEC 8	36.9	47.2	apx 600	30	1.2	23.9
Asahi Type-U	30.2	38.1	apx 900	29	1.16	25.4
AZO 757	78.6	97.1	conf 3100	32.6	1.3	28.9

Table 4.3: AFM data for TCO films.

Sample Name	R_{RMS}	R_a	Thickness	Surface Area	SAR	Avg Inc.
NSG TEC 15	8.85	11	550	25.64	1.02	9.9
NSG TEC 8	32.2	40.5	apx 800	27.26	1.09	17.5
Asahi Type-U	28.5	36	apx 1100	26.97	1.07	15
AZO 757	70.7	88.3	conf 3300	29.74	1.18	22.2

Table 4.4: AFM data for TCO films with 200 nm a-Si layer deposited.

The roughness statistics confirm that the addition of a 200 nm a-Si layer causes a small decrease in RMS roughness with the exception of the relatively smooth NSG TEC 15 superstrate in which changes in roughness appear to be negligible. The table data confirms that for the rougher TCOs the average inclination angle of facets has decreased after a-Si deposition. The smoother TEC 15 actually shows an increase in average incline angle, however, analysis of the full incline distribution shown in Figure 4.29 indicates that this could be a statistical anomaly as the base of the distribution is broader for the bare TCO than after a-Si deposition which corresponds with the trends for the other TCOs.

Optical

The optical transmittance and reflectance measurements for the bare TCOs and a-Si coated TCOs are shown in Figures 4.30 to 4.33. These measurements were carried out using the double beam integrating sphere technique as detailed in Section 3.1.2.

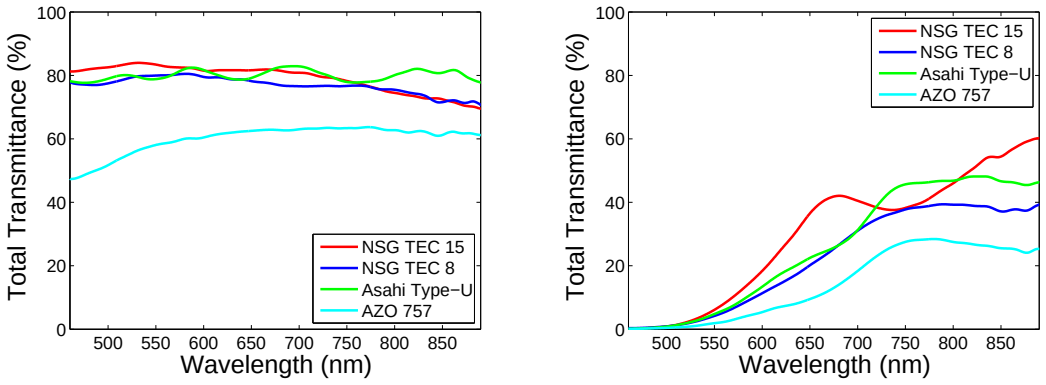

(a) Bare TCO.

(b) After a-Si deposition.

Figure 4.30: Total transmittance measurements.

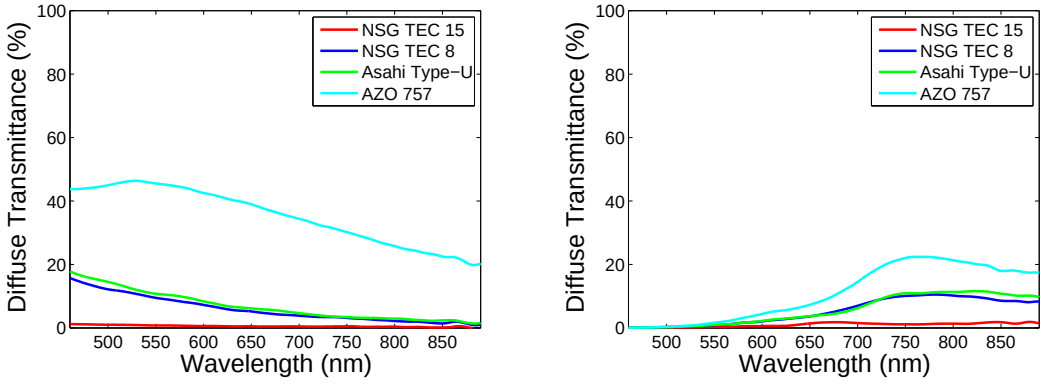

(a) Bare TCO.

(b) After a-Si deposition.

Figure 4.31: Diffuse transmittance measurements.

The transmittance characteristics show that bare NSG TEC 8, TEC 15 and Asahi Type-U all have a similar total transmittance although for the smoother TEC 15 this transmittance is almost entirely specular. In contrast, AZO 757 has a much lower total transmittance but a significant portion is diffuse. After deposition of the a-Si layer it is clear that TEC 15 has the highest overall transmittance through the silicon whilst AZO 757 has the lowest. This aligns with expectations that the texturing has caused the light to scatter within the silicon, thus enhancing absorption and lowering transmittance. Asahi Type-U and NSG TEC 8 have similar characteristics due to the likeness of their surface textures. Interestingly the long wavelength diffuse transmittance of these TCOs is actually higher post a-Si deposition. This is primarily due to the multiple scattering effect of the TCO/a-Si interface and a-Si/air interface. However, a significant portion of the transmittance remains in the zero order direction which indicates that a larger degree of scattering would be preferable. For the case of the much rougher AZO 757, over 80% of the total light transmitted through the a-Si layer is diffuse.

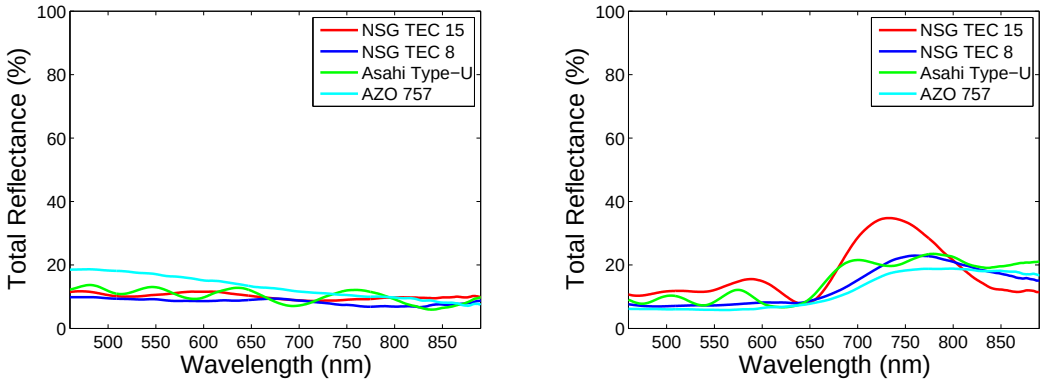

(a) Bare TCO.

(b) After a-Si deposition.

Figure 4.32: Total reflectance measurements.

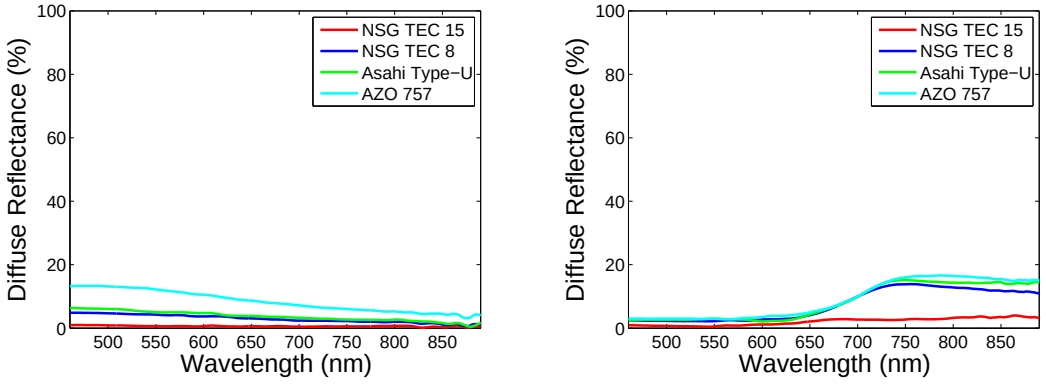

(a) Bare TCO.

(b) After a-Si deposition.

Figure 4.33: Diffuse reflectance measurements.

The reflectance characteristics reveal a baseline total reflectance of around 10% for most of the bare TCOs, with AZO 757 being the exception having an average reflectance of 15%. Part of this reflectance is due to the initial air/glass interface, the rest is primarily due to the textured TCO/air interface which accounts for the large percentage of diffuse reflectance for all samples other than the relatively smooth NSG TEC 15. The total reflectance after a-Si deposition shows distinct interference patterns for NSG TEC 15 and Asahi Type-U. There is a general trend of increased reflectance with increased wavelength, this is due to the lower absorption of longer wavelengths within the a-Si layer which means that long wavelengths can transmit through the a-Si, be reflected at the a-Si/air interface and subsequently transmitted back through the glass/TCO superstrate. The majority of the post a-Si deposition reflectance is diffuse due to the multiple textured interfaces, TEC 15 is once again the exception due to low roughness.

The absorption characteristics for the bare and a-Si coated TCOs have been determined by subtracting the total transmittance and total reflectance from unity. Thus the results show total absorption in the whole multi-layer sample. Results are shown in Figure 4.34.

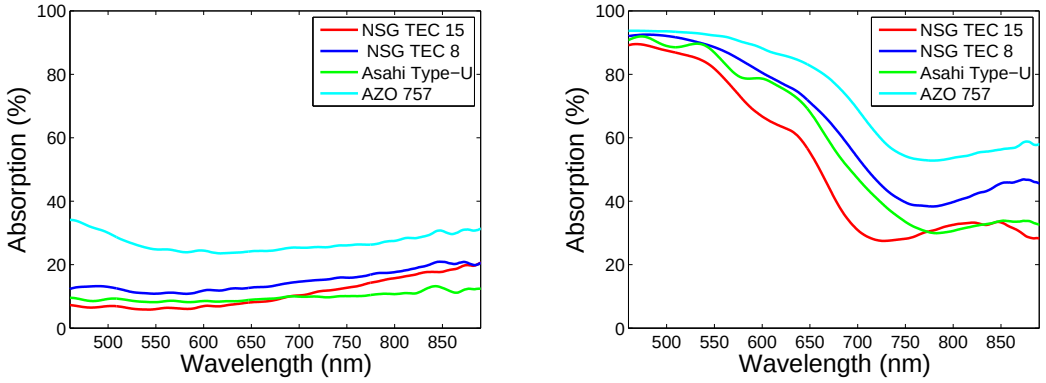

(a) Bare TCO.

(b) After a-Si deposition.

Figure 4.34: Absorption measurements.

The results show that the bare FTOs typically absorb between 10% and 15% over the wavelength range investigated with AZO 757 absorbing roughly twice that at around 30%. Asahi Type-U has particularly low absorption across the spectrum despite being thicker than TEC 8 and TEC 15, this may provide a significant clue with respect to the success of devices fabricated on this superstrate. With the addition of the 200 nm a-Si layer the typical trend is present for all TCOs showing high absorption at short wavelengths which diminishes as wavelength is increased. A significant drop in absorption can be seen beginning at around 600 nm and levelling off at around 750 nm which corresponds with the band gap of a-Si. Absorption at wavelengths longer than 700 nm may still be possible within the silicon layer if parts of the a-Si are actually micro-crystalline. The TCO itself also accounts for some of the long wavelength absorption as does any light that may have been trapped within the device and escaped through the sides of the sample as this would not contribute to the total transmittance or reflectance

characteristics. For a clearer view of the absorption within the actual a-Si layer, the absorption characteristics of the bare TCO have been subtracted from the absorption characteristics of the a-Si coated TCO with the results shown in Figure 4.35.

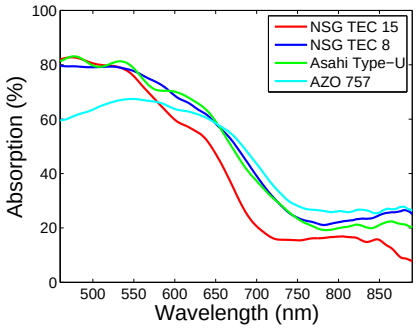

Figure 4.35: Approximate absorption in a-Si layer.

Amorphous silicon layers deposited on Asahi type-U and NSG TEC 8 appear to have almost identical absorption characteristics whilst TEC 15 shows significantly less absorption due to the low roughness causing minimal light scattering. Interestingly, the very rough AZO 757 only shows a small increase in a-Si absorption at longer wavelengths and substantially less absorption at wavelengths shorter than 650 nm, due to absorption in the TCO itself. Even if the short wavelength absorption within the TCO could be reduced, the significant increase in interface surface area that the higher roughness of AZO 757 causes would likely diminish the electrical characteristics of a full device and therefore negate the small increases in long wavelength a-Si absorption. Thus it appears that the roughness of the commercial TCOs has indeed been well optimized and increasing the surface roughness will lead to diminishing returns with regards to light-trapping enhancement along with increasingly detrimental electrical effects.

WARS transmittance measurements were carried out for all samples, with and without a-Si layers. Results are shown in Figures 4.36 to 4.38. TEC 15 results are not shown as the negligible levels of scatter were below the detectable limits of the measurement.

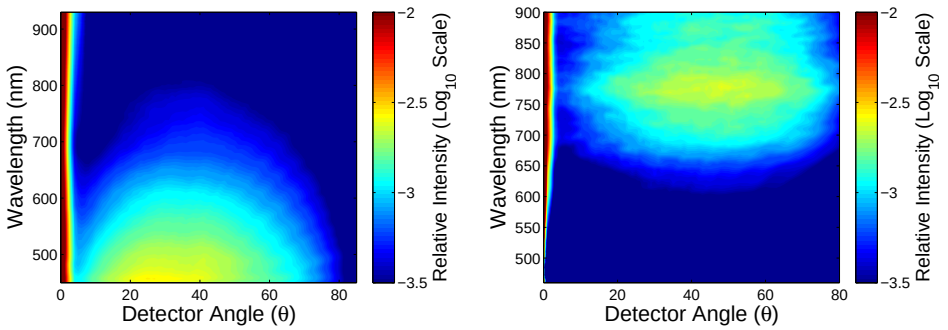

(a) Bare TCO.

(b) After a-Si deposition.

Figure 4.36: WARS measurements for NSG TEC 8.

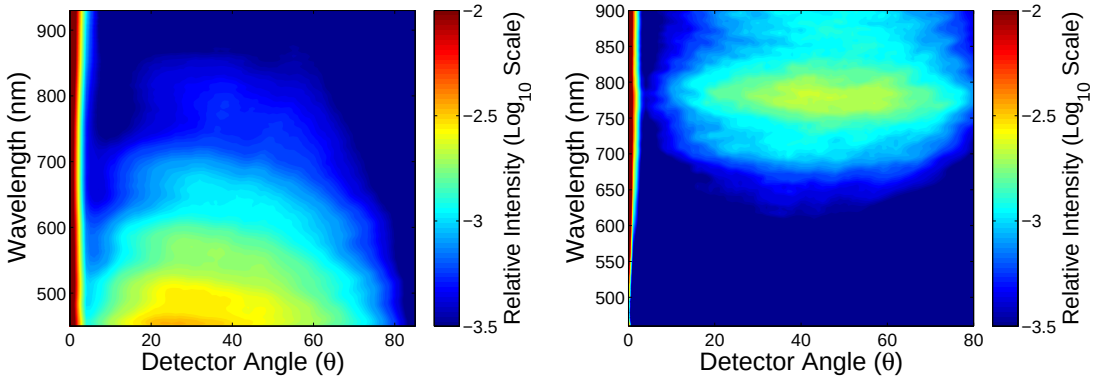

(a) Bare TCO. (b) After a-Si deposition.

Figure 4.37: WARS measurements for Asahi Type-U.

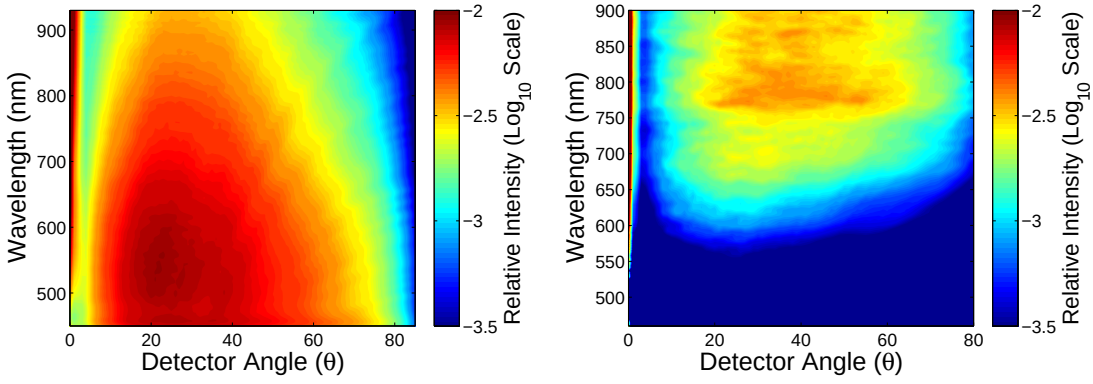

(a) Bare TCO. (b) After a-Si deposition.

Figure 4.38: WARS measurements for AZO 757.

The WARS results reveal that scattering post a-Si deposition is predominantly long wavelength and has a Lambertion like angular distribution. The lack of short wavelength scatter is a positive result caused by absorption of these wavelengths within the silicon. The unabsorbed longer wavelength scattered light is generally evenly distributed due to multiple scattering events at the various textured interfaces. Once again NSG TEC 8 and Asahi Type-U are shown to have remarkably similar optical properties. For all samples, the peak wavelength of scatter after a-Si deposition is around 800 nm. This is just beyond the band-gap of the a-Si, shorter wavelengths show less scatter due to absorption in the a-Si whilst longer wavelengths are significantly larger than most of the surface features and are therefore not scattered by them as detailed in Section 2.2.1. This is supported by the results of AZO 757 in which the scattering intensity remains high up to the longest wavelength measured due to the much larger features of this TCO.

Summary

The results in this section have provided significant insights into the actual absorption enhancements created by interface texturing. It has been shown that increasing TCO surface roughness from a very smooth rms roughness of around 8.5 nm (TEC 15) to that of around 37 nm leads to enhancement of the absorption in a 200 nm a-Si layer of around 10% between 600 nm and 900 nm. However, further increasing the rms roughness to 78 nms leads to only a relatively small increase in long wavelength absorption and significantly reduced short wavelength absorption. This indicates that increasing roughness beyond that of the typical commercial standards will not improve device efficiency for the case of a thin-film a-Si device, however, this may not hold true for alternative absorber materials. Finally, WARS measurements carried out post a-Si deposition have uniquely demonstrated that the diffuse transmittance through the a-Si layer is distributed over a broad range of angles. Whilst increasing the TCO roughness does increase the intensity of the scattering, in this case it appears to have negligible effect on the final angular distribution.

4.4 Conclusions

The properties of several different FTO and AZO superstrates have been comprehensively characterized using a broad range of measurement techniques. Atomic force microscopy has been successfully used to characterize the surface texture properties and the optical results have shown clear trends between increased roughness and increased light scatter into air, which corresponds with theoretical expectations. The angle of scatter has been linked to the incline angle of surface facets with increasing incline angles leading to higher angles of scatter. However, this correlation does not hold true for surfaces with very high aspect ratio features. TCOs significantly rougher than those typically used in the solar cell industry have been shown to provide superior diffuse transmittance but this comes at the cost of increased reflectance and absorption and thus lower total transmittance. Rougher surfaces also typically have a larger surface area which is detrimental to the electrical characteristics of a subsequently deposited device. Analysis of the absorption in a 200 nm a-Si layer deposited onto superstrates with a broad range of RMS roughness values shows that TCOs rougher than the industry standards provide only a small enhancement in long wavelength absorption whilst significantly reducing absorption at short wavelengths. For each of the TCOs studied the haze characteristics showed the typical curve shape of increased wavelength leading to decreased haze. However, the novel WARS results showed that whilst it may not be possible to alter the typical haze characteristics to enhance long wavelength scatter, it is at least possible to significantly alter the angular distribution. AZO 459 is one such experimental example of this in which the angular distribution is skewed towards smaller angles. This shows that there is potential for the manipulation of the angular distribution but none of the experimentally studied TCOs showed the ideal case of a distribution that favoured large angles. It therefore appears that the commercially available superstrate TCOs are indeed well optimized, particularly for the case of a-Si based devices. However, as these TCOs are typically optimized empirically, it is likely that there remains some room for improvement, albeit within a small range consisting of only marginal changes to the size and shape of surface features. Such a high level of surface topography control is extremely difficult to attain experimentally and modelling may therefore provide a more viable and efficient route to optimization of a design which could perhaps then be fabricated using techniques such as nanomoulding.

Chapter 5

Simulation of Textured Transparent Conducting Oxides

Previous studies of scattering from textured TCOs have shown good agreement between conventional scattering measurements and analytical models, however, published results typically contain limited optical information and do not investigate the angular distribution of scattering. In this chapter, the full range of optical results will be directly compared to numerical FDTD simulations. Good agreement between measurements and simulations validates further investigation and optimization using the FDTD technique. This allows for the systematic study of surface texture scaling and analysis of the distribution of scattered light within a silicon layer, resulting in an efficient and cost-effective route to optimized light-trapping for photovoltaic devices.

5.1 Optical Modelling of Textured TCOs

Whilst textured TCOs clearly have fundamental limitations, there is still a degree of optimization that can be carried out in order to obtain an ideal match between TCO texture and the subsequent absorber layer. Texture optimization will vary for different device types and determining the ideal texture can be inefficient and costly if carried out experimentally. Despite this, TCO texture optimization has, to date, been largely empirical and carried out on a trial and error basis. It is logical that a more systematic, numerical approach would be more efficient and has the potential to give superior results but this approach has only gained feasibility in recent years as computational resources have become cheaper and more advanced. When modelling novel structures or designs it is imperative that the model is validated so that the accuracy of simulated results can be determined. In the past, the majority of modelling efforts towards textured TCOs have been analytical approaches based on scalar scattering theory [79], the details of which are discussed in Section 2.3.1. This analytical approach benefits from

being quick and relatively simple but it has significant limitations in that it is based on the assumption that the roughness distribution be approximately Gaussian and it also involves a correction function. Efforts have been made to use modified analytical techniques to model non-Gaussian roughness distributions but these have achieved only limited success [58].

However, in recent years, more accurate numerical modelling techniques such as finite element method (FEM) and finite difference time domain (FDTD) techniques are being found to be increasingly useful. In particular, FDTD techniques, which are detailed in Section 2.3.2 allow for broadband simulation results in a single run and can be used to model arbitrary structures such as textured TCO surface profiles determined using AFM. Furthermore, the optical generation data determined using FDTD simulations can subsequently be used as the input for an electrical FEM simulator, resulting in the full optical and electrical characteristics for a complete device, therefore allowing for complete optimization. For these techniques to be used in such an extensive way they must be accurately validated using experimental results. Several groups have shown good agreement between FDTD simulations of random TCOs, in particular Bittkau et al. have shown correlation between FDTD simulations and near-field scanning optical microscopy (NSOM) measurements [80] and Lacombe et al. have used FDTD to achieve reasonable agreement with a textured TCOs total reflectance and transmittance [81]. However, for more complete model validation, the total simulated haze should also be shown to match experiment and ideally the agreement for the wavelength and angular distribution of scattered light should also be determined. In the following sections of this investigation data gathered from FDTD models is directly compared to total transmittance, haze and complete WARS data. This comprehensive model validation allows for reliable further investigation through FDTD simulation.

5.2 Methods

5.2.1 Ellipsometry: Refractive Index and Film Thickness

In order to optically model a material, the wavelength dependant dielectric constant, or refractive index of the material must be known. For compounds such as TCOs, obtaining this information is non-trivial as variations in the deposition parameters of the film can lead to changes in optical properties. Ellipsometry can be used to determine the refractive index as well as the thickness of a thin-film. Ellipsometry is a non-destructive optical technique in which light is reflected off a sample and the change in polarization caused by the reflection is analysed and matched to a model. Correct analysis of the data allows for accurate determination of the sample's refractive index properties and film thicknesses. However, the accuracy of this technique is substantially diminished for

highly scattering samples, therefore, refractive index values obtained for textured TCOs are likely to have a larger degree of error than those found for smooth samples.

For each of the samples investigated in this chapter the film thickness and wavelength dependent refractive index properties were determined using variable angle spectroscopic ellipsometry (VASE). The specific ellipsometer used was a J.A. Woolam M2000-DI. Each sample was measured at 4 different angles, 60, 65, 70 and 75 to improve measurement reliability. In order to acquire meaningful refractive index and thickness values, measured ellipsometry data must be correctly fitted to a model. This is particularly challenging for semi-transparent, semi-absorbing films such as TCOs and the difficulty of model fitting is further exasperated by the surface roughness of the samples. Due to these challenges it was deemed that a mean squared error (MSE) of 30 or under between the measurement data and the model should indicate an acceptable result. In contrast, for opaque, planar thin-films an MSE of less than 10 is usually achievable. For each TCO the structure was modelled as a general oscillator on a glass substrate (represented by a Cauchy model). Model fitting was carried out over a wavelength range of 300 - 1200 nm. Once an MSE of below 30 was achieved, the refractive index data was then extracted from the model along with approximate values for the film thickness and surface roughness. An example model fit for an ITO film on glass is shown for one measurement angle in Figure 5.1 and the corresponding complex refractive index is shown in Figure 5.2.

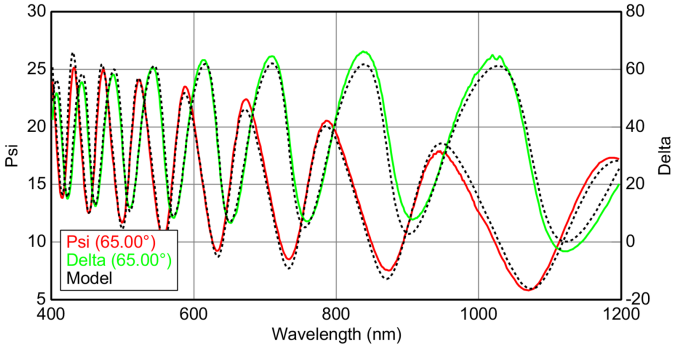

Figure 5.1: Ellipsometry result and model fit for Salford FTO 580.

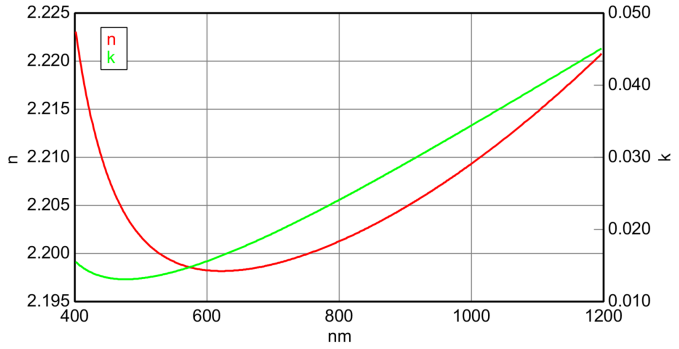

Figure 5.2: Complex refractive index values for Salford FTO 580.

Due to the complexity of modelling semi-transparent, rough samples the refractive index obtained through ellipsometry should only be used as an approximate indicator and should not be considered as an accurate, absolute value. For the subsequent FDTD modelling carried out in this investigation a constant, wavelength independent refractive index has been used. The value chosen for the constant was the average of the measured refractive index values for all TCO samples. Ellipsometry carried out on each of the samples showed their optical refractive index data to be extremely similar so this simplified approach should still provide reasonably accurate results. Additionally, the use of a single, constant refractive index for all TCO simulations has the significant advantage of eliminating effects from refractive index differences in the simulation results, allowing for a more accurate study of the independent effects of texture.

5.2.2 FDTD Simulation Approach

Finite difference time domain (FDTD) simulations were carried out for each of the TCO samples studied in this work using the *'FDTD Solutions'* software by *Lumerical*. When simulating a non-periodic, non-symmetrical structure, a trade-off must be made between the simulated area and available computer resources. Simulating a larger area will provide a more accurate representation of the sample but can take significantly longer to compute, or may not be possible to compute with available resources. To determine the best area size, several simulations were carried out on different simulation volumes of the same structure and the results compared to determine the extent of convergence (see Figure 5.3). A simulation span of 20 μm x 20 μm was found to give a good balance between result accuracy and acceptable computation time with results found to be within an error of 0.14% of larger area simulations . All simulations detailed in Section 4.3 are therefore based on a lateral area of 20 μm x 20 μm.

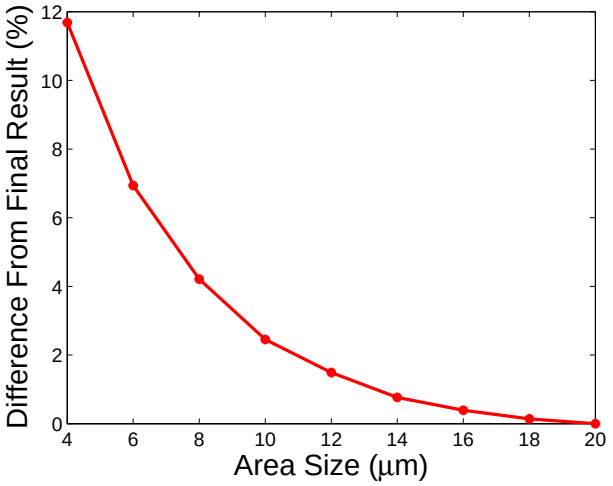

Figure 5.3: Results of convergence test to determine acceptable simulation area size.

In each case, the structure simulated consists of a semi-infinite glass layer with a textured TCO layer on top. The thickness properties of the textured TCO were determined for each sample using values obtained from literature or data from ellipsometry measurements. The TCOs were defined as having a constant, wavelength independent refractive index of 2.1 (see Section 5.2.1). The refractive index of glass was defined using the default materials database properties built into the software. The surface texture of each TCO was imported directly from the topography information gathered using the AFM technique detailed in Section 4.2.2.

With regards to simulation boundary conditions and illumination sources, there are two alternative simulation approaches that should provide accurate results. Both of these methods were investigated within this work in order to determine which is preferable for this specific case. The first approach is to use a plane wave source with periodic boundaries in the X and Y directions. This approach assumes that the TCO structure is periodic, but if a large enough area is simulated then diffraction effects can be minimized and should become negligible. This approach has the advantage that plane waves and periodic boundaries are less computationally expensive to simulate than alternative options. However, one important issue that should be noted is that if the randomly rough surface is modelled as being periodic, then there may be large discontinuities in the surface texture at the boundaries as illustrated in Figure 5.4.

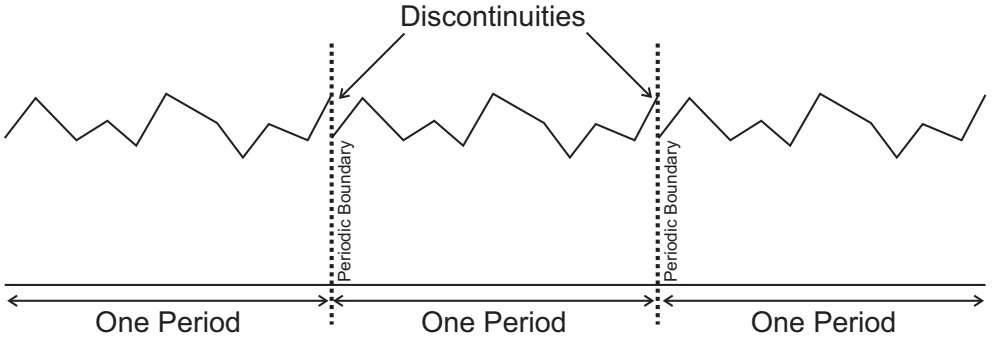

Figure 5.4: Illustration of possible discontinuities at periodic boundaries.

To avoid any spurious results developing from these discontinuities, they should be removed by smoothing out the edges of the topographical data. To achieve this, a custom Matlab script was used which was designed to tile the AFM data and utilize an averaging algorithm to smooth the edges between tiles (see Appendix B). The modified AFM data was then exported for use in FDTD. The result of the smoothing algorithm is clearly shown in Figures 5.5. Figure 5.5(a) shows four copies of the raw AFM data periodically tiled, Figure 5.5(b) shows the same tiling after the edge smoothing algorithm has been applied. Another significant issue with this simulation approach is that the far-field projections calculated from the monitor data may not be accurate as the projection methods used in the software are not strictly intended for periodic simulations.

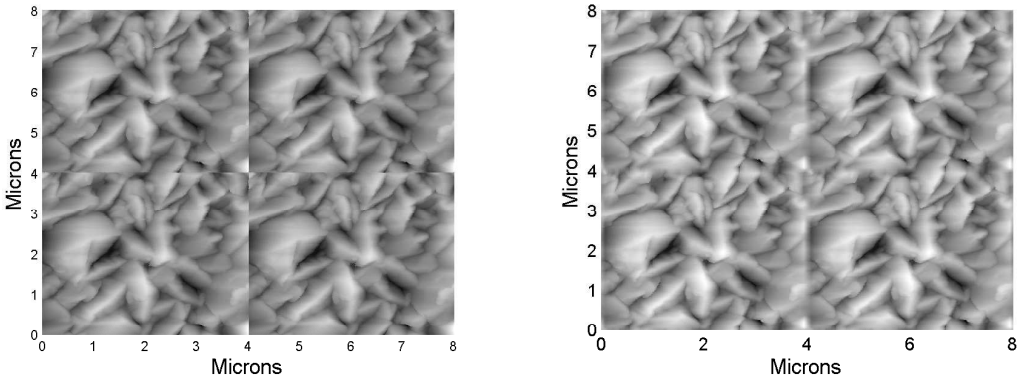

(a) Original data.

(b) After smoothing.

Figure 5.5: AFM image of AZO TCO tiled four times: Before and after the removal of edge discontinuities.

The second simulation approach is to illuminate the sample with a Gaussian beam source and set absorbing PML boundaries in every direction. This approach eliminates the problems of discontinuities at the boundaries and should also provide a more meaningful far-field projection. However, having PML boundaries in the X and Y directions means that some of the scattered light will be absorbed at these boundaries and therefore not detected by the monitor. The use of a Gaussian beam also introduces unwanted angles in the incident light. This effect can be reduced by using a wider beam with lower divergence but this requires increasing the overall simulation area and therefore the time and computer resources required.

Both of the simulation approaches were thoroughly tested. In each case a frequency-domain field and power (FDFP) monitor was set above the textured TCO layer to collect the transmitted optical data and the source was set to originate in the semi-infinite glass layer of the sample, as illustrated in Figure 5.6.

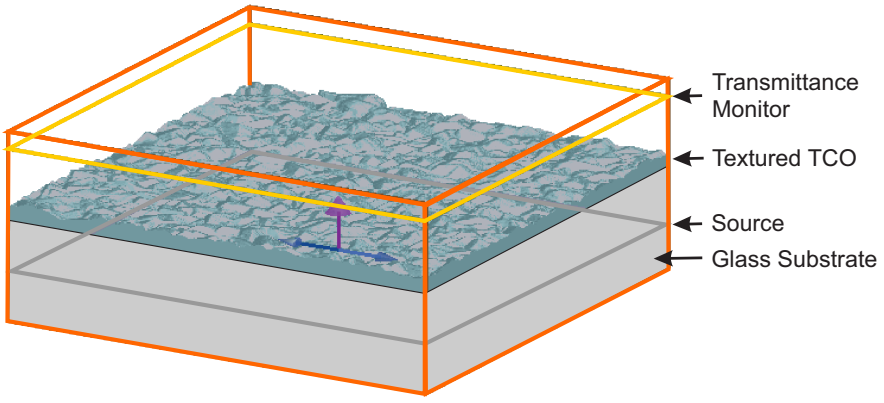

Figure 5.6: Illustration of FDTD simulation set-up.

The reason for the source location is due to the use of a semi-infinite glass layer which is required to reduce simulation size and runtime. For experimental measurements the illumination source originates outside of the glass. The extra reflection at the air/glass interface is therefore not simulated and has to be accounted for mathematically post simulation.

Transmission data was determined using FDTD's monitor transmission function and the scattering of light was determined by projecting the monitor data into the far-field, as detailed in Section 2.3.2. Example results for each method are shown in Figure 5.7.

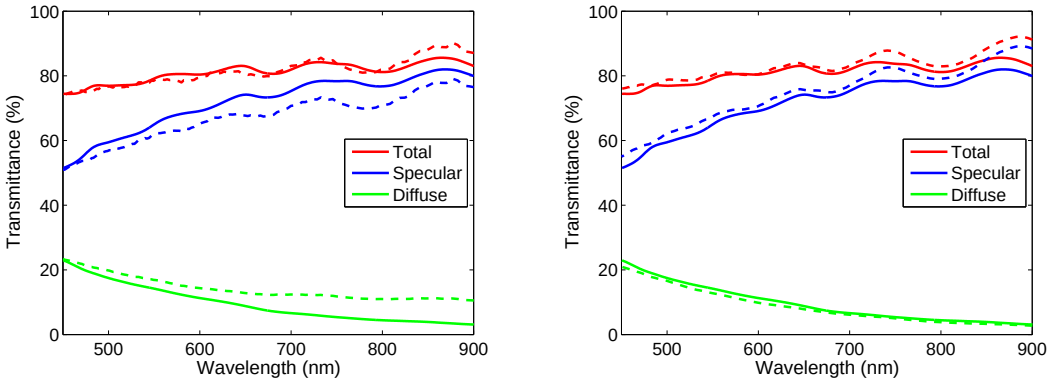

(a) Method 1: Plane wave source with periodic boundaries.

(b) Method 2: Gaussian source with PML boundaries.

Figure 5.7: Comparison of different simulation approaches for an example textured FTO TCO sample. Solid line = integrating sphere measurement, dashed line = simulation result.

As the results show, whilst both methods simulated the total transmittance well, the second method provided the best overall match with experimental measurements. Particularly for the long wavelength scatter where the periodic approach seems to significantly overestimate the intensity of scattered light. Results for other surface topologies showed similar differences; the second method was therefore selected to be used for all subsequent TCO simulations within this work.

5.3 Simulation Results and Discussion

5.3.1 FDTD Simulations Results Vs. Measurements

Each of the textured TCO samples have been simulated using the FDTD approach with the set-up specifics detailed in Section 5.2.2. In order to specifically study the roughness characteristics, each of the TCOs has been modelled as having the same, constant refractive index value. The real part of the refractive index was chosen to be 2.1 based on an average of the values obtained through ellipsometry measurements of each of the TCOs. To reduce simulation complexity and therefore computation time, this value was chosen to be constant for all wavelengths and a value of 0 was chosen for the extinction co-efficient, thus these TCOs have been modelled as non-absorbing. The following simulations results should therefore provide useful information regarding the effects of surface roughness but will not take into account the small variations in refractive index between the different samples.

The measurement and simulation of the total, specular and diffuse transmittance for the two industry standards, Asahi Type-U and NSG TEC 8 are shown in Figures 5.8.

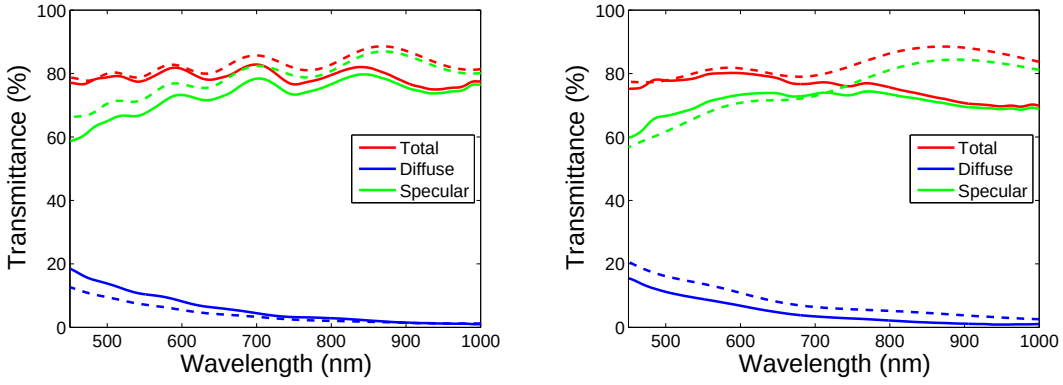

(a) Asahi Type-U.

(b) NSG TEC 8.

Figure 5.8: Measurement (solid line) and simulation (dashed line) results for commercial TCO samples.

For both Asahi Type-U and NSG TEC 8 the simulations show a reasonably close match with experiment, particularly at shorter wavelengths. In both cases the simulations show exaggerated total transmittance at longer wavelengths, this is most likely due to the use of a constant refractive index. In reality, if the refractive index increases with wavelength then the reflectance will also increase, thus lowering the transmittance. Interestingly the simulations underestimate the level of diffuse transmittance for Asahi Type-U and overestimate it for NSG TEC 8. This results in the simulated NSG TEC 8 having higher diffuse transmittance than the simulated Asahi Type-U. Whilst this does not agree with measurements, it does agree with scattering theory as AFM measurements

have shown that NSG TEC 8 is the rougher of the two TCOs. The small mismatches between simulation and measurement will be largely due to refractive index differences between the two TCOs. The commercial standards may also vary between simulation and experiment because it is possible that they are not simple FTO films. For example, there may be additional, very thin layers in Asahi Type-U, possibly added by the Asahi company in order to improve the electrical and optical properties. This is difficult to confirm as information on the fabrication and structure of these commercial products if not freely available. Results for the experimental FTO films fabricated at the university of Salford are shown in Figure 5.11.

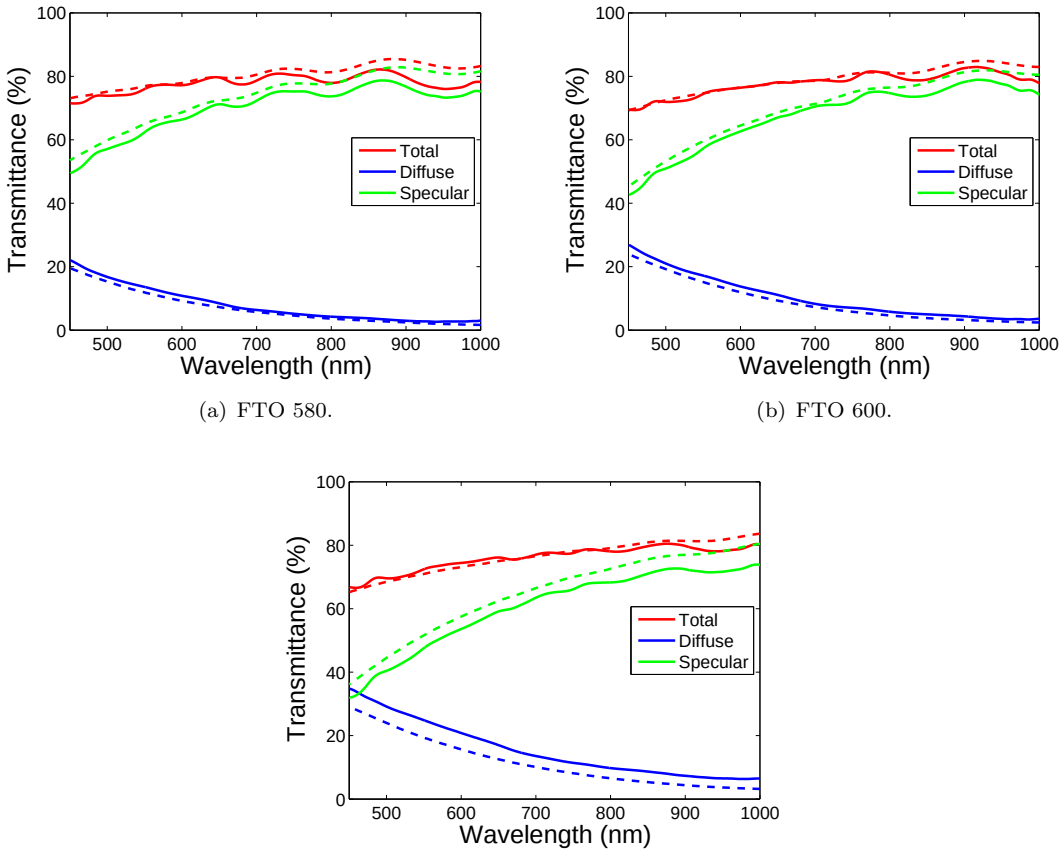

(a) FTO 580.

(b) FTO 600.

(c) FTO 620.

Figure 5.9: Measurement (solid line) and simulation (dashed line) results for experimental FTO samples.

The results show that simulations of each of the experimental FTO films are in good agreement. This indicates that they have similar refractive index properties which is to be expected as they were produced using identical methods with only modest temperature changes. The close matching of results and simulation also indicates that the refractive index of the actual samples does not vary significantly with wavelength. In each case the simulated total transmittance of the TCOs shows a close match with the experimental measurements despite the TCOs being modelled as completely non-absorbing. This suggests that the physical samples do in fact have very little

absorption. The shape of the diffuse transmittance curve is closely matched for all samples and the overall intensity is within 2% for FTO 580 and FTO 600. FTO 620 shows slightly lower simulated diffuse transmittance but the overall trends between samples is correct, showing increasing diffuse transmittance with increasing roughness for both measurement and simulation. Results for the experimental AZO films which were previously characterized in Section 4.3.2, are shown in Figure 5.11.

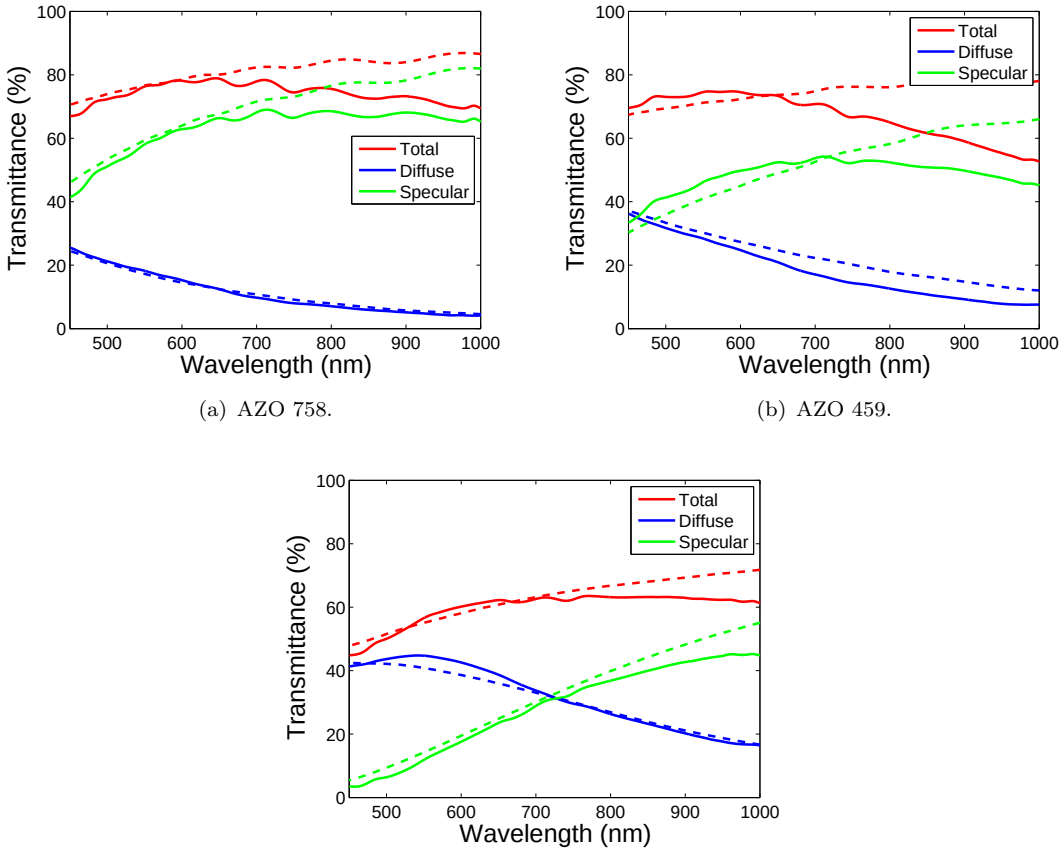

(a) AZO 758.

(b) AZO 459.

(c) AZO 757.

Figure 5.10: Measurement (solid line) and simulation (dashed line) results for AZO samples.

For the AZO films there is reasonable agreement between measurement and simulation. In all cases the shape and intensity of the diffuse transmittance agrees well, however, the long wavelength total transmittance is consistently overestimated in the simulations. This is most likely due to a significant variation in refractive index at these wavelengths. Simulations of the very rough AZOs is also likely to be less accurate than simulation of the smoother FTO films due to the fact that the same area size has been simulated in each case. When the surface consists of small features then many are simulated and the results show a reasonable average across the surface. However, when investigating larger surface features, less are simulated and single structures may begin to dominate, skewing the effects away from the average. This is a difficulty with modelling randomly rough surfaces that can be alleviated by simulation of larger areas at the cost of increased

computer resources and simulation time. However, in general, the simulations of both the FTO and AZO films have shown good agreement which is especially encouraging when taking into consideration the lack of a wavelength dependant refractive index. In particular, the simulated diffuse transmittance characteristics have matched very well with measurements, and it is primarily these characteristics that are of particular interest for the study of light-trapping. The measured and simulated diffuse transmittance is shown for all samples on the same graph for direct comparison in Figure 5.11.

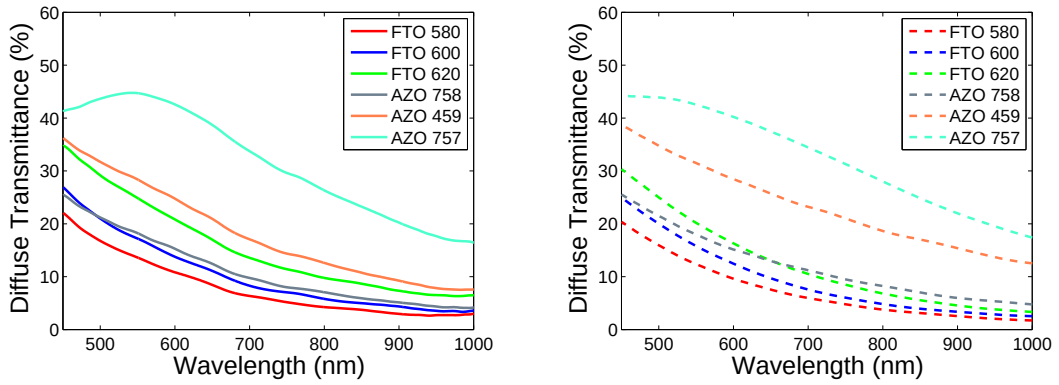

(a) Measurement.

(b) Simulation.

Figure 5.11: Measurement (a) and simulation (b) of diffuse transmittance for FTO samples.

The measured and simulated trends for the diffuse transmittance are in good agreement, with most simulated samples showing the correct shape and overall intensity. This shows that, when correctly set-up, the FDTD technique can be a valid tool for simulation of light scattering from randomly rough TCOs.

To further verify this, the full simulated WARS profile can also be calculated through the use of far-field projections (see Appendix C). This was carried out for each of the experimental FTO films and the results are shown alongside the measurement counterparts in Figures 5.12 to 5.14. In each case smoothing has been applied to both the simulated and experimental data and the simulated data intensity has been scaled by a constant scaling factor to compensate for the default far-field projection being calculated at 1 meter away from the source.

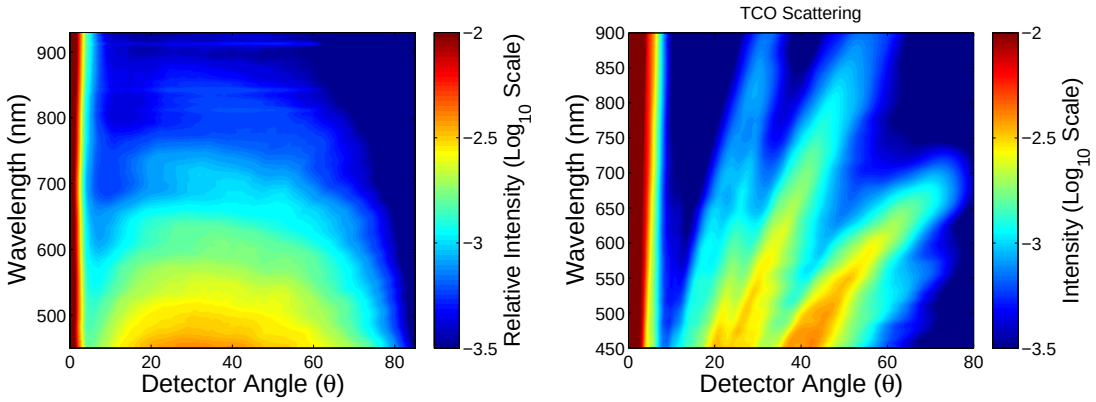

(a) WARS measurements. (b) WARS simulation.

Figure 5.12: WARS measurement and simulation of FTO 580.

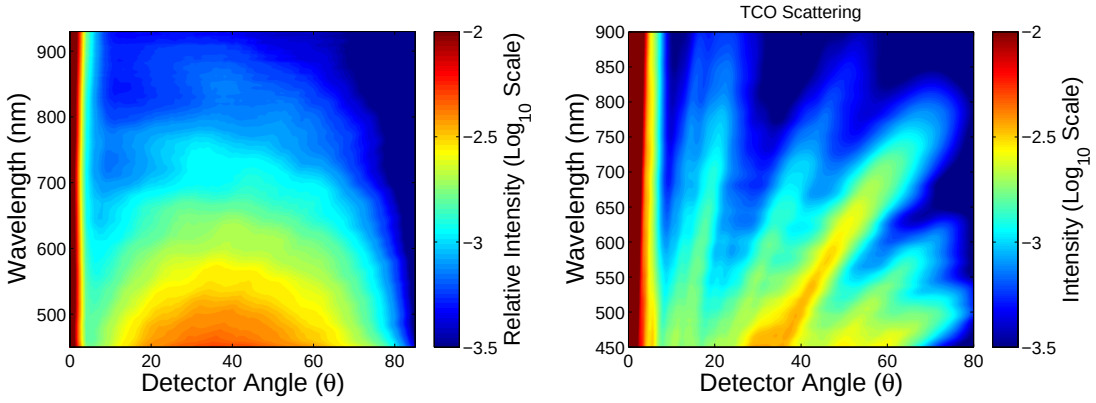

(a) WARS measurements. (b) WARS simulation.

Figure 5.13: WARS measurement and simulation of FTO 600.

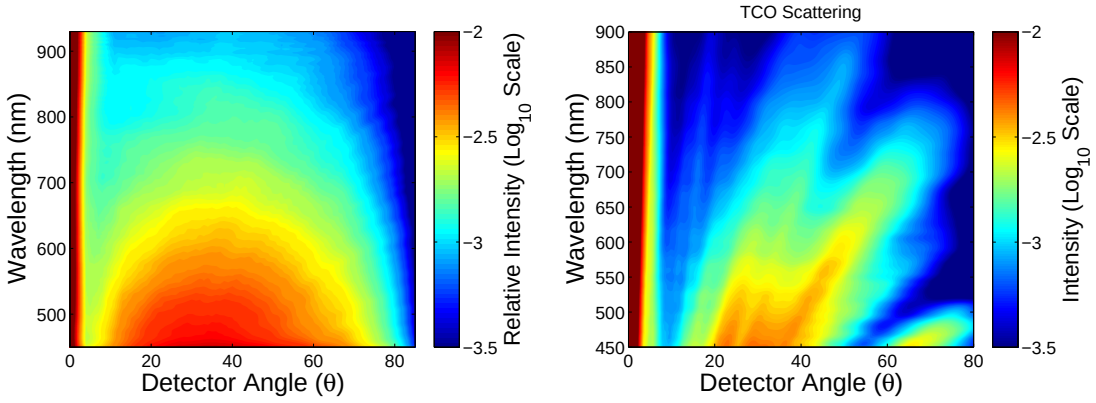

(a) WARS measurements. (b) WARS simulation.

Figure 5.14: WARS measurement and simulation of FTO 620.

Visual comparison of the results show that there are some significant differences between measurement and simulation, however, there are also promising similarities in their key characteristics. In particular, the shorter wavelengths shows the most intense scatter

which is usually centred at angles between 20 and 50 degrees for both the measured and simulated WARS profiles. The simulated WARS results are somewhat dominated by interference effects due to the limited finite simulation area of 20 μm by 20 μm. Simulation of a significantly larger area should provide a better match with the measured results, this will however dramatically increase simulation time beyond acceptable limits for the resources available for this investigation. The similarities between the simulations and measurement results, particularly in the trends between samples, show that the FDTD technique is suitable for predicting the far-field distributions of scattered light when set-up as described in Section 5.2.2.

Finally, the WARS measurements and simulations for the AZO samples are shown in Figure 5.15 to 5.17. As with the FTO results, smoothing has been applied to both the measurement and simulation.

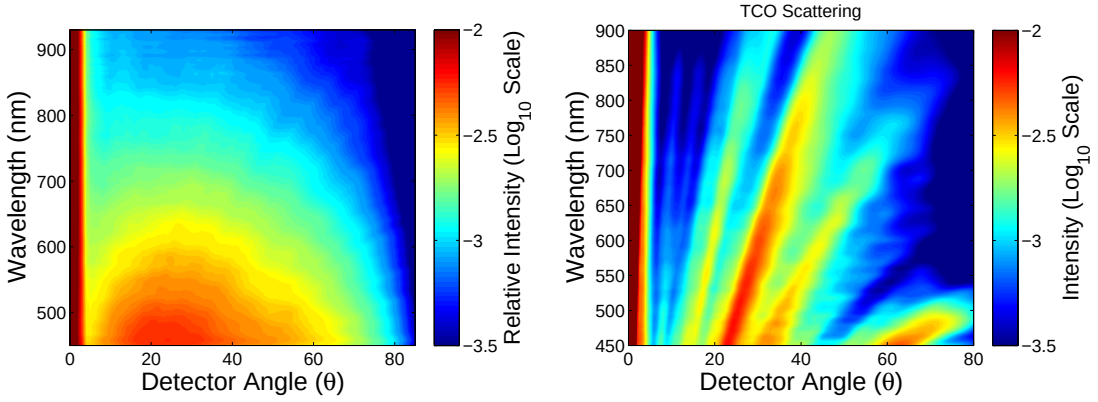

(a) WARS measurements. (b) WARS simulation.

Figure 5.15: WARS measurement and simulation of AZO 758.

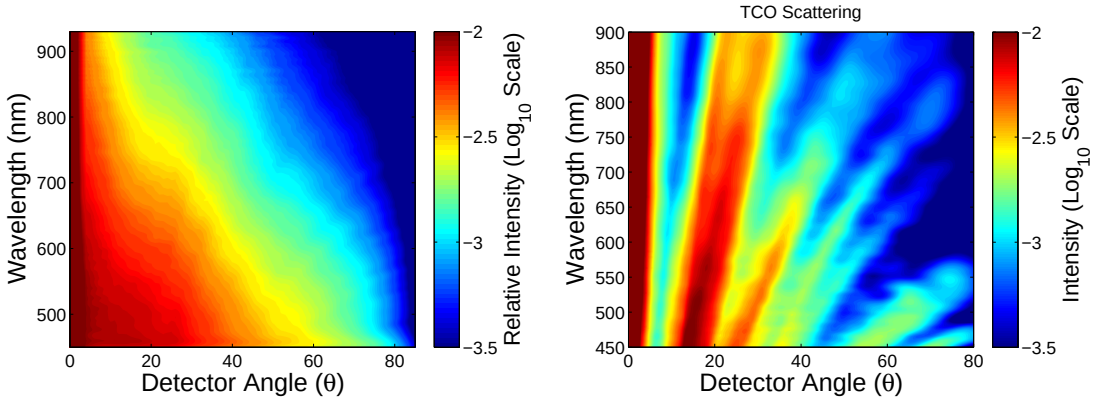

(a) WARS measurements. (b) WARS simulation.

Figure 5.16: WARS measurement and simulation of AZO 459.

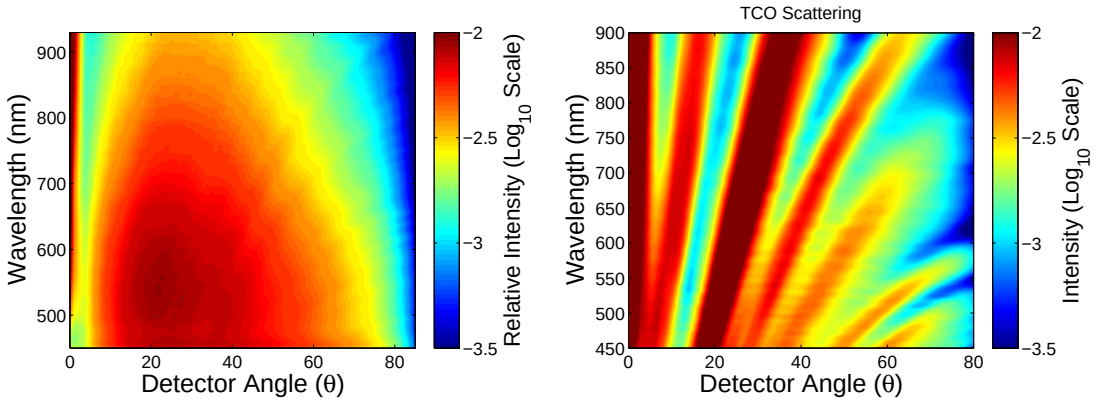

(a) WARS measurements.

(b) WARS simulation.

Figure 5.17: WARS measurement and simulation of AZO 757.

Despite the strong interference effects apparent on the simulated WARS results, there are several noticeable similarities between measurement and simulation of the AZO samples. In each case, the overall intensity is reasonably well matched as is the angular range of scatter. For example, the measurement of AZO 459 is unique in that it has a distinctive lack of scattering at angles larger than around 40 degrees and the same limited angular distribution is present in the simulated results. As with the FTO results, the most straight-forward solution for improving the WARS simulations would be to increase the simulated area, dramatically increasing the time and computer resource requirements. An alternative approach could be to carry out several 20 μm x 20 μm area simulations each based on AFM measurements of different areas of the same sample and averaging the results. This approach would not exceed computer resources in terms of power but would cause a linear increase in simulation time based on the number of averages required. This is the first time that detailed FDTD simulated far-field results have been shown to be comparable to experimental measurements. The resulting validation of this simulation technique means that FDTD can, in principle, be used to accurately probe effects that are difficult or impossible to investigate experimentally, such as the WARS distribution of light within an a-Si layer deposited onto a textured TCO.

5.3.2 Extending the Simulations

Scaling Surface Texture

With the FDTD simulation technique validated for this application in terms of both near-field and far-field results, it is possible to extend the simulation work to further analyse the effects of surface texturing on light scatter. In particular, the use of simulation allows for the geometric altering of the measured randomly rough surfaces which allows links to be made between scattering and specific surface characteristics. In this case, feature size and feature aspect ratio will be investigated. All simulations carried out in the section will be based on the FTO 600 TCO. This TCO has been chosen as it has surface roughness characteristics that are in the middle of the broad range previously investigated in this work. Additionally, FTO 600 also showed the best match between measurement and simulation.

The effects of feature size and of feature aspect ratio have been directly investigated by simple mathematical manipulation of the measured AFM data. To investigate the effects of overall feature size the surface data has been scaled in the X, Y and Z directions. whereas effects of feature aspect ratio are investigated by scaling the data only in the z direction. In each case simulations were carried out at 2, 3 and 4 times the original sizes. This scaling approach is illustrated in Figure 5.18.

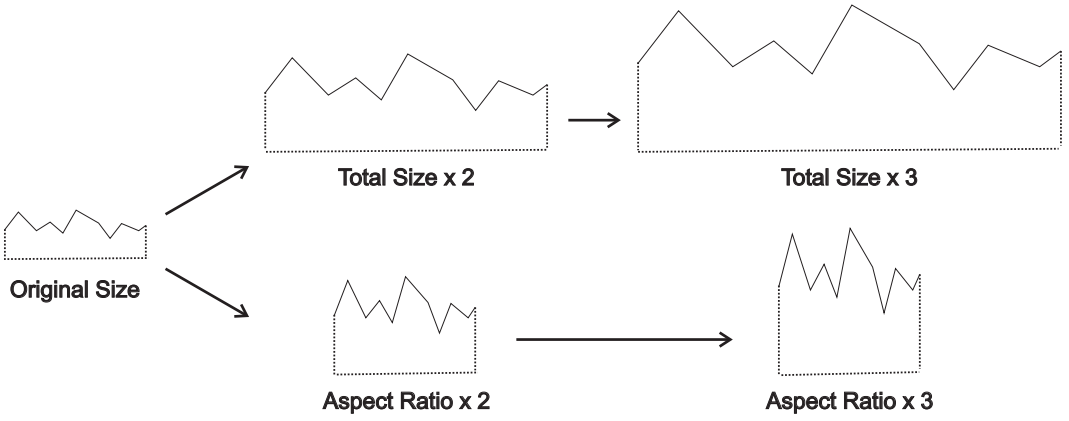

Figure 5.18: Illustration of scaling applied to FTO 600 surface data.

For convenience, simulations of varying total feature size have been labelled 2S, 3S and 4S where the number denotes the scale factor. Similarly, simulations of varying height aspect ratio are labelled 2H, 3H and 4H. The resulting simulated total transmittance for both scaling types is shown for all samples in Figure 5.19.

For the fully scaled simulations there is a clear correlation between feature size and total transmittance which is caused by increased reflectance. The relative decrease in total transmittance reduces for very large feature sizes, however, at this point the total transmittance is far below the acceptable levels for a solar cell front contact.

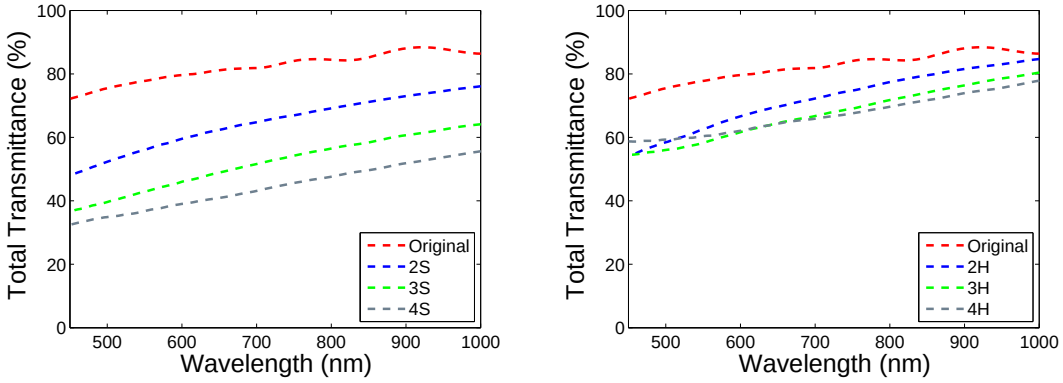

(a) Fully scaled.

(b) Scaled aspect ratio.

Figure 5.19: Simulation results for total transmittance of scaled TCO.

Increasing the aspect ratio of features without altering the lateral scale appears to have a less detrimental effect on the total transmittance. The relationship between height scale and transmittance is also less clear than for the case of full scaling. In general, increasing the height of the structures decreases the total transmittance, however, at short wavelengths the behaviour changes and a height scale of 4 times shows higher transmittance than scales of 2 or 3. The simulated diffuse transmittance results are shown in Figure 5.20.

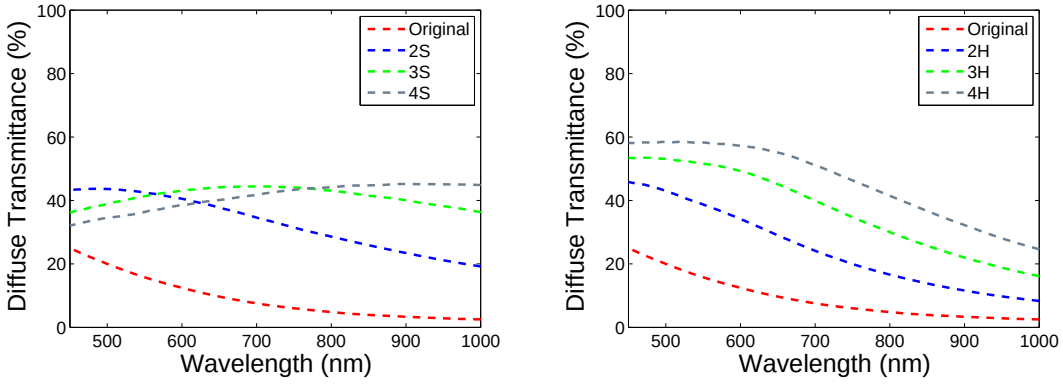

(a) Fully scaled.

(b) Scaled aspect ratio.

Figure 5.20: Simulation results for diffuse transmittance of scaled TCO.

The diffuse transmittance for the fully scaled TCO simulations show no obvious correlations between scale and transmittance intensity. The lack of linearity in these results may be due to the fact that whilst the TCO data is scaled, the area size simulated is kept constant at 20 μm x 20 μm which means that the full surface data is not simulated. However, the results do reveal generally high levels of diffuse transmittance. Scaling and subsequent simulation of the entire structure is unfortunately not possible with the available resources. The aspect ratio scaling simulations reveal a very distinct relationship of increasing scattering with increased aspect ratio. At shorter wavelengths

the scaled aspect ratio simulations show a higher diffuse transmittance than the fully scaled simulations, however, this is due to the lower total transmittance of the fully scaled set. At longer wavelengths, the fully scaled simulations show significantly more diffuse transmittance. The transmittance haze characteristics have also been calculated and are shown in Figure 5.21.

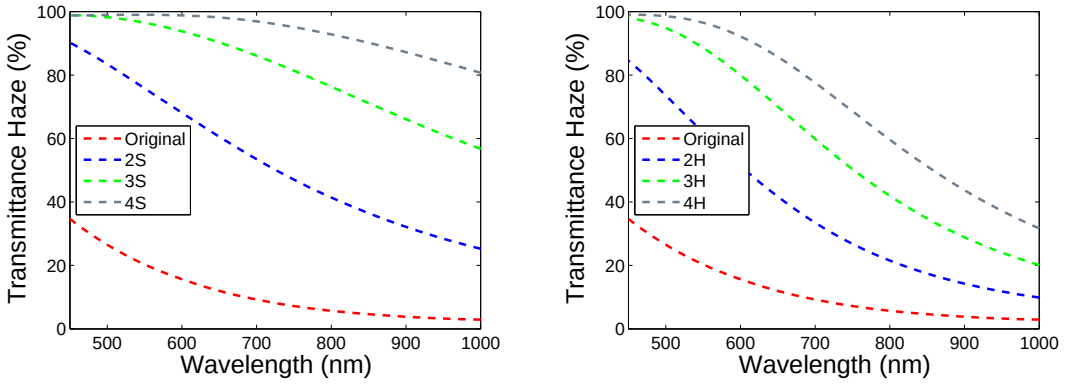

(a) Fully scaled.

(b) Scaled aspect ratio.

Figure 5.21: Simulation results for transmittance haze of scaled TCO.

The transmittance haze results are reasonably similar for the fully scaled and height scaled simulations, with the fully scaled results typically showing slightly higher haze, particularly at longer wavelengths. However, this is largely due to the very low total transmittance of the fully scaled TCOs which would not be acceptable for a solar cell device. For the scaled aspect ratio simulations, a 4 times scale shows significantly higher haze than a 3 times scale yet they have similar total transmittance properties. This indicates that for a purely light-trapping perspective, high aspect ratio features are advantageous in that they can significantly increase light scattering without severe loss of overall transmittance.

Angular Distribution Within Amorphous Silicon

To conclude the extended simulations, a layer of modelled a-Si has been added to the original FTO 600 TCO simulation. This allows for direct investigation of light scatter within the silicon layer. In order to reduce simulation complexity the a-Si has been modelled as semi-infinite. Two simulations were carried out, one with the real and imaginary parts of the refractive index of a-Si taken from the SOPRA database and one with an approximation to a-Si based on a non-absorbing dielectric with constant refractive index of 4.5. For both cases, the simulation was set-up with a transmittance monitor placed inside the a-Si layer, just above the highest feature of the textured TCO a-Si interface. The resulting simulated transmittance for both of the simulated models is shown in Figure 5.22.

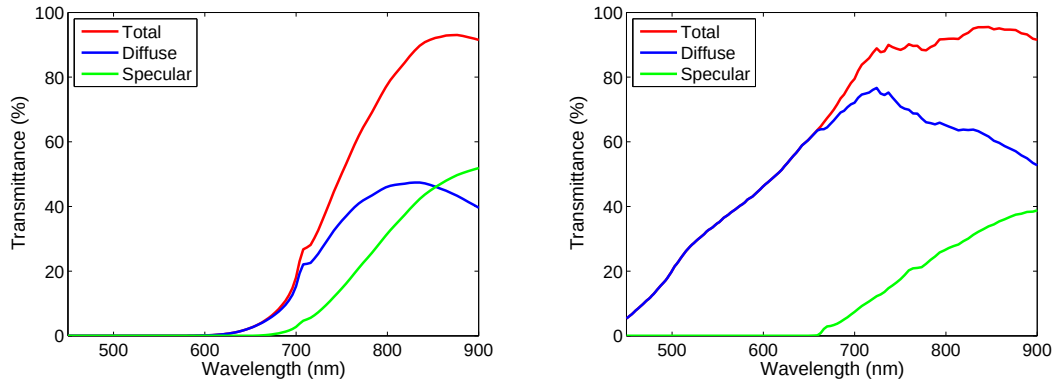

(a) Measured a-Si RI data.

(b) Constant RI of 4.5.

Figure 5.22: Simulation results for transmittance inside a-Si layer.

The results for the a-Si modelled using measured refractive index data should not be taken at face value as the absorption in the a-Si means that the result will change as the arbitrary position of the monitor within the silicon is altered. However, the percentage of the total transmittance that is diffuse should be reliable and largely independent of monitor position. The result of Figure 5.22(a) shows zero transmittance at wavelengths shorter than 600 nm, this is due to absorption in the a-Si. The transmittance then significantly increases at longer wavelengths due to the lower absorption co-efficient of a-Si in this regime, however, at wavelengths of up to around 700 nm the transmittance is shown to be almost entirely diffuse. Diffuse transmittance remains high up to 800 nm and then appears to tail off at longer wavelengths which cannot distinguish the smaller surface features. The results for the constant refractive index approximated a-Si model are useful as there is no absorption within the modelled a-Si layer making results independent of monitor positioning. These results show an impressive diffuse transmittance of near 100% of the total for wavelengths up to around 650 nm, as with the more accurate a-Si model, the percentage of diffuse transmittance begins to decline as wavelength increases.

For a more detailed look at the angular distribution of light within the a-Si layer, far-field projections have been used to obtain a full WARS profile for both types of a-Si model (see Figure 5.23).The results show short wavelength scattering within the a-Si is relatively low intensity for the case of the accurately modelled a-Si this is largely due to absorption within the a-Si layer and also partially due to higher short wavelength reflectance. This is supported by the fact that even the non-absorbing model of a-Si results show low short wavelength intensity. Interestingly, for the constant refractive index model the majority of short wavelength scatter is to large angles between 60 and 90 degrees. In general, both simulation approaches show a relatively even distribution of scattered light although there is a slight but constant trend of decreasing scattering intensity with increased angle of scatter.

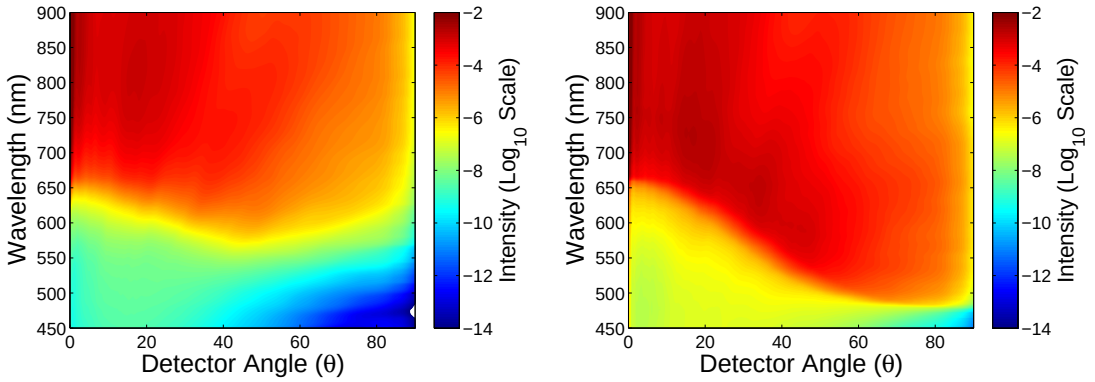

(a) Measured a-Si RI data.

(b) Constant RI of 4.5.

Figure 5.23: Simulation results for WARS characteristics inside a-Si layer.

5.4 Conclusions

The simulation results shown in the first half of this chapter have demonstrated the reasonable accuracy of the FDTD technique for modelling the optical effects of surfaces structured on the nanometer scale. In many cases, particularly the experimental FTO films, the simulations have been in excellent agreement with measurements for both total and diffuse transmittance. This has not only allowed for further investigation through simulation alone but also paves the way for future electrical simulations in which the optical generation calculated using FDTD could be used as an input parameter for solar cell device models. For the few cases where there are significant discrepancies between optical simulation and measurement this can be attributed to the use of an approximate, non-absorbing, wavelength independent refractive index, along with the small finite area of the simulation size. Both of these factors could be improved at the cost of increased simulation time and computer resources. Accurate refractive index data gathered using ellipsometry measurements, ideally from polished samples, could be used to increase the simulation accuracy and a larger area could be simulated by simply using AFM data from a larger scan area and extending the simulation boundaries. However, these improvements are beyond the capabilities of the computer resources available for this investigation. In the short term, the WARS results in particular could be improved by carrying out several simulations of the same size using surface texture data from several different scans of the same sample. Averaging between these results should help reduce the interference effects presently dominating the simulated WARS results.

The extended simulation work has demonstrated the unique ability of simulations to probe characteristics and trends that could be extremely difficult or impossible to test experimentally. It has been revealed that increasing the aspect ratio of features can prove to give superior light-trapping when compared to increasing the total feature size. In particular, increasing the aspect ratio alone can lead to very high diffuse transmittance

whilst maintaining high total transmittance. However, high aspect ratio features are known to lead to fabrication issues such as cracks when depositing subsequent device layers so this approach is unlikely to be feasible for improving solar cell efficiencies. Finally, the simulated WARS results from within the a-Si layer have revealed the stark differences between scattering into air and into a-Si. With scattering in a-Si shown to have a fairly even angular distribution with a high intensity of scattered light even at long wavelengths of up to 900 nm. Interestingly, shorter wavelengths of light are predominantly scattered to larger angles, however, the reflectance of short wavelength light is also relatively high. This unwanted reflectance could be alleviated by the use of smaller surface features to enhance the refractive index gradient effect, however, this will also lead to reduced scattering. It therefore appears that there is very little room for further optimization of light-trapping due to randomly rough surfaces. Many different optical and electrical consequences must be carefully balanced in order to get the most out of light-trapping for thin-film solar cells and the currently available industry standards have been shown to balance these effects well. Improvements are almost certainly possible by increasingly precise optimization and balancing of these effects but the current fabrication techniques used for creating randomly rough TCOs do not generally offer the high level of control required for near-perfect optimization and it is likely that extensive efforts would lead to only small gains. Other, more controllable methods of light scattering should therefore be investigated as radically different approaches could allow for high, controllable scatter with negligible detrimental effects.

Chapter 6

Periodic Metal Nanoparticle Arrays

In recent years there have been many studies on the use of metallic nanoparticles (MNPs) to enhance light-trapping within solar cells by utilizing plasmonics, surface texture and in some cases diffractive effects. These studies have often resulted in a certain degree of success, and optimized arrays of metal nanoparticles have been shown to enhance light-trapping significantly in comparison to planar device alternatives [82, 83]. In only rare instances has metal nanoparticle based light-trapping been shown to give comparable performance to the well established textured transparent conducting electrode technique [53, 54]. Arrays of metallic nanoparticles can be incorporated into a photovoltaic device in numerous configurations and provide a huge parameter space for optimization. Much of this parameter space has already been explored with detailed studies on random arrays placed at the front and back of solar cell structures. This study aims to investigate the relatively less explored configuration in which localized metal nanoparticles are placed periodically within the back-reflector TCO of a thin-film solar cell architecture. This layout eliminates the possibility of parasitic short wavelength absorption within the nanoparticles and allows for useful light-trapping through plasmonic and diffraction effects, ideally leading to more efficient photovoltaic devices.

6.1 Review of Gratings and MNP Arrays used for Light-Trapping

Arrays of nanoparticles have the potential to scatter light and therefore trap it within an absorber layer through the mechanism of plasmonics which includes contributions from diffraction if the array particles are arranged periodically. The fundamental principles of these scattering mechanisms are discussed in Chapter 2. In this section, recent work

based on diffraction gratings and metal nanoparticle arrays used in photovoltaic devices will be reviewed and summarized in order to gauge the light-trapping potential of these structures and to determine criteria for an improved design. Non-MNP based diffraction gratings and randomly arranged MNP arrays are first discussed followed by a review of work involving periodic MNP arrays.

6.1.1 Light-Trapping Using Diffraction

Randomly textured TCOs have become the standard technique for light-trapping within thin-film silicon solar cells, but this scattering mechanism offers little angular selection and is difficult to fabricate in a controlled way. In contrast, diffraction gratings can be designed to distribute specific wavelengths of light to a restricted angular range and should therefore have the potential to outperform random interfaces for light-trapping purposes. In particular, gratings can be designed to scatter the most weakly absorbed light, with energies close to the absorber bandgap, to the highest angles. This approach provides the maximum path length enhancement to the part of the solar spectrum where it is most needed. Early theoretical work in this area has shown the potential superior performance of diffraction gratings, which spurred significant research in the field [84, 85].

Due to the periodic nature of diffraction gratings, they can be accurately modelled using a variety of techniques which can vary significantly in complexity. For this reason, a significant portion of the work in this area has been theoretical with much of it involving finite element modelling techniques [86, 87, 88]. Several groups have modelled 1D diffraction gratings at the front, rear, or throughout a thin-film solar cell structure. In particular Li et al. used the rigorous coupled wave analysis (RCWA) technique to demonstrate that a simple rectangular 1D grating formed in the back metal contact of a thin-film solar cell can provide an average absorption increase of 10% compared to a planar structure [89]. More recently Zhang et al. showed an impressive 50% absorption increase for a structure based on a triangular rear grating with a rectangular front grating, also calculated using RCWA [90]. For studies such as this one, where gratings are placed at the front of the cell, their anti-reflective properties have been investigated in conjunction with diffraction effects. Several studies have investigated the effects of grating period with the results varying significantly depending on the specific solar cell material and grating design used. In general, gratings with periods between 600 nm and 900 nm have been shown to be optimal for c-Si whereas smaller periods of around 300 nm to 400 nm are best for a-Si cells [85, 86, 91, 84, 92, 93].

Several groups have also investigated more complex grating structures such as 1D gratings placed on top of Bragg reflectors [94], multiple gratings throughout the cell with different periods (see Figure 6.1(a) [95]), and novel single grating structures with multiple periodicities (see Figure 6.1(b) [96]). In each case, these complex grating structures have

been shown to provide a theoretical enhancement in solar cell absorption in comparison to planar designs and in some cases in comparison to optimized random texturing. However, these structures are often difficult and expensive to fabricate and therefore not necessarily practical for commercial solar cells. Naqavi et al. address this point in their study on realistic 1D gratings in which easily fabricated grating shapes are investigated, with a sawtooth shape shown to provide the most promising results [97]. Although the majority of literature has focused on simple 1D gratings, several groups have also investigated 2D grating structures which provide diffraction in multiple planes. In each case 2D gratings have been shown to be superior to 1D alternatives for light-trapping purposes [95, 92, 98]. For μc-Si devices in particular, fabricated 2D gratings have even been shown to provide significantly improved light-trapping in comparison to optimized randomly textured TCOs [99].

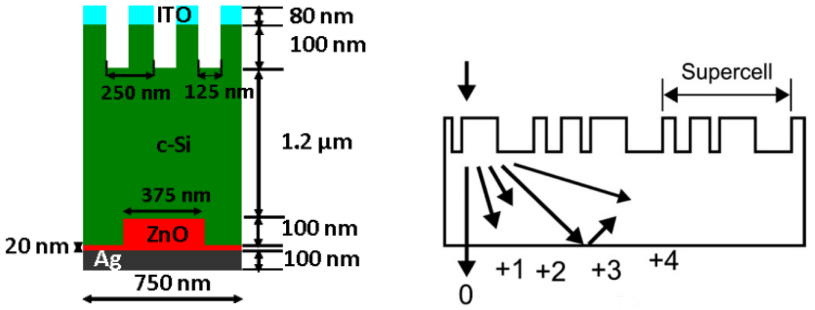

(a) Example of different gratings at multiple interfaces. Reprinted from [95].

(b) Example of supercell grating structure containing multiple grating periods at a single interface. Reprinted from [96].

Figure 6.1: Examples of diffraction grating based device designs.

6.1.2 Light-Trapping Using Plasmonics

Metal nanoparticles have long been known for their unique and interesting optical properties which have been detailed in Chapter 2 . These plasmonic effects can provide significant scattering of light and strong local field enhancement. For these reasons, metal nanoparticles have the potential to provide appreciable improvements in thin photovoltaic devices. One of the first clear demonstrations of the ability of MNPs to enhance solar cell absorption was presented by Schaadt in 2005 [100]. In this work Au nanoparticles were simply deposited on the surface of a c-Si photodiode and a significant increase in photocurrent was observed, with the largest particles (100 nm diameter) showing the most improvement. The authors claim a photocurrent increase of 50-80% due to an improved photon absorption of only 13% which indicates that the normalization procedure used within the work may have been inaccurate. Nevertheless, a significant photocurrent enhancement was observed and several similar studies were subsequently carried out at other institutions. Notably, Derkacs et al. demonstrated an 8.3% efficiency increase by depositing Au spheres onto an a-Si device and Pillai et

al. showed a 33% photocurrent increase by adding Ag particles to a silicon-on-insulator device [101, 50].

Many of the initial key findings for plasmonics within photovoltaics are summarized by Catchpole et al. in their 2008 review paper [102]. This study emphasized that the nanoparticle material, size and surrounding medium all have a significant effect on the resonance. Larger particles lead to a larger scattering cross section and a broader, red-shifted resonance. Red-shifting can also be achieved by increasing the refractive index of the surrounding medium. It is noted that when MNPs are placed near a high index substrate they will preferentially scatter light into the substrate, however, placing MNPs in direct contact with a semiconductor surface should be approached with caution due to high levels of unwanted recombination at the semiconductor/metal interface. Further work by Catchpole and Polman in 2008 used FDTD simulation techniques to demonstrate that cylindrical and hemispherical MNPs could provide superior light-trapping to spheroids and that plasmonic scattering could theoretically surpass the Lambertion limit which restricts the light-trapping potential of random texturing [103]. Ag and Au nanoparticles were investigated with Ag shown to be superior for light scattering into silicon. Whilst much of the previously mentioned work showed enhancements from placing MNPs on top of a solar cell, several more recent studies have shown MNP arrays can cause a significant increases in thin-film solar cell efficiencies when added to the rear of the device. This approach removes any possibility of parasitic MNP absorption of short wavelength light that is typically absorbed within the first pass through the device absorber layer. However, one disadvantage of incorporating MNPs into the rear only is that they will not provide any anti-reflection effect to the front interface of the device. Chen et al. report on an a-Si solar cell device in which the incorporation of nucleated silver nanoparticles into the back-reflector TCO led to a 23% efficiency increase [82]. Similar structures by Tan et al. have also shown efficiencies comparable to optimized textured TCOs (see Figure 6.2) [104, 53].

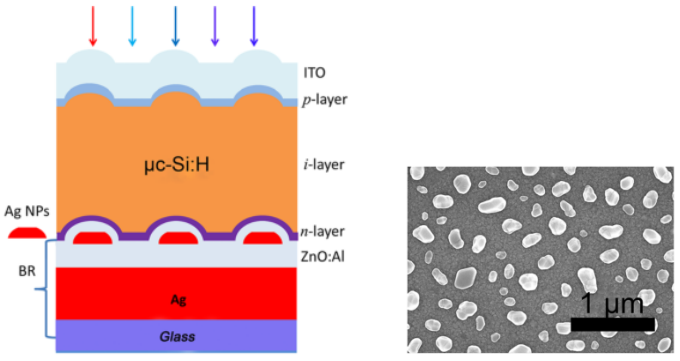

(a) Device structure of μc-Si solar cell with plasmonic back-reflector. Reprinted from [53].

(b) SEM of Ag nanoparticles used within back-reflector. Reprinted from [53].

Figure 6.2: Example of randomly arranged metal nanoparticles used to fabricate a solar cell with a plasmonic back-reflector [53].

However, the addition of MNP arrays can also have a detrimental effect and lead to solar cells with lower efficiencies [105]. This is often due to parasitic absorption within the nanoparticles leading to loss of power through thermal radiative effects or from loss of electron hole pairs due to recombination caused by either the particle itself or the increased surface area of subsequently deposited layers. These negative results are often not reported in the literature, but given that there are many groups worldwide focusing substantial resources towards plasmonic light-trapping, there are relatively few publications describing improved devices, let alone devices that show improved performance in comparison to conventional textured solar cells. Nevertheless randomly arranged MNP arrays remain a strong candidate for light-trapping in thin-film solar cells and, when designed correctly, their potential to increase light absorption has been consistently demonstrated. A significant advantage of random arrays is that they can often be fabricated using a variety of cheap and simple methods. One of the most common techniques used is to simply evaporate and anneal a thin metal film. However, fabrication methods such as this offer very little control which leads to difficulty for design optimization. Alternative, more complex fabrication approaches allow for higher levels of control and optimization including the opportunity for the MNPs to be arranged in a periodic manner which could provide additional light-trapping enhancement due to diffraction.

6.1.3 Periodic Metal Nanoparticle Arrays

Experimental studies of periodic arrays of metal nanoparticles have undergone relatively less research than randomly arranged arrays, largely due to the complexity and higher costs of fabrication. However, it should be noted that whilst fabricating MNP arrays in a controlled way can be costly for research and development, this is not necessarily the case for mass production as technologies such as nanoimprint lithography or interference lithography allow for relatively cheap reproduction of an optimized design. As with the study of diffraction gratings for light-trapping, much of the initial research in this area has been based on numerical studies which have shown very promising results [106, 107, 108, 109, 110]. An important consideration for periodic arrays of nanoparticles is the trade-off between maximizing diffractive orders and otimizing surface coverage, with the former requiring large periods and the latter requiring high particle density and thus small periods. In 2009 Mokkapati et al. described essential design criteria to be used for periodic MNP arrays. In this work, the FDTD techniques was used to demonstrate that particle sizes or around 200 nm with periods of around 400 nm should be optimal [111].

In recent years, several groups have reported experimental work showing successful plasmonic enhanced thin-film solar cells based on 2D periodic arrays of nanodomes patterned on to the metal back-reflector of the device. In this case the particles are

incorporated into the bulk back-reflector and are therefore not localized. Notably, Ferry et al. showed an increase in efficiency from 4.5% to 6.2% between a planar structure and a periodic metal nanoparticle back-reflector design (see Figure 6.3(a)) [83]. Bhattacharya et al. also showed results for a similar design which demonstrated efficiencies comparable to well established textured TCO based architectures [54]. Furthermore, Paetzold et al. presented absorption enhancements compared to planar alternatives for a μc-Si device with a similarly patterned back-reflector (see Figure6.3(b) [112]).

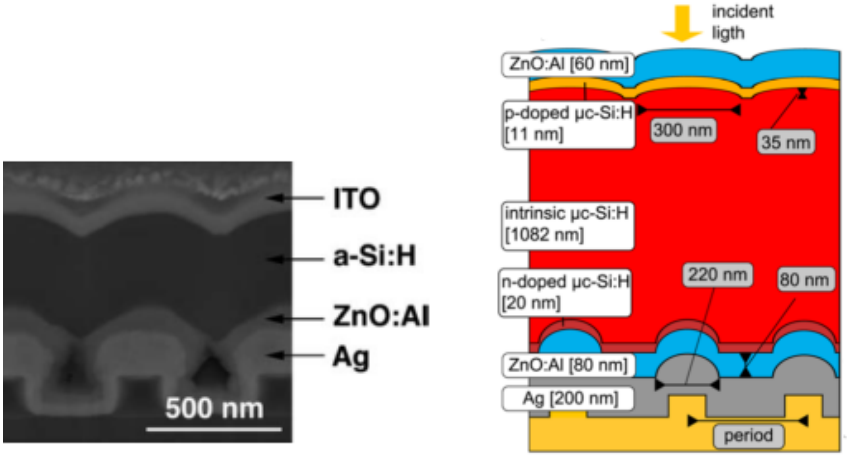

(a) FIB cross section of a-Si device fabricated on nano-patterned back-reflector. Reprinted from [83].

(b) Cross-section of μc-Si solar cell design with plasmonic grating back-reflector. Reprinted from [112].

Figure 6.3: Examples of solar cell designs with periodic plasmonic back-reflectors.

With the potential for periodic arrays of MNPs clear, this investigation aims to explore the use of periodic localized MNP based back-reflectors for thin photovoltaics. The localization of the MNPs allows for a localized surface plasmon resonance to occur which has the potential to further enhance scatter. However, separating the MNP array from the bulk back-reflector also introduces several new parameters such as the distance of the array from the reflector and the spacer material used. Similar work carried out by Sesuraj et al. in 2013 highlighted the potential of this approach by demonstrating the ability to tune the scattering response of MNP arrays by varying the separation distance from the back-reflector and thus modulating the driving field acting in the arrays, however, in this case the MNPs were randomly distributed and non-uniform [113].

6.2 Sample Design, Fabrication and Characterization

Based on the findings of the work discussed in Section 6.1 it was decided that the concept of incorporating periodic arrays of MNPs into the back-reflector of a μc-Si solar cell architecture would be further investigated. This leaves a large parameter space for exploration, with particle size, position within the back-reflector and pitch of the array requiring optimization. In the following sections details of the design and optimization of several different back-reflector designs are given along with the methods used to fabricate and characterize the samples.

6.2.1 Sample Design and FDTD Simulation

This investigation is focused on integrating periodic metal nanoparticle arrays into the back-reflector for thin-film solar cells. This geometry allows a large parameter space for exploration, including parameters such as particle size, shape, spacing and position within the back-reflector. In this section, these parameters have been investigated and narrowed down in order to create feasible design criteria for a set of experimental samples, the fabrication of which is detailed in Section 6.2.2.

For a periodic array of metal nanoparticles, there are two primary scattering mechanisms: plasmonic scattering and diffraction, the physical principles of both of these processes are detailed in Section 2.2. In order to achieve maximum light-trapping using such arrays, both of these effects should be carefully optimized. With regards to diffraction, the wavelengths and angular distribution of scattered light can be calculated by simply using the diffraction grating equation (Equation 2.3). However, the relative intensity of light scattered into different diffractive modes will depend on other parameters such as the grating material and fill factor. Similarly, the plasmonic resonance will depend on the nanoparticle size, shape, material type and surrounding medium. Full optimization of such a broad array of parameters would be inefficient if carried out experimentally. Therefore some parameters have been determined based on previous studies in literature and through simulation. The nanoparticle material was chosen to be Ag as this metal has generally been shown to have a strong plasmonic response, exhibiting larger optical cross-sections and lower absorption than other metals and it has a plasmonic resonance in the wavelength range of interest. A circular disk has been selected for the nanoparticle shape as the high symmetry will simplify results analysis and reduce polarization dependence. A disk shape also lacks sharp corners which are difficult to fabricate and would cause localized field enhancements, the effects of which are not the focus of this investigation.

With the shape and material type chosen, FDTD simulations were focused on determining an appropriate particle size in order to achieve a plasmonic resonance in the wavelength range of interest. For this study, the aim is to increase absorption within a μc-Si solar cell. The band-gap of μc-Si can vary with different deposition parameters

but it is generally close to that of c-Si (1.1eV). Therefore, scattering is required across the 700 nm - 1100 nm wavelength range. The resonance has been determined through simulation by using a total field scattered field (TFSF) source placed around the Ag nanodisk which is suspended in a homogeneous medium. The TFSF source is unique in that it is a 3D cube shaped structure which illuminates the sample from one direction using a plane wave but then subtracts any specular transmittance or reflectance away at the source boundaries. Therefore, transmittance monitors placed inside of the source geometry can detect the total field whilst those placed outside of the source will detect only scattered light. The peak wavelength of scattered light should correspond to the plasmonic resonance for the nanoparticle. This simulation setup is illustrated in Figure 6.4.

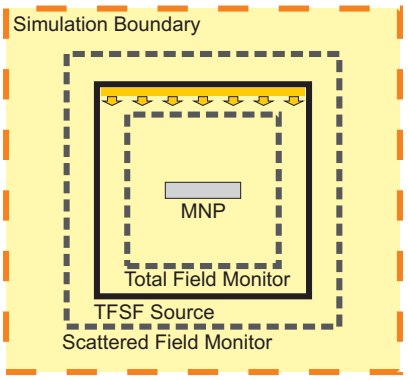

Figure 6.4: Simulation setup to determine plasmonic resonance of nanodisk.

For the case of a thin-film solar cell, the back-reflector typically consists of a thin layer of TCO on a highly reflective metal such as silver or aluminium. The TCO layer is used as a buffer between the metal and the semiconductor in order to reduce recombination at this interface as well as parasitic plasmonic losses that may occur for a rough metal back-reflector. For this work ITO has been selected for the TCO and Ag is used for the back-reflector metal. The nanoparticle arrays will therefore either be embedded within or deposited on top of the ITO/Ag back-reflector. The plasmonic resonance of the nanoparticles will be highly dependent on the surrounding medium. This means that accurate values for the optical properties of the ITO are required to reliably simulate the structure and these were therefore determined using ellipsometry on a test sample. These properties were then used to define the surrounding medium of a modelled MNP in an FDTD simulation. Simulations were carried out for a range of nanodisks diameters and thicknesses with the results shown in Figure 6.5.

The results show that a nanodisk diameter of 200 nm with a 50 nm thickness should provide a broad resonance in the wavelength range of interest, and this value is in good agreement with much of the literature reviewed in Section 6.1. All nanoparticles fabricated within this work have therefore been designed to have these dimensions. The position of the nanoparticle array within the back-reflector will be investigated experimentally. This is likely to have a significant effect on the scattering and also the

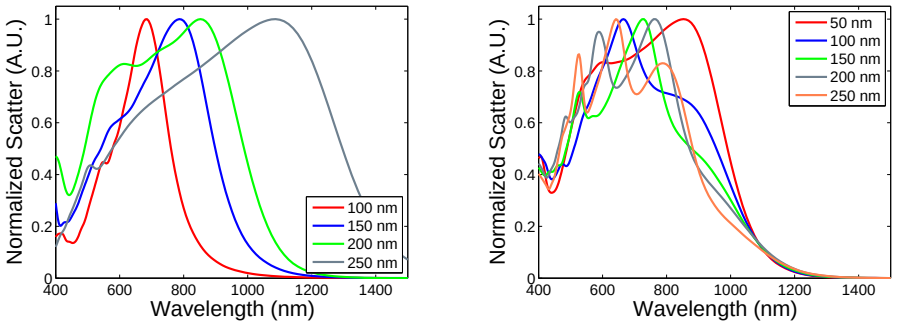

(a) Change in nanodisk diameter, thickness held constant at 50 nm.

(b) Change in nanodisk thickness, diameter held constant at 200 nm.

Figure 6.5: Nanoparticle scattering showing plasmonic resonance for different diameters and thicknesses.

total reflectance of the back-reflector. Three designs were chosen for fabrication, one in which the MNP arrays were deposited onto a 70 nm ITO/200 nm Ag back-reflector (Figure 6.6(a)), one where the MNPs were placed on a 100 nm ITO/200 nm Ag reflector (Figure 6.6(b)) and one simpler design in which the ITO layer is neglected and MNP arrays were deposited directly onto the Ag layer (Figure 6.6(c)). These designs were selected in order to gauge effects such as the necessity for and thickness of the ITO buffer layer and the nanoparticle array distance from the Ag back-reflector. For the designs in which the MNP arrays were placed on an ITO layer, the particles were then also coated in a further thin 10 nm layer of ITO in order to separate them from direct contact with the later deposited μc-Si layer. The various designs studied are illustrated in Figure 6.6.

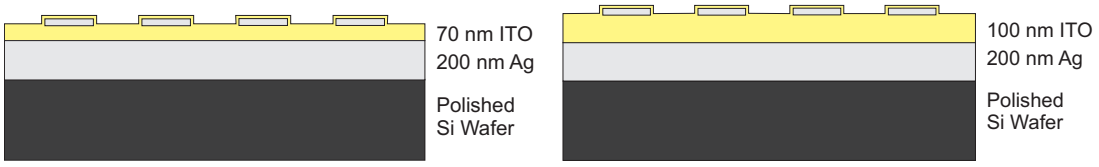

(a) Nanoparticle array embedded in 80 nm ITO layer.

(b) Nanoparticle array embedded in 110 nm ITO layer.

(c) Nanoparticles array directly on Ag, no ITO layer.

Figure 6.6: Alternative periodic metal nanoparticle array positions within solar cell back-reflector.

The final key parameter for exploration is the array period. This parameter was explored for each of the back-reflector designs experimentally and matched to further simulations. Results for these samples are presented and discussed in Section 6.3. It was decided that a range of array periods of 400 nm to 1100 nm would be fabricated with intervals of 100

nm to get a broad range of experimental results so that trends and key characteristics could be clearly identified.

FDTD simulations of the fabricated samples were focused on determining the total reflectance of the back-reflectors. This was achieved through the use of periodic simulations boundaries where the x and y span of the simulation region was set to match the nanoparticle array period. The metal nanoparticle was then specified as a 200 nm diameter, 50 nm thick Ag disk with a curved top designed to best match the SEM cross-sectional image (see Figure 6.16). The nanoparticle was modelled on top of an ITO/Ag or simply Ag substrate in accordance with the various reflector configurations shown in Figure 6.6. A plane wave source was then directed towards the sample and a power monitor was placed behind the source to detect the total reflectance. In some cases extra monitors were added to investigate absorption within the MNPs and the Ag back-reflector layer. An illustration of the typical model for these simulations is shown in Figure 6.7.

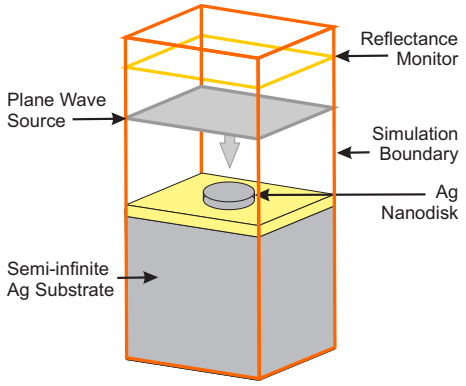

Figure 6.7: Simulation setup to determine reflectance of periodic MNP back-reflector.

For each back-reflector design simulations were carried out for a range of periods between 400 nm and 1100 nm. Simulations were then extended to incorporate a 10 nm ITO capping layer for the ITO/Ag based designs and a 500 nm μc-Si layer on top of the back-reflector. Unlike the case of the TCO simulations in Chapter 4, simulations in this chapter have been restricted to calculating only the total reflectance, and not the far-field distribution of scattering. This is because the far-field projections required to separate simulated diffuse and specular light are not designed to be used with periodic boundaries and will therefore not provide meaningful results.

6.2.2 Sample Fabrication

Bulk Back-Reflector

The Ag back-reflector used as the primary substrate for all samples was fabricated by depositing a 200 nm thick layer of Ag onto a 6 inch polished silicon wafer by means of electron beam evaporation. Specifically, a Leybold Optics LAB700 evaporator was used to deposit Ag at a rate of 0.1 nm/s at a chamber pressure of below $1e^{-5}$ mbar. For back-reflector designs A and B, the same tool was then used to deposit a layer of indium tin oxide (ITO). For all ITO layers deposited within this work the ITO was evaporated at a rate of 0.25 nm/s with a substrate temperature of 200^{o}C at a chamber pressure of around $1e^{-5}$ mbar. In order to evaporate ITO, the use of an ion gun was also necessary, the ion source was set to a bias current of 3A with a source discharge current of 2.75A and the chamber gas flow was set to 18 sccm argon and 25 sccm oxygen. This ITO recipe was previously optimized by Dr. Stuart Pearce at the University of Southampton to provide a resistivity of around $2.2e^{-4}$ Ω.cm and an average transmittance of around 80% for a 400 nm thick layer on a glass substrate. The film thickness and n and k values for the refractive index of the deposited ITO were determined using ellipsometry and are shown for an example 70 nm ITO on Ag sample in Figure 6.8. The thickness uniformity of the layer, also determined using ellipsometry, is shown in Figure 6.9. The refractive index values for the deposited ITO are in line with those reported in literature and the entire film is shown to have a relatively uniform thickness of 70 nm ±2%.

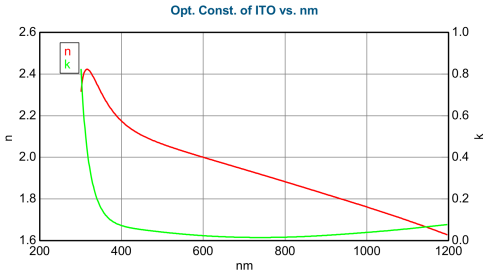

Figure 6.8: Complex refractive index values of 70 nm evaporated ITO.

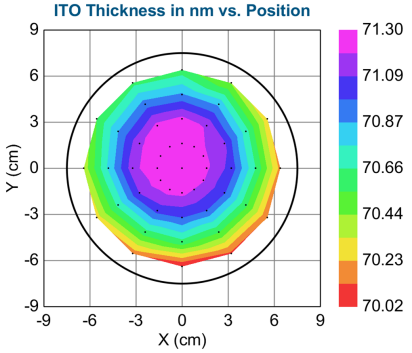

Figure 6.9: ITO layer thickness variation across 6 inch wafer.

The process of evaporating Ag and ITO leads to a back-reflector with low surface roughness, most of which originates from the 200 nm Ag layer. Although the level of texture is relatively low it will still have an effect on the optical properties of the reflector. To determine the exact extent of this roughness, the surface topology of the 70 nm ITO/200 nm Ag substrate was characterized using atomic force microscopy (AFM) as detailed in Section 6.2.3. An image of the surface is shown in Figure 6.10. Statistical analysis of the AFM results shows that the ITO surface has a typical RMS roughness of 8.1 nm.

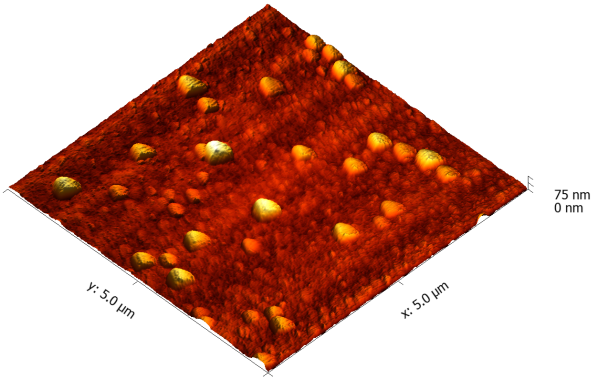

Figure 6.10: AFM plot of surface of 70 nm ITO on 200 nm Ag.

The fabricated Ag/ITO back-reflectors were then used as substrates for metal nanoparticle arrays in accordance with the designs previously shown in Figure 6.6. For design A the back-reflector consists of a 70 nm layer of ITO on 200 nm Ag, for design B a 100 nm ITO layer was deposited on 200 nm of Ag and for designs C the back-reflectors simply consisted of a 200 nm Ag layer.

Metal Nanoparticle Arrays

Metal nanoparticle arrays were fabricated by electron beam lithography (EBL), using a JEOL JBX 9300FS electron beam direct write lithography tool. EBL is an incredibly useful research tool which allows for bespoke material patterning down to a resolution of just a few nanometers. Similar to the technique of photolithography in which a photo-sensitive resist is exposed to photons, EBL works by exposing an electron sensitive material to electrons. Unlike photolithography, EBL uses a tightly focused beam and therefore creates patterns using a raster scan technique as opposed to masked illumination. This allows for the creation of arbitrary patterns with extremely small features, but the serial nature of the technique means that EBL is a slow and costly fabrication method and is therefore more suitable for research and prototyping than mass production.

Array patterns were first designed using L-Edit drawing software to create patterns for several 2 mm x 2 mm arrays of 200 nm diameter circles with a range of periods from 400 nm to 1100 nm as detailed in Section 6.2.1. The electron beam lithography tool requires input patterns to be a set of polygons so the 200 nm diameter circles were consequently approximated using octagon shapes. The patterns drawn using L-Edit software were then imported into a commercial e-beam lithography software tool called Genisys in which proximity effect correction was applied to the patterns. Proximity effect correction is required to account for the scattering of electrons around the substrate, which essentially means that patterns close to each other will require a lower dose than those spaced further apart. The exact spreading of the electrons, known as the point spread function is calculated using separate software in which details of the substrate materials and thicknesses are required as an input. Once the patterns have undergone proximity correction the Genisys software was then used to output pattern files in the appropriate format to be used as a direct input for the JEOL JBX 9300FS electron beam direct write lithography tool.

The physical electron beam lithography process can be summarized in a few key steps. First, the initial substrate (Figure 6.11(a)) is coated in an electron sensitive resist (Figure 6.11(b)). For this work a bi-layer resist was used in order to create an undercut into the lower layer which facilitates a clean lift-off which is required towards the end of the fabrication process to remove unwanted deposited materials. The resists used were 'MMA (8.5)' (methyl methacryllate) and 'PMMA 495k' (poly methyl methacryllate). MMA was deposited first using a 'Brewer Science' spinner to spin coat the wafer substrate. A film thickness of around 300 nm was achieved by spinning the resist at room temperature at a speed of 5000 revolutions per second for 45 seconds. The substrate was then soft-baked at 150^{o}C on a 'Sawatek' hotplate for 70 seconds. Once the substrate had been allowed to cool down the PMMA was deposited using the same spin speed and

time, in this case creating a layer approximately 150 nm thick. The substrate was then soft-baked at 180^{o}C for 70 seconds.

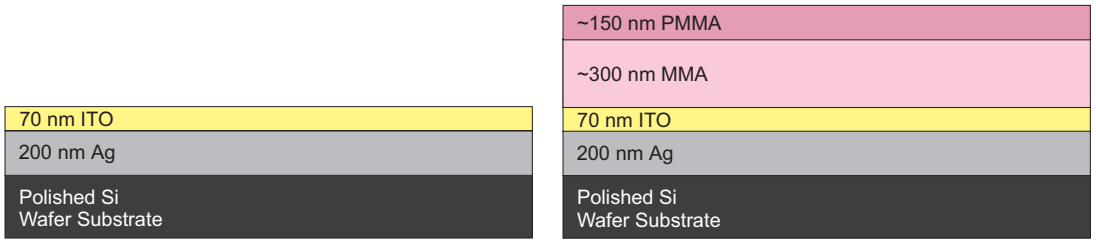

(a) Initial substrate. (b) Substrate coated with resist.

Figure 6.11: Illustration of initial substrate and resist coating.

With the resist prepared, the substrate is then loaded into the EBL tool and the required pattern exposure is carried out. As MMA and PMMA are positive resists, the areas that are exposed to the electron beam become more soluble when placed into developer solutions. MMA is more susceptible than PMMA which means that an undercut is created in the exposed areas (Figure 6.12(a)). Once exposure is complete, the substrates are placed into a developer solution; in this work a solution of MIBK and IPA was used at a 1:3 ratio. Substrates were placed in the solution for 70 seconds and then immediately rinsed with IPA and dried using nitrogen. At this stage the areas exposed to the electron beam have dissolved away leaving a lack or resist in the areas designated for patterning (Figure 6.12(b)).

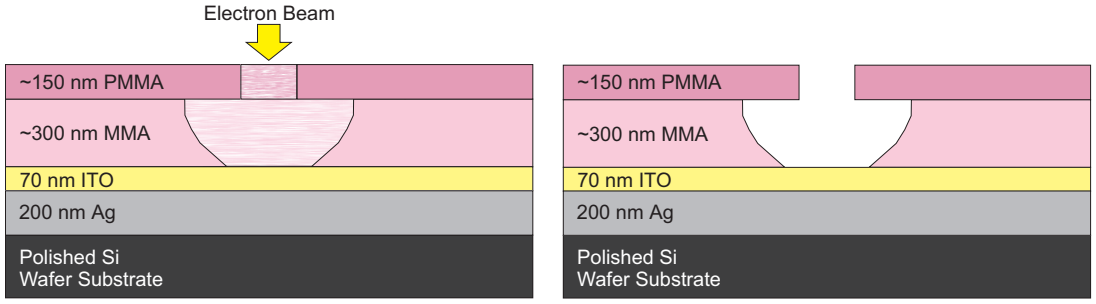

(a) E-beam exposure. (b) After development.

Figure 6.12: Illustration of e-beam exposed resist before and after development.

The samples were then metallized using a LAB700 electron beam evaporator to deposit a 50 nm thick Ag layer. In areas where there is no resist the metal deposits directly onto the substrate, in all other areas the metal simply deposits onto the resist (Figure 6.13(a)). The undercut created by using a bi-layer resist reduces the chance of any contact between the resist and the metal deposited onto the substrate thus allowing full removal of the unwanted metal. For the final step the resist layer is removed by submerging the sample in acetone for 3 hours. The acetone fully dissolves all of the resist leading to removal of unwanted metal, this process is known as lift-off (Figure

6.13(a)). In the final stages of the lift-off a pipette was used to manually apply a small amount of pressure to the sample areas in order to ensure complete removal of resist.

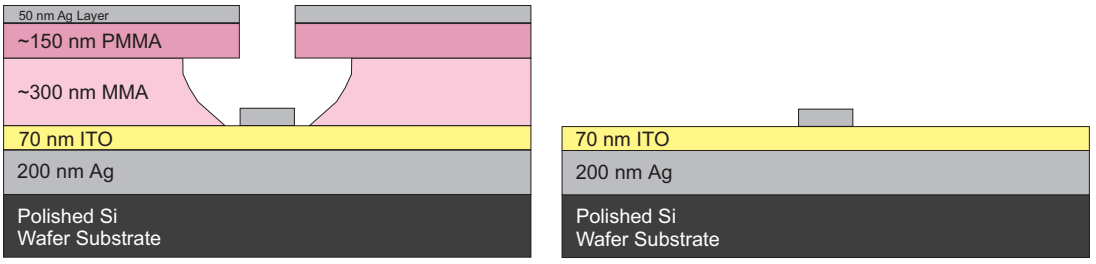

(a) After metallization. (b) After lift-off.

Figure 6.13: Illustration of metallization and lift-off.

This process results in an array of Ag nanoparticles which, in an ideal case, would exactly match the specified pattern. In order to achieve the correctly sized shapes it is crucial that the dose level used for the electron beam exposure is carefully optimized. This was achieved through dose tests by fabricating several replicas of the same pattern using different dose levels for exposure. The optimal dose level for the nanoparticles required for this work was found to be 900 μC/cm^2. This dose led to circular nanoparticles with a diameter only slightly larger than the original specifications. An example SEM image is shown in Figure 6.14 with measurement annotations verifying the nanoparticle diameter, shape and spacing.

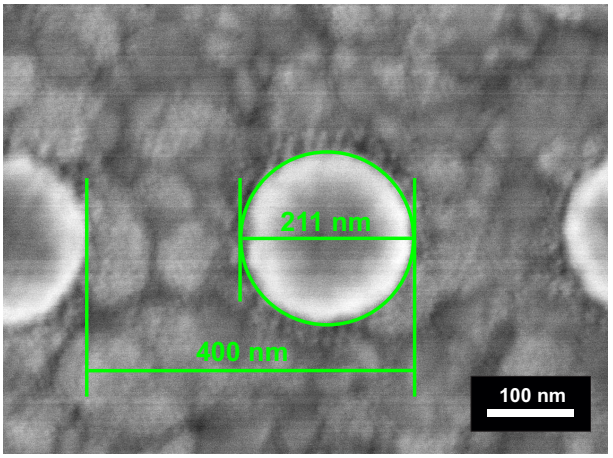

Figure 6.14: Measurements of nanodisk diameter and array pitch.

Example SEM images for each of the specified array periods with arrays consisting of 200 nm diameter, 50 nm thick Ag disks on 100 nm ITO/200 nm Ag back-reflectors are shown in Figure 6.15.

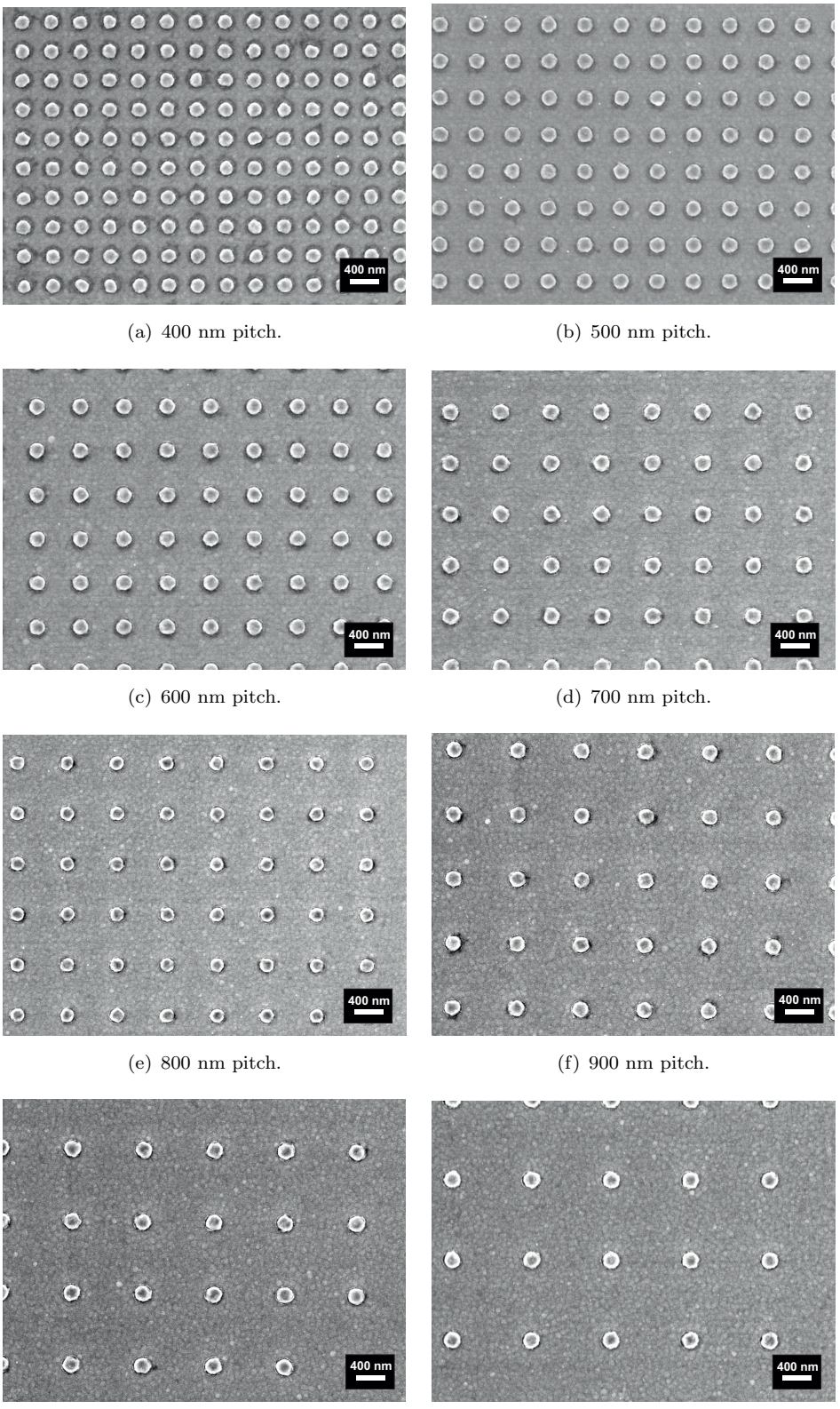

(a) 400 nm pitch.

(b) 500 nm pitch.

(c) 600 nm pitch.

(d) 700 nm pitch.

(e) 800 nm pitch.

(f) 900 nm pitch.

(g) 1000 nm pitch.

(h) 1100 nm pitch.

Figure 6.15: SEM of Ag nanodisks on ITO.

Microcystalline Silicon Pseudo Cells

The necessary small size of the experimental EBL fabricated MNP arrays, along with available equipment limitations and time constraints prohibited the fabrication of full, working solar cell devices. A compromise was therefore reached in which a layer of intrinsic microcrystalline silicon (μc-Si) was deposited on top of the arrays, this layer should closely mimic the optical properties of a working P-N junction based μc-Si photovoltaic device, therefore allowing for investigation into changes in device optical absorption due to the back-reflector MNP arrays. For each of the arrays a 500 nm layer of μc-Si was deposited using an Oxford Instruments PlasmaLab System 100 PECVD tool. For designs A and B (shown in Figure 6.6(a) and 6.6(b)) the nanoparticle arrays were first capped with a 10 nm ITO layer deposited using electron beam evaporation. To ensure that this thin layer was sufficient to completely cover the individual nanoparticles, a focused ion beam was used to create a cross-sectional image of the nanoparticle arrays. The results are shown in Figure 6.16.

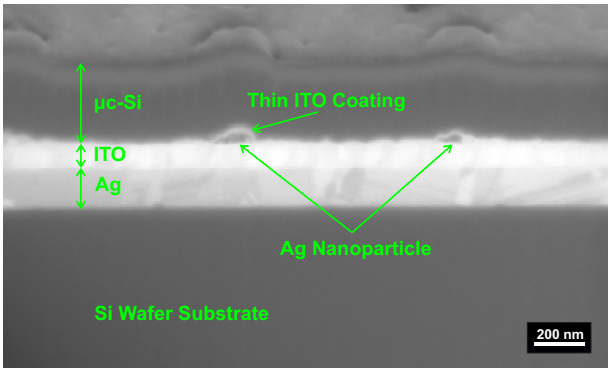

Figure 6.16: Cross-sectional image of nanoparticle array showing even coverage of ITO capping layer.

It should be noted that the results shown are for a sacrificial test sample in which the layer structure and order is correct but the layer thicknesses for the Ag and μc-Si do not match that of the final sample designs. Nevertheless, the SEM image shows a clear thin layer of around 10 nm evenly covering the nanoparticles. The fabricated nanoparticles themselves are shown to have a hemispherical shape, therefore not perfectly matching the disk shape design. This is due to imperfect fabrication procedures and possibly to the high temperatures of subsequent ITO and μc-Si layer deposition causing a slight deformation of the nanodisk shape. This change has been taken into account when creating simulation models in order to obtain a more accurate match with measurement results.

6.2.3 Characterization Techniques

Several techniques have been used to determine the physical and optical characteristics of the samples studied within this chapter. A brief overview of these techniques is provided in this section along with details of the specific tools used and the way in which they were arranged for measurement.

Microscopy

The surface characteristics of fabricated samples have been determined using a combination of scanning electron microscopy (SEM) and atomic force microscopy (AFM). SEM has been used to image the samples surfaces at various levels of magnification, allowing for accurate determination of the lateral size and spacing of nanoparticles and verification of particle shape and array uniformity. The SEM tool used was a Jeol 7500F FEGSEM capable of achieving a resolution of around 1 nm. AFM has been used to verify the height of the particles and to determine the roughness of the deposited Ag and ITO layers. The tool used was a Veeco Caliber AFM and all scans were carried out using a high aspect ratio probe at a resolution of 512 x 512. Finally, a focused ion beam (FIB) was also used to create cross sections through samples to determine the final nanoparticle shape and to ensure even coverage by subsequently deposited ITO and μc-Si layers as detailed in Section 6.2.2. The tool used was an Nvision 40 Crossbeam SEM/FIB.

Ellipsometry

Ellipsometry has been used to determine the optical constants and thickness of the ITO layer deposited as part of the back-reflector design detailed in Section 6.2.2. Whilst ellipsometry was used in previous chapters to determine only approximate values for the refractive index of rough TCOs, in this case accurate values can be determined as the investigated ITO layer is relatively smooth and has been deposited on a highly reflective substrate. A model consisting of a general oscillator on an Ag substrate was fitted to the ellipsometry data with a mean squared error of less than 10 which indicates accurate and reliable results. The specific tool used was a a J.A. Woolam M2000-DI variable angle ellipsometer.

Optical Measurements

To measure the total and diffuse reflectance of samples the integrating sphere technique detailed in Section 3.1.2 was used. The tool used was an RTC-060-SF sphere with a Fianium SC450-2 broadband super-continuum laser and a TE cooled B&W Tek

spectrometer, allowing for accurate measurement of wavelengths between 450 nm and 900 nm at a resolution of around 1 nm. The super-continuum fibre laser provides a broadband source of illumination with a spot size of less than 1.5 mm diameter at the rear port of the integrating sphere. This permits the characterization of small sample areas which is necessary due to the slow and expensive nature of the electron beam lithography technique used to fabricated the samples as detailed in Section 6.2.2. Unlike the TIS measurements carried out in Chapter 4, these measurements are for reflectance and therefore require the sample to be mounted at the back of the sphere. Measurements of diffuse light account for light scattered to angles greater than 5°. The measurements were carried out in double beam mode to ensure reliable and accurate results. Measurement accuracy was determined by characterization of polished silicon, with the results found to agree with theoretical calculations within an error of ±1%.

WARS measurements (see Section 3.2) were executed in reflectance on a selection of samples. For this study, samples were positioned with the initial reflectance interface in the central axis of rotation of the system. In each case the sample was held at normal incidence to the source and scans were carried out over a detector angular range of 90 to 0 degrees, where 0 degrees is the position of the specular reflectance. The high intensity of diffracted light means that, unlike the case of scattering from randomly textured surfaces, the weakest scattering may not be at the largest detector angle. This means that it is not advisable to automatically lower the integration time when the detector saturates as was done with the transmittance WARS TCO measurements in Chapter 4. A constant integration time of 13 seconds was therefore used for each scan and the automatic adjustment feature was disabled. The mini integrating sphere collector was equipped with a 2 mm aperture and was placed on the rotation arm at a distance of 10 cm from the centre of the sample. Measurements were carried out for a single azimuth angle with the samples aligned such that the diffraction along the x-axis would be incident on the detector. As the diffraction grating is a two dimensional pattern based on a square lattice, an azimuth rotation of the sample by 90 degrees in either direction will produce the same measurement result. However, rotating the sample by 45 degrees would produce significantly different results as the arrays are periodic along this axis with a different pitch.

6.3 Results and Discussion

In this section the optical measurements for the fabricated samples are presented and analysed. Results are separated into two main sections, one study is of the ITO thickness and position of the MNP array within the back-reflector and the second is a study of the effect of array pitch for MNP arrays embedded in a 200nm Ag/80 nm ITO back-reflector. In each case, optical results are shown for the back-reflector design with and without a subsequently deposited μc-Si layer.

6.3.1 Effect of Array Position

The effect of the position of the periodic MNP array within the back-reflector and the design of the back-reflector itself has been investigated by fabrication and measurement of the three different designs previously shown in Figure 6.6. For each design, results are shown for a MNP array period of 500 nm and 800 nm and for a planar structure with no MNP array. Corresponding simulations have also been carried out and are presented for comparison.

Back-Reflector

The back-reflector alone, with no μc-Si layer, was first investigated experimentally. The reflectance results for the back-reflector alone will be drastically different to the case of a subsequent silicon layer, however, the case of just the back-reflector is useful for the verification of optical modelling as the root of any poor agreement between simulation and experiment will be easier to identify and correct for a simpler structure. The total reflectance for the three back-reflector designs at MNP array periods of 500 nm, 800 nm and with no MNPs is shown in Figure 6.17. Measurements were carried out for both S and P polarizations with only negligible differences in the results. This is to be expected due to the symmetry of the MNP array designs and the measurements being carried out at close to normal incidence (8 degrees). Therefore, only the P polarization results are presented here.

Analysis of the total reflectance of the planar back-reflectors with no MNPs (Figure 6.17(c)) is straightforward with the pure Ag back-reflector showing typical high reflectance characteristics of Ag and the Ag/ITO reflectors showing varying characteristics due to interference effects. Of the ITO based designs, The 70 nm ITO design shows the most long-wavelength reflectance whilst the 100 nm ITO design provides the highest reflectance for wavelengths shorter than 750 nm. Results for back-reflectors with MNP arrays show more complex features. The measurements of MNP arrays deposited directly onto the Ag is the simplest case as there is no ITO spacer layer and the particles are not isolated from the bulk metal. These results show distinct dips in the reflectance spectra at wavelengths just beyond that of the grating period. This is a well known grating phenomena which occurs when light is diffracted at a grazing angle to the grating. For 1st order diffraction this occurs when the wavelength is close to the grating pitch, for 2nd order diffraction it occurs when the wavelength is close to half that of the grating pitch, these wavelengths are sometimes referred to as Rayleigh wavelengths. The resulting dips in the spectra are commonly known as woods anomalies due to their initial discovery by R. W. Wood in 1902 [114]. As well as these Rayleigh wavelength woods anomalies, the results for MNP arrays on Ag with no ITO also show some similar dips at other wavelengths, for example, at 640 nm in Figure 6.17(b). These could be due to another

type of Wood's anomaly related to the guided complex waves supportable by the grating resonance effects and originally separated from Rayleigh wavelength Wood's anomalies by Hessel and Oliner in 1965 [115]. For the Ag/ITO back-reflectors, far more substantial features in the reflectance are present due to the localization of the array nanoparticles leading to several different resonance effects. Of the two Ag/ITO samples the 100 nm ITO reflector design shows the highest reflectance at wavelengths shorter than 700 nm and the 70 nm ITO reflector design shows the best performance at longer wavelengths.

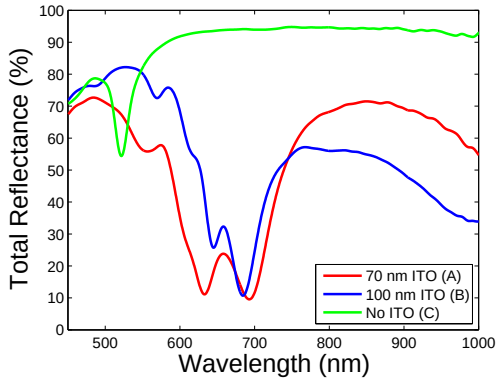

(a) 500 nm period.

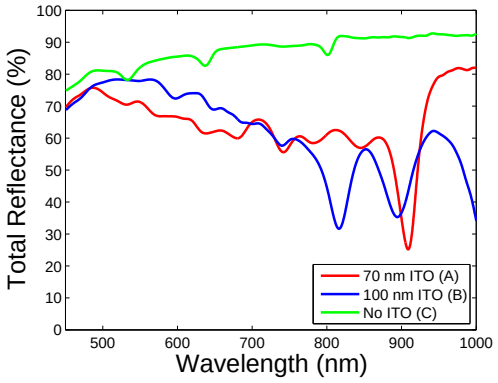

(b) 800 nm period.

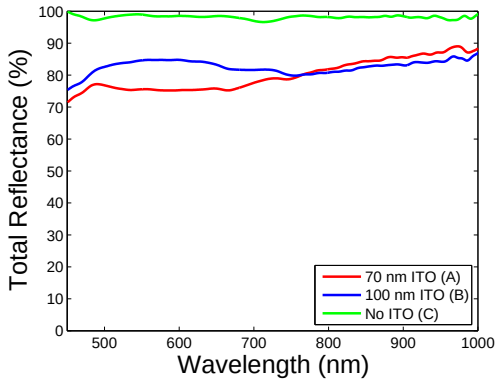

(c) No MNP array.

Figure 6.17: Measured total reflectance of back-reflector for array periods of 500 nm 800 nm compared to no array.

In each case the back reflector designs were also simulated using the FDTD technique. As with the measurements, simulations were carried out for both S and P polarizations with the results for each polarization state found to be identical due to the simulations being carried out at normal incidence. The simulated results (shown in Figure 6.18) show reasonable agreement with the experimental measurements, in most cases verifying the correct trends.

The simplest case of the simulations with no MNP arrays show the best agreement with experiment with the key difference being a higher value of total reflectance apparent in the simulations. This is most likely due to the fact that simulated layers are perfectly

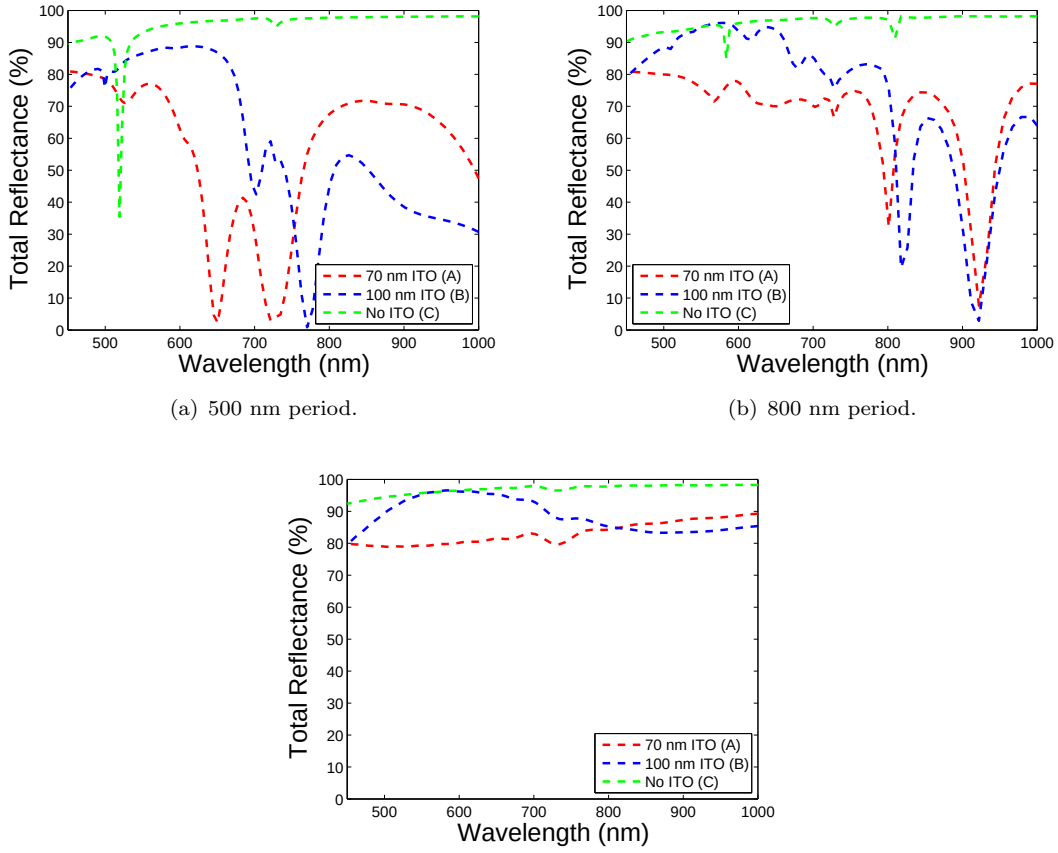

(a) 500 nm period.

(b) 800 nm period.

(c) No MNP array.

Figure 6.18: Simulated total reflectance of back-reflector for array periods of 500 nm 800 nm compared to no array.

planar whereas the physical structures have a small amount of roughness which could lead to increased absorption. Another key difference between simulation and experiment is that the simulations are carried out at normal incidence yet the measurements are at an angle of 8 degrees. One of the few weaknesses of the FDTD simulation technique is that broadband light cannot be truly set at a non-normal angle of incidence. An angle of incidence can be specified for a particular wavelength, typically the centre wavelength, but wavelengths either side of this will be effectively incident at different angles. It was therefore decided that simulations of normal incidence would suffice for approximate matching with measurements at 8 degrees. For simulations of back-reflectors with MNP arrays the overall trends are shown to match those of the measurements, however, the exact positions of peaks in the reflectance data seem to be slightly red-shifted in the simulations. This is likely due to the combined effect of imperfect optical constant values used to model the ITO layer along with the difference in angle of incidence between measurement and simulation. Although the match between measurement and simulation is not ideal, it is still sufficient to accurately predict trends and therefore indicates that simulations can be used to help to understand and optimize the optical effects of the MNP arrays studied.

Measurements of the diffuse reflectance of the different back-reflector designs were also carried out with the results shown in Figure 6.19. Back-reflector substrates with no MNP arrays showed near zero diffuse reflectance and are therefore not shown.

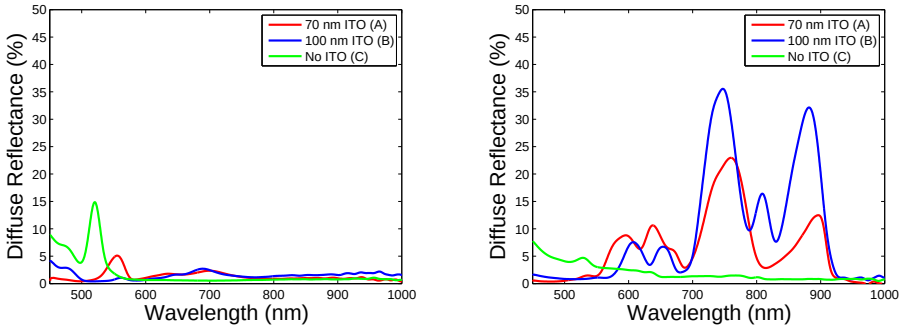

(a) 500 nm period.

(b) 800 nm period.

Figure 6.19: Measured diffuse reflectance of back-reflector for array periods of 500 nm 800 nm.

The diffuse reflectance for the simple case of the pure 500 nm MNP Ag back-reflector (with no ITO) show a peak in reflectance just beyond 500 nm, which corresponds with the dip in total reflectance at the same wavelength due to the Wood's anomaly. The same is true for the 800 nm pitch array on Ag, however, in this case the peak is significantly smaller, as is the dip in total reflectance. The more complex samples, involving an ITO layer, show far more significant features. In particular, for the 500 nm pitch arrays there is a small amount of diffuse reflectance at wavelengths beyond that of the grating period of the square array structure (500 nm) and even beyond that of the period of the diagonal of the structure (707 nm). This is most likely due to plasmonic scattering from the localized MNPs. For the 800 nm pitch arrays there is also a high level of diffuse reflectance beyond the grating period with large peaks and valleys present in the spectra, dominated by interference caused by the thin ITO film and the resonance of the MNPs. WARS measurements have been carried out to further characterize the diffuse reflectance. Example results for an 800 nm MNP array on each back-reflector design are shown in Figure 6.20.

The WARS results reveal several interesting features, many of which will be further investigated in the study of array pitch in the following section of this work. For the results shown here, where the pitch has been kept constant and only the back-reflector design has changed, it can be noted that the patterns of high intensity streaks in the WARS results are largely unaffected by the back-reflector design. This indicates that the thickness of the ITO layer, or lack of it altogether has little effect on the wavelength and angular distribution patterns of the scattering, however, the absolute intensity of light scattered does appear to be strongly affected. Furthermore, the region of broadly distributed, long wavelength scatter is present on both of the Ag/ITO designs but does not appear on the pure Ag design. This suggests that the broad scattering is due to

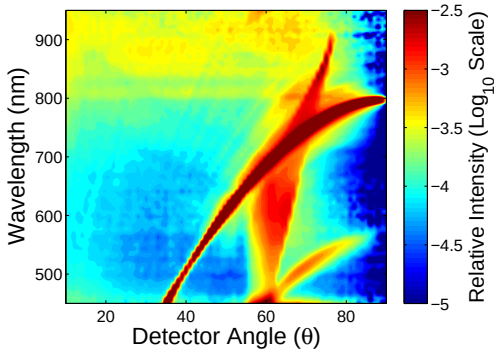

(a) 70 nm ITO.

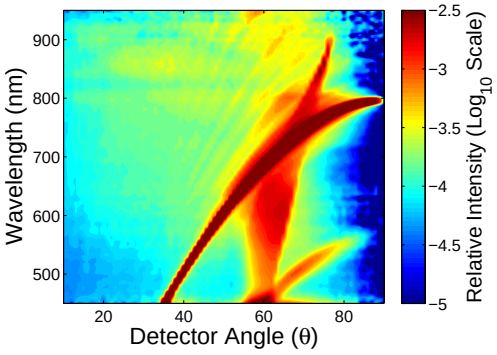

(b) 100 nm ITO.

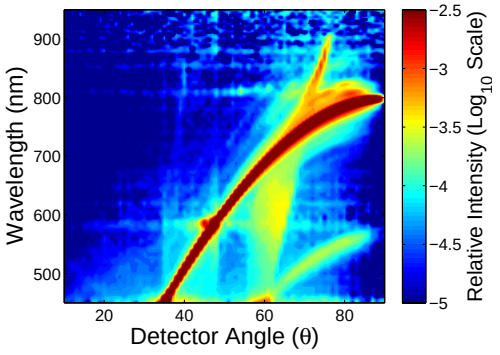

(c) No ITO.

Figure 6.20: Reflectance WARS for different back-reflector designs with 800 nm period MNP array.

the plasmonic resonance of the localized MNPs, and hence is not present for the case with no ITO where the MNPs are no longer localized. It is important to note that the high intensity diffraction effects shown in the WARS results are only present within the planes of periodicity for the MNP arrays. In contrast, the lower intensity plasmonic resonance based scatter can be detected outside of the diffracting planes and therefore provides a significant portion of the total scattered light.

In summary, results for the optical study of the chosen back-reflector designs show that the back-reflector with no ITO has the highest total reflectance, however, it exhibits almost no diffuse reflectance at longer wavelengths due to a lack of plasmonic scattering at the wavelengths studied and what appears to be weaker diffraction than the Ag/ITO reflectors. The Ag/ITO reflectors show similar characteristics, with the 70 nm reflectors having the highest long wavelength total reflectance but the 100 nm reflector showing the most long wavelength scatter. A reasonable agreement between measurement and simulation indicates that the FDTD technique is in principle suitable for the modelling of MNP array back-reflectors and will therefore be used to assist the further investigation of their optical properties for the slightly more complex case of the addition of an absorber layer.

Microcrystalline Pseudo-Cell

The optical results of the back-reflector design are useful for investigating scattering and validating simulations, however, to fully appreciate how the differences in back-reflector designs will affect the absorption in an actual device, μc-Si pseudo-cells have been fabricated by deposition of a 500 nm μc-Si layer on to each of the back-reflector designs. Prior to μc-Si deposition, a 10 nm ITO layer was deposited to coat the MNPs, separating them from the subsequent μc-Si. The results for total reflectance are shown in 6.21.

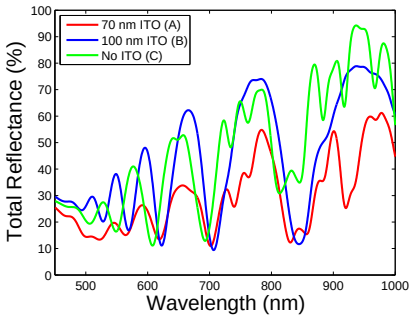

(a) 500 nm period.

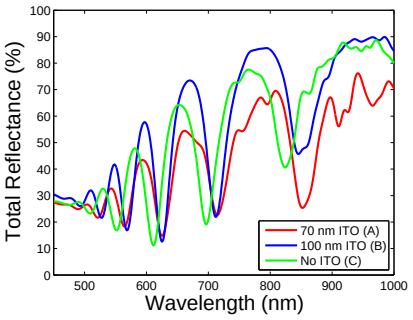

(b) 800 nm period.

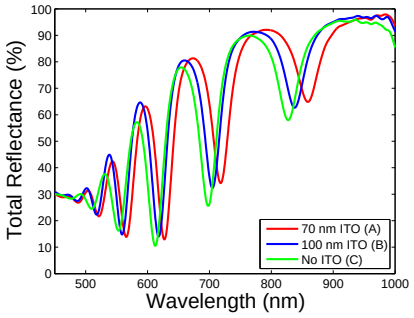

(c) No MNP array.

Figure 6.21: Measured total reflectance of μc-Si pseudo cell for back-reflector array periods of 500 nm 800 nm compared to no array.

For the case of the back-reflector designs with no MNP arrays the total reflectance is near identical for each of the designs. The small differences present in the locations of peaks and dips are simply changes in the interference patterns as the total device thickness changes due to ITO thickness alterations in the various designs. The MNP array results tell a more complex story. Of these samples, the 100 nm ITO design (now 110 nm with capping layer) consistently shows the highest reflectance at shorter wavelengths whilst the pure Ag design shows relatively high long wavelength reflectance. In both cases the 70 nm ITO design (now 80 nm with capping layer) shows the least overall reflectance, indicating the highest absorption within the pseudo-cell structure. Results for diffuse reflectance for the 500 nm and 800 MNP array back-reflectors are shown in Figure 6.22.

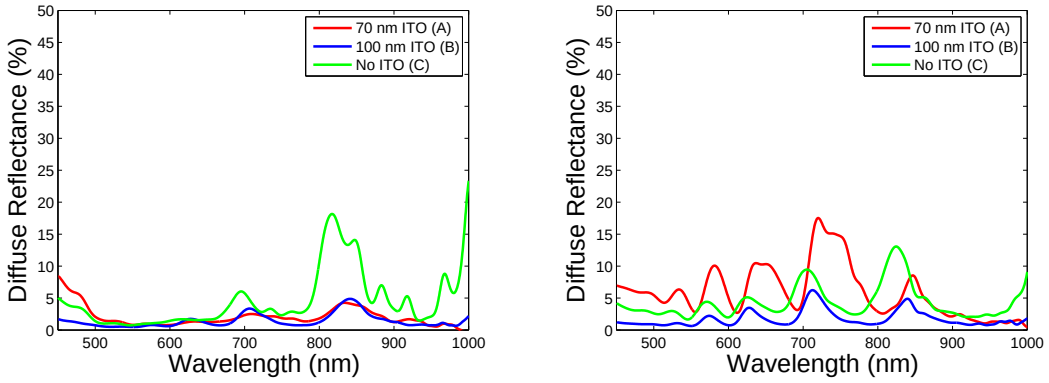

(a) 500 nm period.

(b) 800 nm period.

Figure 6.22: Measured diffuse reflectance of μc-Si pseudo cell for back-reflector array periods of 500 nm 800 nm.

Interestingly the diffuse reflectance of the pure Ag back-reflector is shown to be the highest for the 500 nm MNP pitch designs, however, the 70 nm ITO design shows superior scattering for the larger 800 nm pitch arrays. For all of the arrays the high diffuse reflectance peaks match up with the strong dips in total reflectance. The experimental results show that the 70 nm ITO back-reflector design is the superior of the three investigated as it provides the least total reflectance in all cases, a significant portion of which is diffuse for the MNP array with an 800 nm pitch. This low reflectance indicates high absorption within the pseudo-cell structure, however, more investigation is required to determine how much of this absorption enhancement would actually be useful. This design was therefore selected for further investigation through a detailed study of the effects of MNP array pitch.

6.3.2 Effect of Array Pitch

The effects of MNP array pitch have been investigated by optical characterization of a series of electron beam lithography fabricated samples with periodicities ranging from 400 nm to 1100 nm. These arrays have been characterized using conventional integrating sphere measurements alongside novel WARS measurements with the results for total and diffuse reflectance compared to FDTD simulations to allow for further analysis.

Back Reflector

Measurement and simulation results of total reflectance for the periodic MNP arrays on 70 nm ITO/Ag back-reflectors (80 nm ITO including capping layer) are shown in Figure 6.23 and 6.24 respectively. Results for the full range of periodicities investigated are shown on two separate graphs for clarity.

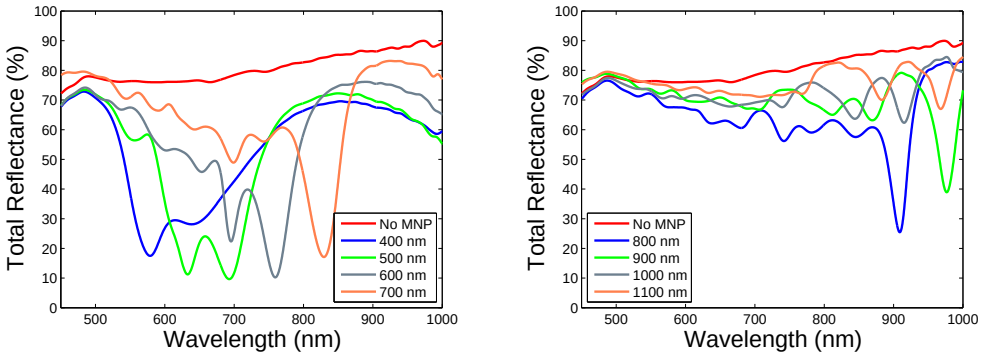

(a) 400 nm to 700 nm pitch.

(b) 800 nm to 1100 nm pitch.

Figure 6.23: Total reflectance measurement of periodic MNP arrays on 70 nm ITO with different periodicities.

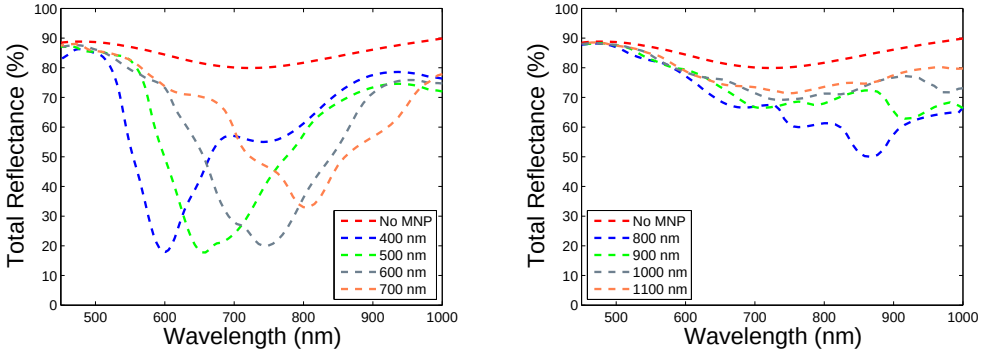

(a) 400 nm to 700 nm pitch.

(b) 800 nm to 1100 nm pitch.

Figure 6.24: Total reflectance simulation of periodic MNP arrays on 70 nm ITO with different periodicities.

The results show that in each case, the addition of a MNP array lowers the total reflectance in comparison to the bare 70 nm ITO/200nm Ag substrate. There is a clear trend between increased overall reflectance and larger array periods and each periodic array shows a distinct minima in reflectance which is due to interference effects between the nanoparticles, Ag substrate and thin ITO spacer layer. The simulations show a reasonable agreement with measurements with the minima in reflectance being present at a similar wavelength and the same trends of increased reflectance with increased period. The decrease in reflectance caused by the addition of MNP arrays indicates that the arrays cause significant absorption, either in the nanoparticles themselves or in the ITO or Ag back-reflector. Absorption in these areas is undesirable but the optical response will change significantly when a semiconductor absorber layer is subsequently deposited as the layers higher refractive index will dramatically change diffraction and plasmonic effects and lead to preferential scattering into the semiconductor. Whilst the optical measurements of the bare back-reflector are therefore somewhat misleading they are still particularly useful for comparison with simulation in order to further validate the FDTD modelling approach. It is also useful to determine how much of the measured reflected light is diffuse, the measurement results for diffuse reflectance are shown in Figure 6.25.

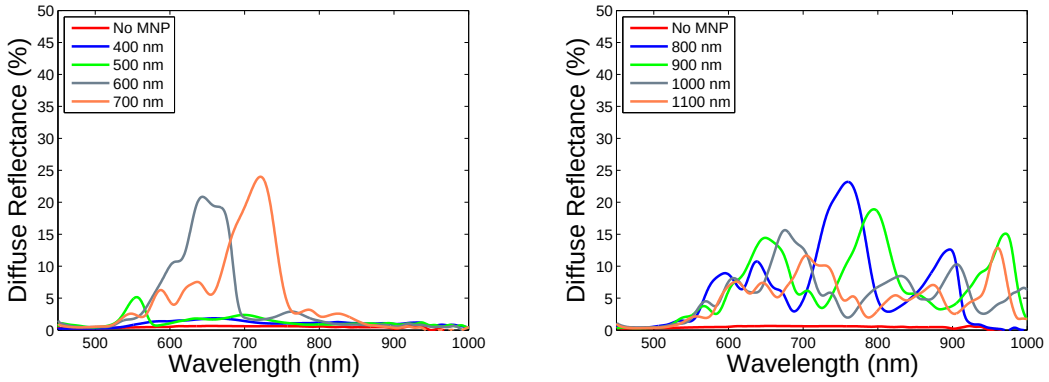

(a) 400 nm to 700 nm pitch.

(b) 800 nm to 1100 nm pitch.

Figure 6.25: Diffuse reflectance of periodic MNP arrays on 70 nm ITO with different periodicities.

As expected, measurements of the planar back-reflector with no MNP array shows near zero diffuse reflectance. The diffuse reflectance for MNP array periods of 400 nm and 500 nm is also low across all wavelengths, however, as the array period is increased, significant scattering becomes present. Several peaks in the diffuse reflectance can be observed and in most cases these can be associated with the square and diagonal periodicities of the arrays. However, the complex shape of the diffuse transmittance curves indicates that there are further effects at play, beyond simple diffraction. To further investigate this, WARS measurements were carried out for all samples, with a selection of example results is shown in Figure 6.26.

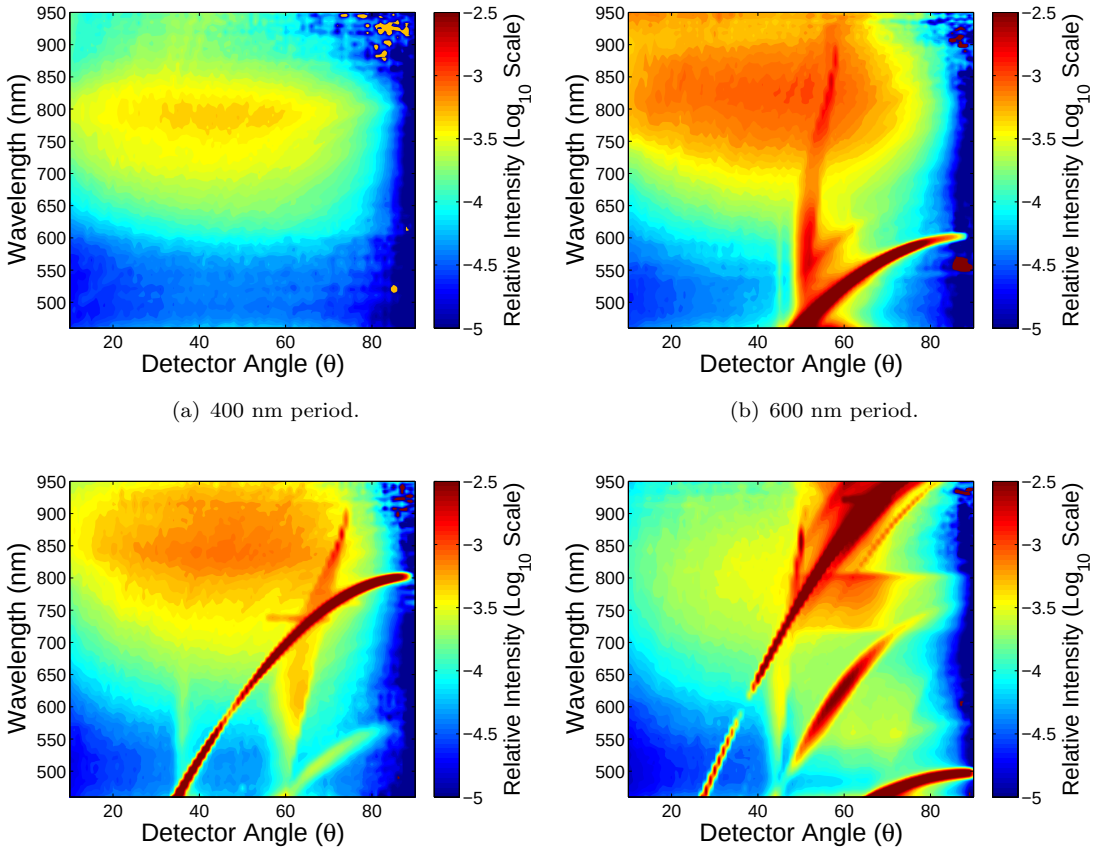

(a) 400 nm period.

(b) 600 nm period.

(c) 800 nm period.

(d) 1000 nm period.

Figure 6.26: WARS measurements for periodic MNP back-reflectors with different periodicities.

The results show unique patterns with fine areas of high intensity scatter to very specific angles along with broad wavelength regions of evenly distributed scattered light. The highest light intensities are present in Figures 6.26(b) to 6.26(d) in the form of thin, dark red streaks across the WARS plot. These high intensity patterns are due to diffraction from the periodicity of the arrays. This explains why the streaks do not appear on the results for the 400 nm pitch array shown in Figure 6.26(a) as only wavelengths shorter than the array pitch will undergo diffraction and the source and detector equipment used do not extend to such short wavelengths. All of the plots show a broad region of well distributed scatter between a wavelength range of around 700 nm to 900 nm. This is likely due to plasmonic scattering from the metal nanoparticles as it matches the predicted frequency for the plasmonic resonance determined though simulation in Section 6.2.1. The theoretically calculated diffraction and plasmonic resonance are shown for an example MNP array period of 1000 nm alongside WARS results in Figure 6.27.

This comparison leaves no doubt regarding the diffraction origins of the high intensity peaks and it is a strong indication that the WARS results are also showing plasmonic scattering. However, WARS measurements of the substrate itself in areas with no MNP

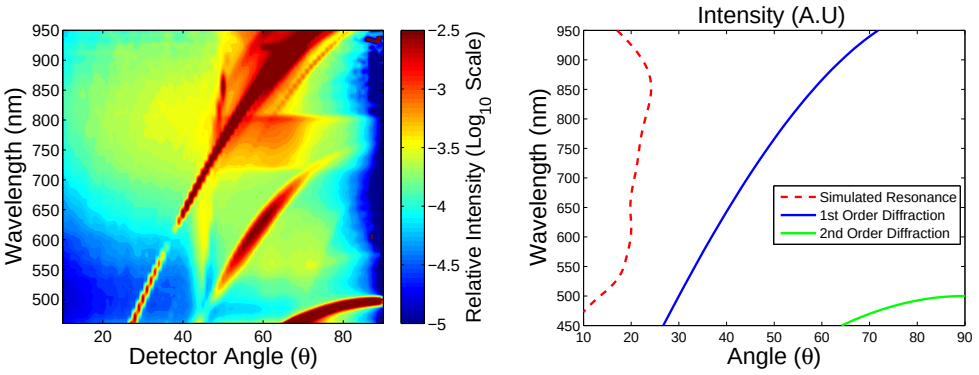

(a) WARS result for 1000 nm period MNP Back-Reflector.

(b) Plot of diffraction grating equation for 1000 nm grating period (bottom axis) and simulated resonance of MNP (top axis).

Figure 6.27: 1st and 2nd order diffraction and simulated resonance of MNP plotted on the same scale as WARS results for 1000 nm grating.

arrays also showed a broad region of scatter at long wavelengths, similar to the results of Figure 6.26(a) although at a weaker intensity. It is possible that this is also a plasmonic scattering effect originating from the 200nm back-reflector Ag layer as the slight roughness of this layer could lead to plasmonic absorption and scattering.

There are several other features in the WARS plots of Figure 6.26 that do not appear to be related to diffracted orders or plasmonics in a straightforward manner. Notably, the 800 nm and 1000 nm pitch array results show diffraction like curves in positions that are not associated with any diffractive order and several other distinct areas of high scatter can be observed, particularly for larger period arrays. The cause of these effects is not clear, it is possible that they are spurious results originating from multiple reflections within the WARS measurement system. Strongly diffracted light from the square and diagonal periodicities of the arrays could be reflecting from other components in the system and then back off the sample and into the detector. This is supported by the fact that the unexplained patterns are in all cases weaker than the initial diffraction and show similar but offset shapes. However, despite several modifications to the measurement arrangement to reduce the possibility of interference from back-reflections, the anomalies in the results remained unchanged. Another possibility is that these effects arise from complex interference between diffracted light and plasmon interactions, and could perhaps be related to the Wood's anomalies present in the previously shown total reflectance characteristics. These anomalies are an interesting and unexpected results which could not have been observed without the use of the comprehensive and novel WARS measurement technique. The anomalies will also not appear in standard FDTD simulations as the ordered MNP arrays investigated here require the use of periodic boundaries within the simulation set-up which leads to non-meaningful far-field projections. This problem could be circumvented by modelling a significantly larger area of numerous particles along with absorbing boundaries, however, the computer

resources required for this are beyond those available for this investigation. Whilst the anomalies in the WARS plots are certainly intriguing, for the case of light-trapping for photovoltaics they will only have a small effect as they are only present in the planes of diffraction and have intensities orders of magnitude below that of the true diffractive orders, their origins are therefore not a key focus of this work.

Microcrystalline Pseudo-Cell

Optical results gathered from the back-reflector have shown promising diffractive and plasmonic scattering. However, adding a silicon layer will substantially change the optical behaviour of the back-reflector and therefore the full device structure must be investigated. To this end, a 500 nm μc-Si layer has been deposited onto each of the back-reflector designs and the measurements and simulations have been repeated. It is hoped that the MNP arrays will lead to a decrease in total reflectance, indicating increased absorption within the device. Results for the measured and simulated total reflectance for each of the arrays are shown in Figure 6.28 and 6.29.

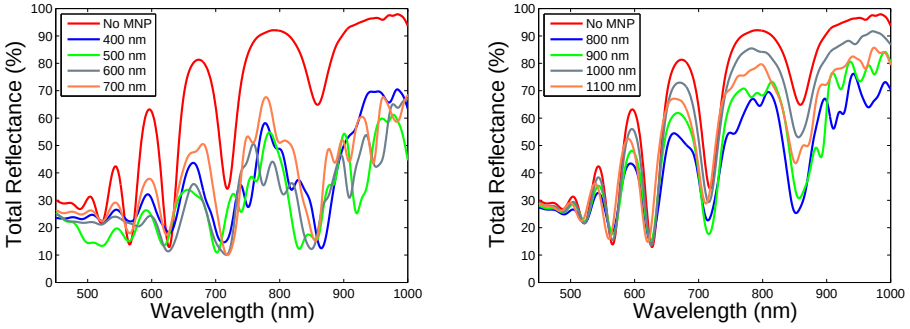

(a) 400 nm to 700 nm pitch. (b) 800 nm to 1100 nm pitch.

Figure 6.28: Measured total reflectance of μc-Si pseudo cell with periodic MNP array back-reflector of different periodicities.

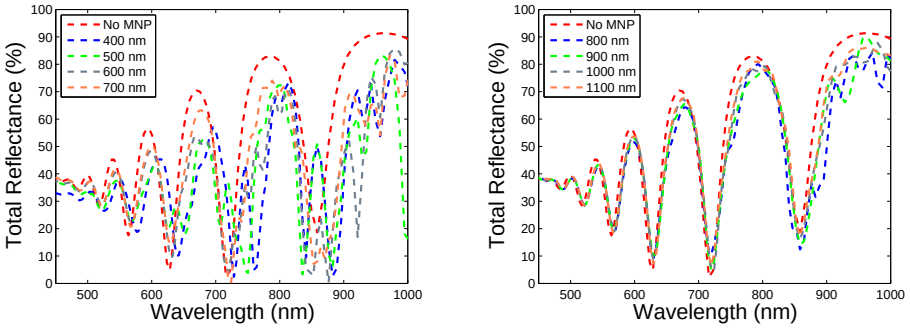

(a) 400 nm to 700 nm pitch. (b) 800 nm to 1100 nm pitch.

Figure 6.29: Simulated total reflectance of μc-Si pseudo cell with periodic MNP array back-reflector of different periodicities.

For each of the investigated array periods the results show a positive result of reduced total reflectance and there is a general trend towards decreasing reflectance with decreased array pitch. This makes sense as the particle sizes are constant for all arrays and therefore increasing the pitch lowers the nanoparticle area coverage, leading to fewer particle interactions with light. The agreement between simulation and measurement is not as good as for the case of the simpler back-reflector study in the previous section. This is to be expected as adding a 500 nm μc-Si layer significantly increases the complexity of the simulation and could lead to errors from inaccuracies in the μc-Si refractive index data and models fitted to it. However, the results do show a similar overall trend of smaller array periods leading to reduced total reflectance with the larger array periods results becoming increasing similar to each other. The measurement results here show a stark difference to those of the back-reflector in air in which larger period arrays were shown to scatter long wavelength light to large angles, thus highlighting the differences made when adding the μc-Si absorber layer. These differences are due to the proximity of a μc-Si layer, shifting the plasmon resonance of the MNPs and also affecting diffraction due to the change in effective wavelength of light and angular changes in accordance with Snell's law. Measurements of the diffuse reflectance from each of the pseudo-cell samples is shown in Figure 6.30.

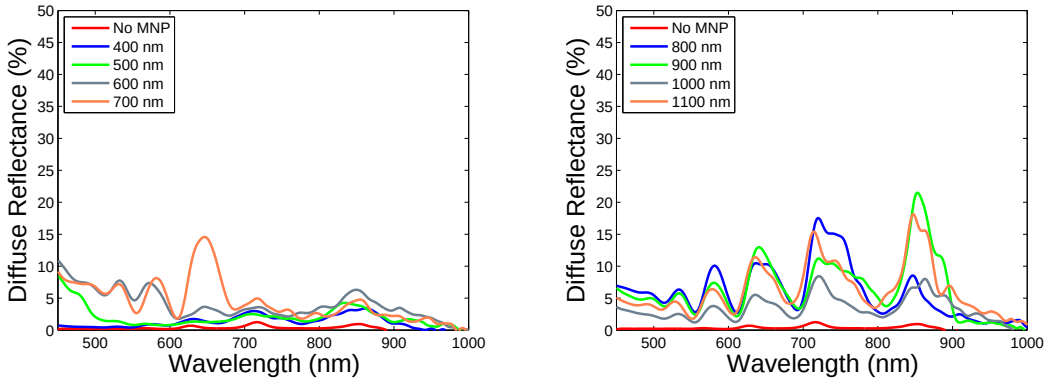

(a) 400 nm to 700 nm pitch.

(b) 800 nm to 1100 nm pitch.

Figure 6.30: Measured diffuse reflectance of μc-Si pseudo cell with periodic MNP array back-reflector of different periodicities.

The diffuse reflectance characteristics show a similar pattern for all of the MNP arrays with peaks in roughly the same position in each case. There does not appear to be a distinct trend for diffuse transmittance intensity. However, arrays with the smallest pitch show the least diffuse reflectance which is largely due to reduced overall reflectance. The peaks in diffuse reflectance match up with the dips in total reflectance and these peaks are even present for the sample areas with no MNP arrays, albeit at a substantially lower intensity. This indicates that the intensity of the reflectance is dominated by the optical interference patterns generated by the thin 500 nm μc-Si layer. The dips in total reflectance naturally correspond to peaks in transmittance through the layer

so a higher percentage of these wavelengths reach the back-reflector and interact with the MNP array where they may undergo scattering. The peaks in diffuse reflectance being present for the sample with no array indicates that some scattering is caused by the 200 nm Ag back-reflector layer, similar results have been reported in literature for cases where a slightly rough Ag layer leads to plasmonic scattering [116]. WARS measurements were carried out in order to further investigate scattering. An example of the reflectance WARS results for a bare 800 nm period MNP back-reflector and a μc-Si coated back-reflector of the same design are shown in 6.31.

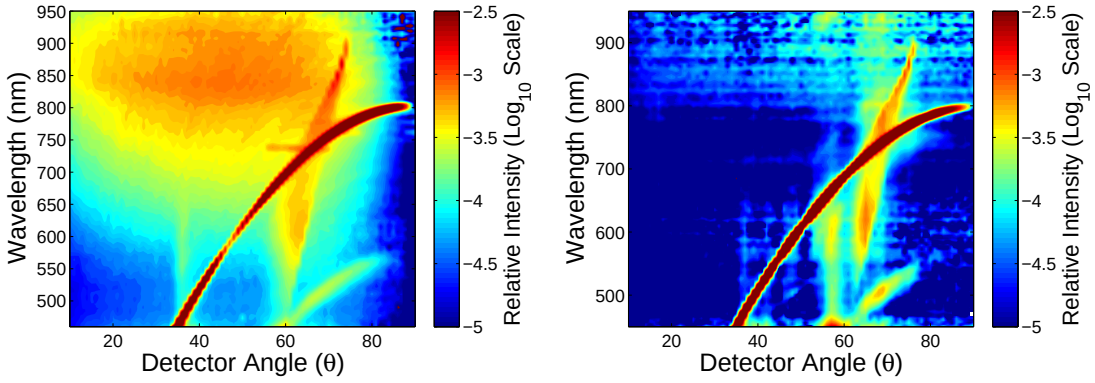

(a) Back-reflector.

(b) Pseudo cell

Figure 6.31: WARS measurements for 800 nm period MNP back-reflector and complete μc-Si pseudo cell.

Similarities can be immediately observed from the two WARS plots, with the primary scattered light clearly being due to diffraction in both cases. The long wavelength, broad plasmonic resonance scattering effect is also present in both plots although it has significantly reduced in intensity and has undergone a red-shift for the case of the pseudo-cell. Interestingly the unexplained, diffraction like scattering patterns are also present in both plots. this arguably gives some credence to the theory that these effects could be spurious results caused by multiple reflections within the experimental arrangement.

At first glance, a clear link cannot be seen between the peaks in diffuse reflectance and the WARS scattering plot. However, more detailed analysis of the results reveals that the high intensity diffractive light actually varies significantly in intensity with wavelength. From a simple visual analysis of the plot in Figure 6.31(b) it can be observed that the diffraction is weakest at around 550 nm, 610 nm and 700 nm and this corresponds exactly to the dips in measured diffuse reflectance. To verify this link, the WARS result of Figure 6.31(b) (for the 800 nm pitch MNP array) has been integrated over the angular range to give a calculated value for the total diffuse reflectance. The result is compared to the diffuse reflectance characteristics of the same sample as measured using the established and reliable integrating sphere technique, see Figure 6.32.

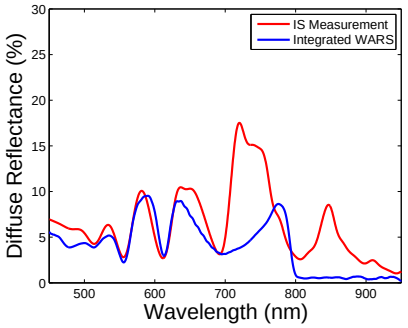

Figure 6.32: Diffuse reflectance results for an 800 nm MNP array pseudo cell, directly measured and calculated from WARS measurements.

The peaks in diffuse reflectance clearly match for both cases and visual analysis of the graph shows that the diffuse reflectance characteristics are heavily dominated by diffraction effects. The peak at 850 nm and high intensity peak between 700 and 800 nm shown only in the integrating sphere measurement result can be attributed to a similar effect in the diffraction from the longer diagonal period of the array, picked up in the three dimensional integrating sphere measurement but not in the single plane WARS measurement. These dips in diffraction intensity are due to the destructive interference of the thin μc-Si film causing diminished intensity for particular wavelengths. The experimental results have shown a clear reduction in reflectance in comparison to the planar case. However, for an actual device it is crucial that the increased absorption is predominantly in the μc-Si layer rather than the Ag MNPs. Ideally this would be determined by fabrication of a working solar cell device and subsequent measurement of the quantum efficiency. However, due to the small size of the experimental MNP arrays and limitations of the available tools and time scales of this work, full device fabrication was not feasible. Therefore, the alternative method of using simulation to further investigate absorption characteristics has been used by placing a cube of power monitors around the simulated MNP to allow for MNP absorption to be approximated. The simulation results for the absorption in the MNPs are shown in Figure 6.33.

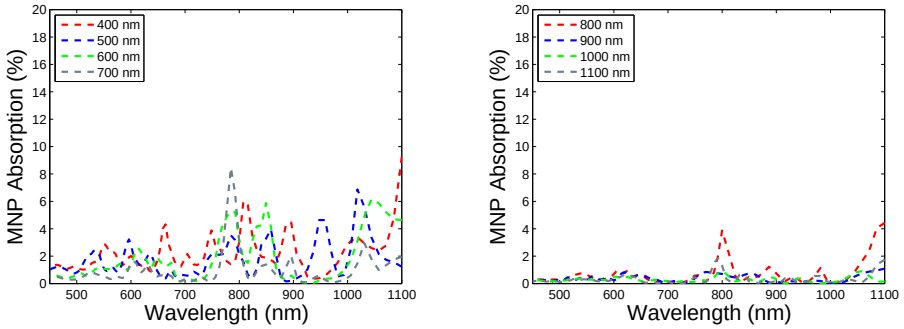

(a) 400 nm to 700 nm pitch.

(b) 800 nm to 1100 nm pitch.

Figure 6.33: Simulated absorption in Ag nanodisks.

MNPs in the smallest pitch arrays show the highest absorption and there is a clear trend of reduced absorption as the array period is increased. However, this trend is largely due to the MNP to surface area ratio and if this is accounted for the results are similar for all arrays. As with the reflectance results, the largest peaks in the simulated MNP absorption data in Figure 6.33 in many cases correspond to the interference patterns of the 500 nm μc-Si layer. Simulation results of the absorption in the 200 nm Ag back-reflector also show small peaks in absorption at identical locations, however, in the case of the simulated flat back-reflector this absorption is only around 0.5% and shows little variance with MNP array pitch. For the case of the most absorbing array, with a pitch of 400 nm, the simulated MNP absorption is 1.3% and the bulk Ag absorption is 0.54% giving a total parasitic absorption of 1.87%. However, experimental results show a decrease in average reflectance from 71% to 40.4%. Indicating that if the simulated MNP absorption is correct, then the 400 nm period array still provides a useful absolute absorption enhancement of 28.73% in comparison to a planar device.

The measurement results have shown a clear decrease in reflectance and simulations have indicated that the majority of the corresponding increased absorption is within the μc-Si layer. However, much of the absorption enhancement may not actually be caused by the diffraction and plasmonic effects of the embedded MNP arrays but could in fact be caused by the replicated periodic structure at the top of the μc-Si layer. The conformal PECVD depositing of μc-Si results in the array pattern being replicated in a scaled up form at the front surface of the pseudo-cell, this effect is verified by the FIB cross sectional image previously shown in Figure 6.16. These μc-Si nanodomes will not only have a diffraction grating effect on light but will also provide anti-reflection for some wavelengths due to the refractive index gradient effect, therefore increasing transmittance into the μc-Si. This has been investigated through simulation by simulating the pseudo-cell structures with and without the nanodome patterned silicon. The resulting simulated total reflectance for the case of a planar front surface is shown for each of the MNP arrays in Figure 6.34.

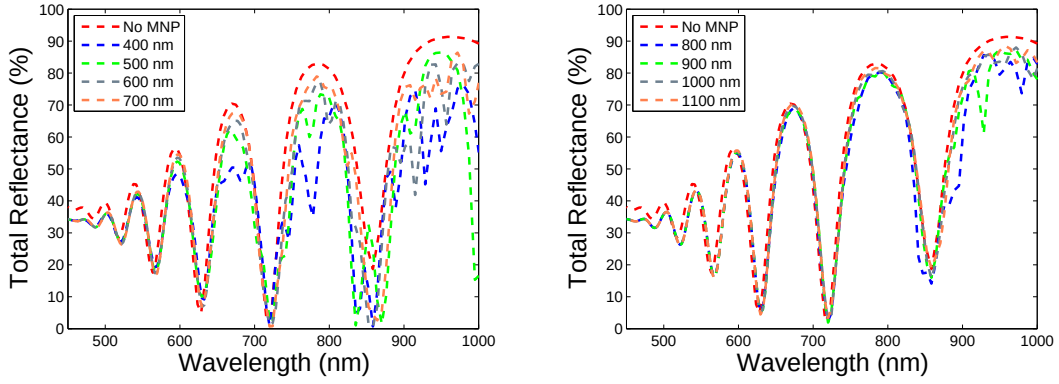

(a) 400 nm to 700 nm pitch.

(b) 800 nm to 1100 nm pitch.

Figure 6.34: Simulated total reflectance of μc-Si pseudo cell with periodic MNP array back-reflector but flat μc-Si top surface.

With the removal of the front μc-Si nanodomes the reflectance has dramatically increased, However, in all cases it is still lower than for the same structure with no MNP arrays. Simulations of the MNP array based devices generally show decreased reflectance and thus increased overall absorption at the longer wavelengths. This is to be expected as the plasmon resonance should occur over this wavelength range. The small difference in short wavelength reflectance between simulations with and without MNP arrays is surprising and is possibly simply due to changes in the meshing of the structure.

A summary of the quantified total reflectance for measurement and simulation results is given in Table 6.1.

Array Pitch	Measured Ref.	Simulated Ref.	Simulated Ref. (Planar μc-Si Top)
No MNP	71.8	48	48
400 nm	40.5	36.43	38.2
500 nm	32.2	36.4	39.6
600 nm	35.9	37.7	41.3
700 nm	44	40.7	42.4
800 nm	50	43.5	43.9
900 nm	54.8	44.5	45
1000 nm	65.4	45.3	45.45
1100 nm	60.1	46.1	45.8

Table 6.1: Integrated reflectance of MNP array pseudo cells.

The data in the table highlights the contribution of the μc-Si nanodomes which have caused a noticeable decrease in the reflectance, particularly for samples with relatively small array periodicities. However, the simulated results demonstrate that even when the μc-Si nanodome is removed there is still an overall decrease in integrated reflectance of between 2.2% and 9.8% depending on array pitch. The highest simulated MNP absorption was found to be 1.3%, significantly less than the reduction in reflectance, thus verifying that absorption in the μc-Si is increased by the addition of back-reflector MNP arrays. The simulated absorption of the μc-Si, MNP and bulk Ag for each array pitch is shown in the bar chart of Figure 6.35. The results for measured absorption are also shown for comparison, in this case an approximation of the absorption within the MNP and bulk Ag has been calculated using the ratio between μc-Si and metal absorption from the simulation results.

The chart clearly highlights the relatively small scale of parasitic absorption which is shown to decrease with increased array pitch. The same trends can be observed for experimental and simulated results, with and without the top μc-Si nanodome, with each case showing the best array pitch to be 500 nm. In this case, the measured total reflectance is more than halved from 71.8% to 32.2%, which equates to an change in total absorption from 28.2% to 67.8%, with simulations suggesting a parasitic absorption of

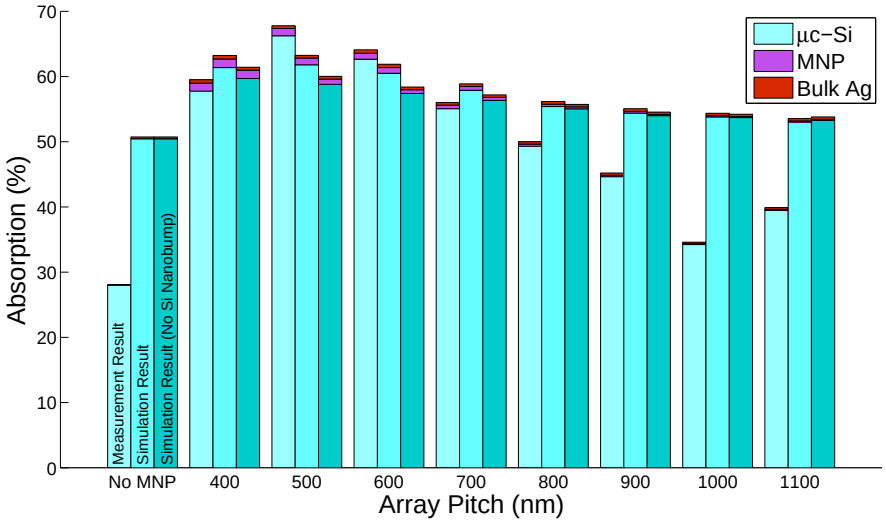

Figure 6.35: Absorption within different parts of the pseudo-cell structure for a planar design and each MNP array pitch studied.

only 1.55%. Furthermore, the previously shown reflectance spectra revealed that the largest increase in absorption is found at long wavelengths, in the region that traditional light-trapping techniques such as textured TCOs have little effect. Although the trends between measurement and simulation show good agreement, the absolute values vary significantly, with the measurement showing significantly less absorption, particularly for the structure with no MNP array and of for those with MNP arrays of a large pitch. This is due to the more pronounced dips in simulation reflectance that are present in Figure 6.29 leading to increased transmittance into the simulated μc-Si layer. The cause of these exaggerated interference patterns is largely due to the perfectly planar layers used in the simulation model which do not exactly match the physical case in which a small amount of roughness is present. It is also possible that the optical constants for the modelled μc-Si layer are inaccurate, in particular, the imaginary part which governs absorption within the material can be difficult to accurately determine using the technique of ellipsometry. Overall, the measurements and simulations have both shown encouraging results with a definitive increase in absorption. The highest absorption measurement of 67.8%, for the 500 nm MNP array equates to a relative absorption enhancement of 140% in comparison to a planar device. This is a similar level to that which could be achieved for the same thickness of μc-Si on a textured TCO, where test simulations have shown the total absorption to be around 65.5%.

6.4 Conclusions

The work presented within this chapter has investigated the potential of incorporating periodic metal nanoparticle arrays into the back-reflector design of a thin-film μc-Si solar cell with the aim of increasing useful absorption within the semiconductor. The study of array position indicates that arrays provide the best results when the MNPs are separated from the back-reflector by a thin TCO layer, therefore localizing the particles. Of the two ITO thicknesses investigated, the 70 nm layer is shown to give the best results and this is also the case for simple back-reflectors with no MNP arrays, such as those typically used for thin-film a-Si solar cells. FDTD simulations of the various back-reflector designs are shown to correctly predict trends, verifying FDTD as a viable tool for this investigation. However, the exact agreement between measurement and simulation is not ideal, with simulations typically showing a slightly red-shifted reflectance spectra.

The comprehensive study of the effect of array pitch, based on the 70 nm ITO/Ag back-reflector design revealed that the best absorption enhancement is achieved from an array pitch of 500 nm. The use of a μc-Si layer to represent a pseudo-cell rather than an active device benefits from the simplicity of the approach, but has the significant drawback that operational device characteristics such as quantum efficiency cannot be measured, therefore making it difficult to determine the usefulness of any absorption enhancement. This limitation was countered through the use of FDTD simulations to approximately determine the extent of absorption within the back-reflector metal or MNPs and the μc-Si layer. The results show that even with parasitic absorption taken into account, the nanoparticles still provide a significant, useful optical enhancement. Further extension of the simulations revealed that a portion of this enhancement is due to anti-reflection from the nanodomes present on the top of the μc-Si layer due to conformal deposition. However, even after the removal of these domes within the simulation, absorption enhancement is still observed, albeit notably diminished. In particular, the remaining absorption enhancement is found at long-wavelengths, where traditional textured TCOs under-perform and where it is most needed within a photovoltaic device. The results shown here clearly demonstrate that the inclusion of MNPs within the back-reflector of a thin solar cell can provide a useful light-trapping enhancement in comparison to a planar alternative. However, for the specific designs studied, the levels of total absorption enhancement are similar to that which could be achieved with the simpler approach of random texturing. It is possible that with further optimization, the MNP array approach could lead to a more significant enhancement but for the current designs the small enhancement over texturing does not justify the increased device complexity and cost. Given that texturing is effective at shorter wavelengths and MNPs can be tuned for long-wavelength scatter, a more optimized design could consist of a combination of the two approaches (see Figure 6.36).

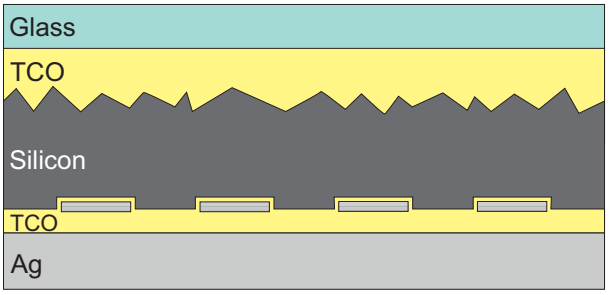

Figure 6.36: Possible design for optimal light-trapping of both short and long wavelength light.

Such a design could prove difficult to fabricate but should be considered for future work. It is also possible that randomizing the MNP arrays could have a positive effect as it would allow for optimization of the MNP surface area coverage without having to consider diffractive orders which can lead to out-coupling of light if not designed carefully.

Chapter 7

Conclusions and Future Work

The need for efficient light-trapping within the growing technology of thin photovoltaics has been highlighted and several light-trapping schemes have been investigated in detail. This study has focused on two specific approaches for the enhancement of absorption through light-trapping: the established approach of sub-wavelength scale random texturing and the more novel approach of a plasmonic grating back-reflector. These key concepts are illustrated along with a planar device structure in Figure 7.1.

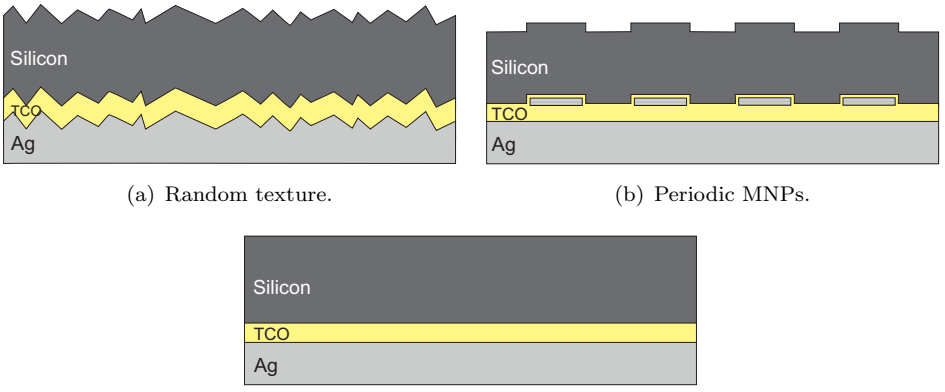

(a) Random texture.

(b) Periodic MNPs.

(c) Planar.

Figure 7.1: Light-trapping designs investigated along with planar architecture.

For accurate comparison and optimization of these light-trapping techniques, a reliable characterization method is crucial, a study of the literature and available commercial options revealed a surprising lack of standardization and tools for the comprehensive determination of scattering. Specifically, for applications which require high power, broadband illumination over a small spot size, no commercial tools exist. A wavelength and angle resolved scattering (WARS) measurement system was therefore designed, developed and thoroughly tested as part of this investigation. Tests showed that the system provides excellent accuracy which was verified by integrating over the full angular range and comparing results to traditional measurements of total diffuse scatter

carried out using an integrating sphere. Extensive characterization of a variety of TCOs carried out using the WARS system highlighted crucial differences in the angular distributions of scattering and allowed links to be made between the average incline angle of facets and the angle of scatter. WARS measurements of MNP based back-reflector designs were able to clearly show the distribution of scattered light due to separate diffraction and plasmonic resonance effects. Furthermore, the custom measurement also revealed anomalous scattering features within the diffracting planes of several samples, the intensity of these features was too low to be significant for the aims of this investigation but their as yet unexplained origins could warrant extensive future work and these features would not have been detected using conventional measurements. The success of the WARS measurement system, which can also be used for more standard measurements of angle of incidence versus specular reflectance or transmittance [117], has led to a second system being built at the University of Southampton, and a third system currently being developed at the University of New South Wales. The WARS measurement has also received interest from industry leading to collaborative projects with 'NSG Pilkington'.

With accurate methods for characterization in place, a variety of commercial and novel textured TCO films were topographically and optically characterized and clear links between surface roughness and light scattering were verified by a systematic study of FTO samples of increasing roughness, fabricated at different temperatures. Significantly rougher experimental AZO samples were shown to provide far superior haze to the FTO samples, however, they also exhibited low overall transmittance. The optical characteristics of the two commercial TCOs were found to be nearly identical but the novel WARS measurement technique proved useful in revealing crucial differences in the angular distribution of scattered light which goes some way to explaining why the Asahi Type-U TCO often gives superior device performance. Analysis of absorption in a-Si layers deposited on to a range of TCOs showed that large increases in roughness, beyond that of the commercial standards, leads to only small increases in useful long wavelength absorption whilst actually reducing short wavelength absorption. This, combined with the fact that larger features also increase surface area and can be detrimental to the electrical characteristics of a device, led to the conclusion that current industry TCOs have been well optimized and the random texturing approach alone is not feasible for improving long-wavelength light-trapping. Finite difference time domain (FDTD) simulations of TCO samples revealed that different approaches to the FDTD model setup could lead to similar results for total transmittance or reflectance but substantial differences in the simulated far-field scatter. The approach of using absorbing (PML) boundaries with a Gaussian source was shown to be dramatically more accurate than that of periodic boundaries and a plane wave source. This approach was used for the simulation of each of the TCOs studied in this work with good agreement between measurement and simulation shown in most cases. This validation of the FDTD approach allowed for further investigation through simulation where it was shown that

scaling a textured interface in the z-axis alone is more effective than full scaling and can lead to large increases in scattering with little reduction in total transmittance. Demonstrating that it may be possible to further optimize TCOs optically, but at the unacceptable cost of increased fabrication issues caused by cracks in layers deposited on to high aspect ratio features and diminished electrical characteristics from increased surface recombination.

The study of periodic Ag nanoparticles incorporated into a typical thin-film solar cell back-reflector has demonstrated the crucial sensitivity of the position of the array within the back-reflector with a separation of 70 nm of ITO between the MNPs and bulk Ag shown to give the best result of the three designs studied. FDTD simulations of back-reflector designs with no semiconductor absorber layers were shown to give reasonable agreement with measurement results, with distinct peaks and dips in the spectra at approximately the same wavelengths and intensity levels, although in several cases the simulation results were shown to be slightly red-shifted. This is possibly due to small inaccuracies in optical constant values. The match between simulation and measurement noticeably diminished when the μc-Si layer was added to the model, dramatically increasing simulation complexity and the potential for error. The differences between these simulations and the measured characteristics have been attributed to two main mechanisms. Firstly, the slight roughness present in a physical device that was not represented in the planar layers of the simulation, leading to stronger interference effects in simulation results. Secondly, the values for the imaginary part of the complex refractive index for the deposited μc-Si layer may have been inaccurate. However, despite the poor agreement between absolute values of the simulation and measurement results, the same trends were still apparent and in both cases the back-reflector design consisting of an MNP array with a 500 nm pitch was shown to be the best. This design results in a total measured integrated absorption of 67.8% with simulations indicating a parasitic absorption of just 1.5%. This compares favourably to simulations of a μc-Si layer of the same thickness modelled on a randomly rough Ag substrate where the total absorption was calculated as 65.5%, the portion of which is parasitic could not be determined due to the complexities of modelling textured structures. Both of these cases show a significant enhancement over a planar structure in which the measured absorption was just 28.2%. It therefore appears that the MNP approach can be used to enhance light-trapping to roughly the same extent as texturing. However, the added complexity of this approach could make it unlikely to be economically viable for the case of the modest gains demonstrated here.

Future work is already in progress for the WARS measurement system, the third version of which has undergone several upgrades at the design stage including an improved laser source with a broader wavelength range and higher total power output, along with the use of multiple, more sensitive, detectors to enable more accurate characterization and to extend the wavelength range of the measurement up to 1700 nm. Further modifications

to the system could allow for the measurement of scattering in three dimensions, rather than the single plane measurement that is currently carried out. The key challenge here would be the mechanical design of the system, ensuring that the centre of rotation is the same for each axis and sourcing a suitable motorized stage capable of carrying out the necessary movement whilst fitting within the confines of the set-up. Modifications could also be made to the alignment procedure of the system where high resolution distance measurement tools could be incorporated to allow for more accurate, fully automated alignment.

With regards to FDTD simulations of textured TCOs, the work here has shown that if the correct approach is taken then good agreement between the measured and simulated total and diffuse transmittance characteristics can be achieved. However, the full WARS characteristics extracted from FDTD simulations showed diffraction like features that were not present in the WARS measurement due to the much larger area probed. As increased computer resources become available, a larger TCO area can be modelled with the FDTD approach which will lead to increased accuracy and eventually a good agreement between WARS measurement and simulation should be achieved. This would pave the way for efficient and accurate investigation of exactly how even subtle changes in surface texture effect the resulting WARS characteristics. This is difficult to study experimentally due to the lack of control in textured TCO fabrication, but as has been demonstrated here, AFM data can be easily altered to allow simulations to investigate resulting effects. For the case of FDTD simulations of periodic MNP arrays, the key challenge for the immediate future is to achieve an improved agreement between simulated and measured reflectance characteristics, particularly for the case in which a μc-Si layer has been added to the model. Improved results should be achievable by a more accurate matching of the modelled MNP shape to that of the physically deposited MNP. This would require several cross-sectional SEM images to be used to accurately determine the average shape of a deposited MNP which could then be input into the model. Simulation of the μc-Si layer could be improved by obtaining more accurate values for the imaginary component of the refractive index. This could be achieved by using alternative characterization methods, for example, the absorption coefficient could be calculated from a series of reflectance and transmittance measurements of planar μc-Si layers, or through more advanced techniques such as photoluminescence. Finally, a small amount of surface roughness could also be added to the simulation to more closely match the physical device structure, although this comes at the cost of increased computer resource requirements.

Once an improved fit between MNP array simulation and measurement has been obtained, the MNP arrays could be further optimized through simulation, allowing for detailed parameter sweeps of the MNP size, distance from back-reflector and distance from absorber layer. The further optimized back-reflector design could then be fabricated, ideally over a large area to allow for deposition of a full working device.

Measurements of quantum efficiency and cell efficiency could then be carried out to conclusively demonstrate useful absorption enhancement. Finally, more novel designs could be investigated which could utilize the long wavelength scattering characteristics of MNP arrays along with other techniques for short wavelength scatter. One interesting approach could be the inclusion of interface texturing at the front of a device with MNPs incorporated into the rear (see Figure 7.2). A design such as this would be quite feasible to model but would require extensive computer resources and experimental fabrication could prove to be prohibitively difficult.

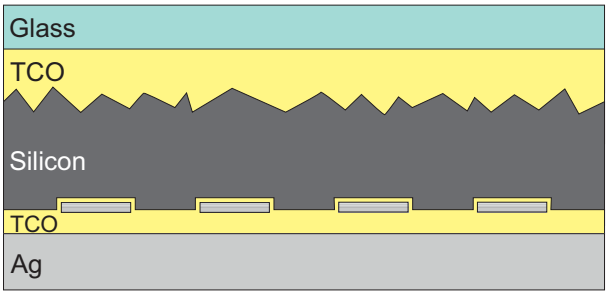

Figure 7.2: Possible design for optimal light-trapping of both short and long wavelength light.

Recent work, also carried out at the University of Southampton has demonstrated that a plasmonic back-reflector design based on randomly distributed nanoparticles can provide an enhancement in comparison to both planar, and textured based μc-Si devices. This approach does not benefit from diffraction effects but the simpler design constraints allow for easier optimization of parameters such as MNP surface area coverage. It is also possible that the best light-trapping arrangement does not lie wholly in the random or periodic domain but rather in a semi-ordered approach, such as a quasi-crystal structure.

In conclusion, it appears that there is still some room for improvement with regards to light-trapping for thin photovoltaics. However, the methods for achieving higher levels of light-trapping are becoming increasingly complex and difficult to realize. Further optimization of light-trapping mechanisms is challenging but can be accomplished with the use of sophisticated characterization and modelling tools such as those demonstrated within this work. This is essential as even modest gains in absorption can lead to thinner, less wasteful and more efficient solar cells, increasing the potential of the technology to overtake traditional fuels and push beyond grid-parity.

Appendix A

- Matlab Code: WARS Data Analysis

The following is an example of the Matlab code used to analyse the raw data outputted from the automated WARS measurement system. The % symbol is used to define comments which have been added to describe the purpose of subsequent code sections.

```
%Script file for automated post processing of WARS results

%clear all previous data
clear all

%<--------------------------specify program parameters
%User specifies filename of Haze data to be used for comparison/calibration
SampleName = 'TCO1Haze';

%User specifies root filename of WARS data
SampleName2 = 'TCO1WARS';

%User set to 0 for single plane data, set to 1 for 3D data (isotropic
%samples only)
Total = 1;

%User sets minumum and maximum scale values
ScaleMax = -2.3;
ScaleMin = -3.3;

%User selects file number and number of measurements to average over
%(if several measurements were carried out on one sample
```

```
FileSelect = 1;
Averages = 1;

%user specified angular step size used for measurement
stepsize = 1;

%set to zero for measurements carried out in reflectance, 1 for
%transmittance
Transmission = 1;

%Set axis for smoothing, 0 = no smothing, 1 = smooth along x axis only, 2 =
%smooth along x and y axis
Nice = 2;

%Set to 1 to normalize WARS data with source measurement, set to 0 to
%normalize with zero order sample transmittance
NormWithSource=1;

%Set scaling factor as determined from calibration measurement
ScaleFactor=15;

%Set number of points for moving average (smoothing)
Sm=10;

%End of user input0---------------------------------------------->


%Program builds full file paths and loads data from files
filepath = strcat('', SampleName2, '_Scan1');
Hazefilename = strcat(SampleName, 'Tran');
load (Hazefilename);

%Haze is calculated from diffuse and total transmittance measurements,
%variables are stored.
RealHaze = (DiffuseTransmittance./TotalTransmittance)*100;
RealHaze = DiffuseTransmittance;
wavelengthHZ = wavelength;

% define wavelength data constants for spectromter (on spectrometer
% datasheet)
a0=226.251847947653;
```

```
a1=0.526010699431936;
a2=-5.53394300019106e-5;
a3=-2.07883774778667e-9;

%calculate wavelength values associated with each data point.
for i=1:1:2048
wavelength(i)= a0+ (a1*i)+(a2*i^2) + (a3*i^3);
end
numwav = length(wavelength);

%alter scales if output is only for single 2D plane
if (Total==0)
    ScaleMax = ScaleMax - 2.5;
    ScaleMin = ScaleMin - 2.5;
end

%Data locations in WARS measurement file
SpecItimeLoc = [0 0 0 0];
SpecPowerLoc = [0 3 0 3];
ScatPowerLoc = [0 2 0 2];
DarkItimeLoc = [0 0 6 0];
SpecDataRange = [0 4 99 2051];
DarkDataRange = [0 1 6 2048];

if (stepsize == 1)
    measurenumber = 89;
elseif (stepsize == 5)
    measurenumber = 15;
end

ScatDataRange = [0 4 measurenumber 2051];
ScatItimeLoc = [0 3 measurenumber 3];
AngleLoc = [0 0 measurenumber 0];

%Load dark data
filedark = strcat(filepath, '_Dark.csv');
DarkData0 = dlmread(filedark,',', DarkDataRange);
DarkDataI = dlmread(filedark,',', DarkItimeLoc);

%begin loop to load and calculate mean of data
for i = 1:1:Averages,
```

```
    if (Averages > 1)
FileSelect = i;
    end

FileNo = int2str(FileSelect);

%load filepaths for data arrays
FileSpecPath(i) = cellstr(strcat(filepath, '_Spec_', FileNo, '.csv'));
FileScatPath(i) = cellstr(strcat(filepath, '_Scat_', FileNo, '.csv'));
FileSourcePath(i) = cellstr(strcat(filepath, '_Beam_', FileNo, '.csv'));

%load specular data into data arrays
SpecFileName = char(FileSpecPath(i));
SpecData0 = dlmread(SpecFileName, ',', SpecDataRange );
SpecDataTest = SpecData0;
SpecDataI = dlmread(SpecFileName,',', SpecItimeLoc);
SpecPower = dlmread(SpecFileName,',', SpecPowerLoc);
SpecItime(:, :, i) = SpecDataI;

%subtract relevant dark data
for n= 1:1:100,
SpecData0(n, :) = (SpecData0(n, :) - DarkData0(7,:))./SpecItime(:,1, i);
if (n == 1)
SpecData = SpecData0(n,:);
else
    SpecData(1,:) = SpecData(1,:) + SpecData0(n,:);
end
end

%Average specular data
SpecDataAVG(:,:,i) = SpecData(1,:)/100;
SpecItime(:, :, i) = SpecDataI;


%load source data into data arrays
SourceFileName = char(FileSourcePath(i));
SourceData0 = dlmread(SourceFileName, ',', SpecDataRange );
SourceDataI = dlmread(SourceFileName,',', SpecItimeLoc);
SourcePower = dlmread(SourceFileName,',', SpecPowerLoc);
SourceItime(:, :, i) = SourceDataI;
```

```
%subtract relevant dark from source
for n= 1:1:100,
SourceData0(n, :) = (SourceData0(n, :) - DarkData0(7,:))./...
    SpecItime(:,1, i);
if (n == 1)
SourceData = SourceData0(n,:);
else
    SourceData(1,:) = SourceData(1,:) + SourceData0(n,:);
end
end

%Average data
SourceDataAVG(:,:,i) = SourceData(1,:)/100;
SourceItime(:, :, i) = SourceDataI;

%Load scattering data
ScatFileName = char(FileScatPath(i));
ScatData0 = (dlmread(ScatFileName,',', ScatDataRange));
ScatDataI = (dlmread(ScatFileName,',', ScatItimeLoc));
ScatPower = (dlmread(ScatFileName,',', ScatPowerLoc));
ScatData(:, :, i) = ScatData0;
ScatItime(:, :, i) = ScatDataI;

%import angular range
Angles = dlmread(ScatFileName,',', AngleLoc);
Angles = cat(1, Angles,0);
%convert to radians
AnglesRad = Angles*(pi/180);

%determine length of data set
num_angles = length(ScatItime(:, :, 1));

%Dark and iintegration time correct scattering data
ScatDataDC(:, :, i) = ScatData(:, :, i);
for n=1:num_angles,
  for s=1:7,
    if (ScatItime(n, 1, i)== DarkDataI(s))
    ScatDataDC(n,:, i) = ScatData(n,:, i)-DarkData0(s,:);
    ScatDataDC(n,:, i) = ScatDataDC(n,:, i)/ScatItime(n, 1, i);
    end
    end
```

```
end

SpecDataDCPC(:,:, i) = SpecDataAVG(:, :, i);
SourceDataDCPC(:,:, i) = SourceDataAVG(:, :, i);

%smooth data
SmScatDataDC = ScatDataDC;
SmSpecDataDCPC = SpecDataDCPC;
SmSourceDataDCPC = SourceDataDCPC;
SmSpecDataDCPC(1,:, i) = smooth(SpecDataDCPC(1,:, i), Sm);
SmSourceDataDCPC(1,:, i) = smooth(SourceDataDCPC(1,:, i), Sm);
for n=1:num_angles,
 SmScatDataDC(n,:, i) = smooth(ScatDataDC(n,:, i), Sm);
end

%flip data array to get in correct orientation and add specular data to
%scattering data array
FlipSmScatDataDC = zeros(num_angles, numwav, Averages);
FinalDataA = zeros(num_angles +1, numwav, Averages);
FlipSmScatDataDC(:, :, i) = flipud(SmScatDataDC(:, :, i));
FinalDataA(:, :, i) = cat(1,SmSpecDataDCPC(:, :, i),FlipSmScatDataDC...
    (:, :, i));
FinalDataB=FinalDataA;

%normalize data (divide all data by source or zero order transmittance
for n=1:(num_angles + 1),
   if NormWithSource==1,
       FinalDataB(n, :, i) = (FinalDataA(n,:, i)./...
           SmSourceDataDCPC(1,:, i));
   else
       FinalDataB(n, :, i) = (FinalDataA(n,:, i)./SmSpecDataDCPC(1,:,i));
   end
end

SpecTran = SmSpecDataDCPC(1,:,i)./SmSourceDataDCPC(1,:, i);

%extract and orient data
FinalDataTrans(:, :, i) = FinalDataB(:, :, i)';
FinalDataTrans(:, :, i) = fliplr(FinalDataTrans(:, :, i));

%correct for out of plane scattering (if sample is isotropic
```

```
 if (Total==1)
   for n=1:measurenumber+1,
     FinalDataTrans(:,n, i) = (FinalDataTrans(:, n, i)*...
         ((4*0.11*sin(AnglesRad(n))/0.0015)));
   end
 end

 if (i ==1)
FinalDataAverage = zeros(numwav, num_angles +1);
 end
 FinalDataAverage = FinalDataAverage + FinalDataTrans(:, :, i);

 %End of averaging loop
end

FinalDataAverage = FinalDataAverage./Averages;

%get data in correct orientation
Angles2 = flipud(Angles);
FinalDataAverageflip = fliplr(FinalDataAverage);

%calculate diffuse transmittance from WARS measurement data (integrate over
% angles)
for i=1:2048,
Haze3(i) = abs(trapz(Angles2(5:91), FinalDataAverageflip(i,5:91)));
Haze3(i) = Haze3(i)./ScaleFactor;
end
RealHaze2 = interp1(wavelengthHZ, RealHaze, wavelength);

%calculate specular data based on a 5 degree cone (as with IS measurements)
for i=1:2048,
SpecCone(i) = abs(trapz(Angles2(1:3), FinalDataAverageflip(i,1:3)));
SpecCone(i) = SpecCone(i)./ScaleFactor;
end

Haze3 = Haze3*100;
HazeMult = Haze3./RealHaze2';
HazeMultAVG = mean(HazeMult(300:800));
HazeMultAVGCalc = HazeMultAVG;

%plot measured and calculated diffuse transmittance for visual comparison
```

```
figure(1)
plot(wavelength, Haze3, wavelengthHZ, DiffuseTransmittance);
 axis manual;
 axis([450 900 0 100])
legend('Haze calculated from WARS', 'Haze Directly Measured',...
    'location', 'best')
SampleNameH = strcat(SampleName, 'WarsHaze');
save(SampleNameH, 'wavelength', 'Haze3', 'wavelengthHZ',...
    'DiffuseTransmittance');
SampleNameIS = strcat(SampleName, 'ISCalc');
%Save data
save(SampleNameIS, 'wavelength', 'Haze3', 'wavelengthHZ',...
    'DiffuseTransmittance','SpecTran' );

%scale all scattering data in accordance with calibration factor
for i=1:2048,
   FinalDataAverage(i, :) = (FinalDataAverage(i, :)./ScaleFactor);
end

%take log of all scattering data for plotting
for i=1:2048,
   FinalDataAverage(i, :) = log10(FinalDataAverage(i, :));
end

%smooth data as definied by user
if (Nice > 0)
    if (Nice > 1)
    for i=1:2048,
    FinalDataAverage(i, :) = smooth(FinalDataAverage(i, :), 5);
    end
    end
    for i = 1:81,
           FinalDataAverage(:, i) = smooth(FinalDataAverage(:, i), 20);
    end
end

%Output WARS contour plot
figure(2)
colormap(jet(64))
contourf(Angles, wavelength, FinalDataAverage, ScaleMin:0.02:ScaleMax,...
    'LineColor', 'none');
```

```
axis([0 85 450 930])
caxis([ScaleMin ScaleMax]);
c = colorbar('location','eastoutside');
ylabel(c, 'Relative Intensity (Log_{10} Scale)', 'FontSize',18,...
    'FontName','Arial')
xlabel('Detector Angle (\theta)','FontSize',20,'FontName','Arial')
ylabel('Wavelength (nm)','FontSize',20,'FontName','Arial')
set(gca,'FontSize',14,'FontName','Arial')

%save data
SampleNameW = strcat(SampleName, 'Wars');
save(SampleNameW, 'Angles', 'wavelength', 'FinalDataAverage');
```

Appendix B

- Matlab Code: AFM Data Manipulation

The following is an example of the Matlab code used to manipulate AFM data, with the key aim of smoothing out edge discontinuities which can occur when simulations programs periodically tile the data. With small modifications the same program is used to geometrically scale AFM data. The % symbol is used to define comments which have been added to describe the purpose of subsequent code sections.

```
% Program to manipulate AFM data and eliminate edge discontinuities

%clear all previous data
clear all

%set AFM data area in um
area = 10;

%set colormap
colormap gray

%set resolution in pixels
resolution = 512;

%specify AFM data filename (txt file)
Filename = 'TCO1';
%program adds .txt extension
FullFilename = strcat(Filename, '.txt');

%specify number of edge pixels to smooth over
```

```
edgelimit = 4;

%specify step size for smoothing loop
edgestep = 1;

%specify number of tiles if tiling is required (can be used to visually
%check for discontinuities
Tiles = 2;

% X and Y axis values are calculated
Xarray = [1:1:resolution];
Yarray = [resolution:-1:1];
X = Xarray*(area/resolution);
Y = Yarray*(area/resolution);

%tile array is initiated
TileXarray = [1:1:resolution*Tiles];
TileYarray = [1:1:resolution*Tiles];

%Z values are imported from text file, file must have no headers
Z = textread(FullFilename);

%data is tiled if required
if Tiles ==2,
TileZ = [Z Z; Z Z];
elseif Tiles == 3,
    TileZ = [Z Z Z; Z Z Z; Z Z Z];
end

%plot original data
figure(1)
mesh(Xarray, Yarray, Z);
axis([0 resolution 0 resolution]);

%plot tiled original data
figure(2)
colormap gray
mesh(TileXarray, TileYarray, TileZ);
axis([0 resolution*Tiles 0 resolution*Tiles]);

%store original data in variable
```

```
OrigZ = Z;

%begin edge smoothing loop
for edgeregion=1:edgestep:edgelimit,

%initialize arrays
loweredge = resolution-edgeregion+1;
zerofiller = zeros(edgeregion, resolution);
zerofillerLR = zeros(resolution,edgeregion);
Zmod = Z;
Zmod2 = Z;
Zmod(1:edgeregion,:) = zerofiller;
Zmod(loweredge:resolution,:) = zerofiller;
Zmod(:,1:edgeregion) =zerofillerLR;
Zmod(:,loweredge:resolution) =zerofillerLR;

%plot result for smoothed data
figure(4)
mesh( Xarray,Yarray,  Zmod);
axis([0 resolution 0 resolution]);

%smooth top and bottom data
Zbottom = Z(loweredge:resolution,:);
Ztop = Z(1:edgeregion,:);
ZBLimit = Zbottom(1,:);
ZULimit = Ztop(edgeregion,:);
edgevalue = (ZBLimit + ZULimit)./2;
Zbottomnew = Zbottom;
Zbottomnew(edgeregion,:) = edgevalue;
Ztopnew = Ztop;
Ztopnew(1,:) = edgevalue;

%smooth bottom data
BottomDiff = edgevalue - ZBLimit;
BottomDiffInc = BottomDiff./edgeregion;
loopmax = edgeregion-1;
for i=2:1:loopmax,
    Zbottomnew(i,:) = Zbottomnew(i-1,:) + BottomDiffInc;
end

%smooth top data
```

```
TopDiff = edgevalue - ZULimit;
TopDiffInc = TopDiff./edgeregion;
for i = loopmax:-1:1,
  Ztopnew(i,:) = Ztopnew(i+1,:) + TopDiffInc;
end

%smooth left and right data
Zright = Z(:,loweredge:resolution);
Zleft = Z(:, 1:edgeregion);
ZLLimit = Zleft(:, edgeregion);
ZRLimit = Zright(:,1);
LRedgevalue = (ZLLimit + ZRLimit)./2;
Zleftnew = Zleft;
Zleftnew(:,1) = LRedgevalue;
Zrightnew = Zright;
Zrightnew(:,edgeregion) = LRedgevalue;

%smooth left data
LeftDiff = LRedgevalue - ZLLimit;
LeftDiffInc = LeftDiff./edgeregion;
for i = loopmax:-1:1,
    Zleftnew(:,i) = Zleftnew(:,i+1) +LeftDiffInc;
end

%smooth right data
RightDiff = LRedgevalue - ZRLimit;
RightDiffInc = RightDiff./edgeregion;
for i=2:1:loopmax,
    Zrightnew(:,i) = Zrightnew(:,i-1) +RightDiffInc;
end

%build test image array
Zmod2(1:edgeregion,:) = Ztopnew;
Zmod2(loweredge:resolution,:) = Zbottomnew;
Zmod2(:,1:edgeregion) =Zleftnew;
Zmod2(:,loweredge:resolution) =Zrightnew;

%plot result
figure(3)
mesh( Xarray,Yarray,  Zmod2);
axis([0 resolution 0 resolution]);
```

```
%tile data
if Tiles ==2,
TileZmod2 = [Zmod2 Zmod2; Zmod2 Zmod2];
elseif Tiles == 3,
    TileZmod2 = [Zmod2 Zmod2 Zmod2; Zmod2 Zmod2 Zmod2; Zmod2 Zmod2 Zmod2];
end

%plot tiled data
figure(6)
mesh(TileXarray, TileYarray, TileZmod2);
axis([0 resolution*Tiles 0 resolution*Tiles]);

Z = Zmod2;
end

%save output
newfilename = strcat(Filename, 'TileMod.txt');
dlmwrite([newfilename], TileZmod2, '\t');
```

Appendix C

- FDTD Solutions Code: Script for outputting far-field data

The following is a sample of the custom script code used within the FDTD Solutions program in order to output far-field data for direct comparison with WARS measurements. The # symbol is used to define comments which have been added to describe the purpose of subsequent code sections.

```
#Set Monitor name
m="Ref";

#get frequency data
f=getdata(m,"f");

#convert frequency to wavelength
wav = c/f*1e9;

#calculate transmission through monitor
Tr=transmission(m);

#plot transmission
plot(wav, Tr, "wavelength(um)","transmission");
setplot("y min", 0);
setplot("y max", 1);

#set number of frequency points and resolution of far field data
nf=length(f);
```

```
res=200;

#initialise matrices
out=matrix(res*2,360,nf);
phiout=matrix(res*2,360);
cone_1=matrix(nf,1);
cone_2=matrix(nf,1);
cone_5=matrix(nf,1);
cone_45=matrix(nf,1);
cone_89=matrix(nf,1);
total=matrix(nf,1);

#begin to loop through wavelengths (frequencies)
for (i=1:nf) {

#calculate farfied (select one code line for plane wave or gaussian)

#code for gaussian source, pml boundaries
#temp=farfield3d(m,i,res*2,res*2,1);
#code for planewave source, pml boundaries
temp=farfield3d(m,i,res*2,res*2,2,20,20);
#code for plane wave source with periodic x and y boundaries
#temp=farfield3d(m,i,res*2,res*2,2,100,100);

#define ux and uy
ux=farfieldux(m,i,res*2,res*2);
uy=farfielduy(m,i,res*2,res*2);

#FF integrate for several different halfangles (gets total light within a...
certain cone.

halfangle = 1;
halfangle4 = 2;
halfangle5 = 5;
halfangle2 = 45;
halfangle3 = 89;
theta0=0;
phi0=0;
cone_1(i) = farfield3dintegrate(temp, ux, uy, halfangle, theta0, phi0);
cone_45(i) = farfield3dintegrate(temp, ux, uy, halfangle2, theta0, phi0);
cone_89(i) = farfield3dintegrate(temp, ux, uy, halfangle3, theta0, phi0);
```

```
cone_2(i) = farfield3dintegrate(temp, ux, uy, halfangle4, theta0, phi0);
cone_5(i) = farfield3dintegrate(temp, ux, uy, halfangle5, theta0, phi0);
total(i) = farfield3dintegrate(temp, ux, uy);

#define theta and phi
theta = linspace(-90, 90, res*2);
for (a=1:360) {
phi = a;
ffsphr = farfieldspherical(temp, ux, uy, theta, phi);
phiout(1:res*2,a) = ffsphr;
}

out(1:res*2,1:360, i)=phiout;
}

#put source values into variables.
sourcen = sourcenorm(f);
sourcep = sourcepower(f);
sourcei = sourceintensity(f);

#save all data for matlab processing
matlabsave("TestFile1",wav,  theta, phi,out, sourcen, cone_1, cone_2, cone_5,...
cone_45, cone_89, total,sourcei, sourcep, Tr);
```

References

[1] A. Sieminski, "International Energy Outlook 2013," tech. rep., US Energy Information Administation, 2013.

[2] BP, "Statistical Review of World Energy 2013," tech. rep., British Petroleum, 2013.

[3] A. Ajanovic, C. Dahl, L. Schipper, L. M. W. Leggett, and D. A. Ball, "The implication for climate change and peak fossil fuel of the continuation of the current trend in wind and solar energy production," *Energy Policy*, vol. 41, pp. 610–617, 2012.

[4] P. H. Gleick, "Environmental consequences of hydroelectric development: The role of facility size and type," *Energy*, vol. 17, no. 8, pp. 735–747, 1992.

[5] G. W. Crabtree and N. S. Lewis, "Solar energy conversion," *Physics Today*, vol. 60, no. 3, pp. 37–42, 2007.

[6] R. F. Service, "Solar energy: Is it time to shoot for the sun?," *Science*, vol. 309, no. 5734, pp. 548–551, 2005.

[7] EIA, "Annual Energy Outlook 2013 with Projections to 2040," tech. rep., U.S. Energy Information Administation, 2013.

[8] S. Moosavian, N. Rahim, J. Selvaraj, and K. Solangi, "Energy policy to promote photovoltaic generation," *Renewable and Sustainable Energy Reviews*, vol. 25, pp. 44–58, 2013.

[9] W. Palz, "Photovoltaic solar energy, spearheading Germanys renewable energy policy: an example to others," *EPJ Photovoltaics*, vol. 3, p. 30901, June 2012.

[10] B. Burger, "Electricity production from solar and wind in Germany in 2013," tech. rep., Fraunhofer Institute for Solar Energy Systems ISE, 2014.

[11] A. W. Copeland, O. D. Black, and A. B. Garrett, "The photovoltaic effect," *Chemical Reviews*, vol. 31, no. 1, pp. 177–226, 1942.

[12] C. E. Fritts, "On a new form of selenium cell, and some electrical discoveries made by its use," *Am. Ass. for the Advancement of Sci.*, vol. 33, pp. 97–108, 1883.

[13] N. Tesla, "Method of utilizing radiant energy," 1901. Patent No. 685,958.

[14] A. B. Arons and M. B. Peppard, "Einsteins's proposal of the photon concept-a translation of the annalen der physik paper of 1905," *American Journal of Physics*, vol. 33, no. 5, pp. 367 – 374, 1965.

[15] D. M. Chapin, C. S. Fuller, and G. L. Pearson, "A New Silicon p-n Junction Photocell for Converting Solar Radiation into Electrical Power," *Journal of Applied Physics*, p. 676, 1954.

[16] J. Zhao, A. Wang, and M. A. Green, "24.5% effciency silicon pert cells on mcz substrates and 24.7% efficiency perl cells on fz substrates," *Progress in Photovoltaics: Research and Applications*, vol. 7, pp. 471–474, 1999.

[17] M. A. Green, "The path to 25% silicon solar cell efficiency: History of silicon cell evolution," *Progress in Photovoltaics*, vol. 17, pp. 183–189, 2009.

[18] W. Shockley and H. Queisser, "Detailed balance limit of efficiency of p-n junction solar cells," *Journal of Applied Physics*, vol. 32, pp. 510–519, Mar. 1961.

[19] D. M. Bagnall and M. Boreland, "Photovoltaic technologies," *Energy Policy*, vol. 36, pp. 4390–4396, 2008.

[20] J. Burschka, N. Pellet, S.-J. Moon, R. Humphry-Baker, P. Gao, M. K. Nazeeruddin, and M. Grätzel, "Sequential deposition as a route to high-performance perovskite-sensitized solar cells.," *Nature*, vol. 499, pp. 316–9, July 2013.

[21] M. Liu, M. B. Johnston, and H. J. Snaith, "Efficient planar heterojunction perovskite solar cells by vapour deposition.," *Nature*, vol. 501, pp. 395–8, Sept. 2013.

[22] G. F. Brown and J. Q. Wu, "Third generation photovoltaics," *Laser and Photonics Reviews*, vol. 3, pp. 394–405, 2009.

[23] M. A. Green, K. Emery, Y. Hishikawa, W. Warta, and E. D. Dunlop, "Solar cell efficiency tables (version 43)," *Progress in Photovoltaics: Research and Applications*, vol. 22, pp. 1–9, Jan. 2014.

[24] G. Beaucarne, "Silicon thin-film solar cells," *Advances in OptoElectronics*, vol. Volume 2007, p. Article ID 36970, 2007.

[25] M. Green, *Solar cells: Operating principles, technology, and system applications.* Prentice Hall, 1982.

[26] D. L. Staebler and C. R. Wronski, "Reversible conductivity changes in discharge-produced amorphous si," *Applied Physics Letters*, vol. 31, no. 4, pp. 292–294, 1977.

[27] Y. Sakai, "Light induced effects in a-si:h films and solar cells," *Materials Reserach Society*, vol. 70, 1986.

[28] J. Poortmans and V. Arkhipov, *Thin film solar cells: fabrication, characterization and applications*. John Wiley & Sons Inc, 2006.

[29] A. Barnett, R. Opila, A. Lennon, J. Ji, D. Lin, Y. Yao, H. Li, M. Curtin, S. Bengtson, D. Stryker, M. Carroll, A. Gerger, A. Lochtefeld, J. Han, and L. Wang, "16.8% Efficient Ultra-Thin Silicon Solar Cells on Steel," *28th European Photovoltaic Solar Energy Conference and Exhibition*, pp. 2641–2644, Nov. 2013.

[30] J. Meier, P. Torres, R. Platz, S. Dubail, U. Kroll, J. A. A. Selvan, N. P. Vaucher, C. Hof, D. Fischer, H. Keppner, A. Shah, K. D. Ufert, P. Giannoules, and J. Koehler, "On the way towards high efficiency thin film silicon solar cells by the ''micromorph" concept," in *Amorphous Silicon Technology*, vol. 420 of *Materials Research Symposium Proceedings*, pp. 3–14, 1996.

[31] D. Domine, *The Role of Front Electrodes and Intermediate Reflectors in the Optoelectronic Properties of High-Efficiency Micromorph Solar Cells*. PhD thesis, Universite de Neuchatel, 2009.

[32] D. Domine, P. Buehlmann, J. Bailat, A. Billet, A. Feltrin, and C. Ballif, "Optical management in high-efficiency thin-film silicon micromorph solar cells with a silicon oxide based intermediate reflector," *Physica Status Solidi-Rapid Research Letters*, vol. 2, pp. 163–165, 2008.

[33] A. Madan, "Progress in four-terminal nano-crystalline Si/amorphous Si solar cells," *Conference Record of the Thirty-first IEEE Photovoltaic Specialists Conference, 2005.*, pp. 1452–1455, 2005.

[34] E. Yablonovitch and G. Cody, "Intensity enhancement in textured optical sheets for solar cells," *IEEE Transactions on Electron Devices*, vol. 29, pp. 300–305, Feb. 1982.

[35] S. Boden, *Biomimetic nanostructured surfaces for antireflection in photovoltaics*. PhD thesis, University of Southampton, 2009.

[36] J. Muller, B. Rech, J. Springer, and M. Vanecek, "Tco and light trapping in silicon thin film solar cells," *Solar Energy*, vol. 77, pp. 917 – 930, 2004.

[37] NSG, "NSG TEC Literature," 2014.

[38] AGC, "Transparent Conductive Oxide (TCO) Film for Thin Film Silicon Photovoltaic Devices," 2014.

[39] K. Sato, Y. Gotoh, Y. Wakayama, K. Adachi, and H. Nishimura, "Reports of the research laboratory," *Asahi Glass Co.*, vol. 42, 1992.

[40] J. Löffler, R. Groenen, J. Linden, M. van de Sanden, and R. Schropp, "Amorphous silicon solar cells on natively textured ZnO grown by PECVD," *Thin Solid Films*, vol. 392, pp. 315–319, July 2001.

[41] U. Dagkaldiran, A. Gordijn, F. Finger, H. Yates, P. Evans, D. Sheel, Z. Remes, and M. Vanecek, "Amorphous silicon solar cells made with SnO2:F TCO films deposited by atmospheric pressure CVD," *Materials Science and Engineering: B*, vol. 159-160, pp. 6–9, Mar. 2009.

[42] J. Meier, J. Spitznagel, S. Fay, C. Bucher, U. Graf, U. Kroll, S. Dubail, and A. Shah, "Enhanced light-trapping for micromorph tandem solar cells by LP-CVD ZnO," in *Conference Record of the Twenty-Ninth IEEE Photovoltaic Specialists Conference, 2002.*, pp. 1118–1121, IEEE, 2002.

[43] J. C. Lee, V. Dutta, J. Yoo, J. Yi, J. Song, and K. H. Yoon, "Superstrate p-i-n a-Si:H solar cells on textured ZnO:Al front transparent conduction oxide," *Superlattices and Microstructures*, vol. 42, pp. 369–374, July 2007.

[44] M. Python, D. Dominé, T. Söderström, F. Meillaud, and C. Ballif, "Microcrystalline silicon solar cells: effect of substrate temperature on cracks and their role in post-oxidation," *Progress in Photovoltaics: Research and Applications*, vol. 18, pp. 491–499, Apr. 2010.

[45] D. Rittenhouse, "Explanation of an Optical Deception," *Transactions of the American Philisophical Society*, vol. 2, pp. 37–42, 1786.

[46] J. Fraunhofer, "Kurzer Bericht von den Resultaten neuerer Versuche über die Gesetze des Lichtes, und die Theorie derselben," *Annalen der Physik und der physikalischen Chemie*, vol. 74, no. 8, pp. 337–378, 1823.

[47] C. Palmer, *Diffraction Grating Handbook*, vol. 46. Newport Corporation, 6th ed., Jan. 2005.

[48] F. Seitz, D. Turnbull, and D. Pines, "Electron Interaction in Metals," *Solid State Physics*, vol. 1, pp. 367–450, 1955.

[49] M. Brongersma and P. Kik, *Surface plasmon nanophotonics*. Springer Verlag, 2007.

[50] S. Pillai, K. R. Catchpole, T. Trupke, and M. a. Green, "Surface plasmon enhanced silicon solar cells," *Journal of Applied Physics*, vol. 101, no. 9, p. 093105, 2007.

[51] H. Atwater and A. Polman, "Plasmonics for improved photovoltaic devices.," *Nature materials*, vol. 9, pp. 205–13, Mar. 2010.

[52] K. Kelly, E. Coronado, L. Zhao, and G. Schatz, "The optical properties of metal nanoparticles: the influence of size, shape, and dielectric environment," *The Journal of Physical Chemistry B*, vol. 107, pp. 668–677, Apr. 2003.

[53] H. Tan, L. Sivec, B. Yan, R. Santbergen, M. Zeman, and A. H. M. Smets, "Improved light trapping in microcrystalline silicon solar cells by plasmonic back reflector with broad angular scattering and low parasitic absorption," *Applied Physics Letters*, vol. 102, no. 15, p. 153902, 2013.

[54] J. Bhattacharya, N. Chakravarty, S. Pattnaik, W. Slafer, R. Biswas, and V. Dalal, "Comparison of optical properties of periodic photonicplasmonic and randomly textured back reflectors for nc-Si solar cells," *Journal of Non-Crystalline Solids*, vol. 358, pp. 2313–2318, Sept. 2012.

[55] H. Davies, "The reflection of electromagnetic waves from a rough surface," *Proceedings of the IEE-Part IV: Institution Monographs*, vol. 101, no. 7, pp. 209–214, 1954.

[56] J. Porteus, "Relation between the height distribution of a rough surface and the reflectance at normal incidence," *JOSA*, vol. 53, no. 12, pp. 1394–1402, 1963.

[57] H. P. Pillai, J. Krč, and M. Zeman, "Optical Modeling of a-Si : H Thin Film Solar Cells with Rough Interfaces .," in *Proceedings of Semiconductor Advances for Future Electronics*, pp. 159–162, 2001.

[58] C. C. Lin, W. L. Liu, and C. ing Hsieh, "Scalar scattering model of highly textured transparent conducting oxide," *Journal of Applied Physics*, vol. 109, p. 014508, Jan. 2011.

[59] H. Horvath, "Gustav Mie and the scattering and absorption of light by particles: Historic developments and basics," *Journal of Quantitative Spectroscopy and Radiative Transfer*, vol. 110, pp. 787–799, July 2009.

[60] Q. Fu and W. Sun, "Apparent optical properties of spherical particles in absorbing medium," *Journal of Quantitative Spectroscopy and Radiative Transfer*, vol. 100, pp. 137–142, July 2006.

[61] M. Vollmer and U. Kreibig, "Optical properties of metal clusters," *Springer Ser. Mater. Sci*, vol. 25, 1995.

[62] R. J. Martin, "Mie Scattering Formulae for Non-spherical Particles," *Journal of Modern Optics*, vol. 40, pp. 2467–2494, Dec. 1993.

[63] K. Yee, "Numerical solution of initial boundary value problems involving Maxwell's equations in isotropic media," *Antennas and Propagation, IEEE Transactions on*, vol. 14, pp. 302–307, Apr. 1966.

[64] H.-L. Yu and C.-C. Hsaio, "Comparison of different measurement methods for transmittance haze," *Metrologia*, vol. 46, pp. S233–S237, Aug. 2009.

[65] S. Schröder, M. Trost, T. Herffurth, A. von Finck, and A. Duparré, "Sophisticated light scattering techniques from the VUV to the IR regions," in *SPIE Optical Engineering + Applications* (L. M. Hanssen, ed.), p. 84950V, International Society for Optics and Photonics, Oct. 2012.

[66] P. A. V. Nijnatten, J. M. C. D. Wolf, and I. J. E. Schoofs, "Spectrophotometer accessories for thin film characterisation," *Spectrum*, 2008.

[67] K. Jäger, O. Isabella, L. Zhao, and M. Zeman, "Light scattering properties of surface-textured substrates," *Physica Status Solidi (C)*, vol. 4, Jan. 2010.

[68] K. Jäger, O. Isabella, R. A. C. M. M. van Swaaij, and M. Zeman, "Angular resolved scattering measurements of nano-textured substrates in a broad wavelength range," *Measurement Science and Technology*, vol. 22, p. 105601, Oct. 2011.

[69] H. Liu, V. Avrutin, N. Izyumskaya, U. Özgür, and H. Morkoç, "Transparent conducting oxides for electrode applications in light emitting and absorbing devices," *Superlattices and Microstructures*, vol. 48, pp. 458–484, Nov. 2010.

[70] L. Prušáková, S. Flickyngerová, M. Fischer, I. Novotný, M. Tijssen, M. Netrvalová, M. Zeman, V. Tvarožek, and P. Šutta, "Analysis of single junction a-Si:H solar cells grown on different TCOs," *Vacuum*, vol. 86, pp. 765–768, Jan. 2012.

[71] A. Luque and S. Hegedus, *Handbook of Photovoltaic Science and Engineering*. Wiley-Blackwell, 2010.

[72] H. Sakai, T. Yoshida, S. Fujikake, Y. Ichikawa, A. Ueda, O. Ishiwata, and M. Nagano, "Effects of the surface morphology of transparent electrode on film deposition and photovoltaic performance of A-SI:H solar cells," *Journal of Non-Crystalline Solids*, vol. 115, pp. 198–200, Dec. 1989.

[73] N. Pilkington, "Global glass handbook 2012, architectural products," tech. rep., 2012.

[74] H. M. Yates, P. Evans, D. W. Sheel, S. Nicolay, L. Ding, and C. Ballif, "The development of high performance SnO2:F as TCOs for thin film silicon solar cells," *Surface and Coatings Technology*, vol. 213, pp. 167–174, Dec. 2012.

[75] S. Y. Guo, L. Sahoo, G. Sosale, and a. E. Delahoy, "Textured, doped, ZnO thin films produced by a new process for a-Si and CIGS solar cell application," *Proceedings of SPIE*, vol. 6651, pp. 66510B–66510B–10, 2007.

[76] D. Dominé, *The role of front electrodes and intermediate reflectors in the optoelectronic properties of high-efficiency micromorph solar cells*. PhD thesis, Université de Neuchâtel, 2009.

[77] J. Pankow, B. To, and T. Gessert, "Comparison between research-grade and commercially available SnO¡inf¿2¡/inf¿ for thin-film CdTe solar cells," in *2008 33rd IEEE Photovolatic Specialists Conference*, pp. 1–5, IEEE, May 2008.

[78] D. N. R. Payne, S. A. Boden, O. D. Clark, A. E. Delahoy, and D. M. Bagnall, "Characterization of experimental textured ZnO:Al films for thin film solar cell applications and comparison with commercial and plasmonic alternatives," in *2010 35th IEEE Photovoltaic Specialists Conference*, pp. 001560–001564, IEEE, June 2010.

[79] P. Beckmann and A. Spizzichino, *The Scattering of Electromagnetic Waves from Rough Surfaces.* Pergamon Press, 1987.

[80] K. Bittkau, T. Beckers, S. Fahr, C. Rockstuhl, F. Lederer, and R. Carius, "Nanoscale investigation of light-trapping in a-Si:H solar cell structures with randomly textured interfaces," *Physica Status Solidi (a)*, vol. 205, pp. 2766–2776, Dec. 2008.

[81] J. Lacombe, K. Chakanga, S. Geissendorfer, K. von Maydell, and C. Agert, "Optical modeling of light trapping in thin film silicon solar cells using the FDTD method," in *2010 35th IEEE Photovoltaic Specialists Conference*, pp. 001535–001539, IEEE, June 2010.

[82] X. Chen, B. Jia, J. K. Saha, B. Cai, N. Stokes, Q. Qiao, Y. Wang, Z. Shi, and M. Gu, "Broadband enhancement in thin-film amorphous silicon solar cells enabled by nucleated silver nanoparticles.," *Nano letters*, vol. 12, pp. 2187–92, May 2012.

[83] V. E. Ferry, M. a. Verschuuren, H. B. T. Li, R. E. I. Schropp, H. a. Atwater, and A. Polman, "Improved red-response in thin film a-Si:H solar cells with soft-imprinted plasmonic back reflectors," *Applied Physics Letters*, vol. 95, no. 18, p. 183503, 2009.

[84] C. Eisele, C. E. Nebel, and M. Stutzmann, "Periodic light coupler gratings in amorphous thin film solar cells," *Journal of Applied Physics*, vol. 89, no. 12, p. 7722, 2001.

[85] C. Heine and R. H. Morf, "Submicrometer gratings for solar energy applications.," *Applied optics*, vol. 34, pp. 2476–82, May 1995.

[86] R. Dewan and D. Knipp, "Light trapping in thin-film silicon solar cells with integrated diffraction grating," *Journal of Applied Physics*, vol. 106, no. 7, p. 074901, 2009.

[87] J. Gjessing, E. S. Marstein, and A. Sudbø, "2D back-side diffraction grating for improved light trapping in thin silicon solar cells.," *Optics express*, vol. 18, pp. 5481–95, Mar. 2010.

[88] M. Kroll, S. Fahr, C. Helgert, C. Rockstuhl, F. Lederer, and T. Pertsch, "Employing dielectric diffractive structures in solar cells - a numerical study," *Physica Status Solidi (a)*, vol. 205, pp. 2777–2795, Dec. 2008.

[89] H. Li, Q. Wang, J. Chen, J. Krc, and W. J. Soppe, "Light trapping in amorphous silicon solar cells with periodic grating structures," *Optics Communications*, vol. 285, no. 5, pp. 808–815, 2012.

[90] W. Zhang, G. Zheng, L. Jiang, and X. Li, "Combined front diffraction and back blazed gratings to enhance broad band light harvesting in thin film solar cells," *Optics Communications*, vol. 298-299, pp. 250–253, July 2013.

[91] M. Solano, M. Faryad, A. S. Hall, T. E. Mallouk, P. B. Monk, and A. Lakhtakia, "Optimization of the absorption efficiency of an amorphous-silicon thin-film tandem solar cell backed by a metallic surface-relief grating," *Applied optics*, vol. 52, no. 5, pp. 966–979, 2013.

[92] A. Bozzola, M. Liscidini, and L. C. Andreani, "Photonic light-trapping versus Lambertian limits in thin film silicon solar cells with 1D and 2D periodic patterns," *Optics Express*, vol. 20, no. S2, pp. A224–A244, 2012.

[93] A. Campa, O. Isabella, R. van Erven, P. Peeters, H. Borg, J. Krc, M. Topic, and M. Zeman, "Optimal design of periodic surface texture for thin-film a-Si:H solar cells," *Progress in Photovoltaics: Research and Applications*, vol. 18, pp. 160–167, May 2010.

[94] J. Michel and L. Kimerling, "Design of Highly Efficient Light-Trapping Structures for Thin-Film Crystalline Silicon Solar Cells," *IEEE Transactions on Electron Devices*, vol. 54, pp. 1926–1933, Aug. 2007.

[95] X. Meng, E. Drouard, G. Gomard, R. Peretti, A. Fave, and C. Seassal, "Combined front and back diffraction gratings for broad band light trapping in thin film solar cell," *Optics Express*, vol. 20, no. S5, pp. A560–A571, 2012.

[96] E. R. Martins, J. Li, Y. Liu, J. Zhou, and T. F. Krauss, "Engineering gratings for light trapping in photovoltaics: The supercell concept," *Physical Review B*, vol. 86, p. 041404, July 2012.

[97] A. Naqavi, K. Söderström, F.-J. Haug, V. Paeder, T. Scharf, H. P. Herzig, and C. Ballif, "¡title¿Enhanced light trapping in realistic thin film solar cells using one-dimensional gratings¡/title¿," in *Enhanced light trapping in realistic thin film solar cells using one-dimensional gratings* (P. Ambs, D. Curticapean, C. Emmelmann, W. Knapp, Z. T. Kuznicki, and P. P. Meyrueis, eds.), pp. 80650A–80650A–8, SPIE-Int. Soc. Optical Engineering, Apr. 2011.

[98] T. K. Chong, J. Wilson, S. Mokkapati, and K. R. Catchpole, "Optimal wavelength scale diffraction gratings for light trapping in solar cells," *Journal of Optics*, vol. 14, p. 024012, Feb. 2012.

[99] H. Sai, H. Fujiwara, and M. Kondo, "Back surface reflectors with periodic textures fabricated by self-ordering process for light trapping in thin-film microcrystalline silicon solar cells," *Solar Energy Materials and Solar Cells*, vol. 93, pp. 1087–1090, June 2009.

[100] D. M. Schaadt, B. Feng, and E. T. Yu, "Enhanced semiconductor optical absorption via surface plasmon excitation in metal nanoparticles," *Applied Physics Letters*, vol. 86, no. 6, p. 063106, 2005.

[101] D. Derkacs, S. H. Lim, P. Matheu, W. Mar, and E. T. Yu, "Improved performance of amorphous silicon solar cells via scattering from surface plasmon polaritons in nearby metallic nanoparticles," *Applied Physics Letters*, vol. 89, no. 9, p. 093103, 2006.

[102] K. R. Catchpole and a. Polman, "Plasmonic solar cells.," *Optics express*, vol. 16, pp. 21793–800, Dec. 2008.

[103] K. R. Catchpole and A. Polman, "Design principles for particle plasmon enhanced solar cells," *Applied Physics Letters*, vol. 93, no. 19, p. 191113, 2008.

[104] H. Tan, R. Santbergen, A. H. M. Smets, and M. Zeman, "Plasmonic light trapping in thin-film silicon solar cells with improved self-assembled silver nanoparticles.," *Nano letters*, vol. 12, pp. 4070–6, Aug. 2012.

[105] R. Santbergen, T. L. Temple, R. Liang, A. H. M. Smets, R. A. C. M. M. van Swaaij, and M. Zeman, "Application of plasmonic silver island films in thin-film silicon solar cells," *Journal of Optics*, vol. 14, p. 024010, Feb. 2012.

[106] W. Bai, Q. Gan, F. Bartoli, J. Zhang, L. Cai, Y. Huang, and G. Song, "Design of plasmonic back structures for efficiency enhancement of thin-film amorphous Si solar cells.," *Optics letters*, vol. 34, pp. 3725–7, Dec. 2009.

[107] P. Chen, Y. Zhong, and H. Liu, "Role of surface plasmon polaritons and photonic modes in light absorption by thin-film solar cells patterned with metallic nanogratings," *Optics letters*, vol. 38, no. 4, pp. 573–575, 2013.

[108] W. E. I. Sha, W. C. H. Choy, and W. C. Chew, "A comprehensive study for the plasmonic thin-film solar cell with periodic structure," *Optics Express*, vol. 18, no. 6, pp. 5993–6007, 2010.

[109] L. Yang, L. Li, W. Kong, and Z. Zhen, "Metal nanoparticles influence on light absorbed power of thin-film solar cell with periodic structure," *Optik* -

International Journal for Light and Electron Optics, vol. 124, pp. 1921–1925, July 2013.

[110] V. E. Ferry, A. Polman, and H. A. Atwater, "Modeling light trapping in nanostructured solar cells.," *ACS nano*, vol. 5, pp. 10055–64, Dec. 2011.

[111] S. Mokkapati, F. J. Beck, a. Polman, and K. R. Catchpole, "Designing periodic arrays of metal nanoparticles for light-trapping applications in solar cells," *Applied Physics Letters*, vol. 95, no. 5, p. 053115, 2009.

[112] U. W. Paetzold, E. Moulin, D. Michaelis, W. Bottler, C. Wachter, V. Hagemann, M. Meier, R. Carius, and U. Rau, "Plasmonic reflection grating back contacts for microcrystalline silicon solar cells," *Applied Physics Letters*, vol. 99, p. 181105, Oct. 2011.

[113] R. Sesuraj, T. Temple, and D. Bagnall, "Optical characterisation of a spectrally tunable plasmonic reflector for application in thin-film silicon solar cells," *Solar Energy Materials and Solar Cells*, vol. 111, pp. 23–30, Apr. 2013.

[114] R. W. Wood, "On a Remarkable Case of Uneven Distribution of Light in a Diffraction Grating Spectrum," *Proceedings of the Physical Society of London*, vol. 18, pp. 269–275, June 1902.

[115] A. Hessel and A. A. Oliner, "A New Theory of Woods Anomalies on Optical Gratings," *Applied Optics*, vol. 4, p. 1275, Oct. 1965.

[116] F.-J. Haug, T. Soderstrom, O. Cubero, V. Terrazzoni-Daudrix, and C. Ballif, "Plasmonic absorption in textured silver back reflectors of thin film solar cells," *Journal of Applied Physics*, vol. 104, no. 6, p. 064509, 2008.

[117] A. Asadollahbaik, S. A. Boden, M. D. B. Charlton, D. N. R. Payne, S. Cox, and D. M. Bagnall, "Reflectance properties of silicon moth-eyes in response to variations in angle of incidence, polarisation and azimuth orientation," *Optics Express*, vol. 22, p. A402, Feb. 2014.